

Part III

Physics Simulations

Chapter 12

Description of Simulation and Analysis Tools

Detailed simulation is the key technique for developing a detector design which achieves the physics objectives of BTeV. To accompany the simulations we have also developed analysis tools which approach those that we will use to analyze data from the experiment.

In this part of the BTeV proposal, we first discuss the simulation and analysis tools we have used to design the detector and to establish its physics reach. Next we present the results of studies of triggering and tagging, which are important to our physics sensitivity, followed by results on a variety of final states that are currently major goals of our physics program. The studies demonstrate, in addition to the excellent capabilities on these particular final states, the breadth and power of the BTeV spectrometer. The results presented here are only a small part of the simulation effort, which is used to study every aspect of detector design. Results of these studies appear throughout Part II and the appendices.

We have used two complementary simulation packages. The first, MCFast [1], is a fast parameterized simulation and analysis environment which allows the user to quickly change the detector design from a geometry file without having to do any coding. It is very useful in developing and refining the detector design. All early work on BTeV was done with MCFast, including the simulations done for the Preliminary Technical Design Report[2] (PTDR), which was submitted in the spring of 1999. The second package, BTeVGeant, is a rather complete simulation of the detector based on the GEANT 3 simulation framework[3]. It has a more complete implementation of all of the physics processes that operate on particles, charged and neutral, as they traverse the detector. Unlike MCFast, the BTeVGeant detector model is implemented by code and, therefore, recoding is required to change the detector model; so BTeVGeant is most appropriate for use only after the design has stabilized. We continue to use both systems: MCFast is used for studies of design changes and optimizations and for fast turnaround on issues for which a detailed simulation is unnecessary; BTeVGeant is used to study subtle backgrounds, tails of distributions, etc. We have especially relied on BTeVGeant for studies of final states that contain electromagnetic showers. BTeVGeant has a more complete and realistic description of the detector, including beampipes, supports, ma-

terial from readout electronics, etc. In order to facilitate comparisons between BTeVGeant and MCFast, BTeVGeant writes a file containing a good approximation of its detector specification in a form that can be input to MCFast; in this way we ensure that that studies done with either system are modeling as much as possible, given the intrinsic limitations of MCFast, the same detector. These comparisons provide new validation of MCFast in the areas which are of most interest to BTeV. Below, we describe both systems, starting with BTeVGeant.

Analysis involves: fitting of charged tracks and calculation of their position, angles and momenta; reconstruction of photons and neutral pions; identification of charged particle types – π , K, or p – based on signals from the Ring Imaging Cherenkov counters; identification of muons and electrons; reconstruction of the primary interaction vertex, or vertices; and reconstruction of secondary and tertiary decay vertices.

We carry this out using a framework which can operate on the output of either BTeVGeant or MCFast (although many calculations using MCFast have the analysis embedded in the simulation program itself, as a user routine). Track reconstruction is done at the trigger level by programs which are optimized specifically for triggering. For analysis, track pattern recognition is not yet done; instead the Monte Carlo truth information is used to collect hits which belong on each track and each track is fitted using a Kalman Filter. This algorithm gives a full covariance matrix for use in vertex fitting. The trigger-level track pattern recognition, which has much fewer resources at its disposal than will the ultimate off-line pattern recognition, has been demonstrated to have high efficiency and few false tracks; therefore the absence of true pattern recognition in the analysis package does not represent a serious overestimate of our efficiency. Shower reconstruction is performed using a package which is derived from the CLEO offline analysis package, which in turn was derived from the Crystal Ball offline analysis package. Particle identification and muon reconstruction are also done at this time. A fitting package is also provided in the analysis framework; this package can perform both mass-constraint fits and vertex fits, with the option of including the beam envelope as a constraint in the vertex fit. Below, we describe three of these packages – the Kalman filter, the shower reconstruction, and the particle identification program. The reconstruction programs used by the trigger are described in chapter 9.

12.1 BTeVGeant

A detector simulation package based on GEANT 3, BTeVGeant, has been developed for the physics studies presented in this proposal. The full detector geometry has been implemented within BTeVGeant, which writes out a simplified geometry description in the format of an MCFast geometry file. This facilitates comparisons between BTeVGeant and MCFast. BTeVGeant is, of necessity, written in mixed languages: Fortran 77, C, C⁺⁺. This allows us to take advantage of both the GEANT 3 tracing package, which is written in Fortran, and the existing BTeV trigger code, which is written in C. The BTeV vertex fitting package is written in Fortran, while the reconstruction code for the electromagnetic calorimeter, our newest package, is written in C⁺⁺. This strategy will allow us to migrate to the GEANT 4

package[4], which is written in C⁺⁺, with relative ease. We have done performance studies of BTeVGeant and have used it for many of the Monte Carlo simulations described in this proposal.

12.1.1 Design Considerations for BTeVGeant

We began development of a detailed Monte Carlo with a complete and up-to-date detector geometry description and a full simulation of the detector response about one year ago. Previously, we had presented results based on a parametric version of the electromagnetic calorimeter and MCFast tracing through the detector. Many physics processes are included in the MCFast modeling of the detector, but some are treated in an incomplete manner. For example, the MCFast model of multiple scattering does not include non-Gaussian tails, which is sufficient for many detector design studies but not for detailed physics simulations.

The GEANT based simulation studies and analyses have been aimed primarily at the following three final states of b-meson decays:

$$\begin{aligned} B_s &\rightarrow D_s K, D_s \rightarrow \phi \pi, K^* K \\ B^0 &\rightarrow D^{*-}(2010) \rho^+ \\ B^0 &\rightarrow \rho \pi \end{aligned}$$

We chose GEANT 3 for our detailed simulations for several reasons. We felt that GEANT 4, the more modern simulation tool kit in C⁺⁺ designed to support LHC experiments, had not been sufficiently tested, nor was it supported at Fermilab. Since we made our decision, however, numerous and very promising benchmarks have been done on GEANT 4 and we plan to incorporate GEANT 4 into future simulation developments.¹

The critical specifications for BTeVGeant are:

- A “hit level” simulation, leading ultimately to a complete digitization of all detector components. By “hit level”, we mean a simulation of the interaction of the track with the detector element, giving for instance a wire position and drift time, or the energy deposition in a block of the electromagnetic calorimeter. A “digitization” is a simulation of the TDC or ADC response, followed by an exact simulation of the data stream. While digitization is crucial for benchmarking the final trigger or reconstruction code, the digitization rarely has a significant effect on the resolution or hit occupancy and, for many studies, the simulated hits need not be fully digitized.
- Generation and tracking of all secondaries and decay products occurring within a beam crossing; secondaries may be generated in the tracking system, in the electromagnetic calorimeter, in the beampipe and in their mechanical support systems.

¹For instance, a member of the Muon Collider and Neutrino Factory group has successfully tested the design of a muon cooling channel in GEANT 4.

- A realistic implementation of the current detector geometry, including the magnets, beam pipes and supports for the tracking chambers and pixel detector. From the GEANT 3-based geometry, a simplified version of it must be generated so that the comparisons and cross-checks with the results obtained with MCFast can be done in a straightforward and convenient manner.
- Simulation of the charged particle reconstruction code and generation of Kalman filtered tracks, allowing tracking and vertexing resolution studies. We use a track fitting technique that is similar to the one in MCFast and which is described in section 12.1.8.
- Production of an output stream of simulated hits (or digitizations) so that trigger algorithms and prototypes of reconstruction code can be studied. The Level 1 and Level 2 trigger algorithms do full pattern recognition using the hits.

12.1.2 The BTeV Detector Geometry in BTeVGeant

We chose to implement the detector geometry by coding it as a GEANT 3 application in which the sizes and positions of the GEANT 3 volumes are declared via Fortran data statements. The disadvantage of this coding style is obvious: in order to understand the geometry the user must read source code and, in order to modify the geometry, the user incurs compilation overhead. MCFast, on the other hand, works from an ASCII geometry file which is much easier to read and to modify.

In addition to filling the GEANT 3 geometry information, each geometry subroutine also fills BTeV specific data structures, which were designed with the event reconstruction code and the trigger simulation code in mind. The trigger and analysis codes do not use the internal GEANT 3 geometry representation. These BTeV specific data structures are serialized and written to the output stream, allowing the offline analysis packages to have access to the same geometry information as was used for the simulation.

We now describe the features of the GEANT 3 implementation of the major subsystems of the BTeV detector; an overview of these subsystems is found in Part II of this proposal and Figure 12.1 shows GEANT 3 drawings of the full detector.

- The spectrometer dipole magnet. The horizontal gap of ≈ 20 inches has been sized to maximize the magnetic field at the interaction point and to leave enough space for the pixel detector and its support system. The yoke inserts, or shim plates, and the main magnet yoke are entered as a set of iron plates. The coils, assumed to be made of solid copper, are described by a set of rectangular boxes.
- The pixel detector: The pixel detector region, shown in Figures 12.2 and 12.3, consists of a cylindrical vacuum tank, the support and cooling structures and the silicon wafers. The pixel tank has, on each end, a thin hemispherical aluminum window, implemented in GEANT 3 as a section of a sphere. The glassy-carbon manifold and the coolant liquid (water + alcohol) are implemented as tubes and small rectangular boxes. There are two pixel planes per station. Each pixel plane is divided longitudinally (along the beam

line) into two regions, one simulating the sensor and readout wafers (pure silicon) and the other simulating the sum of the readout infrastructure, the FLEX-circuit, cooling and the mechanical support (a mixture of copper and plastic). The detector planes are subdivided into a 9×9 checker-board array, with each cell representing one wafer. In order to allow for a hole for the beam, the center wafer in this array is not present. In reality, the wafers will be slightly tilted, ≈ 7 degrees away from perpendicular to the beam, such that the sensitive area of one chip overlaps the dead readout periphery of its neighbor. This detail, known as “shingling”, does not have a significant impact on resolutions, occupancies or pattern recognition complexity and it has been omitted from the description.

- The beam pipe: The pixel tank window and the beam pipe up to the entrance of the Cherenkov counter will be installed in one piece for each arm. The forward tracking devices will be installed around this beam pipe. However, in order to facilitate the simulation of the forward tracking stations, the GEANT 3 description of the beam pipe is subdivided into shorter longitudinal segments; this ensures that the GEANT 3 volumes in different sub-volume hierarchies do not overlap. The flanges connecting the beam pipe to the inner Cherenkov beam pipes have also been included in the description.
- The forward tracking system (FT): A detail of two forward tracking stations is shown in Figure 12.4. There are two distinct sets of forward tracking devices: planes of straw tubes and silicon strip planes. Each have their own container volumes and support structures. For instance, the silicon strip planes are supported from both sides, and over their entire height, by a 5 mm thick carbon plate.
- The RICH detectors: The radiators, gas and aerogel, have been implemented as trapezoidal and rectangular boxes respectively. A track, emitted from the luminous region, will encounter, in order, the Cherenkov entrance window, a negligible amount of Cherenkov gas, the aerogel volume, the main gas volume, the mirror and the exit window. Other details included in the simulation are the readout panel, located outside of the fiducial tracking volume, the beam pipe and the beam vacuum. The full simulation of the response of the RICH detector is done at analysis time and is described in detail in Appendix A.
- The Electromagnetic Calorimeters (ECAL): The BTeV detector has two electromagnetic calorimeters, one in each arm. BTeVGeant can simulate two different options for the ECAL geometry: 1) A planar box-shaped calorimeter built of rectangular lead tungstate, PbWO_4 , crystals, 2.6 cm on side and 22 cm long; and 2) a projective calorimeter built of tapered crystals, $2.6 \times 2.6 \text{ cm}^2$ at the front face and 22 cm long, installed to point at the I.P. While the box-shaped calorimeter was the first to be coded and is still used for the validation of MCFast, the projective geometry is now the BTeV baseline calorimeter. Users of BTeVGeant choose between the two geometry options with a runtime switch.

- The Muon detector. The muon detector, shown in Figures 12.5 and 12.6, consists of hadron filters, beam pipe shielding and detector stations. The hadron filters are implemented as GEANT 3 boxes, filled with iron and with a hole for the beam. Each detector station consists of eight overlapping pie shaped octants. There are 3 views (r, u, v); the u and v views are strung at $\pm 22.5^\circ$ with respect to the r view.

12.1.3 The Magnetic Field Model

The magnetic field which will be produced by the main BTeV dipole magnet has been computed using the Tosca package[5]. In order to simplify and to speed up the simulation and analysis codes, two approximations are made in the model of the magnetic field used by BTeVGeant. First, only the main component of the magnetic field, B_x , is used. Second, B_x is assumed to be piecewise constant with discontinuous jumps occurring at fixed values of z . The sum of $B_x \Delta z$, summed over the region of non-zero field, is constrained to be equal to the integral $\int B_x dz$ from Tosca. The motivation for the second approximation is that it allowed us to use the Kalman filter from MCFast without re-writing the transport routines. Although the simulated hits obtained using this approximate model of the field will not match the real hits, this approximation affects neither the tracking resolution nor the eventual pattern recognition problems. In particular, a constant field is a good model of the field within the volume of the pixel detectors.

12.1.4 Tracking Accuracy

The GEANT 3 propagation routines are coded in single precision, which was found to be insufficient to model the combination of high precision devices and long lever arms which are present in the BTeV spectrometer. We reached this conclusion after benchmarking the position accuracy of the GEANT 3 propagation routines against the MCFast propagation routines, which are native double precision. The tests were performed in the absence of any stochastic processes. When we replaced the single precision GEANT 3 Runge-Kutta integrator with a double precision version of the same code, GEANT 3 produced acceptable results. Although multiple scattering will usually be larger than the inaccuracies in the single precision tracing, we chose to run using the double precision version because it allows us to run the verification suite for the track and vertex fitters. This verification suite includes running with no multiple scattering and with reduced multiple scattering.

12.1.5 Calorimetry Cuts

GEANT 3 permits the user to control the thresholds and cutoffs of the many physics processes which it simulates. Low thresholds give a more realistic and detailed simulation but can require large amounts of computer time. This, in turn, can make it difficult to produce large enough samples of simulated events to make precise statements about efficiency and background rejection. Therefore it is important to tune wisely the cutoffs and thresholds so

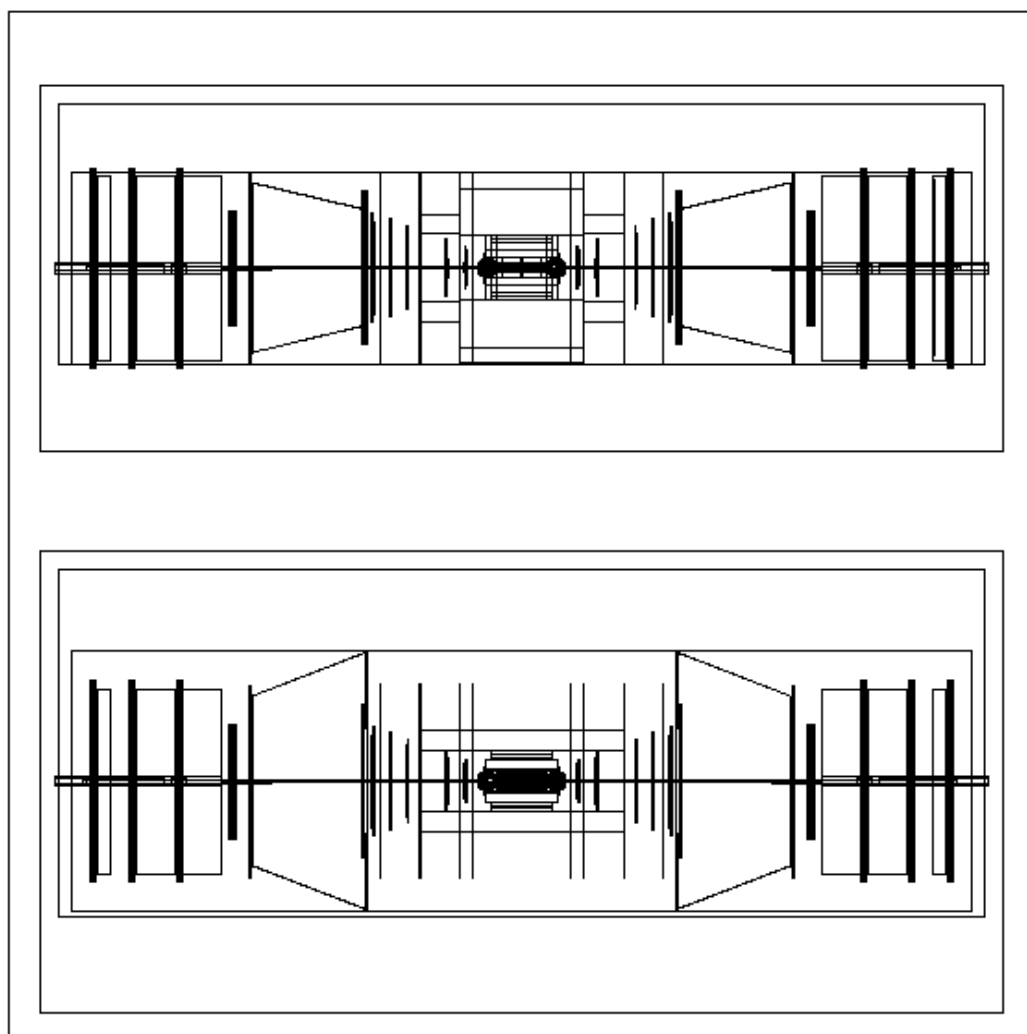


Figure 12.1: The BTeV spectrometer as drawn by BTeVGeant in elevation view (upper figure) and plan view (lower figure). The total length of this representation of the C0 Hall is about 26 m.

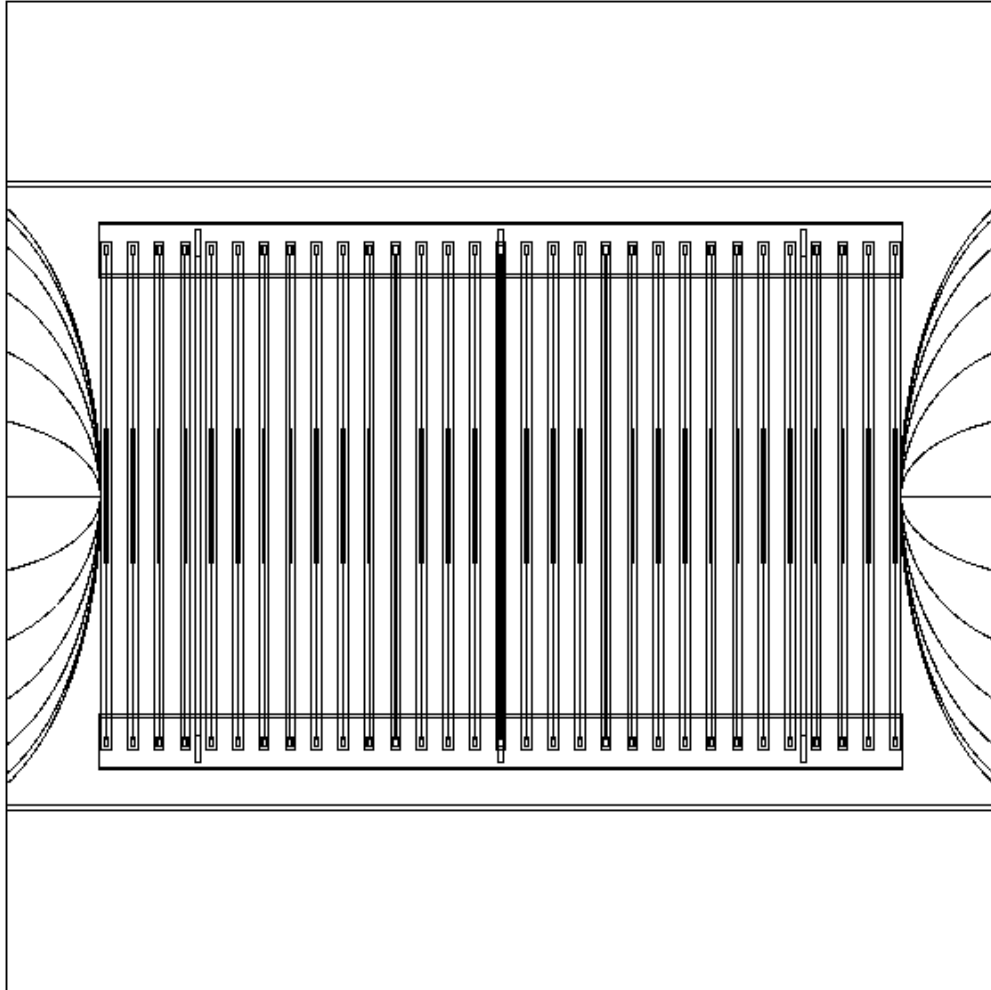


Figure 12.2: The Pixel detector and the hemispherical window, elevation view. The pixel region is 128 cm long. The 31 stations are clearly visible, except the central one which is masked by a structural support. The lines surrounding the planes within a station are fiducial, or buffer volumes, to ease the tracking debugging and do not correspond to real material. The medium inside the tank is vacuum.

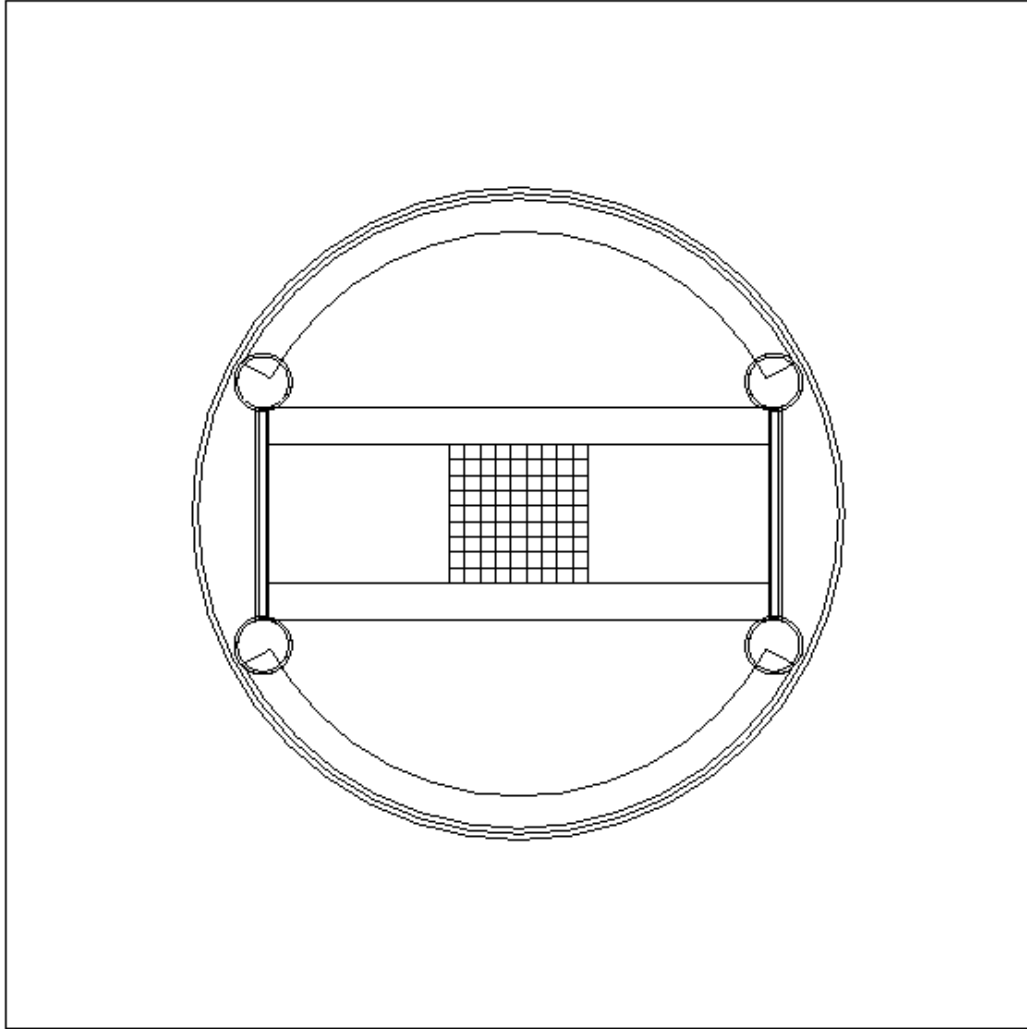


Figure 12.3: The Pixel detector, beam's eye view, showing the layout of the pixel wafers (center), the cooling tube manifolds (left and right, thick lines), the main cooling tube (circle in each corner), the support structure (section of the arc, top and bottom) and the vacuum tank walls. The vacuum tank is 20 inches in diameter. In order to provide the beam hole, the center cell of the 9×9 array of pixel wafers is not present.

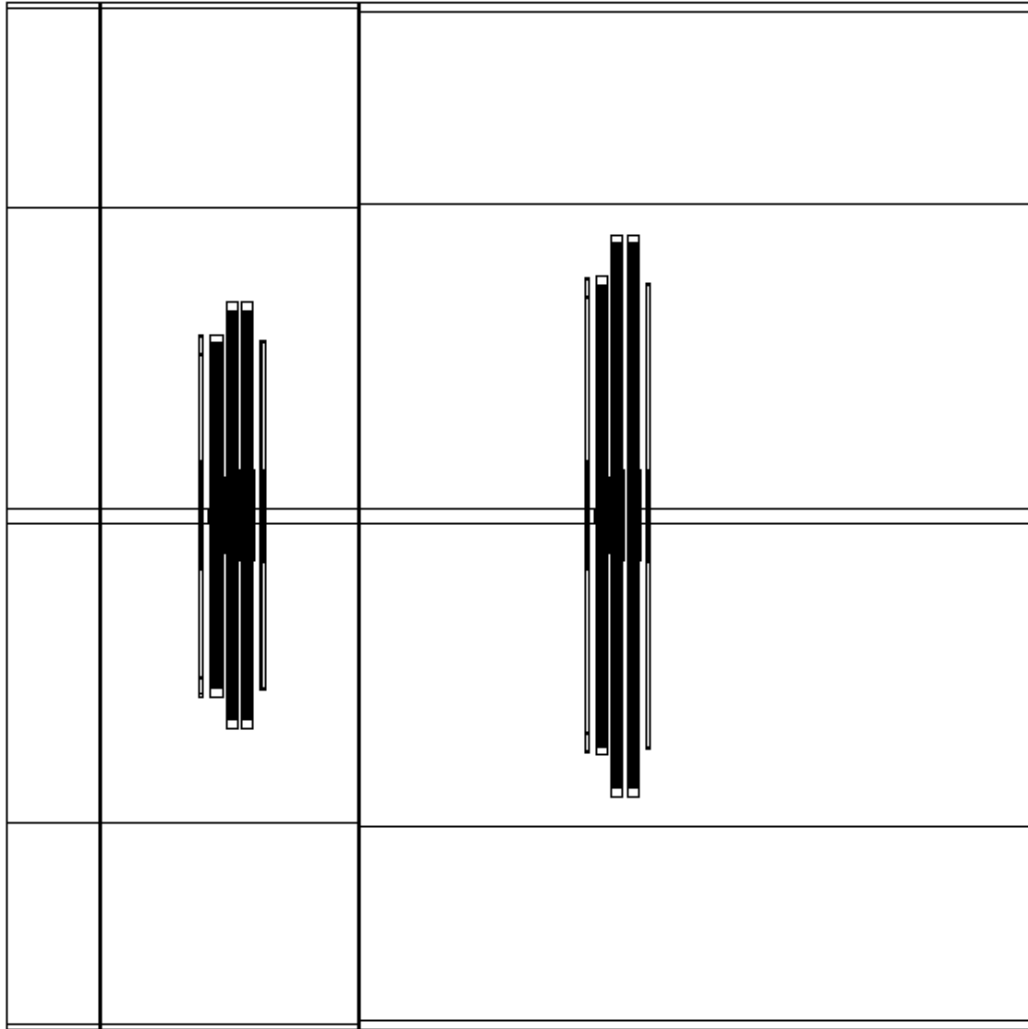


Figure 12.4: An elevation view of the region centered around $z=+1.6$ m, showing straw tube stations 2 and 3; each station consists of three views and three planes per view for a total of 9 planes per station. Upstream and downstream of each straw tube station are forward silicon strip planes and their support structure.

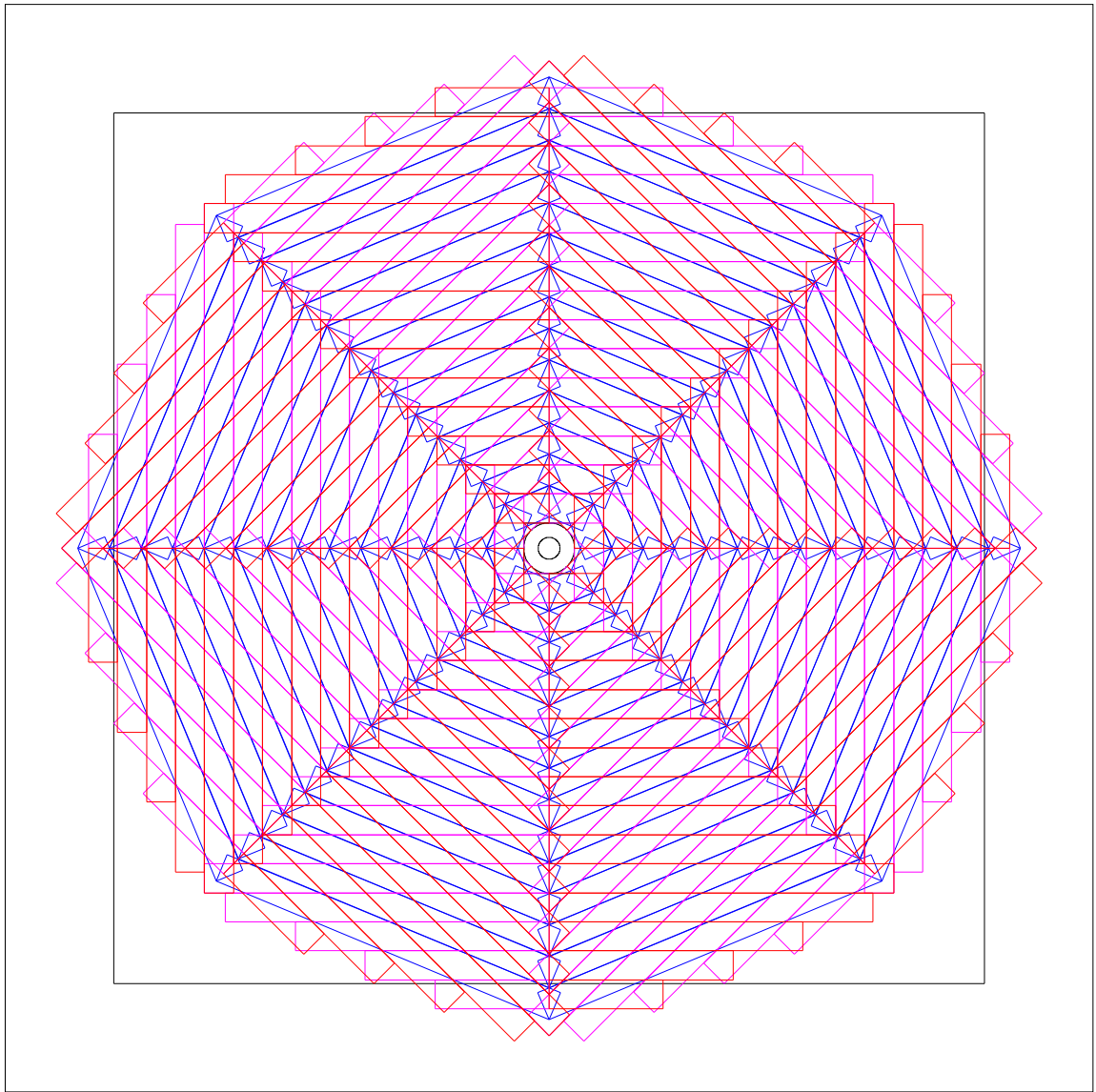


Figure 12.5: A beam's eye view of the muon detector, showing the beampipe shielding, the hadron filter and the layout of the muon planks.

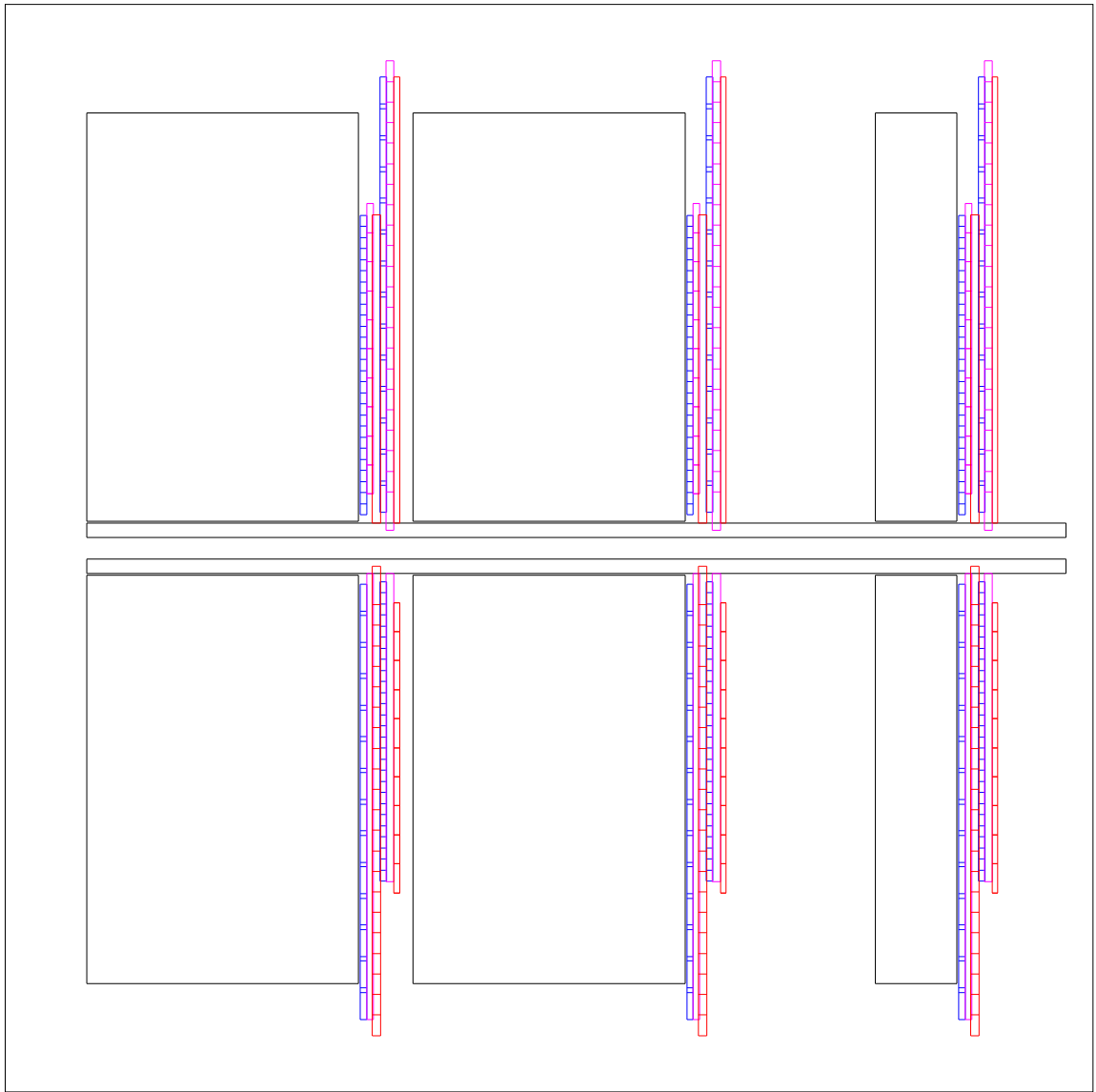


Figure 12.6: An elevation view of the region from 7.8 m to 11.4 m, showing muon stations 1, 2 and 3. Also shown are the hadron filters and the beam pipe shielding.

as to minimize the CPU time without creating an artificially rosy picture of the detector response. For BTeVGeant, most of the CPU time is spent in the simulation of the electromagnetic calorimeter so the proper tuning of the ECAL cutoffs has the largest impact on performance. We describe below how we chose values for the two most significant cutoff parameters, “cutele” and “cutgam”. These are, respectively, the energies below which the tracking of electron and photons is stopped.

We generated 1500 signal events in the channel $D^{*-}\rho^{+}$ and passed these events through BTeVGeant. This was repeated for several different values of cutele and cutgam. The output files from these runs were analyzed using the BTeV ECAL cluster finding code (Section 12.4) to produce photon candidates; a photon candidate was rejected if any reconstructed charged track was too closely associated with it. From each event, pairs of photon candidates were selected and their invariant mass calculated. Figure 12.7 shows the $\gamma\gamma$ invariant mass spectra for the various runs; in each case a clear π^0 signal is present. The spectra correspond to the following choices of cutele and cutgam:

- a) [left upper corner] cutele = 500 keV cutgam = 65 keV
- b) [right upper corner] cutele = 1 MeV cutgam = 65 keV
- c) [left bottom corner] cutele = 1 MeV cutgam = 1 MeV
- d) [right bottom corner] cutele = 1 MeV cutgam = 3 MeV

Each mass spectrum in Figure 12.7 was fitted using a Gaussian to parameterize the π^0 line shape plus a 3rd order polynomial to parameterize the background. The two figures of merit which come from each fit are the resolution on the π^0 mass (σ) and the ratio of signal/background for the π^0 peak. Figure 12.8 summarizes these figures of merit for the four runs. Neither figure of merit shows a significant dependence on either cutele or cutgam.

The investigation of the cutoff parameters was completed by studying the ECAL response for events containing only a single 10 GeV photon, generated at the face of the calorimeter. For this study the two figures of merit were the energy resolution of the reconstructed shower ($\sigma(E)/E$) and the width of the reconstructed shower. These were examined as a function of cutele and cutgam and the results are summarized in Figure 12.9. We see that the width of the showers depends only slowly on cutele but that showers become dramatically narrower as cutgam increases. The energy resolution is not a strong function of cutele nor does it depend strongly on cutgam, for cutgam less than 1 MeV. At cutgam of 3 MeV the energy resolution is artificially lowered due to the decrease in the shower width.

Figure 12.10 shows the CPU time required to run BTeVGeant on the $D^{*}\rho$ events for the different sets of the cutoff parameters. We see that cut set c) consumes significantly less CPU time than either a) or b) while little further improvement is achieved by raising cutgam to 3 MeV, point d). From these studies, we conclude that the appropriate choices are cutgam=1 MeV and cutele=1 MeV.

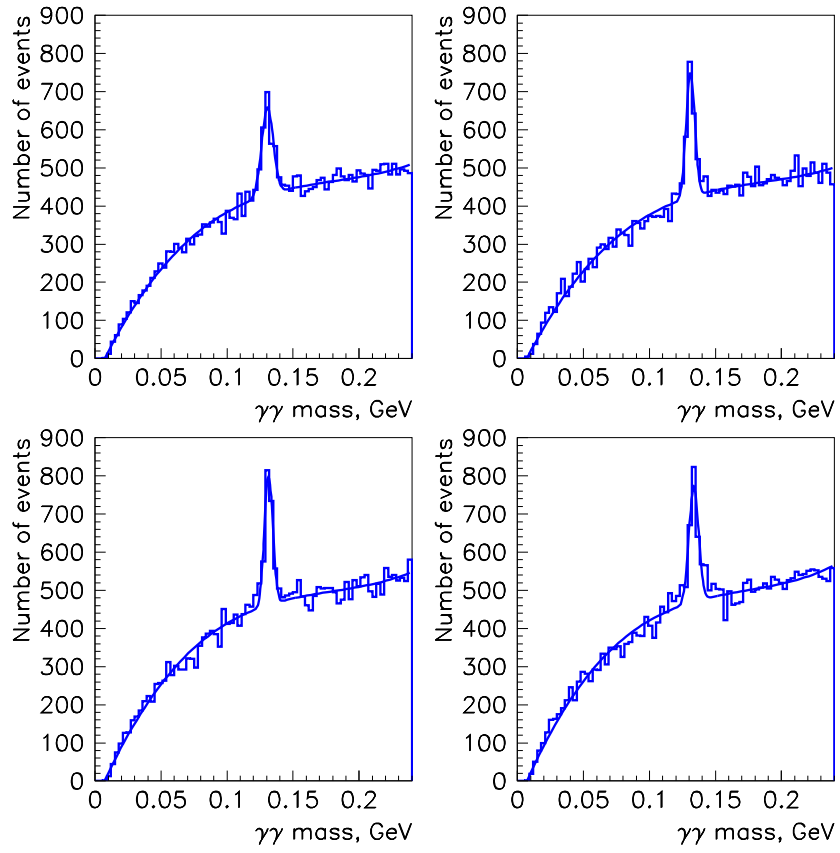


Figure 12.7: Histograms of $m_{\gamma\gamma}$ for the four different sets of cuts: (upper left) $\text{cutele} = 500$ keV, $\text{cutgam} = 65$ keV; (upper right) $\text{cutele} = 1$ MeV, $\text{cutgam} = 65$ keV; (lower left) $\text{cutele} = 1$ MeV, $\text{cutgam} = 1$ MeV; (lower right) $\text{cutele} = 1$ MeV, $\text{cutgam} = 3$ MeV.

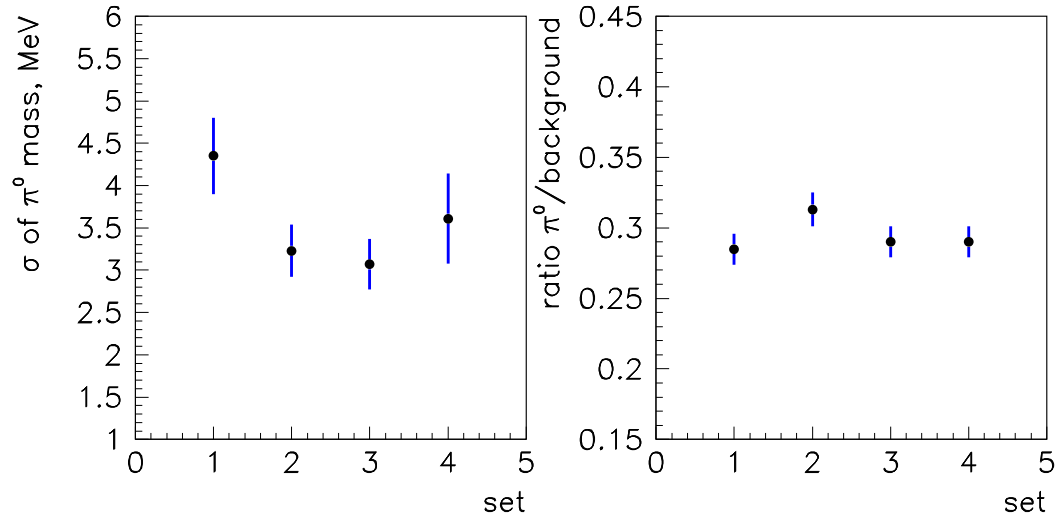


Figure 12.8: The π^0 mass resolution (σ = width of the mass peak) and the ratio of π^0 's/background for the four different sets of gamma and electron cutoffs. The horizontal axis refers to the 4 sets of cuts shown in Figure 12.7.

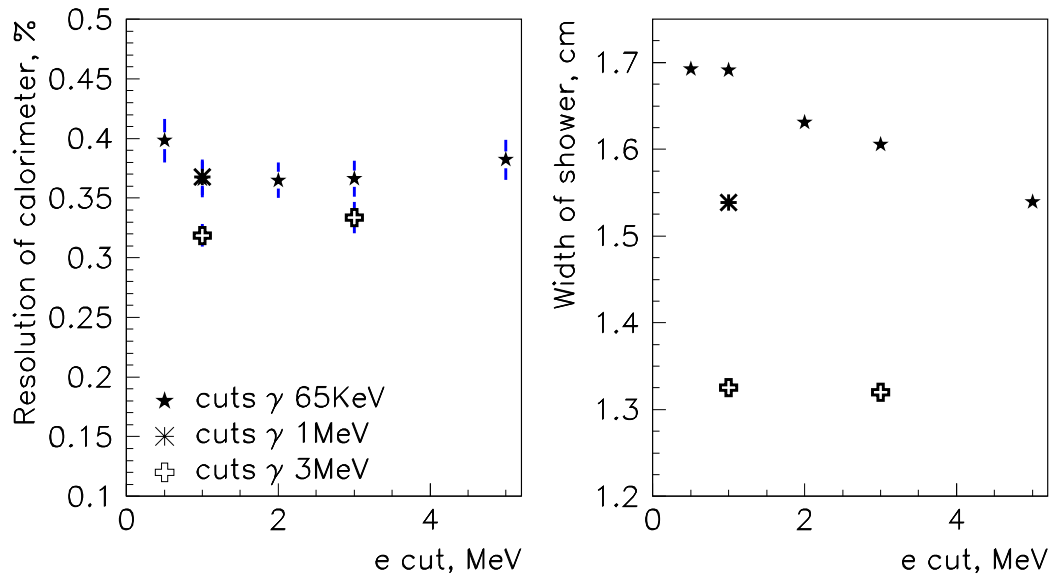


Figure 12.9: The energy resolution ($\frac{\sigma(E)}{E}$) and the width of the showers for different gamma and electron cutoff values

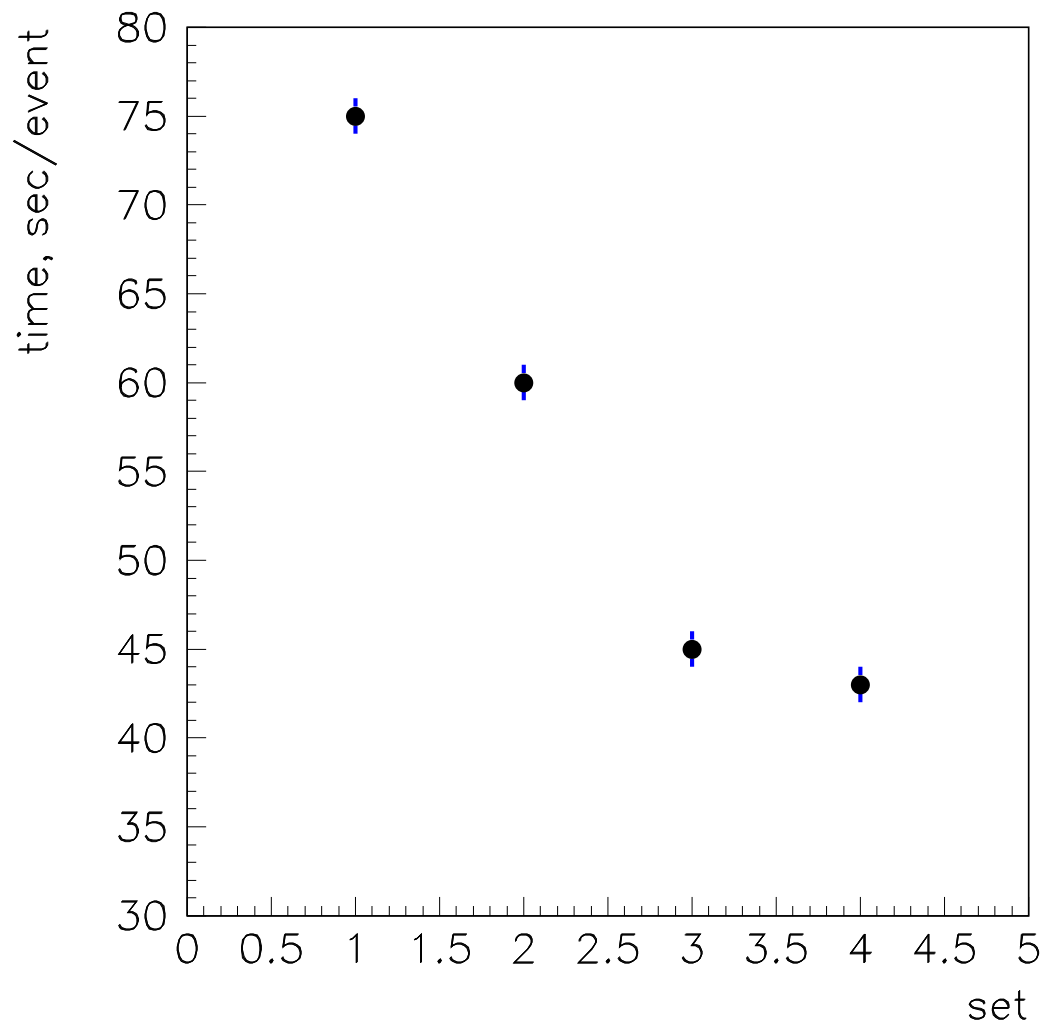


Figure 12.10: The BTeVGeant simulation time for $D^*\rho$ events for the four different sets of cuts. The horizontal axis refers to the 4 sets of cuts shown in Figure 12.7.

12.1.6 Hits and Digitizations

In the language of GEANT 3 a “hit” refers to the intersection of a track with a sensitive volume while a “digitization” refers to the set of ADC and/or TDC values which would be produced by that hit. In a hit level simulation, the appropriate measured quantity, a drift time or position in a plane, is computed from the hit information and is smeared by the nominal resolution of the device; it is not digitized. BTeVGeant currently does a hit level simulation for all detector components and it has hooks in place for a digitization level simulation. Because a hit level simulation is sufficient for most purposes, digitization code exists only for the pixel detector. This choice saves computer time.

For the forward tracking system the plane and wire numbers, or plane and strip numbers, are generated for each hit. The drift times for the straws are not yet digitized but the position resolution is taken into account in the hit generation. This hit level information is used by a prototype of the Level 2 trigger code, and will later be used in the offline tracking pattern recognition code.

Hits in the RICH detector are not yet simulated in BTeVGeant. The full simulation of the response of the RICH detector is done at analysis time and is described in detail in Appendix A.

A hit in a lead tungstate crystal represents the sum of the energy deposited in that crystal by one or more electromagnetic or hadronic showers. The energy stored in the hit is the true energy which would be measured by a perfect device. Effects such as light collection efficiency, readout specifications and imperfections are applied in a parametric way at analysis time. Therefore these can be varied without rerunning BTeVGeant. This approach has been used by CMS and has been shown to be reliable. The data structure for ECAL hits also stores information about which particles or showers contributed to the energy sum in that crystal. This data structure has the same format as that for MCFast ECAL hits and it is described in detail in the MCFast manual [6].

12.1.7 The I/O layer

BTeVGeant reads its input data from StdHep format files using the StdHep package [7]. The code which builds events, or beam crossings, can read events from two separate files, a file of signal events and a file of background events. The mixing of events from these two files to form one beam crossing is discussed in section 12.3.

BTeVGeant writes its output data using the MCFIO I/O package [8], which has been used extensively in the StdHep package [7] and in MCFast [1]. MCFIO can serialize arbitrary data structures, via user-written XDR filters, into machine independent IEEE standard streams. An MCFIO file, or stream, is structured into HEP events, or beam crossings, and each event is viewed as a container of data blocks. In addition to the event data, the first event contains the geometry information (one block for each subdetector), the global volume dictionary and the set of Kalman surfaces. The blocks which comprise the event data are:

- A copy of the original StdHep event, containing the input signal interaction plus zero

or more background interactions (the truth table);

- The pixel, silicon and straw hits;
- Hits in the electromagnetic calorimeter;
- The truth table for tracks produced by decays or interactions in the detector;
- The Kalman-filtered tracks.

12.1.8 Track Pattern Recognition and The Kalman Filter

We regard the performance of the Level 1 and Level 2 trigger simulations which include full pattern recognition as proof that there are practical algorithms which have high efficiency, few false tracks, and reasonable execution time. We have not yet had time to move these algorithms into the analysis package. Therefore, a pseudo pattern recognition is done by using the Monte Carlo truth table to assign hits to tracks; this is the same level of pattern recognition which is done in MCFast.

Two other features of the pseudo pattern recognition simulate the behavior of a real pattern recognition program. If a track curls in the detector (ie. p_z changes sign), the pseudo pattern recognition code only considers hits on the first arc of the track; hits on subsequent arcs are created and are present to confuse real pattern recognition programs. A small fraction of the tracks clip the edge of the magnet yoke or coil and continue downstream to make hits in the forward tracking system. Hits downstream of the encounter with the yoke or coil are ignored by the pseudo pattern recognition.

Tracks with fewer than 10 measurements in the sum of the pixel, straw and forward silicon detectors are not Kalman filtered.

Once hits have been assembled into a track, the track is fitted using a Kalman filter [9, 10, 11, 12]. Its required input is a list of surfaces, or “nodes”, ordered in z . One node is required to represent each hit on the track, each scattering surface and each magnetic field boundary. The notion of a fixed magnetic field boundary arises from the piecewise constant field model used by BTeVGeant; this was discussed in section 12.1.3.

Since most of the GEANT volumes are boxes with faces perpendicular to the beam axis, the scattering surfaces encountered by tracks can be described as surfaces at fixed z .² The magnetic field boundaries also occur at fixed z . These surfaces at fixed values of z are referred to as the “Kalman surfaces”.

In BTeVGeant, assembling the node lists and executing the Kalman filter is done in three distinct phases:

²Two exceptions to this are the hemispherical window of the pixel tank and the beam pipe beyond the pixel tank. The window can be adequately approximated as being at fixed z and the few tracks which cross the beam pipe can be dealt with as follows: the track can be fitted without the beam pipe in the node list; the intersection of the fitted track and the beam pipe can be used to compute the correct location for a node to represent the scattering in the beam pipe; the track can then be refitted, including the scatter in the beam pipe.

- At geometry initialization time, the list of “Kalman surfaces” is defined.
- While Geant is tracing a track through the detector, hit-level information is created. At this time the associated Kalman node is also created.
- When Geant has finished tracing a track, nodes representing the Kalman surfaces are merged into the hit list and the track is Kalman filtered.

At the end of the each event the Kalman filtered tracks are written out as event data. Since the Kalman surfaces, the magnetic fields and the raw hits are also stored in the output stream, we are able to refit tracks in a subsequent analysis program.

12.1.9 Optimization for Production

All of the material in the C0 hall, including walls, supports and the magnet yoke are represented in BTeVGeant. While showers occurring in volumes located far away from the sensitive detectors are very unlikely to produce background hits, they take as much CPU time as showers occurring in the calorimeter. These rare backgrounds will be studied in dedicated runs while, in normal runs, particles will be stopped before they have a chance to initiate showers outside of the region of interest. In order to implement this, particles are stopped whenever they find themselves in a GEANT volume which is on a list of “stop points”. Stop-points are located at the dipole yoke or coils, the walls of the C0 pit, the electromagnetic calorimeter and the muon steel. The stop-point at the ECAL is useful for analyses which consider only charged tracks. Enabling of the stop-points is controlled via the input command file.

Another utility allows us to save considerable CPU time when studying background processes for channels in which a single π^0 or photon is included in an otherwise all charged final state, for example $B^0 \rightarrow \rho\pi$. Such events are simulated in two phases. During the first phase, all of the particles are simulated up to the electromagnetic calorimeter and are then held in temporary storage. The charged tracks are then Kalman filtered and a final-state specific analysis is run. This analysis will accept or reject the event based on the results of the charged particle tracking, the vertex topology and the tracking based triggers. If the analysis determines that this event fails then there is no need to simulate the response of the calorimeter; BTeVGeant will then discard the event and begin processing the next event. If, on the other hand, the event passes the analysis, then it must be fully simulated and BTeVGeant continues with its second phase. In this phase, the particles which were stored during the first phase are popped off their stack and BTeVGeant tracks them through the remainder of the detector, subject to the stop-points. If only a small fraction of background events pass the tracking cuts, then, because the majority of the CPU time is spent in the ECAL simulation, this method results in large savings in CPU time. For the $B^0 \rightarrow \rho\pi$ simulation and analysis, we save a factor of 3 in computing time.

12.1.10 BTeVGeant Production Using a PC Farm

To run as many simulations as possible using BTeVGeant, most BTeVGeant simulations were run on the Fermilab Computing Division PC Farm. This farm consists of 50 worker nodes, each with two 500 MHz Pentium III CPUs. Most BTeVGeant simulation samples used for physics studies were run on ~ 60 CPUs over a period of three months. For decay modes where the electromagnetic calorimeter (ECAL) is not simulated, the simulation time is 10 seconds per event on a single CPU. Including the ECAL increases this to 60 seconds per event.³ Output file sizes are about 150 kBytes per event without the ECAL, and 240 kB with the ECAL. Output file sizes for background files are reduced by not including some of the raw hits in the output. The quoted output file sizes are after compression using the compression program gzip which reduces the total data size from 2.5 TB to 1.2 TB.

The events generated using BTeVGeant are summarized in Table 12.1. Care was taken to properly seed the event generation process. Signal interactions were generated sequentially so as to always use the random number seed from the previous event. The minimum bias interactions embedded in signal interactions were separately generated for each production “run” and seeded by the time-of-day. The total CPU time used for this production is equivalent to that used by running on a single 500 MHz Pentium III CPU for 9.6 years. The output data are stored on the Fermilab Mass Storage System.

Table 12.1: Summary of BTeVGeant simulations run on the Fermilab PC Farm. The data output sizes shown are for the compressed output.

Decay Mode	#Events	Size (GB)	Comments
$B_s^- \rightarrow D_s^- K^+$	100K	9	$D_s^- \rightarrow \phi \pi^-$
	55K	8	$D_s^- \rightarrow K^{*0} K^-$
background from $b\bar{b}$	1000K	90	$b \rightarrow D_s^- X$
background from $b\bar{b}$	1000K	90	$\bar{b} \rightarrow D_s^- X$
$B^0 \rightarrow D^{*-} \rho^+$	125K	35	$D^{*-} \rightarrow \bar{D}^0 \pi^-, \bar{D}^0 \rightarrow K^+ \pi^-$
background from $b\bar{b}$	1000K	175	$b, \bar{b} \rightarrow D^{*-} X$
background from $c\bar{c}$	100K	4	$\bar{c} \rightarrow D^{*-} X$ with embedded cuts
$B^0 \rightarrow \rho \pi$	125K	35	$\rho^0 \pi^0$
	125K	35	$\rho^+ \pi^-$
background from $b\bar{b}$	5000K	400	embed cuts in GEANT for speed up
$B^0 \rightarrow J/\psi K_s^0$	150K	3	embed cuts in GEANT for speed up
background from $b\bar{b}$	40K	10	$b, \bar{b} \rightarrow J/\psi X$ with embedded cuts
$b\bar{b}$	2000K	260	1 million is without ECAL
$c\bar{c}$	200K	4	L1 Trigger applied
Minimum Bias (uds)	1000K	6	L1 Trigger applied

³The lower CPU time of 44 s shown in Fig. 12.10 was for simulating the calorimeter in only one arm.

12.2 MCFast Simulation Package

Early design studies to explore the detector layout, and many of the physics studies for this proposal, were prepared using the MCFast simulation package [1]. MCFast was developed by the Fermilab Computing Division to provide a general framework for simulation and analysis of a variety of detector geometries and detector options. The primary goal of MCFast is fast and accurate detector simulation with the speed and flexibility achieved through parameterization. The program allows the user to trace particles through simple geometrical shapes, does track fitting and provides a fast showering algorithm which can be used to generate hits in calorimeters. User analysis hooks are provided so that the detector simulation and analysis can be unified in one job. Events can be written out using an MCFIO [8] interface similar to that described for BTeVGeant in Section 12.1.7.

MCFast treats tracking devices and scattering surfaces as thin planes. It recognizes detector elements that are either planes perpendicular to the beam (Z-planes) axis or thin cylinders (R-planes) centered on the beam axis. In MCFast v5_0, rectangular planes perpendicular to the x and y axes (X-planes and Y-planes) are also recognized. Another recent refinement is the treatment of pixel detectors in which the wafers overlap. These additions have some cost in execution time but bring added flexibility and functionality to the package. Calorimeters and large volume absorbers (magnet yokes, muon filter) are handled in a different fashion. The normal tracing through the detector list is interrupted and tracing through large volumes is done in a series of small steps. The step size, which depends on the physics process, can also be set by the user.

In the preparation of the PTDR[2], we used MCFast v4_2, which included multiple scattering, dE/dx , and bremsstrahlung in the tracing of charged particles. Decays in flight, pair conversions and secondary hadronic interactions were also included. Hits in sensitive detector elements were generated during the tracing step and then passed to the track fitting package which was based on the same Kalman filter technique that is described for BTeVGeant in Section 12.1.8. Realistic hit generation for the pixel detectors was included as follows: for the narrow dimension of the pixel, the resolution function was modeled as a Gaussian whose width is dependent on the angle of incidence of the track on the pixel plane. Delta rays were not included. The hits could also be fed to the trigger simulation package which did complete pattern recognition and which had its own track fitter and vertex finder. The main limitation of MCFast v4_2 was that the tracing step could not correctly account for multiple scattering in a detector which contained both R-planes and Z-planes. Therefore, the simulations for the PTDR were done without a realistic model for beampipe; this was only possible because the pixel detectors are inside the beampipe.

MCFast v5_0 has been used for many of the physics analyses presented in this proposal. This version contains the same basic features as MCFast v4_2, but in addition there is an integrated tracing package which properly unifies the tracing steps for Z-planes, R-planes, X-planes and Y-planes; this package is implemented in C⁺⁺. The integrated tracing improvements permits tracing and scattering of particles in both the planar elements, such as forward tracking detectors, and the radial elements, such as beampipes, in a consistent

manner. In addition the showering algorithms have been updated and coupled to a more efficient hit generation package for the calorimeters. The Kalman filter track fitter has been separated from the underlying MCFast specific internal structures and has been adapted for use in both MCFast and BTeVGeant. Other improvements to MCFast were included to support operation on the Linux farms.

12.2.1 Charged Particle Tracking in MCFast

MCFast tracking is a two step process. In the first step, tracks are followed from their production point along their trajectory and at each detector surface that is encountered one or more operations takes place. These operations include multiple scattering, energy loss, elastic and inelastic hadronic scattering, bremsstrahlung and pair conversion. If the surface represents a sensitive element then a hit may also be created. In addition, a decay in flight may occur at any point along the track or a shower may start when a particle passes through dense material such as a magnet yoke, calorimeter or hadron filter. The collection of all points on one track which are recorded in this step is referred to as the trace list of the track. In the second step, the trace list of each track is used as the input to a Kalman filter. The output of the Kalman filter has been validated over the full range of momentum and angles which are important for BTeV.

Several approximations are made in the MCFast tracking. Multiple scattering is approximated by a Gaussian distribution. More importantly, the input to the Kalman filter does not contain any pattern recognition errors.

In general, the location of a hit in a tracking detector is taken as the intersection of the particle trace with the detector plane. This is then smeared by the nominal resolution of the device, which is taken from the geometry file. MCFast has an internal parameterization of the resolution of each device and the writer of the geometry file can supply the values of its parameters. Most devices have a default option which will be selected if the user does not supply values for the parameters; an example of such a default is $\text{pitch}/\sqrt{12}$ for silicon strip detectors. For pixel detectors only, there is another option which can be selected via the geometry file: the resolution can be returned, on a hit by hit basis, from a user supplied function. For the BTeV pixel detector several different models of the spatial resolution were used in MCFast simulation studies: the constant σ model, the variable σ model, fast clustering and slow clustering.

The constant σ model was the model used in the simulations for the BTeV EOI. In this model, the spatial resolution is a Gaussian with a constant width which is equal to the $\text{pitch}/\sqrt{12}$. This model is used for both the short and the long measurement directions of the pixel. The default model, the one used for most calculations presented in this document and the one was used in the PTDR, is the variable σ model.

In the variable σ model, the spatial resolution remains Gaussian but the width of the Gaussian for the short dimension of the pixel is a function of the angle of incidence of the track on the pixel plane. The width of the Gaussian for the long dimension of the pixel remains at the pitch divided by $\sqrt{12}$. For reference, the distribution of the x and y angles of

incidence are shown in Figure 12.11 parts a) and b). These figures were made using typical $b\bar{b}$ events and they only include hits from tracks with at least 20 hits. The width of the distribution for $\tan \theta_y$, is greater than that for $\tan \theta_x$ because of the bending of the tracks in the magnetic field of the analyzing dipole. Parts c) and d) of Figure 12.11 show the value of σ , as a function of angle of incidence, for, respectively, pixels which measure x and pixels which measure y . The minimum of the y resolution is offset from $\theta_y = 0$ because of Lorentz force effects.

In the fast clustering model a Monte Carlo simulation is run for each intersection of a track with a pixel plane. This simulation explicitly generates the digitized pulse heights recorded on nearby pixels. A 3-bit linear ADC and a threshold of 2000 e^- were assumed. Once each cluster has been generated, the pulse heights are used to obtain an estimator of the position of the hit; this estimator uses the knowledge of the angle of incidence.

In addition to returning an estimator of the (x, y) position of the hit, the fast clustering model also returns an estimate for the error on that position. This error is used by the Kalman filter and is similar to the error used in the variable σ model. In the long dimension the nominal resolution is the pitch divided by $\sqrt{12}$ and, because almost all clusters are only one pixel wide, the shape of the resolution function is box-like.

The important improvement achieved through the fast clustering method is that its resolution functions are closer to reality, having a box-like component and noticeable tails. Using the fast clustering model, however, adds about 70% to the execution time of a typical physics analysis job. This is a sufficient degradation that this model is not routinely used for physics analyses. The principal weakness of the fast clustering model is that the overlapping of two or more clusters is not considered.

The slow clustering model takes the overlaps into account but at the expense of large increase in CPU time. For this proposal BTeVGeant has been used for these more detailed studies.

12.2.2 Vertexing Package

The MCFast package contains a set of vertex fitting routines which can be used during the analysis phase to combine sets of fitted tracks into vertices. The package can work in the presence of a solenoidal magnetic field, in a dipole field in either the x or the y direction or in a field-free region. The control of the vertex fitting is left to the user who decides which tracks should be grouped to form a candidate vertex. The package also contains utilities to build new “particles” from a list of fitted tracks and the package is able to use these new “particles” in subsequent fits.

The fitting algorithm and its implementation are based on code written for CLEO [13], which has a solenoidal field. The extension of the package work in a dipole field (x or y direction only) is accomplished by rotating the tracks to a new coordinate system in which the magnetic field points along the z direction; the output of the vertex fitter is rotated back to the normal MCFast coordinate system.

The base operation of the package is to perform a vertex fit, returning a vertex position,

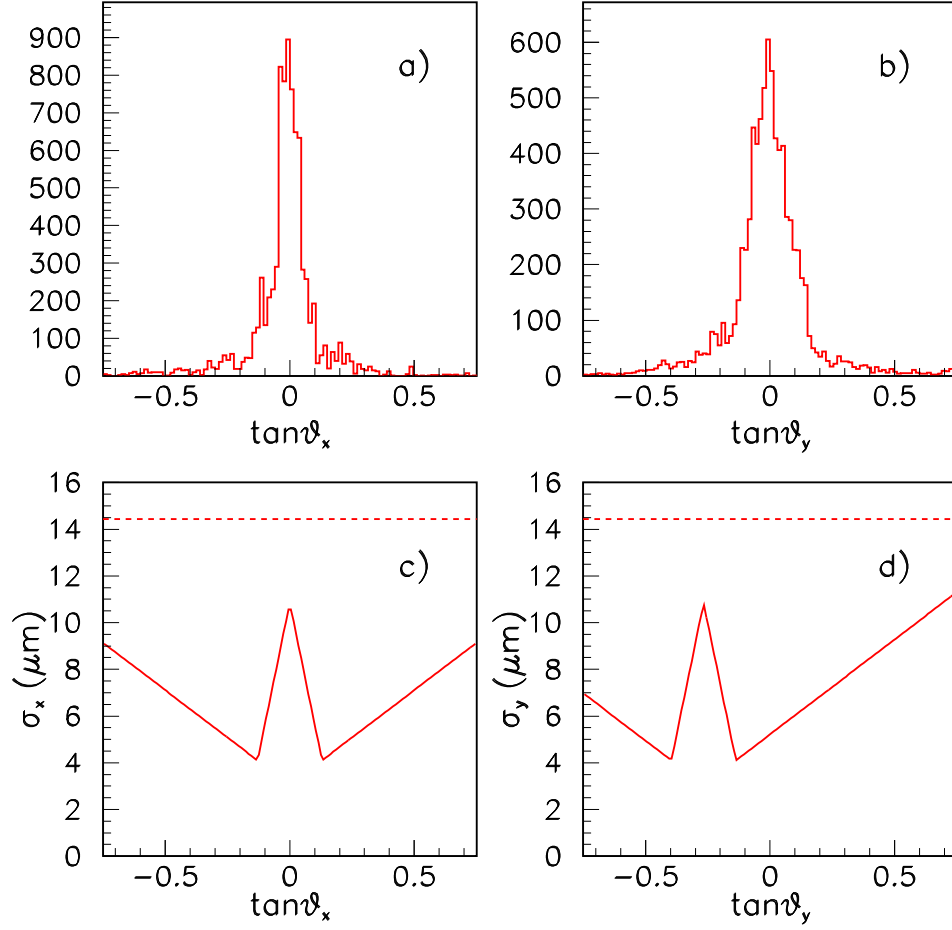


Figure 12.11: The distributions of a) $\tan\theta_x$ and b) $\tan\theta_y$ for hits on tracks, in $b\bar{b}$ events, with at least 20 hits. Here θ_x is the angle of incidence, in the xz plane, of a track which intersects a pixel detector. Similarly for θ_y . For most studies reported in this document, the pixel detectors are modeled as having a spatial resolution function which is Gaussian. The dependence of the σ of the Gaussian on angle of incidence is shown in c) for pixels which measure x and in d) for pixels which measure y . In both cases the solid line shows the value of σ for the short dimension while the dashed line shows the value for the pitch divided by $\sqrt{12}$.

its covariance matrix and the χ^2 . There are options in the package to update the tracks after the fit and to include a beam constraint when fitting the vertex. The package also contains a utility to perform fits with a mass constraint. This vertexing package has been used with both MCFast and BTeVGeant based analyses.

12.2.3 Simulation of Secondary Hadronic Interactions

The approach to secondary hadronic interactions in MCFast is purely phenomenological. No attempt is made to model the underlying hard scattering process. The probability of an interaction occurring is determined by the collision length and absorption length of the material. Energy dependent cross-sections are not used inside MCFast.

The number of charged particles produced in a secondary interaction of a charged pion on a proton target is a function of the center-of-mass energy of the interaction s . The mean number of charged particles n_{ave} is given by,

$$n_{ave} = a + b \log s + c(\log s)^2,$$

where $a = -0.35$, $b = 1.21$ and $c = 0.03$ as given by Dumarchez et al. for pion-proton interactions [14]. The distribution is characterized by KNO scaling which is modeled as a truncated Gaussian. Figure 12.12 can be compared with Figure 5 in Firestone et al. [15]. For a heavier target the mean increases as a function of the atomic number A [16]. The average number of neutrals is assumed to be 50% of the charged multiplicity. The number of secondary particles from an interaction is limited to a maximum of 25 to avoid overflowing arrays.

The momentum distribution of secondary particles is approximately flat in rapidity and approximately Gaussian in p_T with respect to the direction of the interacting particle [17]. The simulated distributions for a particle with momentum 50 GeV/c are shown in Figure 12.13. These can be compared with Figure 30 in Brenner et al. [17] and Fig 69 in [16]. The momentum of each outgoing particle is selected from these distributions and then energy is conserved by rescaling the momenta. The momenta are then rotated into the lab frame and the new particles are added to the StdHep list.

Elastic scattering is characterized by the distribution of four-momentum transfer squared ($-t = p_T^2$). The distribution is given by

$$d\sigma/dt = e^{(bt)}$$

where $b \approx 8$ [18]. The simulated distribution is shown in Fig 12.14.

12.2.4 The MCFast showering subpackage

The MCFast showering works by depositing energy in detector elements using an algorithm based on parameterized shower shape distributions. This procedure produces showers distributed over detector elements which can be processed by realistic shower reconstruction

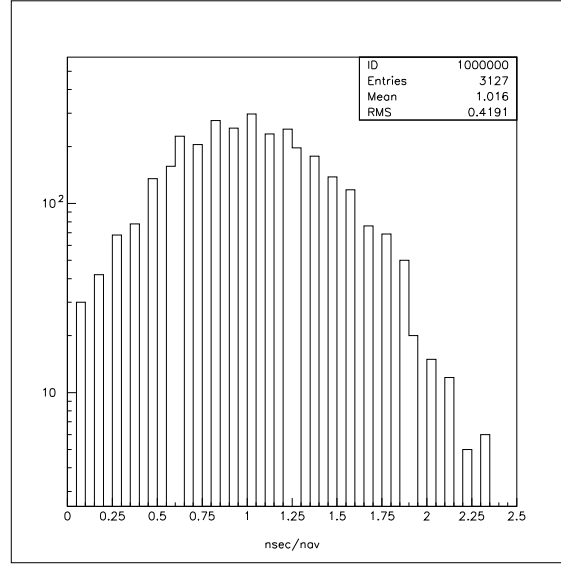


Figure 12.12: KNO scaling in MCFast: The scaled number of secondaries, n_{sec}/n_{ave} , as generated in MCFast.

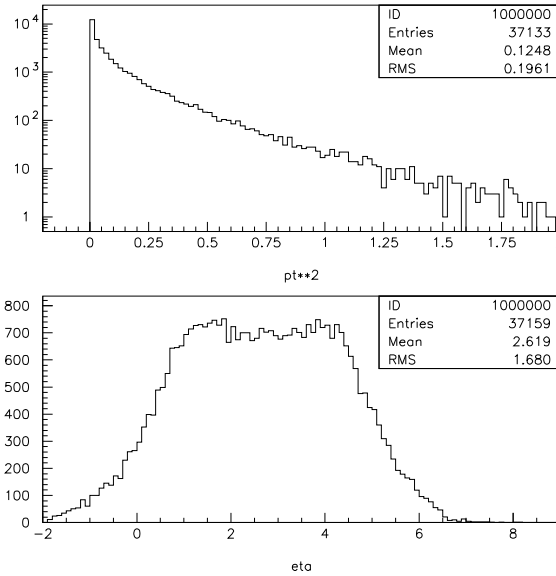


Figure 12.13: Distributions, produced by MCFast, of kinematic variables of secondary particles generated by an incident particle of 50 GeV/c: (a) p_T distribution, (b) η distribution

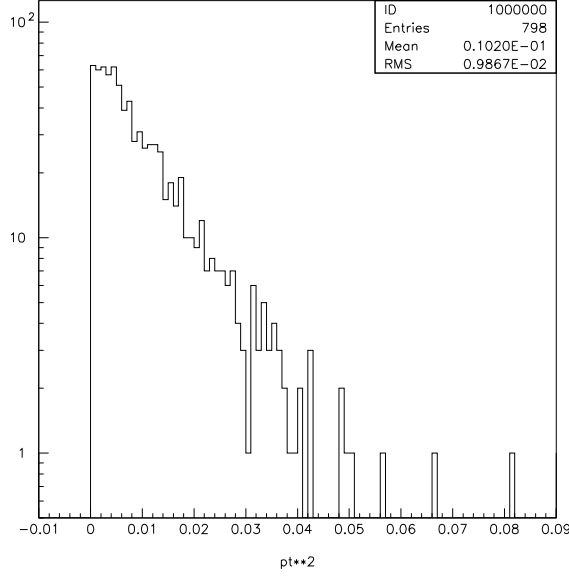


Figure 12.14: Distribution of p_t^2 for elastic scattering from MCFast.

programs. The program executes faster than a full GEANT simulation and represents the energy deposition in detectors quite well. It has been shown to be consistent with GEANT over the range of energies relevant to BTeV.

The MCFast showering subpackage is completely integrated into the MCFast Monte-Carlo package. The user defines tracking systems, calorimeters and absorbers through the detector description file and MCFast takes care of converting particles to showers, through an interrupt to the normal tracing processes at the calculated shower conversion point. In addition, energy losses and multiple scattering in the bulk material of the calorimeters and absorbers are taken into account.

The showering simulation is based on an extensive parameterization scheme. There is no detailed, particle by particle, description of an electromagnetic or hadronic shower. Instead, the energy densities due to the high energy showering processes within volumes are parameterized, and shower fluctuations are simulated globally rather than locally. In the calorimeters, these energy densities are mapped onto a user-controlled readout grid, and calorimetry hits are generated.

Unlike particle tracing in MCFast, the simulation of the shower propagation is intrinsically 3-dimensional. To keep the program simple, only three volume types are recognized: BOX, TUBE and CONE. These shapes must be oriented in such a way that the symmetry axis is along the Z-axis.

At the initialization stage, MCFast computes the surface boundaries for these volumes. At the tracing stage, once such a surface is reached, the calorimetry subpackage returns an estimate of the mean free path length for the particle. For electrons/positrons and photons,

it is simulated according to the formula $f(x) = e^{-x/X_0}$, where X_0 is related to the radiation length. For hadrons $f(x) = e^{-x/\lambda}$, where λ is the absorption length (the mean free path for inelastic interactions). Based on this information and a random number, the location of the interaction inside the calorimeter is computed. Should an interaction occur, the tracing code switches from “particle” tracing to “shower” tracing and the core of the shower is propagated through the remaining geometry elements. This enables the propagation of the shower from one calorimeter to the next.

Upstream of the conversion point, the particle behaves as a minimum ionizing particle (MIP), sensitive to magnetic fields, if any, and undergoing energy loss and multiple scattering. The corresponding energy deposition is recorded as hits in the calorimeter.

Showering starts at the shower conversion point. Unlike normal charged particles, the core of the shower propagates in a straight line. There is no provision for the propagation shower to be sensitive to the magnetic field in the region.

Downstream of the conversion point, the deposited energy is calculated on a step by step basis, according to the shower longitudinal profile formulae. In most cases the step size is one radiation length but this will be reduced if the particle is close to a boundary or it is close to ranging out. After each step, the shower core position, energy and momentum are calculated and the control is given to the hit generation, if requested. There are two options for hit generation either of which can be selected in the command file: all of the energy for this step may be deposited in the current cell or it may be spread over neighboring cells according to a model of transverse shower profiles. The former is a much faster model while the latter is much more accurate.

For electromagnetic showers, the longitudinal profile is described as,

$$dE/dx = E_0 b \frac{(bt)^{a-1} e^{-bt}}{\Gamma(a)},$$

where

$$\begin{aligned} t &= x/X_0, & b &\simeq 0.5, & a &= 1 + bt_{max}, \\ t_{max} &= 1.0 \times (\ln(y) + C_i), & i &= e, \gamma, & (C_\gamma &= +0.5, & C_e &= -0.5) \\ y &= E/E_c, & E_c &= \frac{800 \text{ MeV}}{Z + 1.2}, \end{aligned}$$

where Z is the atomic number and where E_0 is the energy of incident particle.

For hadronic showers, the longitudinal profile is described as,

$$dE/dx = E_0 (wb \frac{(bt)^{a-1} e^{-bt}}{\Gamma(a)} + (1-w)d \frac{(du)^{c-1} e^{-du}}{\Gamma(c)}),$$

where,

$$\begin{aligned} t &= x/X_0 \\ u &= x/\lambda \end{aligned}$$

$$\begin{aligned}
a &= 0.6165 + 0.3183 \ln(E_0) \\
b &= 0.2198 \\
c &= a \\
d &= 0.9099 - 0.0237 \ln(E_0) \\
w &= 0.4634.
\end{aligned}$$

When the shower transverse profile option is enabled, the energy deposited at each step is distributed around the shower axis according to a calculated shower transverse profile. The transverse profile becomes wider as the shower moves deeper into a calorimeter.

The transverse profile for both electromagnetic and hadronic showers is described as

$$\frac{dE}{dR} = e^{(-R/A_1)} + A_2 e^{(-R/A_3)}$$

In this formula, parameters A_1, A_2, A_3 depend on the material properties and on the current shower depth. These dependencies differ for electromagnetic and hadronic showers.

The transverse distribution of deposited energy during each step occurs in a plane perpendicular to the direction of motion of the shower core. Since showers may have crossed calorimeter boundaries, energy deposition is also computed in the corresponding cells of those neighboring calorimeters. Thus, even if a shower develops in an absorber, it still may produce hits in nearby calorimeters.

The total deposited energy is smeared during the process of showering simulation according to the energy resolution formula

$$\frac{\sigma_E}{E} = \frac{a}{\sqrt{E}} \oplus b$$

where a and b are input parameters for the code. For a sampling calorimeter, a visible fraction of energy is calculated.

The analysis of calorimeter hits can be performed through the use of an interface to the cluster finding routines that are described in Section 12.4. The shower shapes are similar though not identical to those produced by BTeVGeant. A comparison between MCFast generated showers and GEANT generated showers is given in Section 13.1.

12.2.5 BTeV Geometry Description for MCFast

The geometry description for our MCFast simulations is derived from the geometry used for BTeVGeant simulations. This MCFast geometry description is used for the MCFast based physics studies presented in this proposal and it includes:

- A dipole magnetic field described by 11 regions of piecewise constant field extending to ± 320 cm, including the fringe field. The description includes a yoke and coils which act as absorbers. The central field region around the vertex detector has a horizontal field of 1.6 T.

- A 20 inch diameter central vacuum vessel with thin planar end walls, surrounding the vertex detector.
- A 1.5 inch diameter Aluminum beam pipe extending from the end walls of the central vacuum vessel, through the forward tracking detector to a flange at $z=380$ cm. The diameter of pipe is increased to 2.5 inches on the far side of the flange.
- A silicon pixel vertex detector with 31 stations of 2 planes each. The silicon sensor plus its electronics and shielding is assumed to have the same amount of scattering as would 900 microns of silicon. The pixel dimensions are 50×400 microns. The resolution of the pixel detectors is parameterized as a function of the angle of the track.
- A forward silicon system with 3 stations of strip detectors per arm. For these simulations, the strip pitch is 100 microns and there are 4 views per station.
- A set of forward tracking chambers with 7 stations in each arm. In each arm the three stations at smallest $|z|$, have large holes to accommodate the forward silicon tracker. There are 9 planes of straws in each station, arranged as 3 views (Y,U,V) with 3 planes per view. The straw chamber resolution is assumed to be 150 microns.
- A RICH detector with aerogel, C_4F_{10} gas and a Pyrex mirror. The RICH performance is normally parameterized during the analysis phase. A more complete RICH simulation is outlined in Appendix A.
- A box-like electromagnetic calorimeter with $PbWO_4$ crystals which are 2.6 cm on a side and 22.00 cm in length.
- A muon system with 3 muon detectors and 2 muon absorbers in each arm.

12.3 Physics Event Generators

Pythia 6.129 [19] was used to generate physics processes for the BTeV simulation studies presented in this proposal. For these studies, Pythia was told not to decay hadrons containing heavy quarks; the decays of hadrons containing heavy quarks were modeled through the CLEO decay Monte Carlo QQ 9.2b [20]. Both BTeVGeant and MCFast use StdHep v4_09 [7] as an interface to the generator packages. The Evgen framework that is provided with the MCFast package provides a uniform command interface to the standard particle physics event generators; other generators such as Herwig [21] and Isajet [22] can be easily used for physics studies.

The size of the interaction region was taken as $\sigma_x = \sigma_y = 50 \mu\text{m}$ and $\sigma_z = 30 \text{ cm}$ corresponding to our current understanding of the projected running conditions in the C0 interaction region. The number of interactions per crossing at a beam crossing frequency of 132 ns is expected to be on average 2 at a luminosity of $2 \times 10^{32} \text{cm}^{-2} \text{s}^{-1}$, which means that there will often be more than one interaction per crossing. The effects of multiple interactions per crossing have been accounted for in these simulation studies. Simulation events include the signal interactions, containing primary b or c quarks, and the so called minimum bias events, which include elastic $p\bar{p}$ scattering, diffractive $p\bar{p}$ scattering and various QCD parton scattering processes producing quarks and gluons. Approximately 1.6% of the minimum bias interactions produce a $c\bar{c}$ pair and approximately 0.13% of the interactions produce a $b\bar{b}$ pair.

In both BTeVGeant and MCFast, each simulated beam crossing is built up from one or more interactions between beam particles. The construction of events utilizes the relationship between multiple, independent Poisson processes: the sum of N Poisson processes, each with mean n_i , is itself a Poisson process with a mean of n , where $n = \sum_{i=1}^N n_i$. For the study of signal processes involving the decay of a b or c quark, a beam crossing is simulated by selecting exactly one $b\bar{b}$ (or $c\bar{c}$) event and a Poisson distributed number of minimum bias events; the mean of the Poisson distribution is 2 interactions per crossing.

12.4 ECAL Cluster Finder Package

12.4.1 Event Information from the ECAL Detector

BTeV plans to use two electromagnetic calorimeters, each about 7.5 m away from the interaction region, one in the forward direction – positive z – and the other in the backward direction – negative z . They are made from PbWO_4 crystals and, in the baseline simulation, each ECAL wall contains 11,850 crystals, each connected to a phototube. In the baseline design for the ECAL, the crystals are arranged in a projective geometry such that each crystal points back to the interaction. See also Chapter 7.

The light generated in each crystal from electromagnetic showers or other charged particles is detected and converted into a digitized signal that is proportional to the number of photons incident on the photocathode. After a calibration step these numbers represent the total amount of energy deposited in each crystal for each event. From the array of energies for each calorimeter, we extract the following information:

- Shower information that includes a total energy and a position measurement.
- Matching information that connects particle tracks and showers.
- Shape information, specifically tuned to recognize overlapping showers and the case of two close by photons coming from the same π^0 .

The two programs employed to simulate BTeV, BTeVGeant and MCFAST, generate the same output structures to describe the hit pattern in the calorimeter crystals. It is a general description of a two dimensional array, but the shape of the segmentation into single crystals, also called cells, is not restricted to rectangles alone. We exploit this feature to simulate two different geometries, one made from parallel blocks of crystals, and the other made from an array of crystals each of which points to the interaction region. The second variant is referred to as the pointing or projective geometry.

Both MCFAST and GEANT have been used to simulate an ECAL made from a stack of parallel crystals. In this geometry, each crystal has the same dimensions of $2.6 \times 2.6 \times 22 \text{ cm}^3$. The inner surface of each crystal is placed $\pm 739 \text{ cm}$ in z , and a hole for the beam is simulated by leaving out the central 6×6 crystal square.

Only GEANT has been used to simulate the projective ECAL. It is simulated as crystals that are segments made from a spherical shell around the center of the detector. Its inner radius is 739 cm, and its thickness is 22 cm, which corresponds to the length of each PbWO_4 crystal. Each segment represents a single crystal and is made from a slice in θ , the angle between a point and the beam line, and ϕ , the azimuthal angle around the beam. The area of each segment is kept close to the area of a $2.6 \times 2.6 \text{ cm}^2$ real crystal, but the shape of the simulated segment is slightly curved. While this does not exactly describe the crystals which will be manufactured, we believe that this model simulates the response of a projective geometry well enough for the purposes of this proposal.

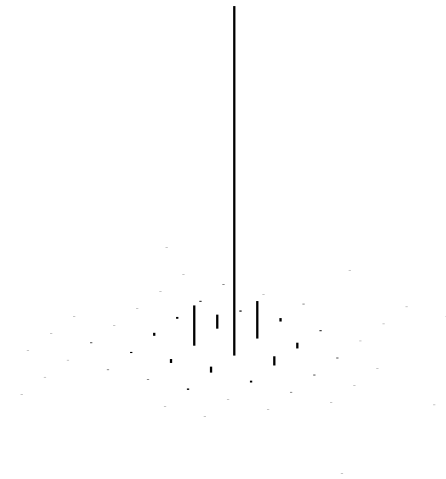


Figure 12.15: Hit pattern in a photon cluster in GEANT; The length of each line represents the energy in a single crystal. The simulation uses an internal energy cutoff to restrict the shower propagation. In this picture GEANT used a value of 100 keV.

12.4.2 Definition of the Cluster Finder Output Data

The cluster finder algorithm is designed to identify specific patterns in the calorimeter hit data. The two defined patterns are:

- Cluster – a region of crystals with connected topology; and
- Bump – a local maximum in the energy response within a cluster.

Figure 12.15 shows the result of the showering simulation in GEANT for a single 20 GeV photon. Our cluster finder algorithm will employ threshold cuts so we can balance the quality of the energy estimate for a shower, which improves with the inclusion of many crystals, and the probability of adding energy from nearby showers, which is minimized by using fewer crystals. We expect a readout related threshold of $\simeq 2.5$ MeV, which removes some of the hits in the shower shown above, and which reduces the data volume produced by the ECAL electronics. However, in this algorithm we added another energy threshold, at the level of 10 MeV, to ensure that the energy estimates use only the core of the shower pattern. In this way we can reduce the likelihood that overlapping showers will contaminate the true energy of each other.

A cluster is the basis of the algorithm. It represents all connected crystals that have an energy higher than the cluster threshold. The shape of a cluster can vary, since it only requires the crystals to be neighbors when it adds them to the same cluster. However, a crystal can only be part of one cluster.

A bump is centered around a crystal cell in a cluster that has the maximum energy deposited into it compared to its adjacent crystals, and thus represents a local maximum.



Figure 12.16: Geometrical placement of cells in the parallel (left) and pointing (right) ECAL simulations.

It has a fixed shape made from rings of neighboring cells. Figure 12.16 shows parts of the crystal arrangement from the parallel and projective ECAL geometries. The gray colored squares are considered neighbors of the cell filled with black color. All these cells belong to the bump, even if they are also in another bump or even in a different cluster. They only need to have an energy larger than the energy threshold. If a cell is part of more than one bump, an unfolding algorithm will partition the energy of that cell assigning some fraction of its energy to each bump to which the cell belongs.

12.4.3 General Algorithm

The first step in the cluster finder algorithm is to create connected regions of crystals with an energy higher than a tuneable threshold, known as the clustering threshold. The program uses a table of neighbor coordinates per cell to grow a cluster outwards from a starting cell. Thus, the same code is used for all supported geometries. The starting cell is selected from the list of cells that are sorted by energy and contain energies higher than the pedestal threshold. Any energy lower than this threshold is always ignored; therefore, a cell with a low energy response is not added to any cluster. A cell can only be assigned to one cluster, and after it has been added to a growing cluster, it is no longer considered when the code starts a new cluster.

After all cells are used to build clusters, each cluster is searched for local maxima. The same table of neighbors is used to compare a candidate cell's energy with each of its adjacent cells' energy. If it is found to be a local maximum, the cell is used as the center of a bump. Again, we use a tuneable threshold to control the minimum energy of a center cell in a bump.

Each object, i.e. cluster or bump, that is generated contains data recording its energy, position, and shape. A program using the output of the cluster finder can efficiently access those items from memory. Also, a list of crystals assigned to each object is stored, in case an analysis requires additional information.

The most important data generated for clusters and bumps are the total energy and the position. These algorithms impose the previously mentioned energy threshold cut on the energy of a cell before it is used. By imposing this cut we can improve the resolution of these measurements using a calibration function to correct for the expected difference between the energy sum and the real energy in the shower. The total energy of a cluster is measured

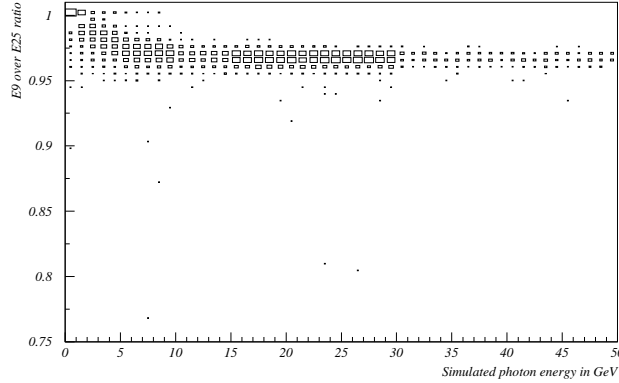


Figure 12.17: Measured ratio of E9 over E25 versus simulated photon energy.

using the overall energy sum for all crystal cells with a response that crosses the energy threshold. If the clustering threshold is higher than the energy threshold, then the cluster threshold will truncate the energy summation at the edge of the cluster.

The energy algorithm for a bump is different from that for a cluster. It is assumed that a bump represents an electromagnetic shower, initiated by a photon or electron. Due to the shape of the shower propagation, most of the energy is contained in the center cell and its nearest neighbors (for square segments there are 8 neighbors), with small leakage into further away neighbors. The sum of the energy in these cells is referred to as E9, since it contains contributions from up to 9 cells. To estimate the total energy of such a shower, we chose to use all adjacent cells and all cells of the next closest ring. This energy sum is called E25, since we add 25 cells in total, if they all cross the energy threshold. We use the ratio E9/E25 to test the hypothesis that the bump represents an electromagnetic shower. Figure 12.17 shows the distribution of this ratio for single photon events simulated by GEANT.

We use the second moment and the derived value of the “second moment mass” for a cluster to identify showers that contain two photons from the same π^0 but which only have one local maximum. The second moment is defined as

$$M(2)^2 = \sum_{cells} E_{cell} (\vec{C} - \vec{x}_{cell})^2 / \sum_{cells} E_{cell}$$

where \vec{C} is the unit vector to the center-of-gravity of a cluster, E_{cell} is the energy response of each cell in a cluster, and \vec{x}_{cell} is the unit vector to that cell. We find the values of this variable for single photon showers, $(M(2, \gamma))$, by using GEANT simulations and then obtain the “second moment mass” using,

$$m^2 = (M(2, cluster)^2 - M(2, \gamma)^2) E_{cluster}^2$$

This variable will peak at the invariant mass of the π^0 if the cluster contains the two photons from the decay of one π^0 . Figure 12.18 shows the distribution of m^2 for γ and π^0 particles with energies of 40 GeV and 70 GeV. At 40 GeV a clear separation between merged π^0

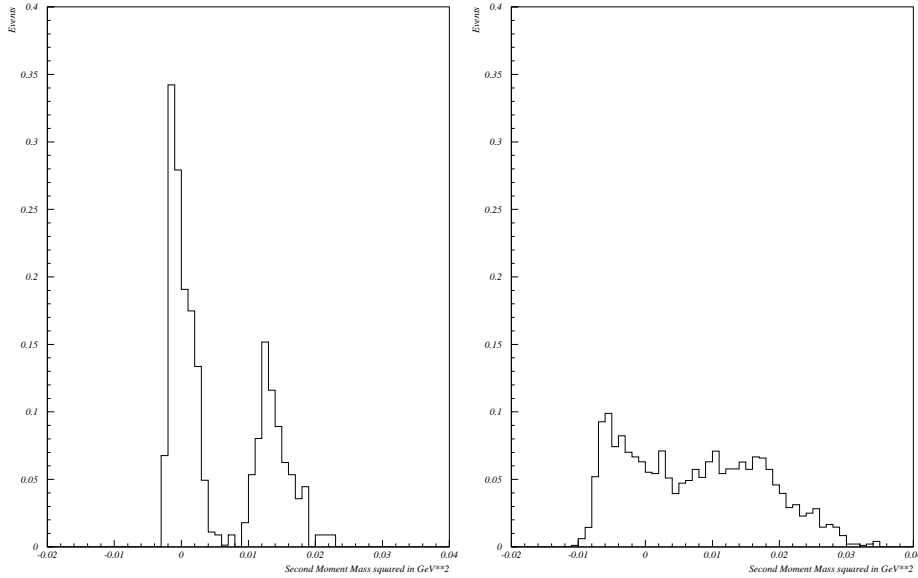


Figure 12.18: Second moment mass squared distribution for 40 GeV (left) and 70 GeV clusters (right). The simulated events contain either a single γ or a single π^0 . Each contribution due to one of the particle species is normalized to 1.

showers and photon clusters is visible. When the energy of the cluster reaches 70 GeV it becomes more difficult to distinguish the two sources for clusters. Still, a cut to suppress 99% of all photons will have an efficiency of about 64% for finding a π^0 cluster with that energy.

12.4.4 Important Corrections

Various effects introduce biases into the raw results obtained using the algorithms described above. There are basic geometric effects and effects due to limitations on the measurements. These effects can change event by event, and differ from photon to photon in the same event. The clustering code corrects for these effects either directly, as for the impact angle of the photon, or on a statistical basis as in the case of the expected average loss in the energy measurement. Here is the list of corrections put into the clustering code:

1. Average energy measurement residual, which depends on the total energy found in the bump.
2. Position bias correction for the center-of-gravity of the bump, “S curve correction.”
3. Unfolding of overlapping showers that share the energy response from the same cell.
4. Correction of shape and position measurements for the primary vertex position.

5. Correction of the impact position for the non-projective geometry, “z-depth correction,” which is used in the MCFast simulation.

The described algorithm and corrections can be improved with further study.

12.4.5 Implementation and Performance

The core of the clustering algorithm was written as a library that accepts user and simulation data input, generates the above described objects, and gives access to the information stored in them. The described calibration and correction parameters were found using single photon and π^0 event data.

We then tested the performance of the calorimeter and the clustering code by analyzing simulations of two different classes of events: the first class of events was artificial events in which only a single γ or a single π^0 was produced; the second class was realistic events, which included selected B meson decay chains plus a Poisson distributed number of background interactions per event. Some of these results are discussed in Chapter 7 of this proposal.

Next, we show the general performance of the cluster finder algorithm by plotting the finding efficiency for events which contain only a single photon. The finding efficiency for a photon was measured by,

- analyzing the simulated events using the cluster finder library,
- looking for the neutral shower that gives the closest match with the momentum vector from the generator level,
- and then accepting only those showers where the measured energy agrees with the generated photon’s energy within 3σ .

In all analyses, we impose standard cuts to select neutral shower candidates, using the ratio of E9 over E25 to select showers consistent with the shower shape of an isolated photon, and demanding that the shower be well isolated from charged tracks which project onto the ECAL. The latter cut is only relevant when analyzing B events, not single photon events. Figure 12.19 shows the obtained efficiencies for events containing only a single photon. The finding efficiency is not 100%, because it includes effects from the material, such as e^+e^- pair creation, between the creation point and the impact point in the ECAL. As expected, there is no change in the efficiency with the energy of the photon, however we do see a change with the radial position in the ECAL. The reason is the change in the total radiation length seen by the photon when crossing various detector components. Also, at the physical edge of the ECAL we lose efficiency due to leakage of parts of the shower into a region with no crystals. This result should be compared to the radial finding efficiency when the photon is embedded in realistic events, as shown in Chapter 7.6, which includes the effects of masking due to tracks and nearby showers.

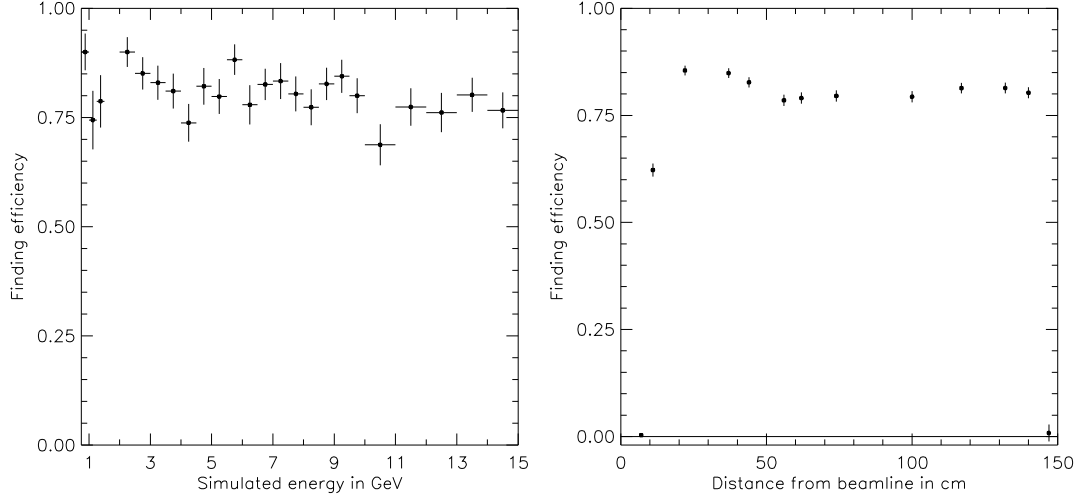


Figure 12.19: Fraction of correctly found photons in the calorimeter. (a) versus simulated energy, at fixed radius (100 cm), (b) versus radius of impact point in ECAL, at fixed energy (10 GeV). See the text for the selection criteria.

12.4.6 Electron Identification using the ECAL Cluster Finder

The clustering algorithm was used to measure the performance of the calorimeter for identifying electrons and positrons. A sample of $B^0 \rightarrow D^{*-} \rho^+$ events simulated using BTeVGeant was used in this study, this sample contains a mean of 2, Poisson distributed, non-beauty background interactions per event.

For reconstructed (charged) tracks that enter into the calorimeter acceptance, Fig. 12.20(a) shows the distance of the closest reconstructed bump for both electrons, (positrons implied also), and hadrons. Pions, kaons and protons are taken together for this study. About 85% of all electrons with momentum greater than 1 GeV/c have a matching bump within 2.5 cm. For these tracks with matching bumps, Fig. 12.20(b) shows the ratio of the reconstructed bump energy to the track momentum (E/p). As expected, the E/p values for electrons are sharply peaked near 1 whereas hadrons have low values of E/p . The dotted line in Fig. 12.20(b) shows the E/p values for the approximately 15% of the hadrons which deposit energy in essentially a single crystal. These are either non-interacting hadrons or ones that have decayed to a muon before entering the calorimeter. Figure 12.20(c) shows the shower shape variable $E9/E25$ for tracks with matching bumps, for both electrons and hadrons.

Electron identification using the calorimeter information can be provided for tracks that enter into the acceptance of the calorimeter. The simple criteria used for this study in identifying a track are:

- The track must have a matching bump in the calorimeter within 2.5 cm.
- $0.90 < E/p < 1.05$.

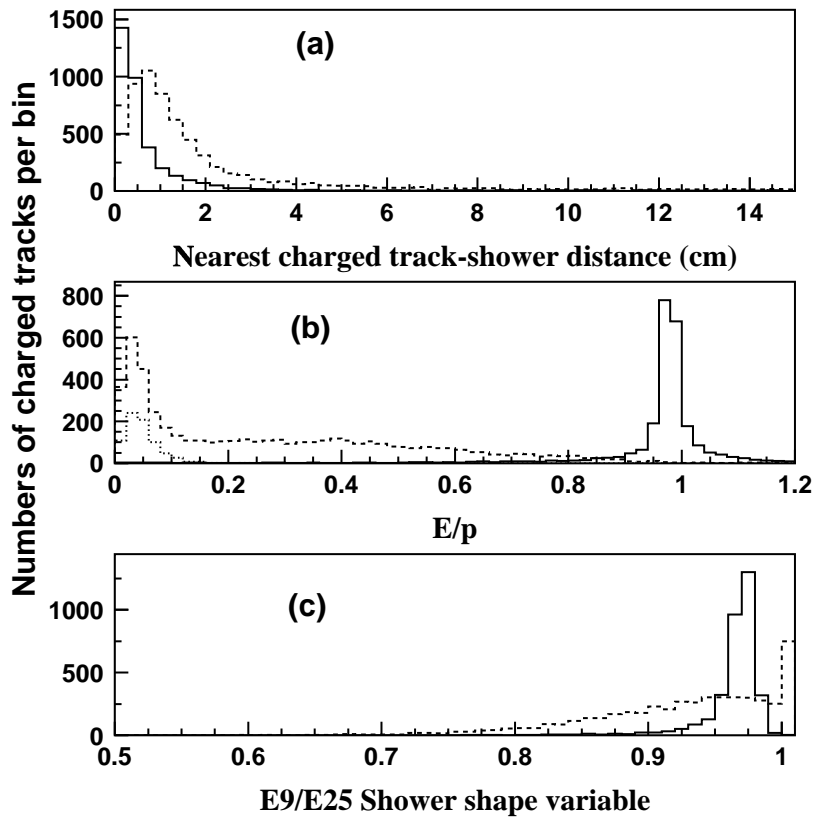


Figure 12.20: (a) Distance of charged tracks to the closest reconstructed bump in the calorimeter for electrons/positrons (solid line) and for $\pi/K/p$ hadrons (dashed line); (b) E/p for reconstructed charged tracks for electrons (solid line), all hadrons (dashed line), and hadrons with $E9/E25=1$ (dotted line); (c) $E9/E25$ shower shape variable for electrons (solid line) and hadrons (dashed line).

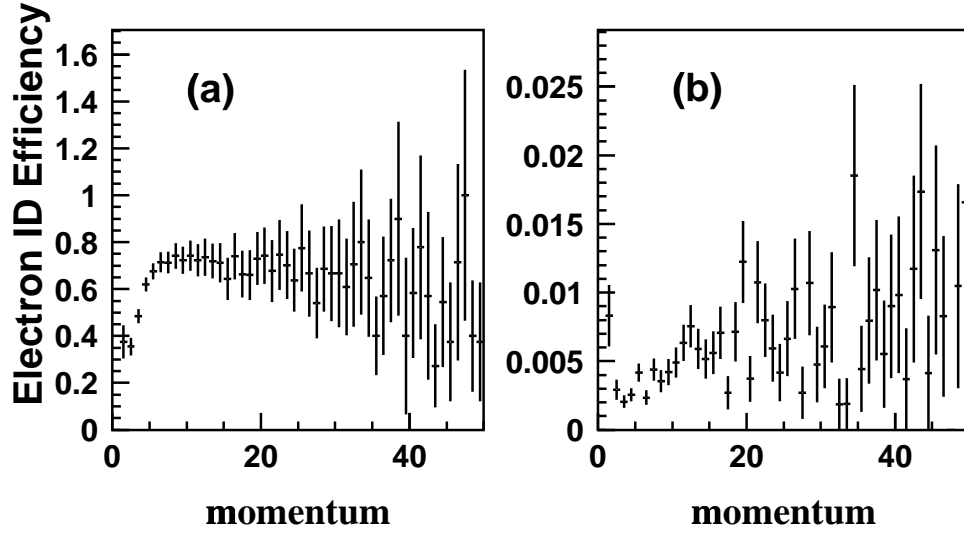


Figure 12.21: Electron identification efficiency as a function of track momentum in GeV/c for (a) electrons; and (b) hadrons.

- $E9/E25 > 0.90$.

Figure 12.21(a) shows the efficiency for correctly identifying an electron as a function of its momentum using these criteria. The level of misidentification of a hadron as an electron is shown in Figure 12.21(b) and is less than about 1%. By tightening the selection criteria on E/p and $E9/E25$ this misidentification rate can be significantly reduced with little loss in the efficiency for identifying real electrons.

Bibliography

- [1] P. Avery *et al.*, “MCFast: A Fast Simulation Package for Detector Design Studies”, in the Proceedings of the International Conference on Computing in High Energy Physics, Berlin, (1997). Documentation can be found at <http://www-pat.fnal.gov/mcfast.html> .
- [2] The BTeV Collaboration, http://www-btev.fnal.gov/public_documents/ptdr/ptdr.html .
- [3] GEANT: CERN Program Library Long Writeup W5013, http://wwwinfo.cern.ch/asdoc/geant_html3/geantall.html .
- [4] A description of GEANT4 is available at <http://wwwinfo.cern.ch/asd/geant4/geant4.html> .
- [5] TOSCA is a Finite Element Analysis package for electromagnetic calculations and is distributed by Vector Field.
- [6] The MCFast calorimetry package is described in, http://www-pat.fnal.gov/mcfast/version_doc/v5_0/simulator/calor_user_guide.ps .
- [7] A description of StdHep is available at <http://www-pat.fnal.gov/stdhep.html> .
- [8] A description of MCFIO is available at <http://www-pat.fnal.gov/mcfio.html> .
- [9] P. Billoir, Nucl. Instrum. Meth. **A225**, 352 (1984).
- [10] Paul Avery, <http://www.phys.ufl.edu/~avery/fitting.html>, Fitting Theory V: Track Fitting Using the Kalman Filter.
- [11] M.Regler and R. Fruwirth, “Reconstruction of Charged Particle Trajectories”, Plenum Publishing Company (1989).
- [12] R. Bock *et al.*, “Data Analysis Techniques for High-Energy Physics Experiments”, Cambridge University Press (1990).
- [13] Paul Avery, <http://www.phys.ufl.edu/~avery/fitting.html>, “Applied Fitting Theory VII: Building Virtual Particles” and “The Data Analysis and Kinematic Fitting With the KWFIT Library.”

- [14] J. Dumarchez *et al.*, “Average Multiplicity and KNO Scaling in Hadron-Hadron Interactions”, *Il Nuovo Cimento* **66A**, 114 (1981).
- [15] A. Firestone *et al.*, “ π^-p interactions at 360 GeV/c: Measurement of the total and elastic cross sections and the charged-particle multiplicity distribution”, *Phys. Rev. D* **14**, 2902 (1976).
- [16] H. Fesefeldt, “GHEISHA: The simulation of Hadronic Showers - Physics and Applications”, PITHA 85/02.
- [17] A. Brenner *et al.*, “Experimental Study of single-particle inclusive hadron scattering and associated multiplicities”, *Phys. Rev. D* **26**, 1497 (1982).
- [18] C. W. Akerlof *et al.*, “Hadron-proton elastic scattering at 50, 100, and 200 GeV/c momentum”, *Phys. Rev. D* **14** 2864 (1976).
- [19] H. U. Bengtsson and T. Sjostrand, *Comput. Phys. Commun.* **46**, 43 (1987).
- [20] QQ is developed and maintained by the CLEO Collaboration. See <http://www.lns.cornell.edu/public/CLEO/soft/qq/> For the studies reported here, it is used for its model of the decays of hadrons containing heavy flavors.
- [21] G. Marchesini and B.R. Webber, *Nucl. Phys.* **B310**, 461 (1988); *Nucl. Phys.* **B330**, 261 (1988);
I. G. Knowles, *Nucl. Phys.* **B310**, 571 (1988);
G. Abbiendi, *et al.*, *Comp. Phys. Comm.* **67**, 465 (1992).
- [22] F. Paige and S. Protopopescu, Brookhaven National Laboratory Report BNL-37066 (1985) (unpublished).

Chapter 13

Comparison of MCFast and BTeVGeant for the Calorimeter and Tracker

This chapter describes studies which were done to compare various quantities computed using BTeVGeant with the same quantities computed using MCFast. The two programs were described in Chapter 12. The purpose of these studies was two-fold, to catch errors in the representation of the detector inside the programs and to demonstrate the validity of the approximations and parameterizations made in MCFast. The first section of this chapter compares the simulation of the electromagnetic calorimeter and the second section compares the simulation of the tracking system.

13.1 MCFast vs. BTeVGeant showering

This section describes the comparison of the showering results generated by the two simulation packages, MCFast and GEANT. The showering in MCFast is parameterized, but gives a reliable representation of the longitudinal and transverse profiles of electromagnetic showers which can be used for many physics and trigger studies. In fact, many of our early studies of photon detection efficiency done with MCFast have been confirmed by BTeVGeant. Studies which involve examining the details of the shower shape, such as merged π^0 reconstruction, can also be done with MCFast, but we chose to use the more detailed simulation provided by BTeVGeant for the analyses presented in this proposal.

The clustering algorithm used for reconstructing showers is exactly the same for BTeVGeant and MCFast. The output of the clustering step can be used to illustrate some of the differences between the two showering models. For this study, we have used events containing only a single photon with a fixed energy of 20 GeV originating at the center of the BTeV detector and at an angle of about 100 mrad from the beam line so that the shower will be well contained in the calorimeter. The details of the upstream detector differ slightly in the two simulation packages; the MCFast geometry description is missing some of material in the support structures. The size, composition and layout of the two calorimeters is the same in MCFast and BTeVGeant. We reconstructed clusters from hit patterns generated by

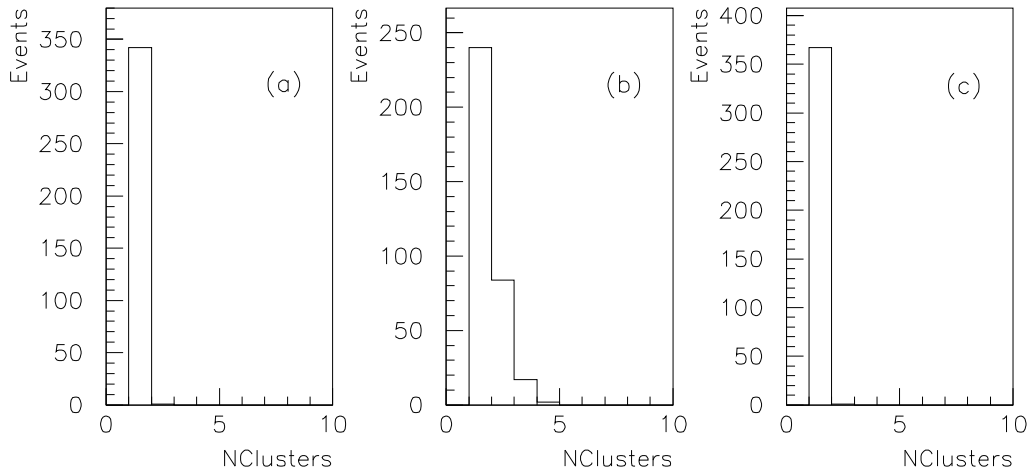


Figure 13.1: Comparison of the number of found clusters in the BTeV calorimeter for single photons of 20 GeV; (a) GEANT with a 40 MeV cluster threshold, (b) GEANT with a 10 MeV cluster threshold, (c) MCFast with a 40 MeV cluster threshold. In each case, the primary cluster contains most of the energy. The secondary clusters are made from only one or two crystals, each containing a small amount of energy.

the two packages in the crystal calorimeter and compared the resulting reconstructed cluster information. A cluster is a set of crystals that form a connected region. Each crystal in a cluster must have an energy greater than the cluster threshold in order to be included in the cluster. The default cluster threshold is 40 MeV for both BTeVGeant and MCFast shower reconstruction.

A shower generated by a single photon should make one cluster in the calorimeter. To ensure that the original photon actually initiated the shower in the electromagnetic calorimeter (ECAL), we excluded photons that pair converted in the detector elements in front of the ECAL. MCFast sometimes creates two clusters because it randomly deposits discrete amounts of energy in its modeling of the transverse shower spread. The energy deposition is calculated for each trace step and then subdivided into a number of discrete energy packets called subhits. Each subhit is distributed randomly around the shower axis according to the formulae given in Section 12.2.4. An electromagnetic shower in MCFast is truncated at 4.5 Moliere radii from the shower axis.

During the reconstruction of a cluster, we impose a clustering threshold, or a minimum energy for a cell to be included in a cluster. The total number of crystals in the reconstructed cluster can vary with the cluster threshold. In MCFast, the default smallest subhit produced for a 20 GeV photon shower is normally higher than the default 40 MeV cluster threshold, so the number of hits in the reconstructed cluster is not sensitive to reducing the cluster threshold. GEANT showering produces hits in a large number of crystals but many contain subthreshold energies, so the number of hits per cluster can be very sensitive to the cluster energy threshold.

Figure 13.1 shows a plot of the number of clusters found in single 20 GeV photon events.

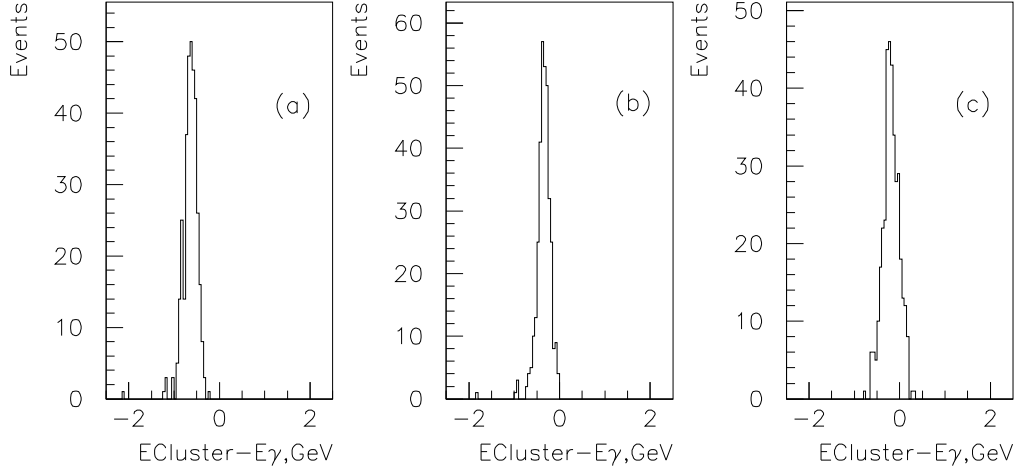


Figure 13.2: Comparison of the relative difference between the cluster energy and total energy from a 20 GeV single photon; (a) BTeVGeant reconstructed with a 40 MeV cluster threshold per crystal, (b) BTeVGeant with a 10 MeV cluster threshold per crystal, (c) MCFast with a 40 MeV cluster threshold per crystal

As expected, both MCFast and BTeVGeant normally create one cluster of crystals in each event. The MCFast shower model occasionally produces an extra cluster containing a small fraction of the total energy. The second cluster is not produced when the number of subhits in the modeling of the transverse shower spread is increased. GEANT produces disconnected clusters when the cluster threshold is decreased to 10 MeV. These secondary clusters contain only a small fraction of the total energy.

Figure 13.2 shows the difference between the sum of crystal energies in the largest reconstructed cluster and the total energy of the photon. The width of the distribution is largely due to the smearing expected from photo-statistics. Showers generated by BTeVGeant and reconstructed with a cluster threshold of 40 MeV (a) have a small tail on the negative side of the distribution, which indicates that the shower simulation produced a significant number of hits with energies less than the clustering threshold and thus the overall energy in the shower was underestimated in reconstruction. Reducing the cluster threshold improves the situation, both shifting and sharpening the peak, as it adds in energy from the outer edges of the shower. MCFast (c) does not have a large tail since most hits are above the cluster threshold, but the distribution is broader. Note that leakage out of the back of the crystals would result in an overall shift of the distribution.

For electromagnetic showers, the shower energy is normally determined during analysis from the bump energy (E_{25}), which sums the energy in the 25 blocks surrounding and including the seed crystal which is the crystal with a locally maximum amount of energy (see Section 12.4). The bump energy E_{25} is not as sensitive to the detailed simulation of the shower shape as the reconstructed cluster energy since most of the energy from a photon is mostly contained within 25 crystals in the BTeV calorimeter. Figures 13.3 and 13.4 show the reconstructed bump energies from the sum of 25 and 49 crystals surrounding the center of

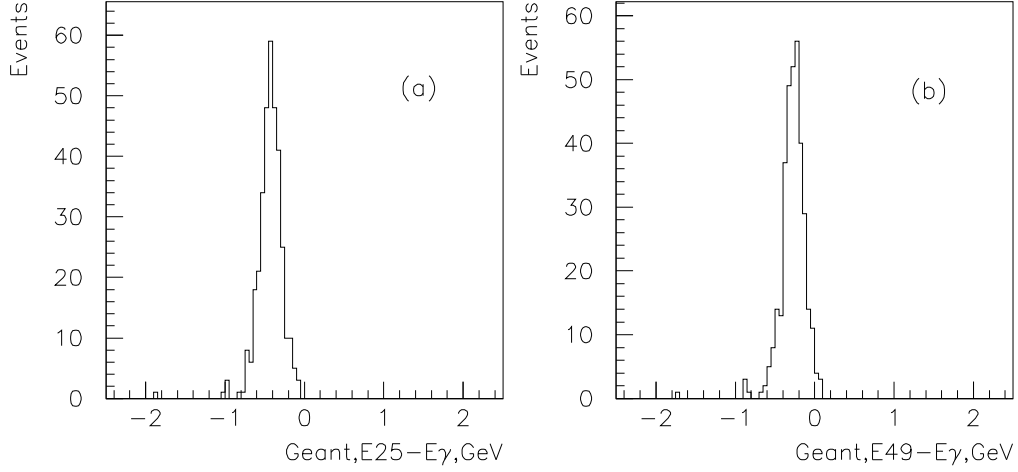


Figure 13.3: The difference between the photon energy and the reconstructed bump energies for 20 GeV photons as simulated by BTeVGeant. The bump energy is determined from the sum of crystal energies (a) E25 – summing 25 crystals around the peak; and (b) E49 – summing 49 crystals.

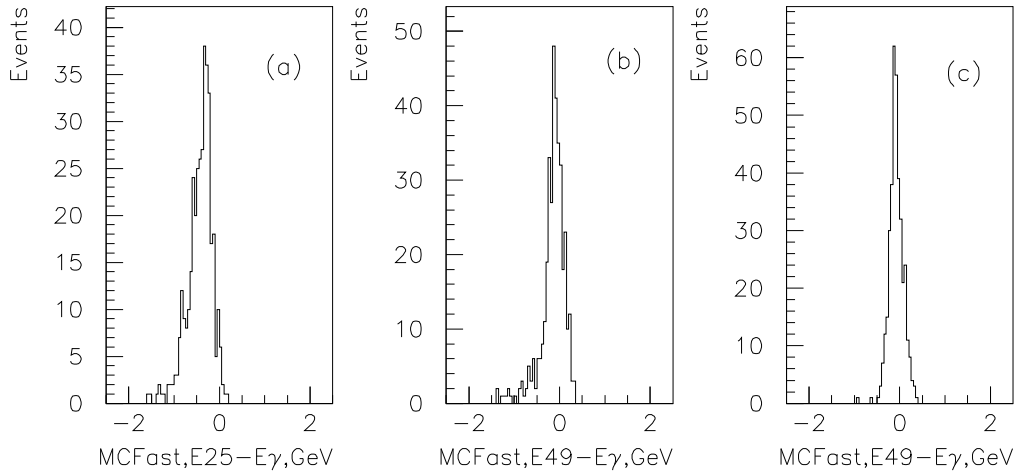


Figure 13.4: The difference between the photon energy and the reconstructed bump energies for 20 GeV photons as simulated by MCFast. The bump energy is determined from the sum of crystal energies (a) E25 for default MCFast; (b) E49 for default MCFast showers with 25 subhits per step in the transverse shower spread step; and (c) E49 for MCFast showers with 100 subhits per step.

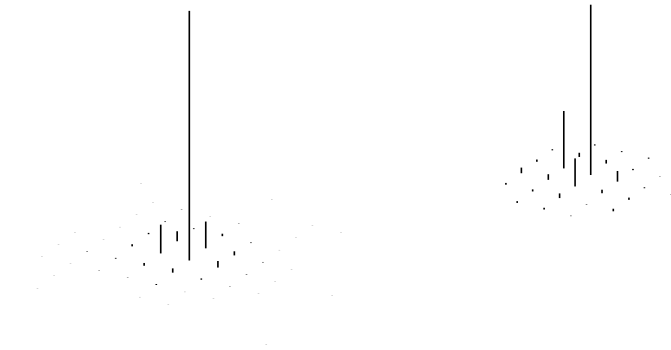


Figure 13.5: Comparison of the hit pattern in a 20 GeV photon cluster as generated by (left) BTeVGeant, (right) MCFast. The length of each line represents the energy in a single crystal. Both plots use the same scale. The minimum energy per crystal is 40 MeV.

the bump. There is slightly more leakage to the outer row of crystals in MCFast. The energy resolution improves when 100 subhits are created during each transverse shower spread step.

In general, the BTeVGeant electromagnetic showering model distributes the energy from a shower over more crystals than MCFast and each crystal at the edge of the cluster contains less energy. BTeVGeant deposits more of the energy close to the shower core and small amounts of energy over a large region transversely. MCFast generates a somewhat wider shower core with truncated tails. Figure 13.5 shows the energy pattern in a cluster from BTeVGeant and MCFast for a cluster threshold of 40 MeV per crystal.

The difference in the showering models can also be seen by looking at the number of crystals above the clustering threshold. The total number of crystals will be less if the bulk of the deposited energy stays close to the shower core. Figure 13.6 shows the number of crystals that were used to form the reconstructed cluster. As discussed previously, many crystals in the BTeVGeant simulation do not cross the default threshold of 40 MeV, and therefore are not added to the cluster. MCFast and BTeVGeant with a 10 MeV cluster threshold produce nearly the same number of hit crystals per primary cluster.

During reconstruction the details of the shower shape are important for distinguishing between electromagnetic and hadronic showers. The showers in MCFast are similar enough that it is possible to develop efficient selection criteria for photons and electrons in both cases. The hadronic shower shape in MCFast is also parameterized. Full event simulation including electromagnetic and hadronic showers using MCFast has given us a reasonable prediction of the photon efficiency as compared to the more detailed BTeVGeant. Test beam data with photomultiplier readout are not readily available to us, so a complete detailed data vs. Monte Carlo comparison has not yet been done.

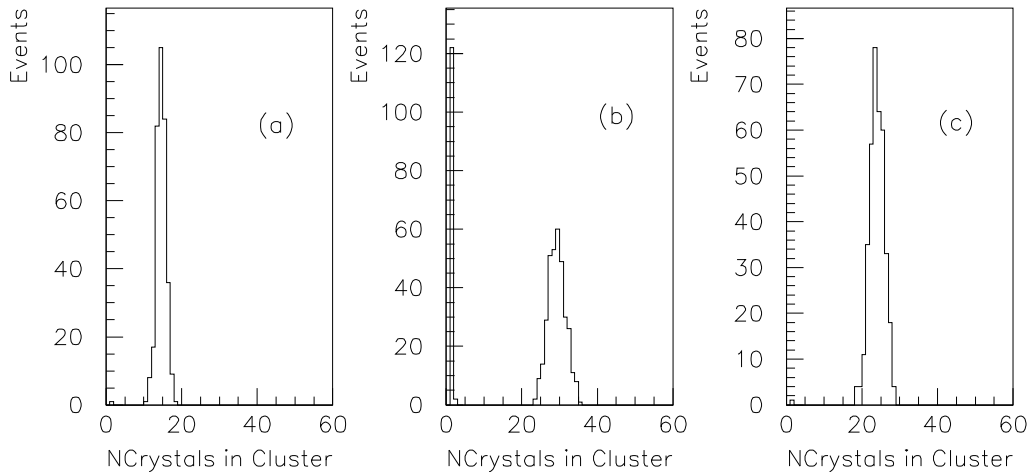


Figure 13.6: Comparison of number of crystals per cluster; (a) BTeVGeant reconstructed with a 40 MeV cluster threshold per crystal, (b) BTeVGeant with a 10 MeV cluster threshold per crystal, (c) and MCFast with a 40 MeV cluster threshold per crystal

13.2 MCFast vs. GEANT tracking

13.2.1 Introduction

This section describes comparisons between the BTeVGeant model of the BTeV tracking system and the MCFast model of the same system. The comparison is made both in low level quantities, such as occupancies and multiplicities, and in high level quantities, such as mass and vertex resolutions.

In order to ensure that the same detector was simulated by the two programs, the MCFast geometry file was generated automatically by BTeVGeant. Because BTeVGeant allows a more sophisticated model of detector elements, some of the finer details of the BTeVGeant model are simplified or are missing from the MCFast model.

BTeVGeant and MCFast read the same input files but differences in the detector response arise as the input tracks are propagated through the detector. Most prominently, BTeVGeant has a highly developed and complete model of hadronic interactions between particles and the detector material, while MCFast uses a greatly simplified model. In addition, MCFast uses a Gaussian model of multiple scattering while BTeVGeant uses the Moliere model, which has non-Gaussian tails. BTeVGeant explicitly models δ -ray production but MCFast does not. MCFast has simplified models of other processes such as pair creation and bremsstrahlung. MCFast has vacuum, rather than air, between major detector elements — this is most significant in the model of the forward tracking system. In MCFast, showers which develop in one medium, such as the muon shield or the calorimeter, cannot create hits in neighboring tracking systems;¹ in BTeVGeant, showers do create hits in neighboring tracking volumes.

¹They do deposit energy in neighboring calorimeters and that energy is recorded in the calorimeter hit structure.

There is one other subtle effect: as a particle passes through a diffuse medium, such as the RICH gas, BTeVGeant models the scattering as occurring at many places along the track; MCFast models the scattering as occurring at a thin plane at the center of the gas volume. The net effect of these differences is that the two programs produce different estimates for device occupancy, track multiplicity and track parameter resolution. These, in turn, imply different trigger efficiencies, different efficiencies for analysis cuts and different mass resolutions.

The following sections will demonstrate that, although the two programs produce very different estimates of occupancies, they produce very similar estimates for most quantities of physics interest.

13.2.2 Occupancies

Figure 13.7 shows the multiplicity of pixel clusters and the multiplicity of various trigger primitives for $B_s^0 \rightarrow D_s^\pm K^\mp$ events which were processed using BTeVGeant and which passed analysis cuts similar to those described in section 16.4.1. Figure 13.8 shows the same information except that the events were simulated using MCFast. These figures are similar to Figure 14.1, except they were prepared using events from a different channel; otherwise the information in the caption to Figure 14.1 applies. From these figures one sees that BTeVGeant produces about 20% more pixel hits than does MCFast. This causes a small, barely noticeable, increase in the doublet yield but no significant change in the yields of triplets or tracks.

The major impact of higher multiplicity is the possibility that it might confuse pattern recognition algorithms. Of the systems discussed in this proposal, the Level-1 trigger has the most potential to be confused by this increased multiplicity. Because the absolute occupancy remains small, the impact of the increase in occupancy is expected to be negligible. This was confirmed by studying the trigger efficiency for the $B_s^0 \rightarrow D_s^\pm K^\mp$ events used to make Figures 13.7 and 13.8. The trigger efficiencies were measured to be $69 \pm 1\%$ and $68 \pm 2\%$, for BTeVGeant and MCFast, respectively. These numbers differ from those presented in Chapter 14 because different cuts were used to define the events for which the trigger efficiency was measured.

In MCFast, the response of the muon system is also simplified; most importantly hadronic showers in the shielding material do not leak out of the back of the shielding block to create hits in the muon counters. Section 8.3.2 describes a BTeVGeant based study of the sources of noise in the muon system; none of the dominant noise sources are modeled in MCFast. An equivalent statement is that, in MCFast, all hits in the muon counters are produced by real muons, including muons from decay in flight of B mesons, D mesons, kaons and pions. A figure of merit to compare the two programs is the average occupancy of the muon counters for beam crossings which contain a Poisson distributed number of minimum bias interactions, with a mean of two interactions per crossing. In BTeVGeant the average occupancy was determined to be 1.2% while in MCFast it was determined to 0.015%.

On the other hand, both MCFast and BTeVGeant properly range out muons as they

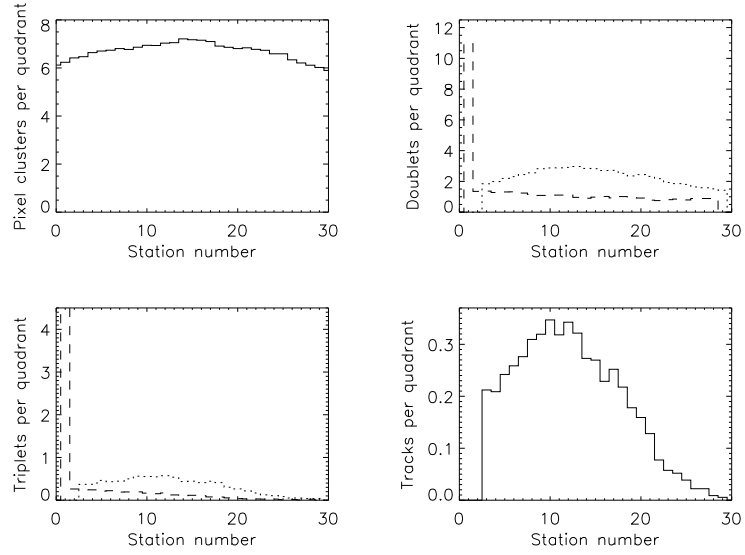


Figure 13.7: Multiplicities of pixel hits and trigger primitives for events generated with BTeVGeant. See the text for details.

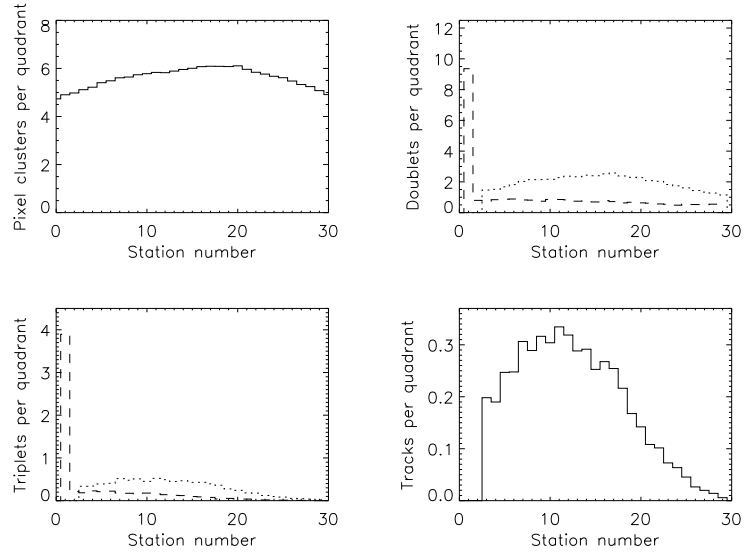


Figure 13.8: Multiplicities of pixel hits and trigger primitives for events generated with MCFast. See the text for details.

Straw Occupancies, 2 Minimum Bias Events

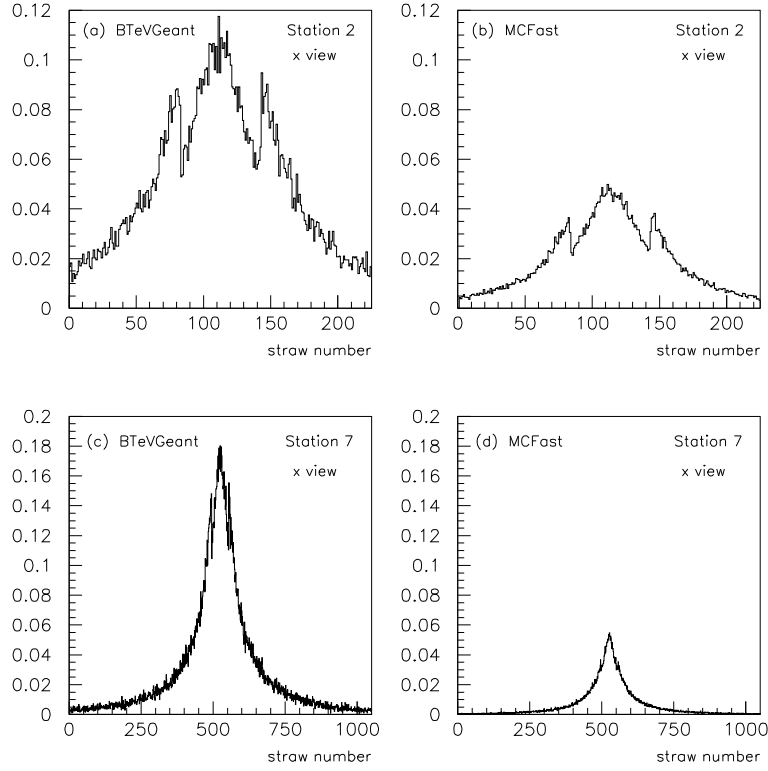


Figure 13.9: Comparison of straw chamber occupancies as computed by BTeVGeant (left) and MCFast (right). Station 2 (top) is the station which is second most downstream and station 7 (bottom) is the station which is closest to the interaction region. For all parts of the figure, the vertical axis the probability per beam crossing that the straw will have a hit.

suffer ionization energy loss in the shielding material. Therefore both programs can be used for determining the efficiency for fiducial cuts on muons. The bottom line is that MCFast cannot be used for determining the rates at which hadrons fake muons but it can make use of an externally supplied parameterization of fake rates.

The occupancies in the forward tracking system are also underestimated in MCFast; the reasons for this are similar to those discussed above for the muon system. Figure 13.9 compares the occupancies of several straw planes, as computed in BTeVGeant, with those computed by MCFast. The gross features of the distributions are the same but MCFast underestimates the rates by a factor which varies from about 2 far from the interaction region to about 3 close to the interaction region. The same general behavior is seen in the strip detectors: MCFast underestimates the occupancies by a factor of about 2 to 3. For the strip detectors BTeVGeant predicts an occupancy which is at most $\simeq 1\%$ in the hottest

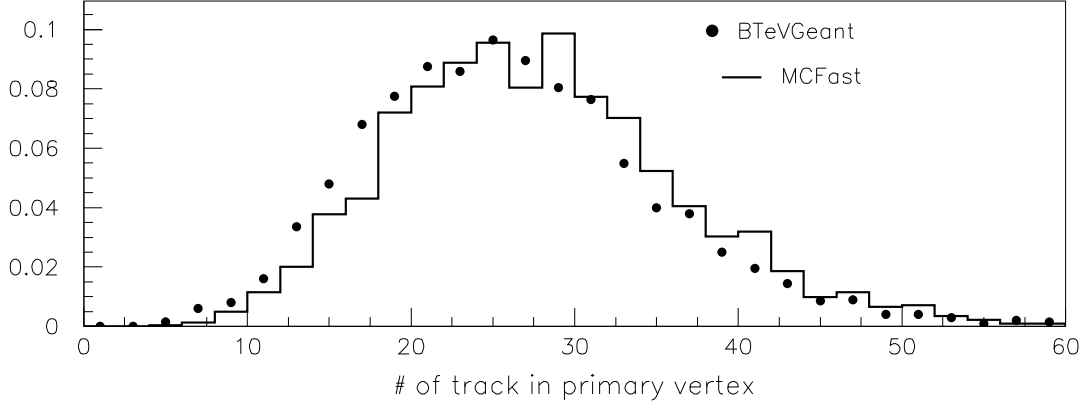


Figure 13.10: Primary vertex multiplicity for $B^0 \rightarrow \pi^+\pi^-$ candidates which pass the analysis cuts described in Section 16.1.

regions. This study shows that it is important to use BTeVGeant for any study which is sensitive to occupancies in the forward tracking system; for other studies, such as questions about resolutions, both packages will give reasonable answers.

13.2.3 Efficiency and Resolution for $B^0 \rightarrow \pi^+\pi^-$

The comparison of high level tracking quantities was done using the decay mode $B^0 \rightarrow \pi^+\pi^-$ which was analyzed as described in Section 16.1. These studies were performed using approximately 23,000 generated $B^0 \rightarrow \pi^+\pi^-$ events. The efficiency for the B^0 candidates to pass all analysis cuts was determined to be $8.0 \pm 0.2\%$ using BTeVGeant and $8.8 \pm 0.2\%$ using MCFast; these numbers exclude the trigger efficiency. Other results from the study are shown in Figures 13.10 and 13.11. Each of the histograms in Figure 13.11 has been fitted to a Gaussian and the results of those fits are reported in Table 13.1.

One of the reasons for moving from MCFast to BTeVGeant was the concern that MCFast would seriously underestimate the amount of tails in the distributions of important physics quantities. It is clear from the figure that this is not a serious problem in any of the distributions. For example, in the mass resolution plot, Figure 13.11e), the BTeVGeant result has 1.7 % of the signal more than $\pm 3\sigma$ from the mean, while the MCFast result has 0.9 % of the signal more than $\pm 3\sigma$ from the mean.

Inspection of the figures shows that the agreement between the two packages is excellent for Δ_{DCA} and reasonably good for both ΔL and the primary vertex multiplicity. The agreement on the mass resolution is not as good. The disagreement in the mass resolution, 29 MeV/ c^2 for BTeVGeant vs 22 MeV/ c^2 for MCFast, is not yet understood in detail and is being investigated. The quantities ΔL and Δ_{DCA} are sensitive mostly to the behavior of the pixel detector, but the mass resolution is sensitive to all of the details in the model of the tracking system, including the details of multiple scattering throughout the downstream

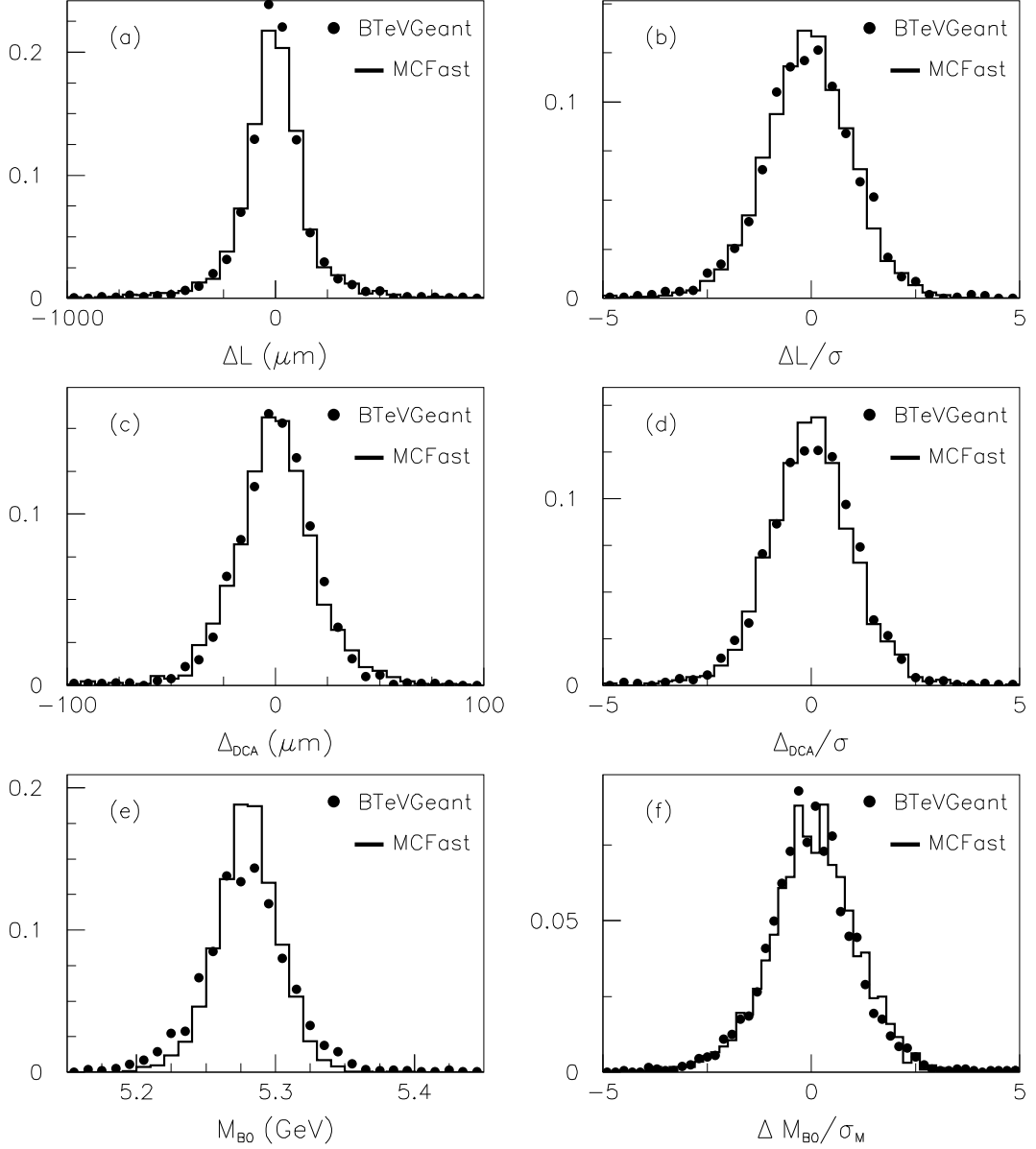


Figure 13.11: Comparisons between MCFast and BTeVGeant using $B^0 \rightarrow \pi^+\pi^-$ candidates which pass the analysis cuts described in Section 16.1: a) the measured decay length minus the generated decay length, ΔL , for the B^0 candidate; b) $\Delta L/\sigma$, where σ is the error on ΔL ; c) the measured DCA minus the generated DCA, Δ_{DCA} , where DCA is the distance of closest approach of the B^0 candidate to the primary vertex; d) $\Delta_{\text{DCA}}/\sigma$, where σ is the error on Δ_{DCA} ; e) the measured $\pi^+\pi^-$ invariant mass; f) $\Delta M/\sigma$, where ΔM is the measured $\pi^+\pi^-$ invariant mass minus the generated B^0 mass and where σ is the error on ΔM . Each figure has about 1850 entries for BTeVGeant and about 2030 entries for MCFast.

Quantity	Units	MCFAST		GEANT	
		Mean	σ	Mean	σ
ΔL	(μ)	$-8. \pm 2.$	$119. \pm 2.$	$-6. \pm 3.$	$114. \pm 2.$
$\Delta L/\sigma$		$-0.05 \pm .02$	1.00 ± 0.02	$0.04 \pm .02$	1.03 ± 0.02
Δ_{DCA}	(μm)	-0.3 ± 0.3	17.6 ± 0.3	0.3 ± 0.4	17.0 ± 0.3
$\Delta_{\text{DCA}}/\sigma$		-0.00 ± 0.02	0.963 ± 0.014	0.00 ± 0.02	0.959 ± 0.015
$M_{\pi\pi}$	(GeV/c^2)	5.2800 ± 0.0005	0.0219 ± 0.0003	5.2790 ± 0.0007	0.0289 ± 0.0005
$\Delta M/\sigma$		0.04 ± 0.02	0.989 ± 0.015	-0.09 ± 0.02	0.982 ± 0.015

Table 13.1: Results obtained by fitting each histogram in Figure 13.11 to a Gaussian. The fits were performed over an interval of approximately $\pm 3\sigma$ about the mean.

spectrometer. In any case, most of the results presented in this proposal have been computed using the poorer, BTeVGeant, mass resolution.

Finally, the histograms in the right-hand column of Figure 13.11 indicate that, for both programs, the Kalman filter correctly determines the covariance matrices of the tracks and that the mass and vertex fitters correctly propagate those errors.

Chapter 14

Trigger Simulations for Levels 1 and 2 and a brief discussion of Level 3

14.1 Introduction

The vertex trigger is the primary physics trigger for BTeV. We trigger on B events by taking advantage of the main difference between heavy quark events and typical hadronic events—the presence of detached beauty or charm vertices. The vertex trigger finds these vertices by utilizing the superior pattern recognition capabilities of the pixel detector to reconstruct tracks and vertices in the first stage of the trigger, Level 1, and in all subsequent stages of the trigger.

The baseline design of the vertex trigger consists of three levels. Each level contributes to the reconstruction of events, and successive levels impose more and more refined selection criteria to select B events and reject light-quark background events. At Level 1 the vertex trigger reduces the trigger rate by a factor of 100 while maintaining high efficiency for B decays that can be successfully reconstructed in the spectrometer. The tracks and vertices found by the Level 1 trigger are passed to Level 2. At Level 2 the reconstruction of tracks and vertices is improved by reviewing the pixel data used at Level 1, by including additional pixel hits in the tracks, and by introducing data from the forward tracking system. At Level 3, all of the data for a beam crossing are available and can be used to impose the selection criteria for the final trigger decision. The trigger rate is reduced by an additional factor of 20 by Levels 2 and 3.

In this chapter we focus primarily on simulations of the Level 1 vertex trigger, with simulation results for Levels 2 and 3 presented at the end of the chapter. We present results for a Level 1 trigger that has been extensively modified compared to the trigger scheme that was presented in the BTeV Preliminary Technical Design Report (PTDR). The new Level 1 trigger is designed to work with the redesigned pixel system, which has less material than the PTDR pixel system due to a reduction in the number of pixel planes and substrates (see Chapter 4). Eliminating one of three pixel planes per tracking station has significantly reduced the amount of material in the pixel detector; however, the new

vertex trigger must achieve a level of performance comparable to the PTDR trigger using only two-thirds of the pixel measurements. Our simulations show that this goal has been accomplished, and additional improvements in the trigger performance relative to the PTDR have been achieved.

Moreover, our simulations of the vertex trigger have improved compared to simulations performed for the PTDR. As before, our simulation results are based on a genuine reconstruction package that processes pixel-hit clusters generated by a Monte Carlo program. The Monte Carlo track information is only used to monitor the performance of the trigger algorithms; it is never used to prompt the pattern recognition or reconstruction algorithms.

There are two significant changes that improve the simulation of the vertex trigger. The first change is that our results are now based on simulations of pixel clusters generated by a GEANT Monte Carlo program. We use GEANT to simulate particle trajectories in heavy- and light-quark events, and to generate hits from hadronic interactions, photon conversions, decays in flight, and delta rays. The second change in our trigger simulation is the way in which we simulate pixel clusters. We introduce non-Gaussian tails to generate realistic pixel hits that include the effects of low-energy delta rays. These non-Gaussian tails are based on parameterizations of 1999 BTeV test beam data (see Appendix A). Together with the GEANT simulation, these changes represent a significant improvement in the level of realism used to simulate the Level 1 vertex trigger.

14.2 Level 1 Trigger

As described in Chapter 9, the Level 1 trigger is a detached-vertex trigger that receives data from the pixel detector, reconstructs tracks and vertices, selects B events, and reduces the overall event rate by a factor of 100. B events are found by looking for B -decay tracks that have a large impact parameter with respect to a primary vertex. The trigger reconstructs primary vertices for every beam crossing, and counts the number of tracks with an impact parameter that is in an acceptable range. Tracks with very large impact parameters are not counted to exclude tracks associated with other primary vertices, and strange particle decay daughters. The decision to select an event is based on a cut that requires a minimum number of tracks with acceptable impact parameters.

The design of the Level 1 trigger is tied closely to the design of the pixel vertex detector. Compared to the BTeV PTDR, the pixel vertex detector now has two pixel planes per tracking station instead of three. With only two planes per station, the PTDR strategy of finding track mini-vectors in a single three-plane station had to be abandoned. Instead, the new Level 1 trigger finds track segments that span three tracking stations. A potential problem with this approach is that an overwhelming number of pixel cluster combinations may need to be considered for pattern recognition, since track segments are now found over a much larger region of the pixel detector compared to the very localized regions used to find mini-vectors. The solution is to restrict the pattern recognition to a subset of pixel clusters in order to reduce the number of combinations that must be considered by the trigger hardware.

We impose several restrictions to reduce combinatorics in the Level 1 trigger. These

restrictions are implemented so that they do not degrade the track reconstruction efficiency for tracks that are needed to implement an effective trigger. Details of the pattern recognition algorithm are presented in Chapter 9; here we provide a description of three important features that account for the performance of the Level 1 trigger algorithm.

The first key feature of the algorithm is that it considers only a fraction of the available pixel data to initiate pattern recognition, while maintaining high efficiency for tracks from primary vertices and B -decay vertices. Pixel clusters that are used to “seed” the pattern recognition are restricted to an *inner* region (i.e., pixel clusters close to the beam region, within 1 cm of the inner edge of each pixel plane) or an *outer* region (clusters within 1 cm of the outer edge of a pixel plane or in the two outermost stations). This geometric restriction (see Fig. 9.4 in Chapter 9) provides an effective means to limit the number of pixel cluster combinations that must be considered for pattern recognition. Fig. 14.1a shows simulation results for the average number of pixel clusters for one quadrant of a pixel plane (solid histogram) for all 31 tracking stations for minimum bias events with an average of two interactions per beam crossing. Dotted and dashed histograms represent the number of clusters in the inner and outer regions, respectively. These histograms show the fraction of hits used to “seed” the pattern recognition.

The second important feature of the Level 1 algorithm is that it uses pixel clusters in a manner that further limits the number of pixel cluster combinations that must be considered for pattern recognition. The *inner* pixel clusters are used to find the beginning of a track, while the *outer* pixel clusters are used to find the end of a track in the pixel detector. Furthermore, the pattern recognition imposes cuts that require that tracks must enter the pixel detector at the inner edge of the detector (i.e., the tracks must come from the beam region), and tracks must exit the pixel detector at the outer edge of the detector or at the two outermost tracking stations (the first and last stations in the detector). These requirements eliminate many of the tracks associated with hadronic interactions or photon conversions that originate in the pixel detector, and may cause false triggers if they were to be reconstructed as tracks having a large impact parameter with respect to a primary vertex. The requirements also eliminate beam-halo tracks that do not cross an inner edge of the pixel detector.

The third key feature of the Level 1 algorithm is that each stage in the algorithm reduces the number of trigger primitives that must be considered by subsequent stages. This is an important feature, since it reduces the amount of data that must be passed through successive stages of the trigger hardware. For example, the first stage of the Level 1 algorithm considers pairs of pixel clusters (called doublets) from adjacent tracking stations. Ideally these doublets represent the first two pixel clusters that define the beginning of a track (these are called *interior doublets*), or the last two clusters at the end of a track (*exterior doublets*). Usually the two clusters that make up a doublet come from two different tracks, and it is conceivable that the total number of doublets could exceed the total number of pixel clusters and could overwhelm the next trigger stage. However, our simulations show that the number of doublets found by the Level 1 algorithm is less than the number of pixel clusters, so the algorithm is able to reduce the number of trigger primitives that must be examined by

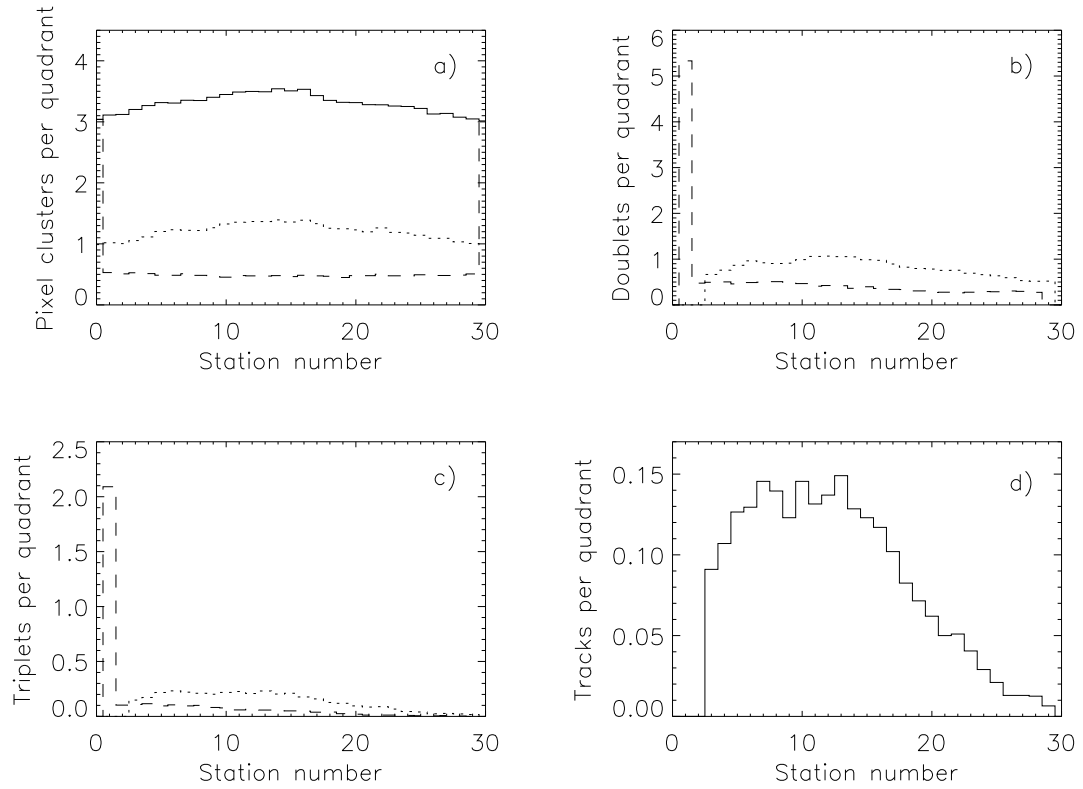


Figure 14.1: a) the average number of pixel clusters per quadrant (solid line) for 31 tracking stations for minimum bias events with an average of two interactions per crossing. The dotted and dashed histograms show the number of pixel clusters in the inner and outer regions, respectively. Histograms in b) and c) show the average number of interior (dotted) and exterior (dashed) doublets and triplets per quadrant directed at one arm of the two-arm BTeV spectrometer, and d) shows the average number of tracks found for the same arm of the spectrometer. Histograms of doublets, triplets, and tracks directed at the other arm of the spectrometer are mirror images of histograms in b), c), and d).

the next stage of the trigger. This is evident in Fig. 14.1b, which shows the average number of interior doublets (dotted histogram) and exterior doublets (dashed histogram) directed at one arm of the two-arm BTeV spectrometer. The number of doublets is less than the number of pixel clusters for all tracking stations, except for Station 1. Here the number of exterior doublets exceeds the number of pixel clusters (note the histogram bin with more than 5 entries in Fig. 14.1b), since Station 1 is an outer station where tracks are exiting the pixel detector. The larger number of exterior doublets in this station means that additional hardware is needed to provide more data paths, which introduces additional parallelism (the same thing occurs for Station 30 for exterior doublets directed towards the other arm of the spectrometer). This additional parallelism also reduces the number of histogram entries for Station 1 in Fig. 14.1c. The figure shows the average number of interior and exterior *triplets* found by the Level 1 algorithm. At this stage in the trigger, the doublets are combined with pixel clusters in the neighboring, third, tracking station to produce triplets. The algorithm finds fewer triplets compared to the number of doublets found by the previous trigger stage. Finally, Fig. 14.1d shows that the number of tracks found by the last stage of the algorithm is less than the number of triplets found by the previous stage. In this case the tracks are found by combining an interior triplet (the beginning of a track) with an exterior triplet (the end of a track), and once again the algorithm is able to reduce the number of trigger primitives.

14.2.1 Level 1 Trigger Studies

All studies of the Level 1 trigger are performed using GEANT. We generate pixel clusters for the vertex-detector geometry described in Chapter 12, and include hadronic reinteractions, photon conversions, decays in flight, and delta rays. As mentioned above, we introduce non-Gaussian tails that include the effects of low-energy delta rays. All studies are performed with an average of two interactions per beam crossing, except when we vary the number of interactions to study the trigger response for more extreme running conditions.

We study the performance of trigger algorithms using minimum bias events and different types of B -events. We have studied a variety of cuts, implemented at various stages in the trigger, and have chosen to use a few cuts in addition to the final vertexing cuts to help reject minimum bias interactions. For example, the Level 1 pattern recognition eliminates low momentum tracks (tracks with $p < 3$ GeV/c) to avoid tracks that may suffer from excessive multiple scattering and could easily be reconstructed as having a large impact parameter with respect to a primary vertex. Moreover, all tracks are required to pass through at least four tracking stations to remove erroneous combinations of pixel clusters that can mimic what appear to be acceptable 3-station tracks (in these cases the interior and exterior triplets are usually constructed from identical pixel clusters). Lastly, a clean-up step removes all tracks that share pixel clusters with any other tracks. This method of removing fake tracks is simple, and perhaps overly severe, but it is effective in eliminating fake tracks at an early stage in Level 1. We have not performed an exhaustive study of possible trigger cuts, so we anticipate additional improvements resulting from future studies of the Level 1 trigger.

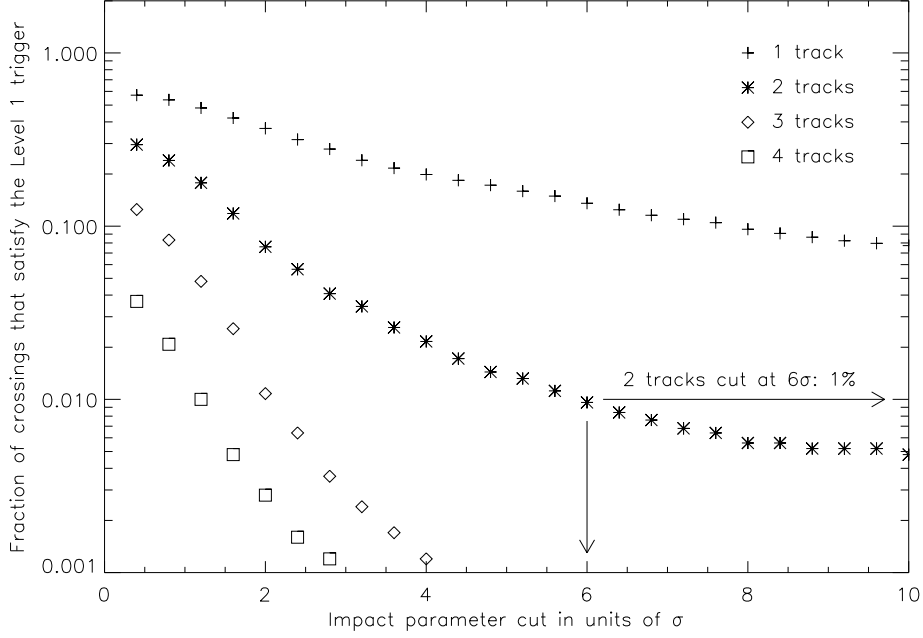


Figure 14.2: Trigger response for minimum bias events with an average of two interactions per beam crossing. The figure shows four sets of points requiring at least 1, 2, 3, or 4 detached tracks. The arrows show a cut that requires at least 2 detached tracks with an impact parameter that exceeds 6σ , and achieves 99% rejection.

The Level 1 vertexing cuts are the final cuts that determine the Level 1 efficiency for B -events and the rejection of minimum bias events. These cuts are selected to provide 99% rejection for minimum bias crossings. The vertexing cuts require that at least n tracks (all directed at one arm of the BTeV spectrometer) miss a primary vertex by at least $m\sigma$. The impact parameter is required to be less than 2 mm to exclude tracks that may be associated with other primary vertices in crossings with more than one interaction. The 2 mm cut also rejects daughter tracks from strange-particle decays. Fig. 14.2 shows the trigger response for minimum bias crossings for a range of vertexing cuts. There are four sets of points corresponding to the requirement of $n = 1, 2, 3$, or 4 detached tracks. The horizontal scale specifies the minimum impact parameter for detached tracks. For purposes of this proposal, the requirement of 2 tracks at 6σ is used. This provides a Level 1 rejection for minimum bias events of a factor of 100. For the actual experiment we would likely run with a mix of prescaled triggers

With the vertexing cuts set to achieve the desired minimum bias rejection, we can study the trigger efficiency for different types of B -events. For $B_s \rightarrow D_s^+ K^-$ we obtain the trigger efficiencies shown in Fig. 14.3. Our cut, requiring at least 2 tracks with a minimum impact parameter of 6σ , gives us a trigger efficiency of 74% for this decay mode. Trigger efficiencies

Table 14.1: Level-1 trigger efficiencies for minimum-bias events and various processes of interest that are required to pass off-line analysis cuts. All trigger efficiencies are determined for beam crossings with an average of two interactions per crossing using the Monte Carlo code shown in the table.

Process	Eff. (%)	Monte Carlo
Minimum bias	1	BTeVGeant
$B_s \rightarrow D_s^+ K^-$	74	BTeVGeant
$B^0 \rightarrow D^{*+} \rho^-$	64	BTeVGeant
$B^0 \rightarrow \rho^0 \pi^0$	56	BTeVGeant
$B^0 \rightarrow J/\psi K_s$	50	BTeVGeant
$B_s \rightarrow J/\psi K^{*0}$	68	MCFast
$B^- \rightarrow D^0 K^-$	70	MCFast
$B^- \rightarrow K_s \pi^-$	27	MCFast
$B^0 \rightarrow 2\text{-body modes}$ ($\pi^+ \pi^-$, $K^+ \pi^-$, $K^+ K^-$)	63	MCFast

for other B -decay modes are shown in Table 14.1.

It is important to realize that the Level 1 trigger, which requires at least two detached tracks, is able to trigger on B events that involve decay modes with fewer than two charged tracks at the B -decay vertex. An example of this is the $B^- \rightarrow K_s \pi^-$ mode listed in Table 14.1. Since this mode has only one track associated with the B^- decay vertex, the majority of triggers come from detached tracks associated with the other B decay in the event.

Most of our studies of the Level 1 trigger efficiency are based on the decay mode $B_s \rightarrow D_s^+ K^-$. These include studies of pixel noise and inefficiencies, described in the next section. Although we have not intentionally optimized cuts for this particular decay mode, it is conceivable that the current set of Level 1 cuts are more favorable for $B_s \rightarrow D_s^+ K^-$ than for other decay modes (such as the other modes listed in Table 14.1). Fig. 14.4 shows the trigger efficiency for this B_s decay mode versus the rejection for minimum bias crossings. The arrows indicate our current Level 1 vertex cut. The figure shows that we have an effective cut that maintains high efficiency for $B_s \rightarrow D_s^+ K^-$, and achieves 99% rejection for minimum bias crossings.

14.2.2 Pixel Noise and Inefficiency Studies

The Level 1 pattern recognition is exceptionally robust with respect to pixel inefficiencies and noise hits in the vertex detector. Fig. 14.5, which shows the trigger response for $B_s \rightarrow D_s^+ K^-$ and minimum bias crossings versus the number of noise hits in each pixel plane, summarizes the results from our noise and inefficiency studies. There are three sets of points that correspond to three different pixel efficiencies. There is a noticeable decrease in

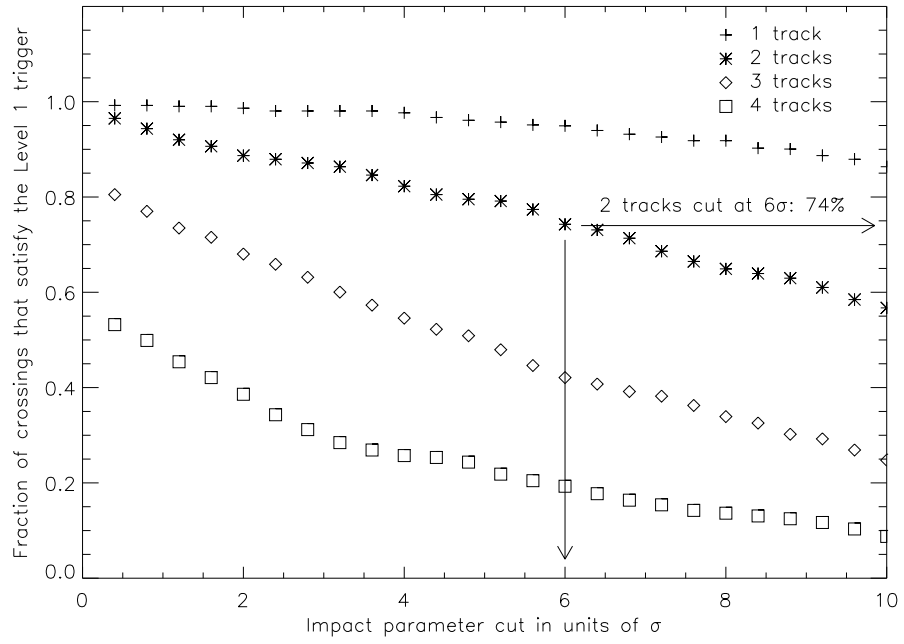


Figure 14.3: Trigger efficiency for $B_s \rightarrow D_s^+ K^-$ events with an average of two interactions per beam crossing. The figure shows four sets of points requiring at least 1, 2, 3, or 4 detached tracks. The arrows show a cut that requires at least 2 detached tracks with an impact parameter that exceeds 6σ , and gives a trigger efficiency of 74%.

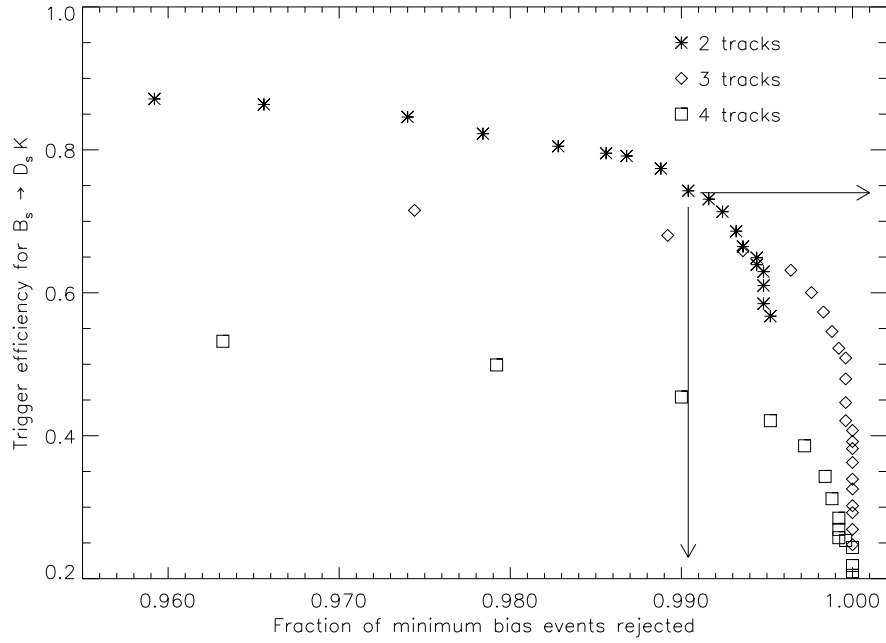


Figure 14.4: Trigger efficiency for $B_s \rightarrow D_s^+ K^-$ vs. rejection for minimum bias events. The figure shows three sets of cuts requiring a minimum impact parameter for 2, 3, or 4 tracks. Increasing the impact parameter cut increases the fraction of minimum bias events that are rejected, and the arrows indicate the cut (2 tracks at 6σ) that we use to achieve 99% rejection.

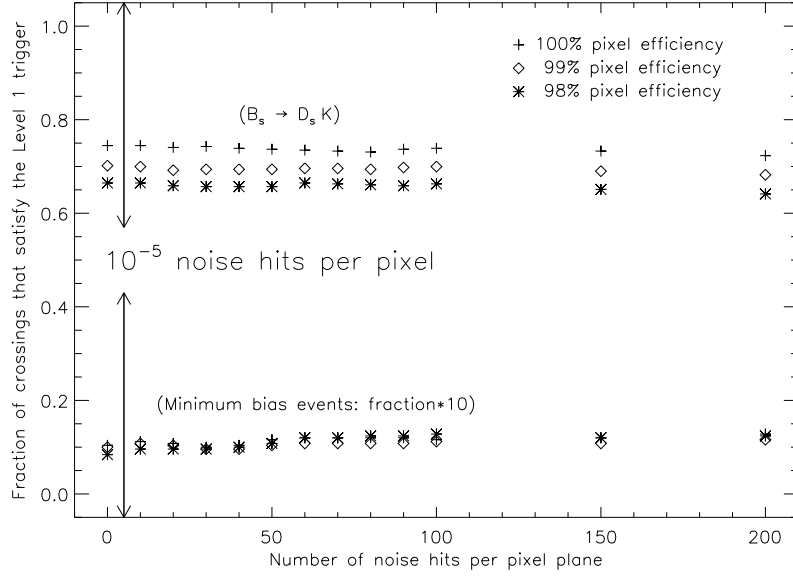


Figure 14.5: Fraction of $B_s \rightarrow D_s^+ K^-$ and minimum bias crossings, with an average of two interactions per crossing, that satisfy the Level 1 trigger for three different pixel efficiencies (three sets of points) vs. the number of noise hits that have been added to each pixel plane in the vertex detector. Results for minimum bias crossings have been multiplied by 10.

the trigger efficiency for $B_s \rightarrow D_s^+ K^-$ with decreasing pixel efficiency (we observe a slightly different behavior for minimum bias crossings, described below). We expect to achieve a pixel efficiency that exceeds 99%, so the trigger efficiency for $B_s \rightarrow D_s^+ K^-$ should exceed 70%—a trigger efficiency that is less than the first set of points (plus signs) and greater than the second set of points (diamonds).

We add noise hits to the trigger simulation to study how sensitive the pattern recognition is to spurious pixel clusters. We have studied two types of noise distributions without observing any significant difference. In the first study we generate a uniform distribution of noise over an entire pixel plane. In the second study (results are presented in Fig. 14.5) we generate pixel hits that mimic the distribution of GEANT hits distributed over a pixel plane. This may be a more realistic representation of correlated noise in the pixel detector. We expect the noise level in the detector to be less than 10^{-5} noise hits per pixel, which corresponds to about 5 additional pixel hits per plane. In our studies we add up to 200 pixel hits per plane, and observe a slight (few percent) decrease in the trigger efficiency for $B_s \rightarrow D_s^+ K^-$. This decrease probably results from the clean-up step in the Level 1 trigger that removes tracks with shared hits.

For minimum bias crossings we get results that are similar to the results obtained for $B_s \rightarrow D_s^+ K^-$. At low noise levels we observe a decrease in the “trigger efficiency” with decreasing pixel efficiency. However, in contrast to the $B_s \rightarrow D_s^+ K^-$ results, we observe a

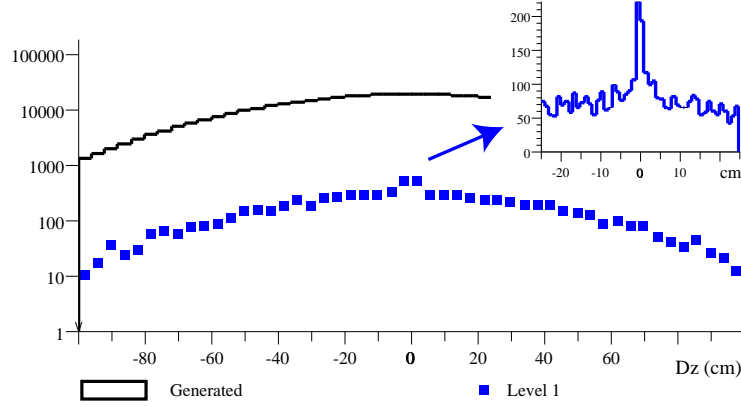


Figure 14.6: Distance between primary vertices

very slight increase in the fraction of minimum bias crossings that satisfy the Level 1 trigger as the number of noise hits increases. We believe that the pattern recognition is substituting noise hits for the “correct” hits that belong to a track, which tends to increase impact parameters and cause false triggers. This behavior appears to be even more noticeable (the effect is exaggerated in Fig. 14.5 by multiplying the minimum bias results by 10) for lower pixel efficiencies. Here the noise hits are used in place of pixel clusters that are lost due to pixel inefficiencies. Needless to say, Level 1 is exceptionally stable with respect to noise, and we do not expect any noticeable deterioration in the trigger performance for the amount of noise expected to occur in the pixel detector.

14.2.3 Multiple-Interaction Studies

At the design luminosity of $2 \times 10^{32} \text{ cm}^{-2}\text{s}^{-1}$ there will be an average of two interactions per crossing. As long as primary vertices are relatively far apart, the Level 1 vertex trigger can identify individual vertices and assign each track to the correct primary vertex. A key feature of Level 1 (and subsequent trigger levels) is that detached tracks are required to have an impact parameter that is less than 2 mm to exclude tracks associated with other primary vertices. As soon as the distance between two primary vertices becomes fairly small, the trigger begins to “see” a primary vertex with detached tracks, which are associated with the other primary. Fig. 14.6 compares the distance between primary vertices for all generated events and those accepted by the Level 1 trigger. It can be seen that multiple interactions cause false triggers only when the distance between vertices is less than a few centimeters.

Another way of observing the level of confusion that is introduced by having multiple interactions in a single beam crossing is to look at the fraction of minimum bias crossings that satisfy the Level 1 trigger as a function of the number of interactions per crossing. Since we desire to trigger on a fixed fraction of the interactions, a linear response would be ideal. As can be seen in Fig. 14.7 the trigger response does deviate from a linear response for 3

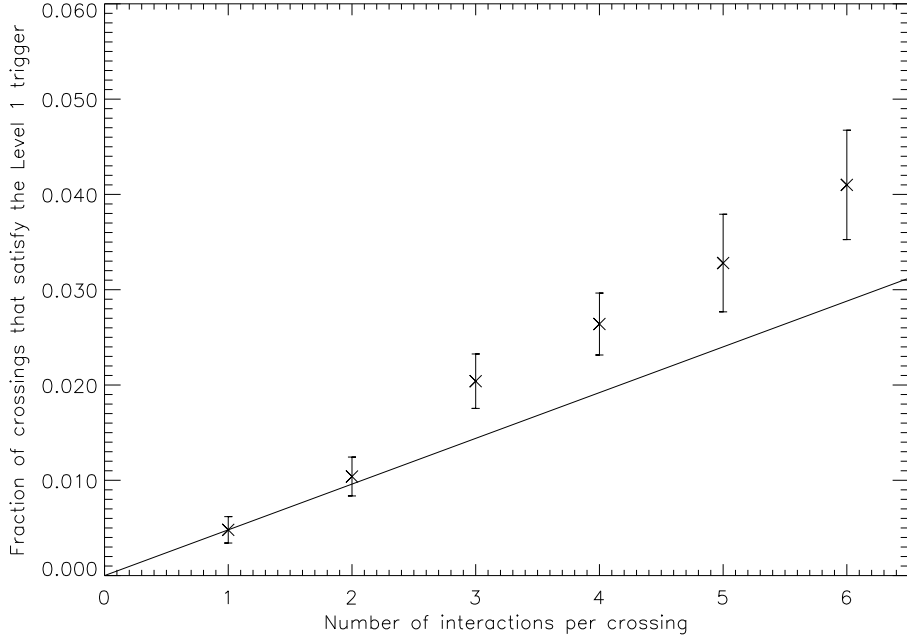


Figure 14.7: Fraction of minimum bias crossings that satisfy the Level 1 trigger vs. the number of interactions per crossing.

interactions/crossing and above. However the deviation is quite tolerable considering that we are planning to run at a mean of 2 interactions/crossing.

14.3 Status of the Level 2 Trigger

The Level 2 trigger algorithm is in its initial stage of development. Work on it could begin only after the Level 1 algorithm, which was rewritten to handle the pixel doublet scheme, was completed. Here, we discuss what we have achieved in the short time we have been studying this and project where we expect to wind up.

14.3.1 Brief description of the Level 2 Algorithm

The Level 2 trigger starts from the information obtained at Level 1, namely the pixel tracks and primary vertices. Only the tracks associated with the Level 1 primary vertex that had the required number of detached tracks—and therefore fired the Level 1 trigger—are considered. The first step is to add pixel hits to these tracks. By design, the Level 1 algorithm makes no attempt at finding all the hits associated with a given track in order to speed up the pattern recognition. At Level 2, the majority of hits that are added are between the inner and outer Level 1 track segments. The average number of additional hits is approximately

10 per track. By adding these missing hits and using a Kalman filter to fit these tracks, the momentum resolution improves by roughly a factor of two (from $\langle \sigma_P/P \rangle \approx 6.5\%$ to $\langle \sigma_P/P \rangle \approx 3.5\%$). The pointing accuracy to the vertex region is also improved.

The second phase of Level 2 consists of a complete vertex pattern recognition using the Kalman fitted tracks. First, primary vertices are reconstructed by assembling pairs of tracks that make an acceptable 3-dimensional vertex. More than one such primary vertex is allowed. Second, secondary vertices are sought using tracks that are not part of any of the primary vertices. These secondary vertices are presumably heavy quark decays. While a primary vertex must occur in the luminous region (within a radius of $150\ \mu\text{m}$), the secondary vertex must (i) have relatively few tracks, (ii) occur within $5\ \text{cm}$ of a primary, and (iii) must point away from the primary. Finally, the remaining “bachelor” tracks are assigned to one of the primary vertices, one by one, based on the distance of closest approach (DCA) of the track to the vertex. If no secondary vertex and no bachelor tracks are found, the crossing is rejected. Bachelor tracks which pass within a radius of $2\ \text{mm}$ from the beam and with a DCA of 5σ , as well as tracks from secondary vertices, are considered “detached.”

The third phase consists of confirming and improving the detached tracks by matching hits from the inner two forward tracking stations to these tracks and refitting them. This improves the momentum resolution by a factor of ≈ 2 , reaching $\langle \sigma_P/P \rangle \approx 2\%$. In addition, new Level 2 tracks are sought in the pixel detector. Such tracks must come from the relatively small part of the luminous region surrounding the most populated primary vertex. The first hit of these types of tracks must be found within 5 pixel stations from the primary. The goal is to find a few more detached tracks, possibly improving the position accuracy of secondary vertices. The cuts used in this track reconstruction phase are tuned for low momentum tracks (down to $\approx 1\ \text{GeV}/c$), where the Level 1 track reconstruction code (by design) is relatively inefficient. These tracks are added to the appropriate existing vertices, based on their DCA to these vertices, or kept as detached bachelor tracks ($\text{DCA} > 5\sigma$).

Various criteria based on vertex topology and the transverse momenta of the detached tracks have been considered. We find that the scalar sum of the transverse momentum of all detached tracks¹ $\Sigma|p_t|$, is relatively robust against variation in the total charged track multiplicity in B decays. This is shown in Fig. 14.8.

14.3.2 Timing

A complete prototype of the preliminary Level 2 code has been written and its timing has been benchmarked on a Pentium III 400 MHz processor. The Level 2 code takes roughly $115\ \text{ms}$ per crossing, at the nominal luminosity of $2 \times 10^{32}\ \text{cm}^{-2}\text{s}^{-1}$. The goal of $\approx 50\ \text{ms}$ per crossing on a $2.5\ \text{GHz}$ processor has therefore already been reached. Although some effort has been made to organize the data structures and tune the algorithm for speed, particularly the vertex finding, this is by no means fully optimized code. Thus, we still have the possibility to increase the rejection and/or the efficiency of signal events for this Level 2

¹Once again, tracks from secondary vertices are considered detached.

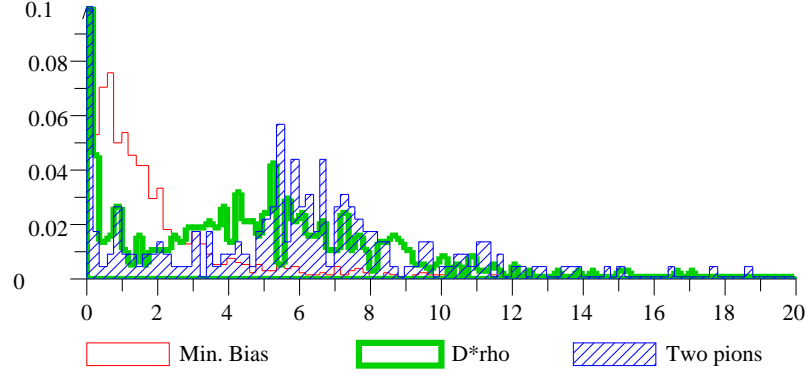


Figure 14.8: The histogram of the detached p_t sum, $\Sigma|p_t|$, for two final states of interest and minimum bias events. The first bin corresponds to cases where no Level 2 detached track has been found. The probability for such occurrence (per crossing) is 32% for minimum bias and $\approx 15\%$ for B events.

trigger by adding more code; for instance, improved forward tracker reconstruction and/or better vertex pattern recognition.

14.3.3 Signal efficiency and background rejection

The efficiency of this Level 2 trigger has been measured on the $B^0 \rightarrow D^{*+}\rho^-$ and $B^0 \rightarrow \pi^+\pi^-$ final states as well as on minimum bias events. For signal events, only events passing detailed analysis cuts discussed in the following chapter are considered. That is, as for Level 1, we are measuring our triggering efficiency on the B sample of interest. Based on the integral of the distributions shown in Fig. 14.8, the efficiency for signal and background is shown in Fig. 14.9. Requiring $\Sigma|p_t| > 2.2$ GeV/c gives a rejection factor of 5 with efficiencies of 70% for $B^0 \rightarrow D^{*+}\rho^-$ and 75% for $B^0 \rightarrow \pi^+\pi^-$. We expect to be able to improve the performance in the next iteration based on our analysis presented below.

The major sources of inefficiency for B events have been identified:

- Approximately 15% of the Level 1 triggers on B events are false triggers. That is, either the primary vertex with the Level 1 detached tracks is not the primary vertex from which the $b\bar{b}$ pair originated, or the detached tracks are not coming from any of the descendants of the B particle. While the latter class of events is partially recovered by the Level 2 algorithm, the former is definitely lost because the Level 2 trigger only considers the “triggering” primary vertex. Note that we would have to spend more computing time to recover this $\approx 10\%$ inefficiency. We plan to study the benefit of attempting to analyze at Level 2 the complete set of tracks and vertices obtained at Level 1.

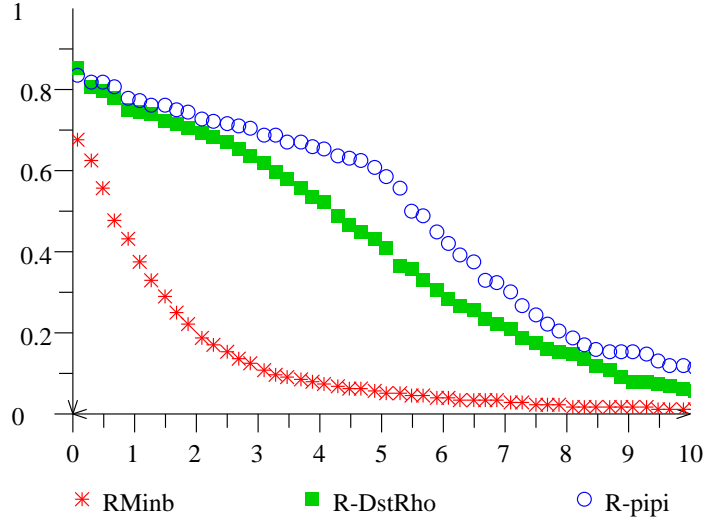


Figure 14.9: The efficiency of the Level 2 trigger vs. detached P_t sum, Pt_D , for two final states of interest and minimum bias events. The first bin corresponds to cases where no Level 2 detached tracks have been found. The probability for such occurrences (per crossing) is 32 % for minimum bias and $\approx 15\%$ for B events.

- The Level 1 tracking efficiency is about 90%. This is only partly recovered at Level 2 by searching for additional tracks. There is room for improvement here.

As intended, the algorithm triggers mostly on tracks coming from the $b\bar{b}$ system, as shown in Table 14.2. The sources of background events found in the minimum bias sample passing the Level 1 and Level 2 triggers have also been studied:

- About 10% of the detached tracks are “noise” tracks, due to decays in flight, or, more likely, reinteractions (electromagnetic and hadronic) in the detector. Most of this background is evidently removed by the stringent fiducial cuts placed on the track at the vertices. The remaining sample is not, in fact, a dominant source of false Level 2 triggers.
- The probability of finding one or more pions from a K_s^0 decay in the detached, minimum bias, track sample is about 40%. Approximately 1/4 of these minimum bias events have two such pion tracks. Likewise, the probability of finding at least one charged track from a hyperon decay (Λ , Σ) is about 20%. This occurs despite the beam proximity fiducial cut and the maximum transverse impact parameter cut of 2 mm. We are studying ways to specifically address these problems.
- In about 63% of the minimum bias events surviving the Level 2 cuts, there is at least one track originating from a different primary vertex and, in about one half of the

Table 14.2: The average multiplicity of Level 2 detached tracks $\langle N_{sec} \rangle$ from various sources in events passing the analysis cuts and the Level 1 + Level 2 trigger. A noise track is a track not coming from either a primary vertex or from a heavy quark or strange decay (e.g. secondary interactions). Also listed are the probability $P_{\geq 1}$ ($P_{\geq 2}$) to find at least one (two) of these tracks in the sample of Level 2 detached tracks.

Level 2 Track origin	$\langle N_{sec} \rangle$	$P_{\geq 1}$ (%)	$P_{\geq 2}$ (%)
Noise	0.06	6	0
Primary	1.2	47	25
From the $D^* \rho$	1.55	95	88
From the opposite B decay	0.95	52	27

sample, the primary vertex causing the trigger is contaminated by tracks originating from a different primary vertex. Although the primary vertex resolution along the beam axis is around 100–200 μm , the vertex pattern recognition algorithm can easily be fooled by $p\bar{p}$ collisions occurring with a few cm of each other. This, along with strange decays, is the dominant source of the remaining background. We plan to study this problem as well.

We expect to recover the missing tracking efficiency and to mount a successful attack on the K_s and hyperon decays. Our goal is to achieve a combined Level 1 and Level 2 trigger rejection of about 1000 to 1 and an overall triggering efficiency for interesting B events of about 50% for almost all classes of B decays that are of interest to us. At the moment, we are only slightly low in efficiency and about a factor of two low in rejection. However, we have many ideas that we have yet to try, and we are using less computing power than budgeted for the baseline Level 2/3 farm. Finally, we have both the bandwidth and computing power to handle the number of events that are passed by the current algorithm at Level 3 (see below). Because of the uncertainties on this, and to be totally safe we have included a 100% contingency in the cost of the Level 2/3 farm. In the yield calculations below, we assume that our efficiency goals will be achieved. Based on current Level 1 efficiencies, we use a 90% Level 2 efficiency estimate in our simulations.

A final remark on charm events. The Level 1 trigger enriches the charm sample by about a factor of two, while the preliminary Level 2 trigger, due to its transverse momentum bias, does not enhance the charm yield. Should BTeV hunt for specific charm decay modes, however, such as two-body final states of the D^0 , the Level 2 mass resolution can be used at little cost in bandwidth.

14.4 Level 3 Trigger Strategy

Our objective is to write out about 4000 events per second with an average size of 50 Kbytes. The rejection we require at Level 3 is small – only a factor of 2 to 4. The data reduction,

whose purpose is to reduce tape costs, must also be approximately a factor of 4.

Concerning event rejection, the tasks of the Level 3 trigger are

- to reject the surviving minimum bias events; and
- then to decide which of the remaining events, most of which are B or charm events, to keep.

Because the B and charm rates at the Tevatron are so high, the second task is difficult to achieve because the events that reach this stage are, for the most part, genuine B or charm events. However, many of them are unreconstructable because of their decay mode or because some of their decay products are outside the detector's acceptance. These events will not contribute to our physics reach and can be safely discarded. On the other hand, we do not want to design a trigger that focuses on an overly restrictive list of “fashionable” decay modes since new ideas and new data will cause any such list to change frequently.

Our strategy is to use two complementary approaches:

- We conduct a systematic and exhaustive search through a list of inclusive, and semi-inclusive, decay modes. We include all the obvious candidates and various semi-inclusive decays to leave the door open for surprises. We propose to use virtually all the relevant information from most of the subdetectors to test the relevant set of hypotheses, but without doing a complete reconstruction of the event. For instance, a Level 2 detached track from a secondary vertex can be tentatively identified as a kaon or pion without having to reconstruct or identify all the rings in the Cherenkov detector.
- We use a vertex-topology filter to select B -like (also charm-like) vertex topologies without regard to specific decay modes. These selections, because they do not use all the available information, are not as strict and we have to design cuts which balance signal efficiency against rejection.

We plan to take the “OR” of the events that survive these two algorithms. The virtue of this approach is that the first method can be made nearly 100% efficient on the key modes of interest at the time of data-taking. It is moderately efficient on a wide variety of other modes but can inadvertently exclude something that later becomes interesting. The second method is more inclusive but may have lower efficiency on some key modes of interest. There is, of course, a very large correlation between these two triggers. A prescaled sample of generic Level 2 events satisfying very loose cuts will also be kept to keep the experiment open to new states of interest and to calibrate the cuts used in the two Level 3 algorithms.

The Level 3 trigger must also reduce the size of the events. There are many methods for data reduction, including using standard data compression techniques before the events are actually logged to tape. Since this will probably not achieve the desired reduction, we have to consider additional tactics. Since the direction of the $b\bar{b}$ system is known, there is no point keeping the information from the opposite end of the spectrometer (last straw station,

RICH, calorimeter, and muon detector). Since the charged particle reconstruction in that hemisphere is only needed to improve the accuracy of the primary vertex, and only the first few stations of the forward tracker are needed to accomplish this, many of the forward tracker hits from that arm can also be dropped. This alone achieves a reduction of nearly a factor of two. If these two methods are not quite enough, there are many other opportunities for data reduction which don't compromise our physics reach. For example, even on the "signal side", we can discard hits and write out only fitted track vectors for charged tracks clearly associated with accompanying minimum bias interactions. (The tracking information may be needed for the particle identification or calorimetry in the offline analysis.) In the same spirit, while considering an exclusive hadronic decay to all charged tracks, the only role of the calorimeter is for electron identification for away side tagging. Only pulse heights from blocks surrounding the detached charged tracks from the other B in the event are needed to test the electron hypothesis. Therefore, the calorimetry data block can be reduced considerably. (This strategy should be used for events which come in under the first trigger algorithm only.)

In order to illustrate the first of the two Level 3 trigger algorithms, we assembled a simple filter for two track B decays. The analysis proceeds by looping on all Level 2 tracks, of opposite signs, requiring that: (i) both tracks are significantly detached from the primary vertex, (ii) the two tracks form a 3-dimensional vertex, and (iii) the vertex is detached from the primary by 5σ . After a loose mass cut of $\pm 100 \text{ MeV}/c^2$, the rejection factor for minimum bias events is $\approx 50,000 : 1$ (all trigger levels included). Note that this filter accepts all hadronic, two body mesonic decay modes, as well as e^+e^- and $\mu^+\mu^-$, of the B_0 and B_s . Evidently, the momentum measurement on these two tracks can be improved using the entire forward spectrometer (using little CPU time compared to the full Level 2 task), and additional vertex cuts similar to those used in the analysis described in Section 16.1 will also be used. This will easily reduce the above rate, which is already only a few percent of the total bandwidth allowed to tape, to well below 1% of the total allowed bandwidth. Similar filters, possibly using data from other detectors, can be constructed for all other decay modes of interest.

Chapter 15

Flavor Tagging

15.1 Introduction

For charged B mesons, the flavor of the heavy quark (b or \bar{b}) is determined by the charge of the B meson. For neutral B mesons (B_d and B_s) the quark flavor can usually be determined from the flavor of its decay products, for example by the charge of the kaon in the decay chain $B_s \rightarrow \psi \bar{K}^*$, $\bar{K}^* \rightarrow K^- \pi^+$. If the flavor of the b quark at its production point is determined independently, these modes can be used to measure $B_s \leftrightarrow \bar{B}_s$ and $B_d \leftrightarrow \bar{B}_d$ oscillations, which are sensitive to V_{ts} and V_{td} , respectively. Decays to CP-eigenstates do not identify the b quark flavor. In fact, amplitudes for these decays interfere with the mixing amplitude producing CP-violating effects. Measurements of CP-asymmetry, resulting e.g. in determination of $\sin 2\beta$ via $B_d \rightarrow \psi K_S^0$, again require determination of the b quark flavor at the production point — so called “flavor tagging.” Every tagging method sometimes produces false identifications and the effectiveness of flavor tagging is characterized by an effective tagging efficiency ϵD^2 , where $\epsilon = (N_R + N_W)/N$, D is a “dilution” factor $D = (N_R - N_W)/(N_R + N_W)$, N is the number of reconstructed signal events, N_R the number of right flavor tags in this sample, and N_W is the number of wrong flavor tags. Since the measurements mentioned above are among the most important goals of the BTeV program, a high effective tagging efficiency is a crucial design criterion for the experiment.

This section presents the results of a study of the tagging power of several tagging methods which can be used in the BTeV detector. The events studied contain decays in the channel $B_s \rightarrow D_s K$ which passed the final analysis cuts in the study described in section 16.4.1. For this analysis, each signal event was accompanied by a Poisson distributed number of background events, with a mean of two background interactions per beam crossing. For this study, Pythia was used to generate the physics events and BTeVGeant was used for the detector simulation. Mixing of the opposite side B meson was not switched on in Pythia.

15.2 Away Side Tagging

In $p\bar{p}$ collisions at 2 TeV in the center-of-mass, by far the dominant source of b quark production is via production of $b\bar{b}$ pairs. The away side tagging methods rely on determination of the flavor of the other b quark in the event. The flavor of the away side b can be determined from the charge of the lepton emitted in its semileptonic decay, the charge of vertices found on the away side or from the charge of the kaon produced in its $b \rightarrow c \rightarrow s$ cascade.

The first few steps of the away side algorithm are common to all away side tagging methods. First, all primary interaction vertices in the event were found. Next, a list was built of tracks which were candidates to come from a secondary vertex. To be a candidate, a track must have a momentum greater than 3.0 GeV/c and must not pass within 3σ of any primary vertex. This list served as input for the various tagging methods.

15.2.1 Lepton Tagging

While lepton tagging is a very clean tagging method, the branching ratio of $b \rightarrow X\ell^-\nu$, about 10% per light lepton generation, is relatively small compared to the branching ratio into other tagging modes. The lepton tagging algorithm also must deal with possible wrong-sign tags which result from the cascade $b \rightarrow c \rightarrow \ell^+$. Because leptons from $b \rightarrow \ell^-$ and $b \rightarrow c \rightarrow \ell^+$ have quite different transverse momentum (p_T) distributions, good separation can be achieved.

Candidates for muon tags were selected from the secondary track list if they had a momentum greater than 4.0 GeV/c and were within the geometric acceptance of the muon detector. If there was more than one muon tag candidate in an event, the highest p_T muon was chosen to be the tag. A tagging muon with $p_T > 1.0$ GeV/c was considered to be from the process $b \rightarrow \ell^-$, while one with $p_T < 0.5$ GeV/c was considered to be from the process $b \rightarrow c \rightarrow \ell^+$, thereby flipping the sign of the tag. The muon tagging efficiency was found to be $\epsilon = 4.5\%$ with a dilution $D = 0.66$, which gives an effective tagging efficiency of $\epsilon D^2 = 2.0\%$.

Candidates for electron tags were selected using a parametrized electron efficiency and hadron misidentification probability based on the results described in Section 12.4. The tag was required to have $p_T > 1.0$ GeV/c and assumed to come from the process $b \rightarrow \ell^-$. There were not enough events to study electrons from $b \rightarrow c \rightarrow \ell^+$. If there was more than one electron tag candidate the highest p_T electron was chosen. The electron tagging efficiency was found to be $\epsilon = 2.3\%$ with a dilution $D = 0.68$, which gives an effective tagging efficiency of $\epsilon D^2 = 1.0\%$.

15.2.2 Kaon Tagging

Because of the large branching ratio for $b \rightarrow c \rightarrow K^-X$, kaon tagging is the most potent tagging method at $e^+e^- B$ factories. At BTeV, in which the multiplicity of the underlying event is much greater, excellence in both particle identification and vertex resolution is

required to exploit kaon tagging. Both are strong points of our forward detector geometry.

Candidates for kaon tags were selected from the secondary track list if they were identified as kaons in the RICH detector. If there was more than one kaon tag candidate in an event, the kaon with the largest normalized impact parameter with respect to the primary vertex was selected. In events with multiple primary vertices, the signal B defines which primary is used to calculate the normalized impact parameter. The kaon tagging efficiency was found to be $\epsilon = 18\%$ with a dilution $D = 0.52$, resulting in an effective tagging efficiency of $\epsilon D^2 = 4.9\%$.

15.2.3 Vertex Charge Tagging

In this method a search was made for a detached vertex which is consistent with being from the charged decay products of the other b . The charge of that vertex determines the charge of the b . When the opposite side b hadronizes into a \bar{B}^0 , the tagging vertex has a neutral charge and there is no useful vertex tagging information in the event. However this method has the advantage that it is not affected by mixing of the away side b .

The vertex charge tagging algorithm exploits a correlation between the signal B meson and the tagging b hadron: they are produced relatively close in pseudorapidity (η) and, therefore, their decay products appear in the same arm of the detector.

Tracks from the secondary list were accepted provided they had $p_T > 100$ MeV/c and provided they had $\Delta\eta < 4$ with respect to the direction of the signal B^0 candidate. The tracks from the secondary list were sorted into candidate vertices and only vertices with a detachment of at least 1.0σ from the primary vertex were accepted. If more than one vertex was found in an event, the one with the highest transverse momentum was selected; if no secondary vertices passed the selection cuts and if there was at least one track with $p_T > 1.0$ GeV/c, then the highest p_T track was selected. If the charge of the selected track or vertex is non-zero, then it determines the flavor of the away side b .

This tagging method is similar to jet charge tagging used by other experiments but we have not yet investigated the possibility of weighting the tracks by their momenta.

The results of this study indicate that we can achieve a tagging efficiency $\epsilon = 32\%$ and a dilution $D = 0.36$, which results in an effective efficiency $\epsilon D^2 = 4.1\%$.

15.2.4 Combining Away Side Tagging Methods

In many events, several of the same side tagging methods may give results; moreover it can happen that two methods will give contradictory answers. We have not yet optimized the method of combining all tagging information but have used the following simple algorithm. The methods were polled in decreasing order of dilution and the first method to give an answer was accepted. That is, if lepton tagging gave a result, the result was accepted; if not, and if kaon tagging gave a result, the kaon tag was accepted; if not, and if the vertex charge tagging gave a result, the vertex charge tag was accepted. The results of the away side tagging studies are summarized in Table 15.1.

15.3 Same Side Tagging

The same side tagging method uses the correlations which arise between the signal B meson and the charge of nearby tracks produced either in the fragmentation chain or in B^{**} decays. For B_s mesons, the correlation is with a charged kaon, while for B_d decays the correlation is with a charged pion.

Here we present a study of same side tagging for B_s mesons. For this study tracks were selected provided they had a momentum greater than 3.0 GeV/c, were identified as kaons in the RICH and had an impact parameter with respect to the primary vertex less than 2σ . It was further required that the system comprising the B_s candidate plus the candidate tagging track have an invariant mass less than 7.0 GeV/c². If more than one track passed these cuts, then the track closest in ϕ to the B_s direction was selected. With this algorithm the same side tagging efficiency was found to be $\epsilon = 40\%$ with a dilution of $D = 0.26$, which results in an effective efficiency $\epsilon D^2 = 2.6\%$.

For same side tagging of B_d events we expect to use B^{**} decays. We have not used the flag in Pythia to turn on B^{**} production so we have used a sample of $B \rightarrow \psi K_s$ decays where the B and the next pion in the StdHep list have an invariant mass in the range 5.6 - 5.8 GeV/c². We assume that 30% of B_d events will come from B^{**} decays and so weight these events accordingly and assume that the other 70% of the events will have equal numbers of right sign and wrong sign tags. Very preliminary results indicate we can achieve a tagging efficiency $\epsilon D^2 = 2.2\%$.

15.4 Summary of Tagging

The results from this chapter are summarized in Table 15.1. These results are preliminary and one should be aware that all algorithms have yet to exploit the full power available to them. In particular, the vertexing information has yet to be fully exploited. For example, the $b \rightarrow \ell^-$ and $b \rightarrow c \rightarrow \ell^+$ samples differ not only in their p_T spectra; they have distinctly different topological properties. Similarly, kaon tagging can be improved if there is evidence that the kaon comes from a tertiary vertex, indicative of the $b \rightarrow c \rightarrow K^-$ cascade. Finally, the vertex charge algorithm should expect to find two vertices on the away side, the b decay vertex and the c decay vertex; the charge of both vertices provides tagging power. Other tagging methods have yet to be studied such as using a D^* from the decay of the opposite side B . Finally, we have not yet explored the optimal use of the correlations among all of the methods.

Many of the physics reach studies presented in chapter 16 require values of ϵ and D as inputs. As argued in the preceding paragraph, the results quoted in Table 15.1 probably underestimate the tagging power of BTeV. Therefore most physics results in chapter 16 are presented using nominal values of $\epsilon = 0.7$ and $D = 0.37$, giving $\epsilon D^2 = 0.1$. The studies presented in the present chapter should be regarded as evidence that these nominal values lie well within the ultimate reach of the experiment.

Tag Type	ϵ	D	ϵD^2
Muon	4.5%	0.66	2.0%
Electron	2.3%	0.68	1.0%
Kaon	18%	0.52	4.9%
Vertex Charge	32%	0.36	4.1%
Same Side Kaon	40%	0.26	2.6%
Same Side Pion	88%	0.16	2.2%
Total for B_s			14.6 %
Total for B_d			14.2 %
Total for B_s with overlaps	65%	0.37	8.9%

Table 15.1: Results, to date, of first generation studies of tagging power. In the text it is discussed that these studies are incomplete and that they likely underestimate the tagging power which can be realized at BTeV.

Chapter 16

Specific Physics Final States

The simulation tools described in the preceding chapters have been used to explore the physics reach of the BTeV detector. The channels selected for this study include standard B physics benchmarks, channels which illustrate the capabilities of particular detector components and channels which highlight the unique capabilities of BTeV. The standard benchmarks include, $B^0 \rightarrow \pi^+\pi^-$, $B^0 \rightarrow J/\psi K_S^0$ and studies of B_s mixing using $B_s \rightarrow D_s\pi$ and $B_s \rightarrow J/\psi \bar{K}^{*0}$. The channel $B^0 \rightarrow D^{*-}\rho^+$ has a large branching ratio and it is used to explore the capabilities of the electromagnetic calorimeter; studies with this mode show that BTeV has the segmentation and resolution required to extract a strong signal, even in the presence of the background events which accompany the signal events. While this result had previously been demonstrated with MCFast based studies, it is reaffirmed here using a BTeVGeant based study, in which noise levels are significantly higher and all resolutions have realistic non-Gaussian tails. The analysis techniques developed during the $B^0 \rightarrow D^{*-}\rho^+$ study were applied both to the study of $B \rightarrow \rho\pi$, an important mode for constraining the CKM angle α , and to the study of $B \rightarrow J\psi\eta^{(\prime)}$, the mode which directly measures the CP angle χ . One of the particular strengths of BTeV is the ability to constrain the CKM angle γ using a variety of techniques; results are presented here for the decay modes, $B_s \rightarrow D_s K^-$, $B^\pm \rightarrow D^0 K^\pm$, and $B \rightarrow K\pi$. The chapter concludes with estimates of the sensitivity for rate processes such as $B \rightarrow K^{(*)}\mu^+\mu^-$ and $B \rightarrow X_s\mu^+\mu^-$. Taken together, these studies illustrate the excellent physics reach of BTeV.

16.1 A study of $B^0 \rightarrow \pi^+ \pi^-$ (and $B_s \rightarrow K^+ K^-$)

The decay of $B^0 \rightarrow \pi^+ \pi^-$ is the traditional choice for measuring $\sin(2\alpha)$, but the evidence of large penguin amplitudes in the observation of $B^0 \rightarrow K^+ \pi^-$ by the CLEO collaboration [1] implies that a simple extraction of $\sin(2\alpha)$ from this mode is no longer likely. However, since this mode has been used to benchmark so many experiments, it is still worthwhile to understand. In addition, it may be useful for the extraction of γ when combined with a measurement of $B_s \rightarrow K^+ K^-$ as explained in Part I.

The data for this study are generated using Pythia while QQ is used to decay the heavy particles. The detector simulation is performed using the BTeVGeant simulation package. We also compare our result with the result obtained using MCFast. Each signal event which is simulated by BTeVGeant (or MCFast) contains one signal interaction ($b\bar{b}$) and n background interactions (minimum bias), where n has a Poisson distribution of mean 2. This corresponds to our design luminosity of $2 \times 10^{32} \text{ cm}^{-2} \text{ s}^{-1}$.

To find this decay we select two oppositely charged tracks with a displaced vertex and an invariant mass close to the B_d mass. Most of the background rejection against random combinations comes from the displaced B vertex and the momentum balance of the $\pi^+ \pi^-$ combination with respect to the direction of the B . While particle identification is vital to reject backgrounds from decays like $B^0 \rightarrow K^+ \pi^-$, $B_s \rightarrow \pi^+ K^-$ and $B_s \rightarrow K^+ K^-$, it has a small effect on random combinations since most particles are pions.

To start this analysis, we first fit the primary vertices using all tracks which have at least 4 silicon pixel hits. A good primary vertex is required to have $\chi^2/N_p < 4$, where N_p is the number of tracks in the primary.

For the two tracks to be considered as B -daughter candidates, they must satisfy the following criteria:

- Each track must have $P_T > 0.5 \text{ GeV}/c$ and at least one track must have $P_T > 1.5 \text{ GeV}/c$.
- Tracks must have at least eight silicon pixel hits to ensure precise tracking.
- Each track must project into the RICH detector acceptance, because we require particle identification.
- The distance of closest approach (DCA) of the track with respect to the primary vertex must be less than 1 cm, which reduces backgrounds from long lived particles, e.g. K_s , hyperons. We also require that the normalized DCA (DCA divided by its error) with respect to the primary of each track be > 3 which removes tracks from the primary.
- Both tracks are in the same arm of detector.

We attempt to fit a secondary vertex with pairs of tracks that satisfy the above criteria. Vertices with $\chi^2 < 4$ are kept for further analysis. For each secondary vertex found, the following selection criteria are applied:

- The absolute distance between the primary and secondary vertices (L) must be greater than 0.5 mm and $L/\sigma_L > 4$.
- Consider all other tracks that do not come from this primary vertex. Form a χ^2 with each of these tracks and our selected two tracks for a secondary vertex. Combinations with $\chi^2 < 10$ are rejected, since this might be a many-body B decay.
- The B^0 direction is calculated from the primary and secondary B vertex positions. The transverse momentum imbalance with respect to that direction must be less than 0.5 GeV/c.
- The invariant mass of the two tracks (assumed to be π^\pm) must be within $57.5 \text{ MeV}/c^2$ (2σ) of M_{B^0} .

Figure 16.1 shows a comparison of signal and background for several of the variables used above. The background distributions are generated considering all oppositely charged two-track combinations except for the signal $\pi^+\pi^-$.

Using the selection criteria defined above gives an acceptance and reconstruction efficiency of 8% for $B^0 \rightarrow \pi^+\pi^-$, not including trigger efficiency or particle identification.

It has been shown by the BCD group [2] that the dominant background to $B^0 \rightarrow \pi^+\pi^-$ comes from random combinations of tracks in events coming from B 's. Tracks from real B 's are already displaced from the primary vertex and have a higher probability of faking a secondary vertex compared to $c\bar{c}$ and minimum bias events.

In addition to background from generic $b\bar{b}$ events, there are several exclusive decay modes of B mesons that can mimic a $B^0 \rightarrow \pi^+\pi^-$ decay. The decay $B_s \rightarrow K^+K^-$, which is due to a hadronic penguin decay mechanism, is the most important, along with other contributions from $B^0 \rightarrow K^+\pi^-$ and $B_s \rightarrow \pi^+K^-$. Recent CLEO measurements of some of the B^0 decay modes give $\mathcal{B}(B^0 \rightarrow \pi^+\pi^-) = 0.43 \times 10^{-5}$ and $\mathcal{B}(B^0 \rightarrow K^+\pi^-) = 1.7 \times 10^{-5}$ [1]. In order to normalize the B_s contribution, we use a B_s production rate which is 35% of the B^0 rate [3] and assume that the penguin and $b \rightarrow u$ decays of the B_s have the same branching ratios as the B^0 . Using these results as input, and without π/K discrimination, the two-pion mass plots for the four different two-body decay modes are shown in Fig. 16.2. These plots make it clear that kinematic separation is inadequate to discriminate among these decays.

The BTeV detector will have an excellent RICH detector for particle identification. We can virtually eliminate two-body backgrounds using the RICH detector. We passed the simulated background tracks (all tracks including all other interactions in that event), through the RICH simulation code. The efficiency vs background contamination is shown in Fig. 16.3. For an 80% $\pi^+\pi^-$ signal efficiency, the contamination from $\pi^\pm K^\mp$ (K^+K^-) is 4.0% (0.5)%.

Since the primary purpose of the Level 1 trigger is to reject light quark backgrounds, there is a strong correlation between triggered events and reconstructed events. The BTeVGeant simulation shows that 64% of the selected events pass the Level 1 trigger condition. Given a Level 2 efficiency of 90%, this leaves us with 23,700 events per year of running after applying the acceptance, reconstruction efficiency, particle ID efficiency, and trigger efficiency but before flavor tagging.

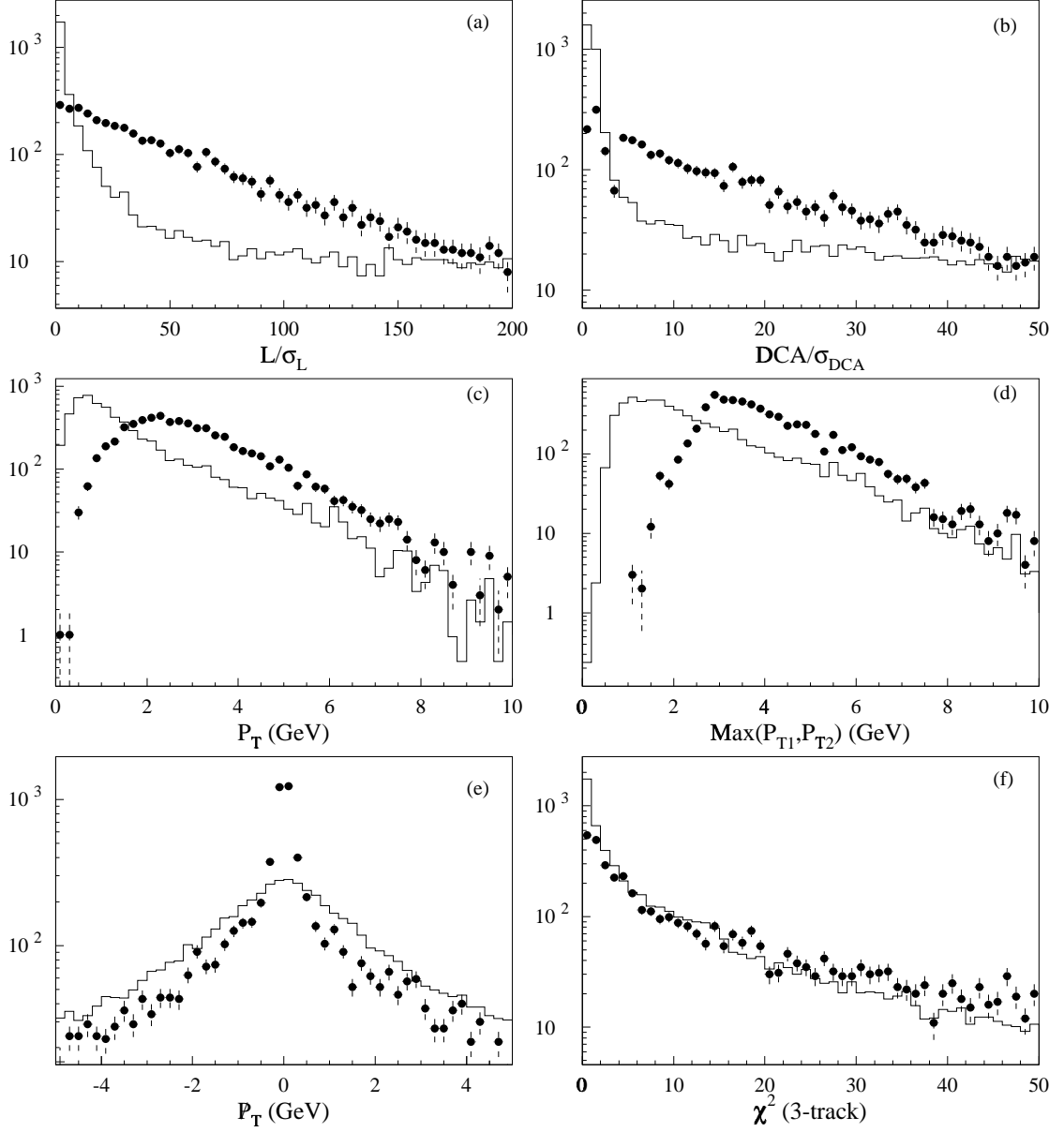


Figure 16.1: Distribution of signal (circles) and background (line) for the most important vertex and kinematic variables. (a) Normalized distance between primary and secondary vertex, L/σ_L , (b) Normalized DCA of track with respect to the primary vertex, DCA/σ_{DCA} (c) Transverse momentum of a track, (d) Maximum value of transverse momentum of two tracks, (e) P_T imbalance of $\pi^+\pi^-$ with respect to the B^0 direction, and (f) χ^2 of secondary vertex using the $\pi^+\pi^-$ with an additional track candidate.

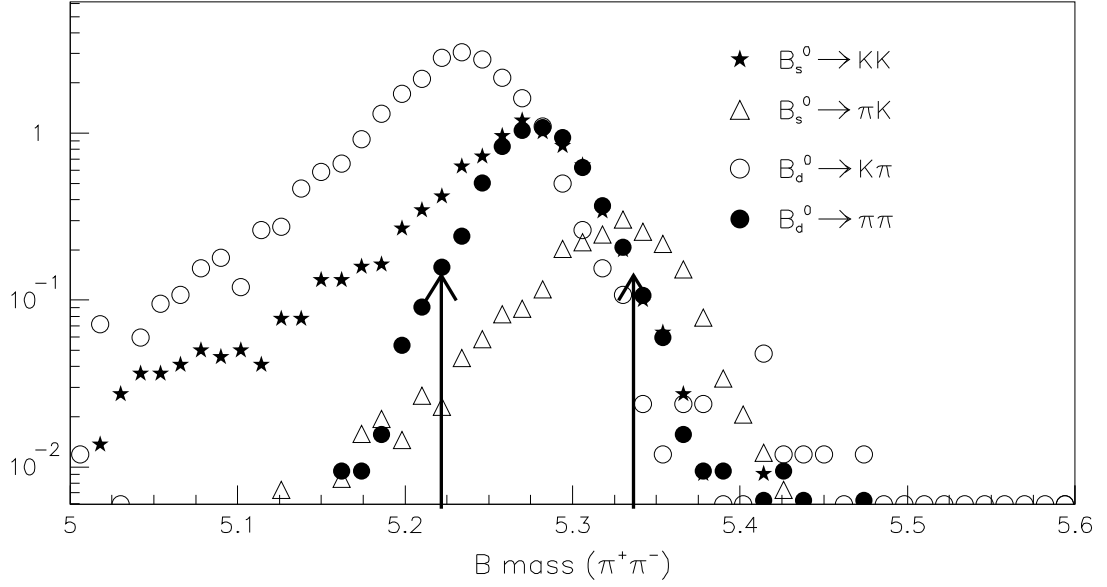


Figure 16.2: Two body ($\pi^+\pi^-$) mass plot without particle identification. Different decay channels are normalized by their production cross sections. The arrows indicate the range of the signal mass window. (Note the log scale.)

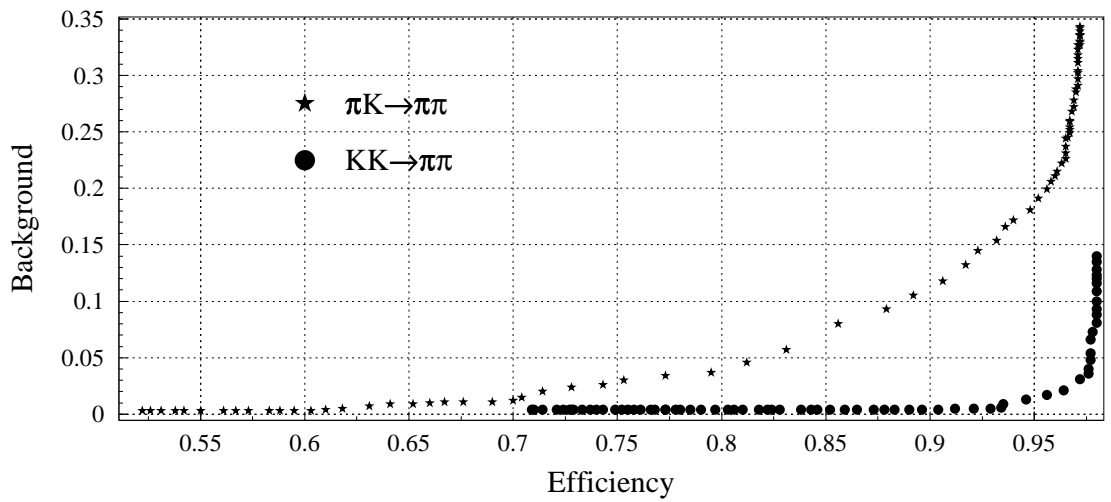


Figure 16.3: RICH event selection: $\pi^+\pi^-$ signal efficiency vs contamination from other two-body decay modes

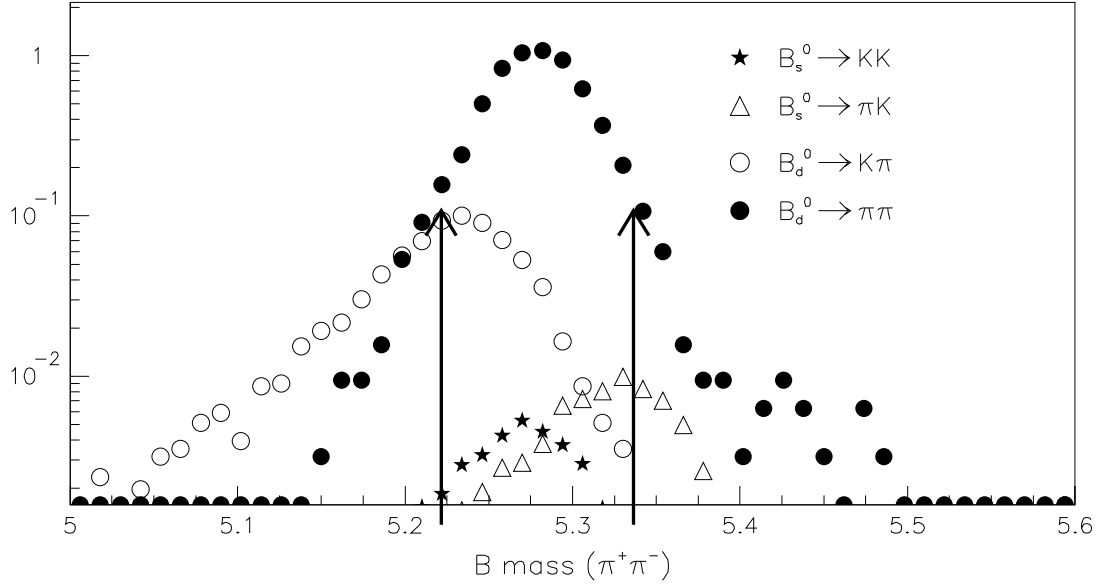


Figure 16.4: Two body ($\pi^+\pi^-$) mass plot with particle identification, normalized by their production cross sections. The arrows indicate the range of the signal mass window. (Note the log scale.)

Besides the two-body B decay background samples, we did a full BTeVGeant simulation of $b\bar{b}$ backgrounds. In order to reduce the CPU time required to simulate a sufficiently large data sample of $b\bar{b}$ decays, we investigated a method to preselect events at the generator level which are likely to cause difficulties. We found that the difference between the reconstructed and generated P_T of the tracks is fairly small and Gaussian (in the low P_T region, where we have our selection criteria). This is shown in Fig. 16.5. On the basis of the small observed differences, we preselected the generator events before the BTeVGeant simulation. The preselection criteria are based on the P_T (>0.4 GeV/c) of each track, the sum of the P_T (>1.8 GeV/c) of two tracks, the opening angle of the tracks, the extrapolation of tracks to the RICH chamber, etc. In order to reject background at the generator level, we had to sacrifice a small fraction of event selection efficiency.

These preselection requirements reduce the generic $b\bar{b}$ event sample by a factor of 100. From this sample, only 4 events (two $\pi^+\pi^-$, one $K^+\pi^-$ and one π^+K^-) have a $\pi^+\pi^-$ mass that lies within $200 \text{ MeV}/c^2$ of M_{B^0} . Applying the RICH identification leads to an 80% efficiency for the two $\pi^+\pi^-$ events and a 4% efficiency for each of the $K^+\pi^-$ and π^+K^- events. Thus, we have 1.68 background events. If we scale to the B signal region which is $115 \text{ MeV}/c^2$ and multiply by the combined Level 1 and Level 2 trigger efficiency ($64\% \times 90\%$), we expect $\approx 4,600$ $b\bar{b}$ background events from one year of running BTeV at the design luminosity of $2 \times 10^{32} \text{ cm}^{-2}\text{s}^{-1}$.

The remaining contributions (from the two-body decay channels) are listed in Table 16.1

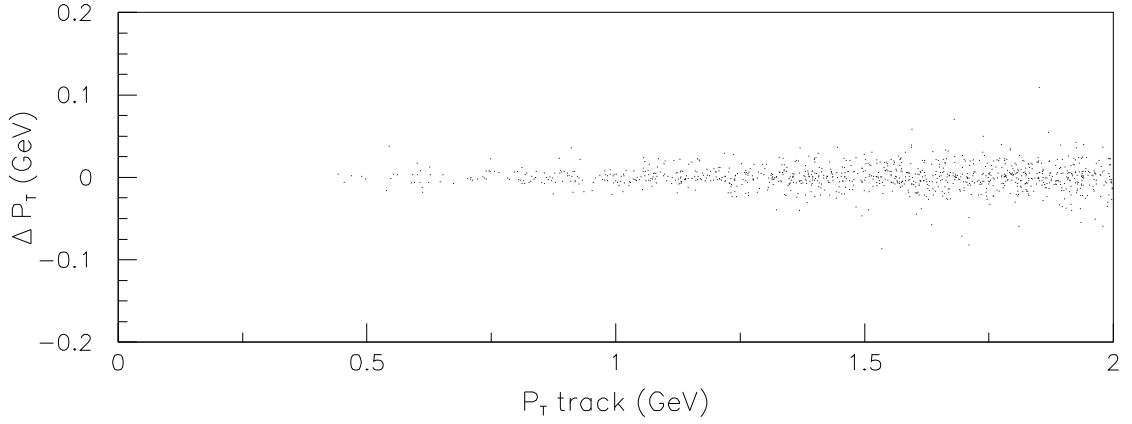


Figure 16.5: ΔP_T vs P_T for pion tracks where ΔP_T is the difference between the generated and reconstructed P_T .

and add up to 3,200 events per year. Therefore, the total background is 7,600 events per year leading to a signal-to-background ratio of 3:1 with a 25% error.

The effective tagging efficiency (ϵD^2), discussed in Chapter 15, is estimated to be 10%. Using the tagging efficiency and the $B^0 \rightarrow \pi^+ \pi^-$ yield, we can obtain an uncertainty on the CP asymmetry. Based on one year of running at the design luminosity, we expect an uncertainty on a_{CP} of 0.024, as summarized in Table 16.1.

We have repeated this analysis using the MCFast simulation. The reconstruction efficiencies obtained from each simulation agree (8.0% in BTeVGeant and 8.8% in MCFast). This result shows that the simulations of the tracking system in BTeVGeant and MCFast are quite similar.

As mentioned in Part I, measuring both $B^0 \rightarrow \pi^+ \pi^-$ and $B_s \rightarrow K^+ K^-$ may allow an extraction of γ . To this end, we have also looked for $B_s \rightarrow K^+ K^-$ signal events. This analysis is nearly identical to the $B^0 \rightarrow \pi^+ \pi^-$ analysis after interchanging $B^0 \rightarrow \pi^+ \pi^-$ and $B_s \rightarrow K^+ K^-$ samples from signal to background (and vice versa). As in the $B^0 \rightarrow \pi^+ \pi^-$ analysis, other two-body decay modes can mimic our signal as shown in Fig. 16.6.

From the RICH simulation, we find that at an 80% signal efficiency for $B_s \rightarrow K^+ K^-$, we accept 5% (1.5)% $\pi^+ \pi^-$ ($K^+ \pi^-$, $\pi^+ K^-$) background events as $K^+ K^-$. It is clear from Fig. 16.7 that by using the RICH information we can reject most of the backgrounds which are coming from other two-body decay modes.

The expected $B_s \rightarrow K^+ K^-$ yield, including the acceptance, reconstruction efficiency, trigger efficiency, and particle ID efficiency is 33,000 events per year at the design luminosity. This is summarized in Table 16.1.

Luminosity	$2 \times 10^{32} \text{ cm}^{-2} \text{ sS}^{-1}$
Running time	10^7 sec
Integrated Luminosity	2000 pb^{-1}
$\sigma_{b\bar{b}}$	$100 \mu\text{b}$
Number of $B\bar{B}$ events	2×10^{11}
Number of B^0 events	1.5×10^{11}
$\mathcal{B} (B^0 \rightarrow \pi^+ \pi^-)$	0.43×10^{-5}
Reconstruction efficiency	8.0%
Trigger efficiency (Level 1)	64%
Trigger efficiency (Level 2)	90%
RICH I. D. efficiency	80%
Number of reconstructed ($\pi\pi$) $B^0 \rightarrow \pi^+ \pi^-$	2.37×10^4
Background after RICH rejection	
$B^0 \rightarrow K^+ \pi^-$	0.27×10^4
$B_s \rightarrow \pi^+ K^-$	0.03×10^4
$B_s \rightarrow K^+ K^-$	0.02×10^4
B -generic	0.46×10^4
S/B	3
Tagging efficiency $\epsilon \text{ D}^2$	10.0%
δa_{CP}	2.36×10^{-2}

Table 16.1: Projected yield of $B^0 \rightarrow \pi^+ \pi^-$ and the uncertainty on a_{CP} from the BTeVGeant simulation.

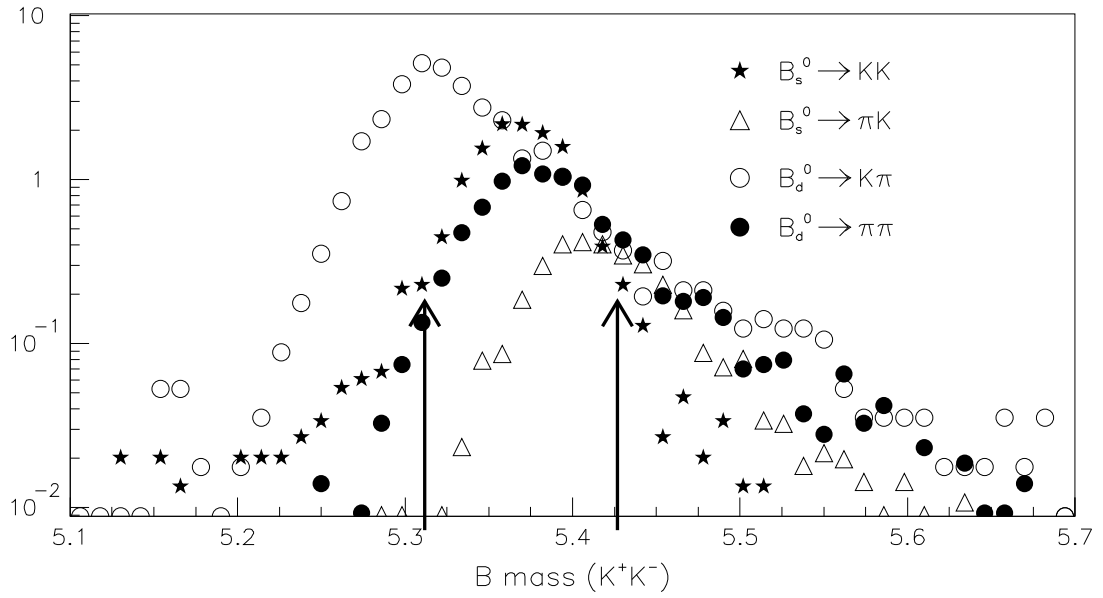


Figure 16.6: Two body (K^+K^-) mass plot without particle identification. Different decay channels are normalized by their production cross sections. The arrows indicate the range of the signal mass window. (Note the log scale.)

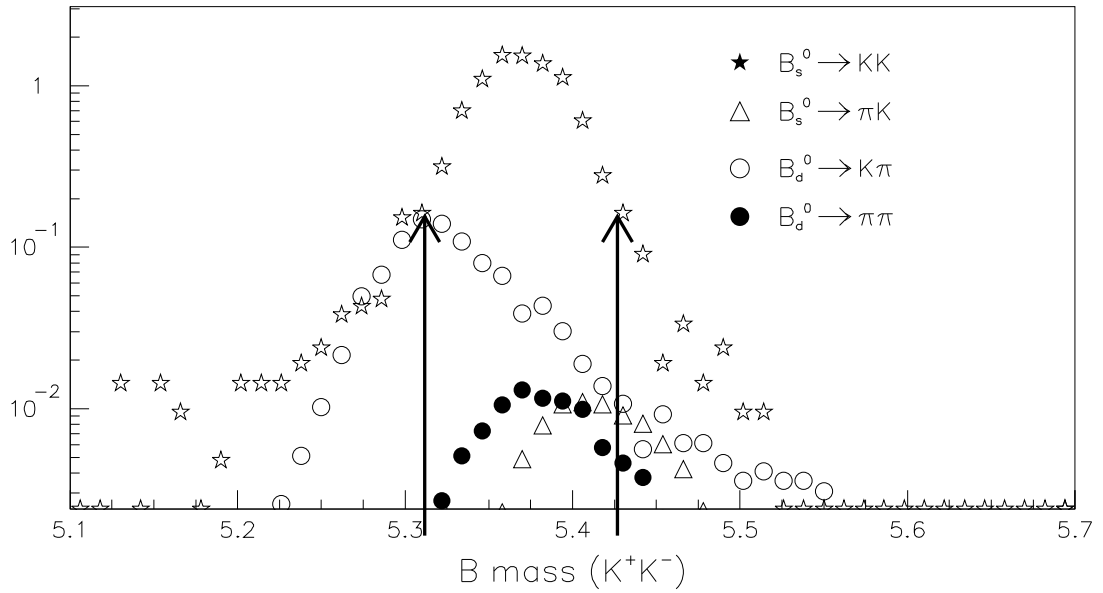


Figure 16.7: Two body (K^+K^-) mass plot with particle identification and normalized by their production cross sections. The arrows indicate the range of the signal mass window.

Luminosity	$2 \times 10^{32} \text{ cm}^{-2} \text{ s}^{-1}$
Running time	10^7 sec
Integrated Luminosity	2000 pb^{-1}
$\sigma_{b\bar{b}}$	$100 \mu\text{b}$
Number of $B\bar{B}$ events	2×10^{11}
Number of B_s events	0.52×10^{11}
$\mathcal{B} (B_s \rightarrow K^+ K^-)$	1.7×10^{-5}
Reconstruction efficiency	8.1%
Trigger efficiency (Level 1)	64%
Trigger efficiency (Level 2)	90%
RICH I. D. efficiency	80.0%
Number of reconstructed (K K)	
$B_s \rightarrow K^+ K^-$	3.29×10^4
Background after RICH rejection	
$B^0 \rightarrow K^+ \pi^-$	0.39×10^4
$B_s \rightarrow \pi^+ K^-$	0.04×10^4
$B^0 \rightarrow \pi^+ \pi^-$	0.04×10^4
B -generic	0.04×10^4
S/B	6.6

Table 16.2: Projected yield of $B_s \rightarrow K^+ K^-$ and fake rates.

16.2 Measuring $\sin 2\beta$ using $B \rightarrow J/\psi K_s^0$

As discussed in Section 1.5, the decay $B_d^0 \rightarrow J/\psi K_s^0$ is the golden mode for measuring the angle β in the unitarity triangle. While we expect that $\sin 2\beta$ will have been measured before the BTeV experiment begins, the collaboration aims to significantly improve that measurement. This section will present the reconstruction efficiency, trigger efficiency and signal to background ratio for the decay chain $B_d^0 \rightarrow J/\psi K_s^0$, $J/\psi \rightarrow \mu^+ \mu^-$, $K_s^0 \rightarrow \pi^+ \pi^-$.

For this study, Monte Carlo events were generated using Pythia and QQ as discussed in Section 12.3 and the detector response was simulated using BTeVGeant. The output of BTeVGeant was analyzed as would be real data.

When designing analysis cuts, it is important to understand both the efficiency of the cuts on signal events and the power of the cuts to reject background. Because of the narrow widths of the J/ψ and the K_s^0 , the dominant source of background entries is combinations of real $J/\psi \rightarrow \mu^+ \mu^-$ decays with real $K_s^0 \rightarrow \pi^+ \pi^-$ decays. CDF found that prompt J/ψ 's are a large fraction of total J/ψ production [4] and, extrapolating from their results, one expects that J/ψ 's from B decays comprise only about 5% of the total J/ψ production. However, the background from prompt J/ψ production is strongly suppressed by the topological cuts, leaving decays of the type $b \rightarrow J/\psi X$ as the dominant source of background.

The analysis was performed as follows. Each event was required to have an identified primary vertex that was successfully fitted with an acceptable χ^2 . A track was identified as a muon candidate provided the Monte Carlo truth table indicated that it was a muon, it had a momentum of more than 5.0 GeV/c and it had a hit in the most downstream muon detector. J/ψ candidates were formed by combining pairs of oppositely charged muon candidates and requiring that the invariant mass of the $\mu^+ \mu^-$ pair be within 3σ of the known mass of the J/ψ . It was also required that the $\mu^+ \mu^-$ pair pass a fit to a common vertex, that the vertex fit return an acceptable χ^2 and that the vertex be detached from the primary vertex by at least $L/\sigma_L > 4$, where L is the distance between the two vertices and σ_L is the error on L . As illustrated in Figure 16.8, this cut rejects 99.95% of the background from prompt J/ψ 's while keeping 80% of the signal. A fit was performed to constrain the mass of the candidate to that of the J/ψ .

All other tracks with a momentum of at least 0.5 GeV/c were accepted as pion candidates, provided they missed the primary vertex by $b > 3\sigma$, where b is the impact parameter between the track and the primary vertex and where σ is the error on b . K_s^0 candidates were selected by combining oppositely charged pairs of pion candidates and requiring that the invariant mass of the $\pi^+ \pi^-$ pair be within 3σ of the known mass of the K_s^0 . It was also required that K_s^0 candidates pass a fit to a common vertex and that the vertex fit return an acceptable χ^2 . A fit was performed to constrain the mass of the candidate to that of the K_s^0 .

A B candidate was defined as the combination of a J/ψ candidate and a K_s^0 candidate which pointed back to the primary vertex. To reduce combinatorial background it was required that the K_s^0 candidate point back to the J/ψ vertex within 3σ and that the K_s^0 impact parameter with respect to the J/ψ vertex divided by its impact parameter with respect to the primary vertex be less than 2.0.

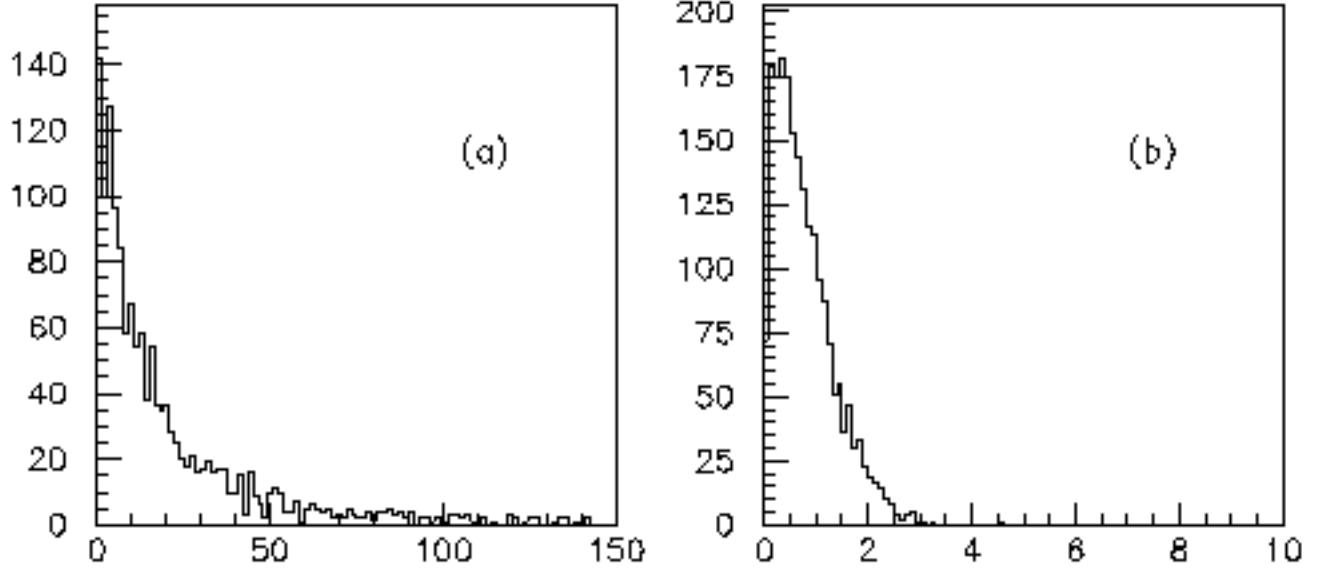


Figure 16.8: Distributions of L/σ_L for (a) J/ψ candidates from the decays of b-hadrons and (b) prompt J/ψ candidates. The prompt candidates are suppressed by requiring $L/\sigma_L > 4$.

The invariant mass spectrum of B candidates which pass the above criteria is shown in Figure 16.9. A clear signal with a width of $\sigma = 9.3 \text{ MeV}/c^2$ is seen at the mass of the B_d . The efficiency for a $B_d \rightarrow J/\psi K_S^0$ decay to fall into the mass peak is 0.040 ± 0.002 and the mean resolution on the proper decay time is 50 fs.

As mentioned above, the dominant source of background is decays of the type $b \rightarrow J/\psi X$. This background was studied by generating large samples of such decays, using Pythia and QQ; these samples were passed through the MCFast based detector simulation and analyzed as real data. This study predicted that the signal to background ratio in this channel is approximately $S/B = 10$.

The BTeV Level 1 trigger, described in chapters 9 and 14, was run on events which passed the analysis cuts, and it was found to have an efficiency of $52 \pm 3 \%$. This decay mode can also be triggered by muon and dimuon triggers. Section 8.3, which describes the algorithms and performance of the muon trigger, estimates a trigger efficiency of 50% for this decay mode. There is, as yet, no calculation of the total Level 1 trigger efficiency which takes into account the correlations between the two triggers. For this proposal it will be estimated that the combined Level 1 trigger efficiency is 75%.

Section 14.3.3 discusses the performance of the Level 2 tracking trigger. There is, as yet, no calculation of the total Level 2 trigger efficiency which takes into account the correlations between the muon and tracking triggers. For this proposal it will be estimated that the combined Level 2 trigger efficiency is 90%.

In Section 15, it is estimated that the tagging efficiency for B_d decays is $\epsilon D^2 = 0.10$.

There are two methods which can be used to extract $\sin(2\beta)$ from the reconstructed,

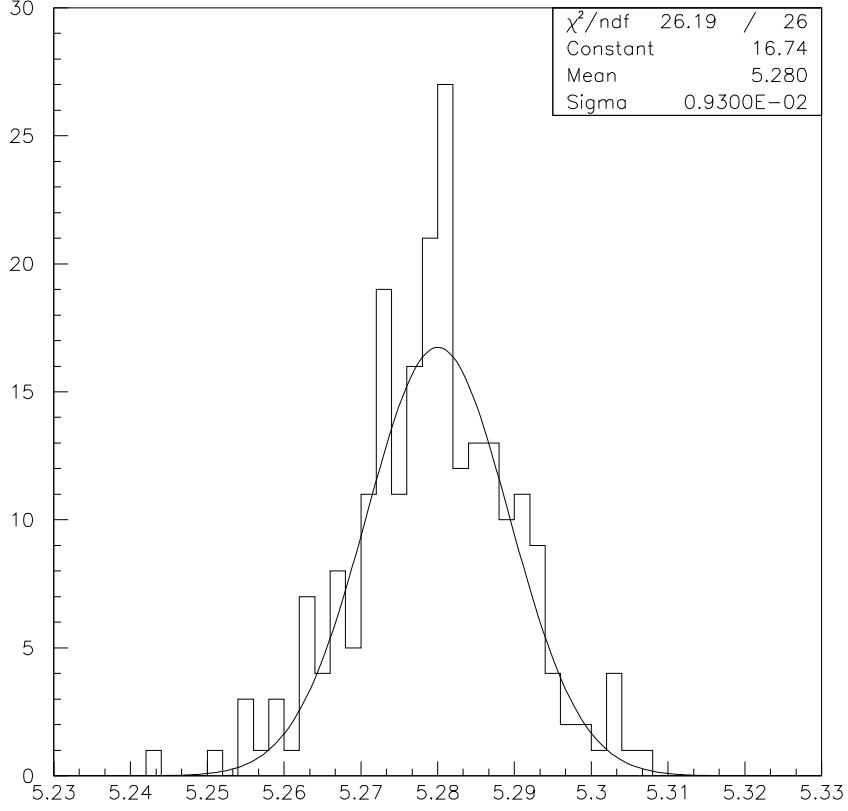


Figure 16.9: The $J/\psi K_s^0$ invariant mass distribution for candidates which survive the selection criteria described in the text.

tagged $J/\psi K_s^0$ candidates, a time integrated method and a time dependent method. The sensitivity of the time integrated method is given by,

$$\delta(\sin(2\beta)) = \frac{1 + x_d^2}{x_d} \sqrt{\frac{1}{\epsilon D^2 N}} \sqrt{\frac{S + B}{S}},$$

while the sensitivity of the time dependent method is given by,

$$\delta(\sin(2\beta)) = e^{\frac{x_d^2 \Gamma_d^2 \sigma_t^2}{2}} \sqrt{\frac{1 + 4x_d^2}{2x_d^2}} \sqrt{\frac{1}{\epsilon D^2 N}} \sqrt{\frac{S + B}{S}},$$

where N is the number of tagged decays, $x_d = 0.723 \pm 0.032$ [5] is the B_d mixing parameter, σ_t is the resolution on the proper decay time and where $\Gamma_d = 0.641 \pm 0.016 \times 10^{12} \text{ s}^{-1}$ [5] is the natural width of the B_d . For the B_d , the time dependent method yields a sensitivity which

is about 20% better than that given by the time integrated method. In previous documents the BTeV collaboration has reported the sensitivity on $\sin(2\beta)$ using the time integrated method but in this document the superior, time dependent, method will be used.

The above discussion is summarized in Table 16.3 which reports a sensitivity of $\delta\sin(2\beta) = 0.025$.

Luminosity	$2 \times 10^{32} \text{ cm}^{-2} \text{ s}^{-1}$
Running time	10^7 sec
$\sigma_{b\bar{b}}$	$100 \mu\text{b}$
Number of $B\bar{B}$ events	2×10^{11}
$\mathcal{B}(\bar{b} \rightarrow B_d)$	0.4
Number of B_d^0 or B_d^0	1.6×10^{11}
$\mathcal{B}(B_d^0 \rightarrow J/\psi K_s^0)$	4.45×10^{-4}
$\mathcal{B}(J/\psi \rightarrow \mu^+ \mu^-)$	0.061
$\mathcal{B}(K_s^0 \rightarrow \pi^+ \pi^-)$	0.6861
$\epsilon(\text{Geometric} + \text{cuts})$	0.04
Level 1 Trigger efficiency	0.75
Level 2 Trigger efficiency	0.90
Number of reconstructed $B_d^0 \rightarrow J/\psi K_s^0$	80,500.
Tagging efficiency ϵD^2	10%
S/B	10
Resolution on proper decay time	0.043 ps
B_d Lifetime	1.56 ps
x_d	0.723
$\delta\sin(2\beta)$, time integrated	0.030
$\delta\sin(2\beta)$, time dependent	0.025

Table 16.3: Summary of the sensitivity to $\sin(2\beta)$ using $B \rightarrow J/\psi K_s^0$. The time dependent method provides the better sensitivity.

16.3 $B^0 \rightarrow D^{*-} \rho^+$

16.3.1 Introduction

We have studied the performance of the BTeV detector for the decay $B^0 \rightarrow D^{*-} \rho^+$, which has been adopted as a benchmark decay containing a π^0 . This decay has been observed and studied in e^+e^- collisions on the $\Upsilon(4S)$ resonance by CLEO. It is therefore possible to compare the predicted performance of BTeV with the CLEO result, which currently defines the state of the art in γ and π^0 detection in heavy quark decays. The branching ratio $B^0 \rightarrow D^{*-} \rho^+$ is measured to be 0.0068 ± 0.0034 [5].

This decay, and the closely related decay $B^0 \rightarrow D^{*-} \pi^+$, also provide a method, albeit a difficult one, of measuring the CKM angle α [6]. This is done by studying the differences in the four related rates

$$\Gamma(B_d(t) \rightarrow f), \Gamma(B_d(t) \rightarrow \bar{f}), \Gamma(\bar{B}_d(t) \rightarrow \bar{f}), \Gamma(\bar{B}_d(t) \rightarrow f) \quad (16.1)$$

where f represents the various final states $D^{*\mp} \pi^\pm, \rho^\pm, a_1^\pm$, etc. These processes have an interference term which is governed by

$$\lambda = \frac{q < f | \bar{B}_d >}{p < f | B_d >} = \rho \exp^{i(\phi + \Delta)} \quad (16.2)$$

where ρ is the amplitude ratio and Δ is a strong phase. The weak phase can be shown to be

$$\phi = -2\beta - \gamma = -\pi + \alpha - \beta. \quad (16.3)$$

Since β will be known at the time this measurement will be made, this can be viewed as a method of measuring α which is quite different from other methods. The main difficulty in this method lies in the small size of the amplitude ratio, ρ :

$$\rho \approx \left| \frac{V_{ub}}{V_{cb}} \right| \times \left| \frac{V_{cd}}{V_{ud}} \right| \approx 0.02. \quad (16.4)$$

The small asymmetry means that a large number of events and an excellent understanding of systematics is required for this measurement. If the measurement can be made, its great virtue is that it is not contaminated by Penguin diagrams.

16.3.2 Analysis

For this study, we have generated the signal events with Pythia and QQ using the correct helicity structure of the decays determined by CLEO. For our study of the background, we make the assumption that the main source of background events is assumed to be from true B decays of all kinds (i.e. all types of B hadrons) which produce a D^{*-} in the decay chain. For both the signal and background simulation, the B event is accompanied by minimum bias interactions, with the average per generated B being 2. The detector simulation is performed using BTeVGeant with the thresholds and conditions described in chapter 12. The analysis relies especially on the Kalman filter, the vertex package and the electromagnetic cluster finder.

The signal we are studying follows the decay chain

$$\begin{aligned}
B^0 &\rightarrow D^{*-} \rho^+ \\
\text{where } D^{*-} &\rightarrow \bar{D}^0 \pi^- \\
\text{and } \bar{D}^0 &\rightarrow K^+ \pi^- \\
\text{and } \rho^+ &\rightarrow \pi^+ \pi^0.
\end{aligned}$$

At present, we have only looked at \bar{D}^0 decaying into $K^+ \pi^-$, although $K^+ \pi^- \pi^+ \pi^-$ should also be copious. The ‘signal’ sample we are using consists of 40,000 events in which there is a B^0 which is forced to decay according to the above chain, while the away side \bar{B} -hadron is decayed generically by QQ. The ‘background’ sample consists of 200,000 events in which there is a D^{*-} in the final state. The D^{*-} may come from either the B or \bar{B} . The \bar{D}^0 which is the daughter of the D^{*-} always decays to $K^+ \pi^-$.

The analysis goes as follows: For the \bar{D}^0 , we require a $K^+ \pi^-$ combination with invariant mass between 1.840 and 1.890 GeV/c^2 . It must decay downstream of the primary vertex and must have a pion (bachelor pion) with the correct sign with which it makes a mass difference of $145.5 \pm 2.0 \text{ MeV}/c^2$.

With these requirements, we obtain the $D^{*-} - D$ Q-value shown in Fig. 16.10. The fitted width of this peak is 583 keV.

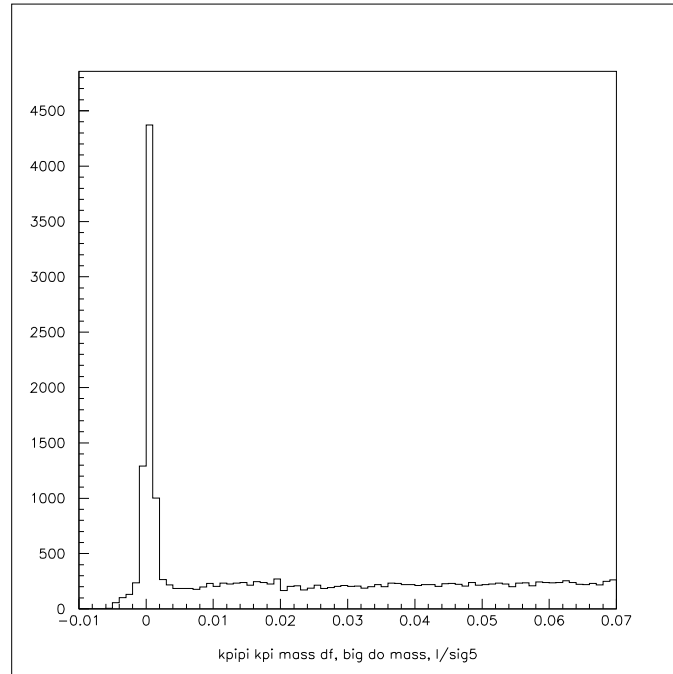


Figure 16.10: The $D^{*-} - D$ Q-value, $M(K^+ \pi^- \pi^-) - M(K^+ \pi^-) - 0.1455$, in GeV/c^2 .

The \bar{D}^0 must form a vertex with the bachelor pion and an oppositely charged pion with

total mass less than $5.15 \text{ GeV}/c^2$. The vertex formed by these tracks must have at least an 8 standard deviation separation from the primary vertex.

The π^0 is formed by taking pairs of reconstructed showers, “bumps” in the language of our cluster finder, found in the same arm, with mass between 126 and $140 \text{ MeV}/c^2$ and which make a good transverse momentum balance about the B direction with the charged tracks in the B candidate (This last requirement is discussed below). To find the π^0 , we run the calorimeter cluster finder described above. We exclude all shower candidates whose energies are less than 0.750 GeV or which occur within 20 cm of the beam axis (to stay away from the region of very high occupancy near the beam). We eliminate showers from hadrons or electrons by excluding showers if any charged track points within 10 cm of the shower’s centroid — an ‘isolation’ cut. We eliminate showers for which the ratio of energy in the 9 blocks around the shower center to the energy in the 25 blocks around the shower is less than 0.85 — a ‘shower shape’ cut. Showers failing this cut are more spread out than normal electromagnetic showers and may be due to neutral hadrons, hadrons overlapping genuine electromagnetic showers, or partially merging electromagnetic showers. In any case, their energies and angles are likely to be incorrectly measured. In Fig. 16.11, we show the invariant mass distributions of all pairs of neutral showers for various values of the isolation cut. A clear π^0 peak is evident. The width of the π^0 mass peak is $3.5 \text{ MeV}/c^2$. The background in these plots is combinatoric background due to the presence of many additional photons in the event underlying the B and in the accompanying minimum bias events.

At this point, we form the invariant mass of the oppositely charged pion and all π^0 candidates and require the $\pi^+\pi^0$ mass to be compatible with the ρ^+ mass, that is, between $0.540 \text{ GeV}/c^2$ and $1.0 \text{ GeV}/c^2$. This is not a very powerful cut because of the large natural width of the ρ^+ .

If we plot the invariant mass of the D^{*-} and the ρ^+ using only the requirements described so far, the background levels are unacceptably high. The reason for this is that we have to consider all π^0 candidates which, in combination with the bachelor pion, satisfy the very loose “ ρ ” requirement. This leads to many false ρ combinations which eventually produce a large combinatoric background in the final $D^{*-}\rho^+$ invariant mass plot.

To defeat this background, we exploit the fact that the pixel detector provides information about the parent B^0 which can be used to eliminate π^0 s which are not associated with the B^0 decay. There are two equivalent ways to understand this. One way is to consider that the B direction is determined by the line connecting the primary vertex with the intersection of the D^* and the charged pion from the ρ . The direction of this line is known with an accuracy which varies but is often better than a few milliradians. We accept only $\rho \rightarrow \pi^+\pi^0$ candidates which balance the transverse momentum around the direction of the B as determined from the pixel detector. One can implement this by taking the cross product of the ρ momentum vector against the B direction and then requiring it to “balance”, i.e. be equal in magnitude and opposite in direction, within resolution, the cross product of the D^* momentum vector against the B direction. We have used this method. Alternatively, the ‘pointback’ method is to form a composite object out of the $D^*\rho$ combination and to require the resulting B candidate to project through the B vertex as determined by the

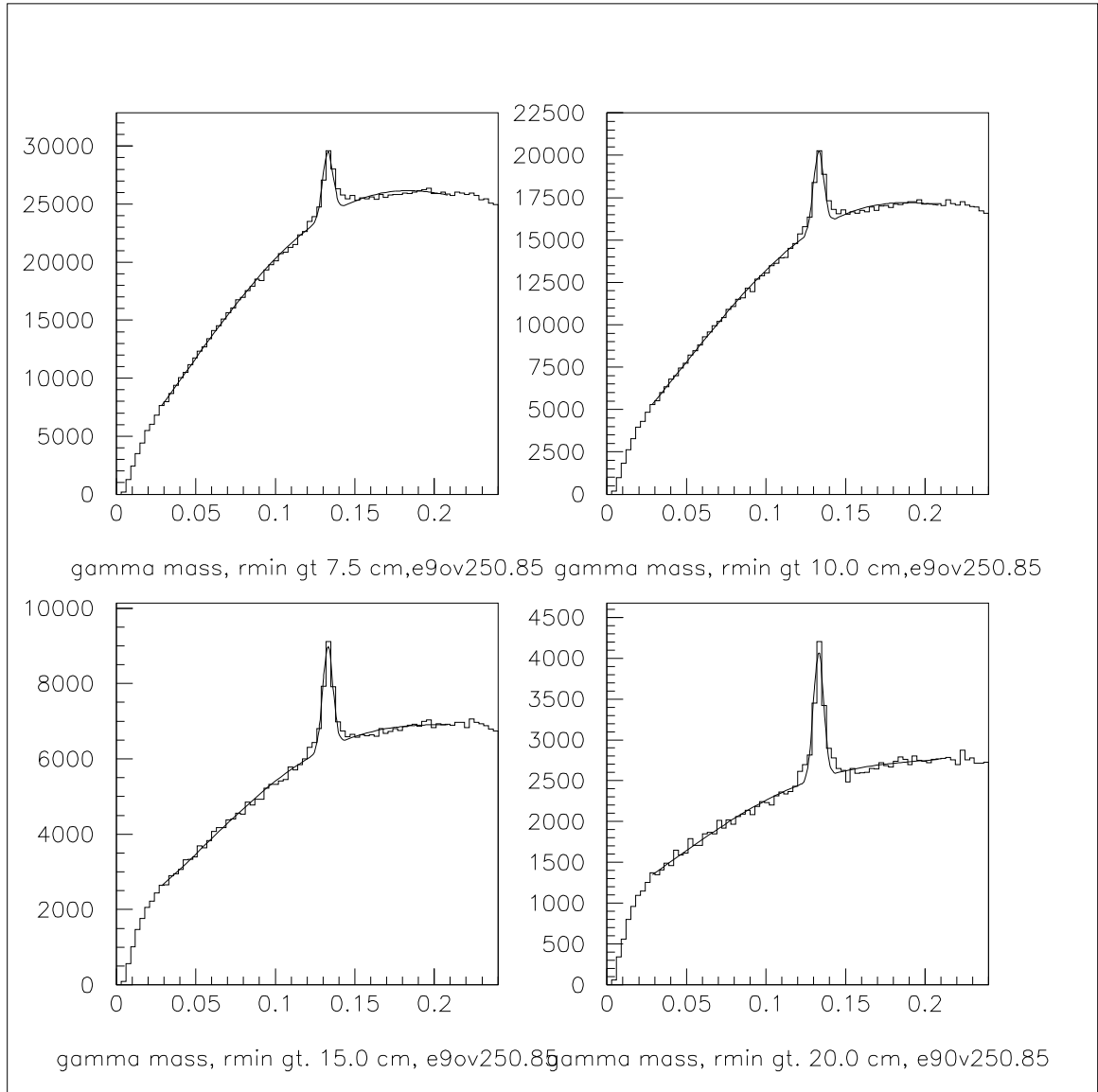


Figure 16.11: Four different sets of cuts on the $\gamma\text{-}\gamma$ mass spectrum: (upper left) $R_{min} < 7.5$ cm and $E9/E25 < 0.85$; (upper right) $R_{min} < 10.0$ cm and $E9/E25 < 0.85$; (lower left) $R_{min} < 15.0$ cm and $E9/E25 < 0.85$; and (lower right) $R_{min} < 20.0$ cm and $E9/E25 < 0.85$. The fit is to a Gaussian and a fourth order polynomial. Most analysis work used the cuts of the plot in the upper right corner.

pixel detector to the primary vertex position (also determined by the pixel detector). The P_t balance method and the pointback requirement are equivalent and serve to reduce the combinatoric background because random π^0 's will rarely combine with the charged pion to satisfy the balance requirement. Figure 16.12 shows schematically how these requirements work. Figure 16.13 shows the polar angle resolution on the B direction for the final signal events in this analysis. The resolution is about 1 milliradian. Figure 16.14 shows the P_t balance variable we cut on:

$$\frac{|P_t(D^*)| - |P_t(\rho)|}{|P_t(D^*)| + |P_t(\rho)|}. \quad (16.5)$$

The D^* and ρ are also required to be produced back-to-back in the plane perpendicular to the B direction.

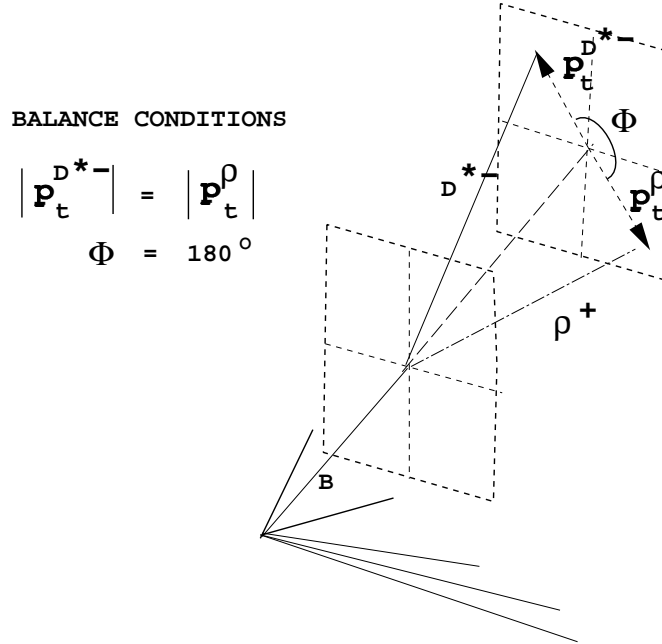


Figure 16.12: P_t balance about the B direction.

Figures 16.15 and 16.16 show the effect of the P_t balance cut on the signal and background, respectively. The cuts used are 0.15 on the P_t balance variable and a requirement that the cosine of the azimuthal angle between the P_t vector of the D^* relative to the B and the P_t vector of the ρ relative to the B be less than -0.98 . The invariant mass peak of the final state signal, (Fig. 16.15), which contains 4 charged tracks and two photons has a width of about $35 \text{ MeV}/c^2$. The number of background combinations in the vicinity of the signal, (Fig. 16.16), is reduced by a factor of more than 15 by this technique. The yield of signal events is hardly affected by these cuts.

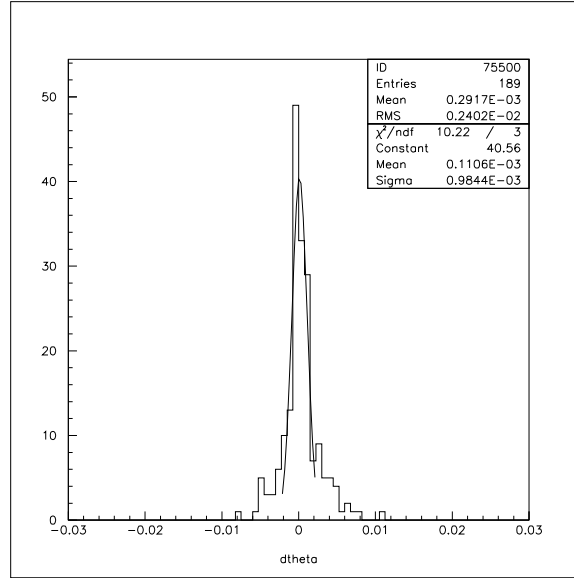


Figure 16.13: Resolution on B polar angle, θ , measured from the fitted primary and B vertices. The quantity plotted is $\theta_{\text{measured}} - \theta_{\text{generated}}$. The width of the “core” of the distribution is about 1 milliradian.

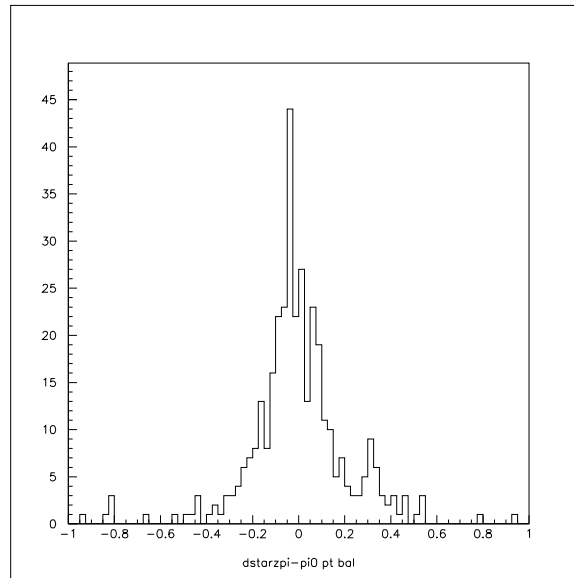


Figure 16.14: Distribution of the P_t balance variable for signal events.

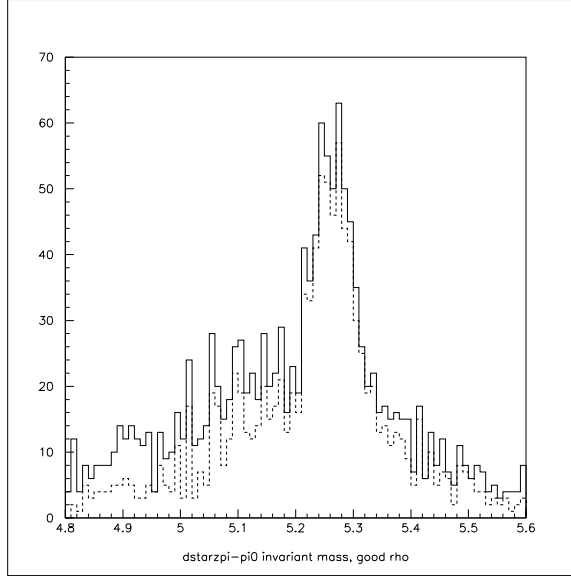


Figure 16.15: Effect of P_t balance cuts on signal events. Both histograms show the invariant mass of the $D^*\rho$ system. The solid histogram is before the P_t balance cuts and the dashed histogram is after the cuts. The number of events is only slightly affected.

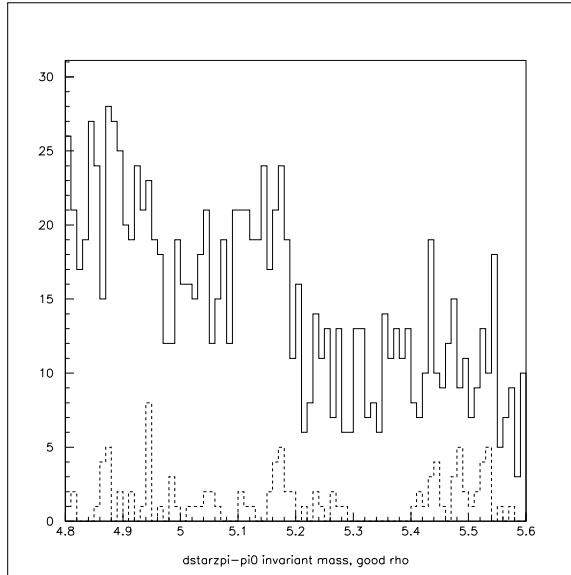


Figure 16.16: Effect of P_t balance cuts on background events. Both histograms show the invariant mass of the $D^*\rho$ system. The solid histogram is before the P_t balance cut and the dashed histogram is after the cuts. The number of events is reduced by a factor of more than 15.

The invariant mass distribution shown in Fig. 16.15 for signal events has a peak sitting on top of a broad “background”. Comparison of the events in this distribution with generator information reveals that almost all the events in the broad side structures are real signal events with the correct charged track assignments. The background is due to either correct photon assignments where one of the photon’s energy has been mismeasured due to the presence of other showers nearby, or to pairings of one correct photon with an incorrect, very low energy, photon which replaces the correct one.

The π^0 s expected for this state have an average energy of only about 6 GeV. They are rather fragile in the sense that any energy from other sources that overlaps the signal photons will either cause signal to be lost or its resolution to be degraded. Fig. 16.17 shows the effect on the signal shape when different cuts are placed on the energy of the π^0 . Both size and quality of the signal are affected by these cuts. Sensitivities are quoted below for each of these four signals.

The background is obtained by subjecting the D^* inclusive B decay events, generated as described above, to the same analysis as the signal events. We use the calculation below to establish the correct absolute normalization of the signal and the background distributions and to derive the total yield and the signal-to-background ratio.

The calculation of the number of events per year at the BTeV design luminosity of $2 \times 10^{32} \text{ cm}^{-2}\text{s}^{-1}$ and the signal-to-background ratio is shown in Table 16.4. The number of signal events per year is expected to be about 70,000 - 100,000. The signal-to-background ratio depends on the cuts but is about 2:1. If we simply restrict the mass interval over which we define the signal, this improves to over 3:1 for the tightest cut, with a loss of about 7% of the signal. We have now run enough background events so that we have a reasonable sample for studying the cuts to try to reduce the background further.

16.3.3 Background from Charm

At the Tevatron, charm production is expected to be an order of magnitude larger than B production. The copious production of D^* s from charm is a potential background to the $B^0 \rightarrow D^{*-}\rho^+, \pi^+$ signals. We have generated 100,000 events with a D^* which we then force to decay to $D^0\pi$ and the D^0 to $K\pi$. We pass these through our analysis programs and no events survive. We place a 90% confidence level upper limit on the yield per year of 25,000. The 90% confidence level upper limit on the signal-to-background from charm is 4/1 and is probably much better. The conclusion is that the background will be mainly from B decays, not charm.

16.3.4 Effect of Multiple Interactions

We have described how BTeV defeats the combinatoric photon background even in the presence of an average of two minimum bias events per crossing. We studied the signal-to-background ratio as a function of the number of interactions per crossing. The result is shown in Fig. 16.18, where we plot the $D^{*-}\pi^+$ invariant mass for various values of the number

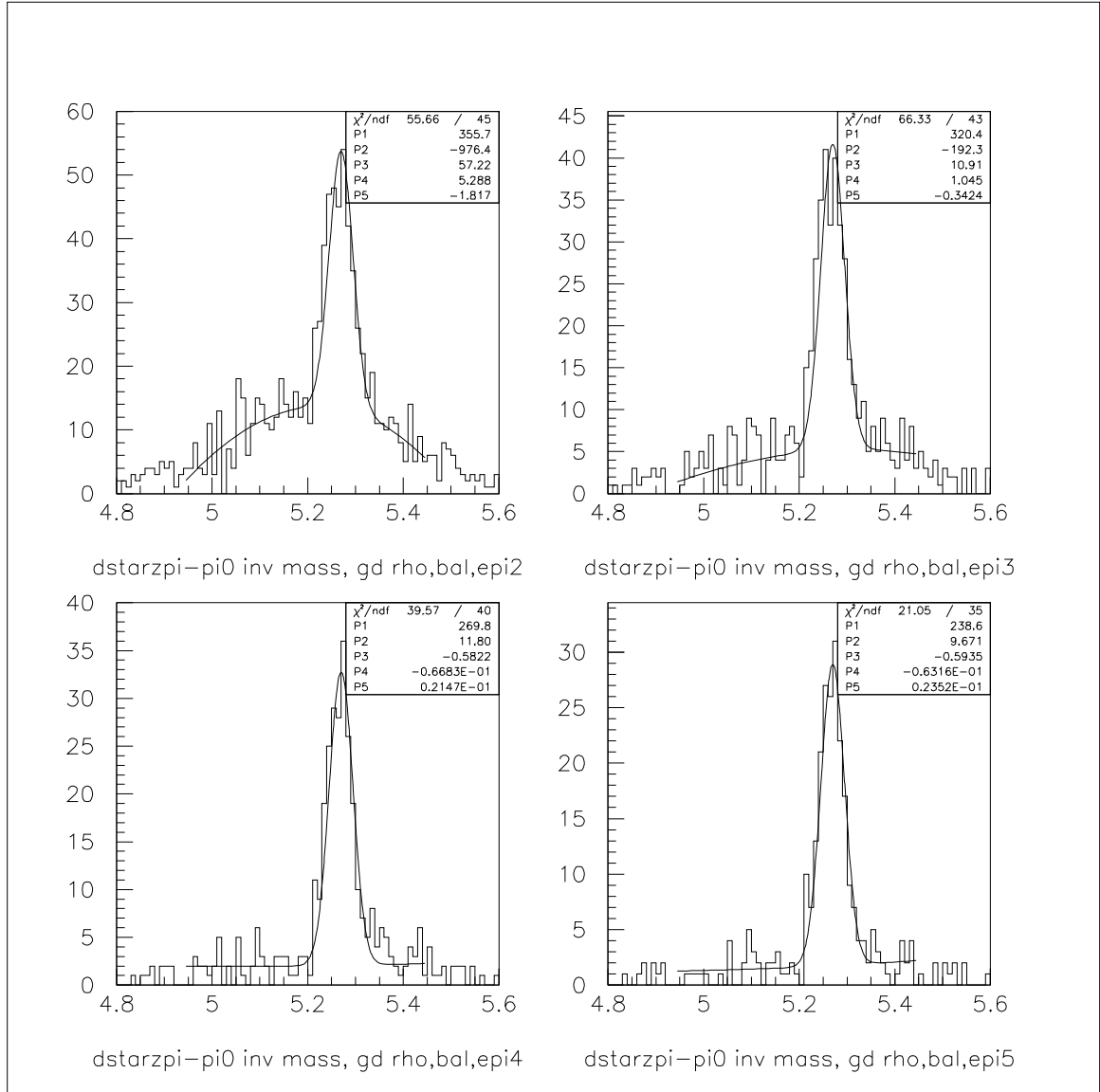


Figure 16.17: $D^*\rho^+$ invariant mass for four values of the minimum allowed π^0 energy: (upper right) 2 GeV; (upper left) 3 GeV; (lower right) 4 GeV; and (lower left) 5 GeV. As the π^0 energy requirement is raised, the tails of the mass peak disappear.

Quantity	Value
bb events/year	2×10^{11}
Signal:	
B^0/\bar{B}^0 /year	1.5×10^{11}
$\mathcal{B}(B^0 \rightarrow D^{*-}\rho^+)$	0.007
$\mathcal{B}(D^{*-} \rightarrow \bar{D}^0\pi^-)$	0.68
$\mathcal{B}(\bar{D}^0 \rightarrow K^+\pi^-)$	0.04
No. events produced per year	
$B^0 \rightarrow D^{*-}\rho^+, D^{*-} \rightarrow \bar{D}^0\pi^-, \bar{D}^0 \rightarrow K^+\pi^- + \text{CC}$	2.86×10^7
Width of signal	32 MeV/c ²
Mass window	5.20 - 5.34 GeV/c ²
Number of MC signal events recon. in mass window:	
π^0 Energy > 2.0 GeV (efficiency= 0.79%)	314
π^0 Energy > 3.0 GeV (efficiency= 0.69%)	277
π^0 Energy > 4.0 GeV (efficiency= 0.58%)	232
π^0 Energy > 5.0 GeV (efficiency= 0.53%)	212
Trigger efficiency - Level 1	0.63
Trigger efficiency - Level 2 (estimate)	0.90
Overall Trigger Efficiency	0.57
Expected no. events reconstructed and triggered per year:	
π^0 Energy > 2.0 GeV (S/N = 1.07)	12.8×10^4
π^0 Energy > 3.0 GeV (S/N = 1.56)	11.2×10^4
π^0 Energy > 4.0 GeV (S/N = 1.95)	9.4×10^4
π^0 Energy > 5.0 GeV (S/N = 2.39)	8.6×10^4
Background (in 140 MeV/c ²):	
D^* production fraction	0.22
$\mathcal{B}(D^{*-} \rightarrow \bar{D}^0\pi^-)$	0.68
$\mathcal{B}(\bar{D}^0 \rightarrow K^+\pi^-)$	0.04
$D^{*-} \rightarrow \bar{D}^0\pi^-, \bar{D}^0 \rightarrow K^+\pi^- + \text{CC}$	2.4×10^9
Number of MC BG events in mass window 4.8 - 5.6 GeV:	
π^0 Energy > 2.0 GeV (efficiency = 0.05%)	102
π^0 Energy > 3.0 GeV (efficiency = 0.03%)	58
π^0 Energy > 4.0 GeV (efficiency = 0.02%)	40
π^0 Energy > 5.0 GeV (efficiency = 0.015%)	30
Trigger effic. assumed to be same as signal	0.57
π^0 Energy > 2.0 GeV	12.0×10^4
π^0 Energy > 3.0 GeV	7.2×10^4
π^0 Energy > 4.0 GeV	4.8×10^4
π^0 Energy > 5.0 GeV	3.6×10^4

Table 16.4: Details of the calculation of the signal and background events obtained in one year of running for the decay $B^0 \rightarrow D^{*-}\rho^+$

of generated primary vertices in the crossing. The signal-to-background ratio obviously degrades after about 4 interactions/crossing.

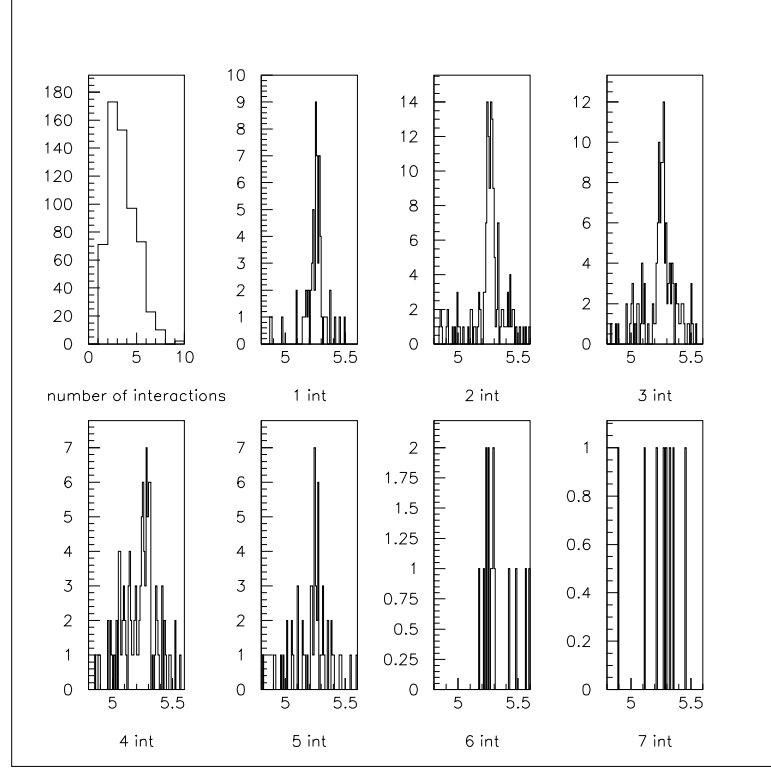


Figure 16.18: The top left plot shows the number of interactions per crossing for this analysis. The next seven plots show the $D^* - \rho^+$ invariant mass plot when there are 1 to 7 interactions in the crossing.

16.3.5 The CLEO result

We can compare BTeV's signal-to-background and yield to CLEO's. The most up-to-date CLEO data are presented in B. Barish *et al*, CLEO CONF 97-01, EPS 97-339 [7].

The CLEO data sample consists of 3.1 fb^{-1} taken on the $\Upsilon(4S)$ and 1.4 fb^{-1} taken on the continuum at a center-of-mass energy 60 MeV lower. CLEO has always taken on-resonance and off-resonance data with approximately 2:1 ratio of luminosities. In the next generation of e^+e^- b -factories, the design luminosities are approximately $3 \times 10^{33} \text{ cm}^{-2}\text{s}^{-1}$, which could yield 30 fb^{-1} in a "Snowmass" year of 10^7 s . Thus the reported CLEO yields, given below, should be multiplied by a factor of 6.7 to compare with the expected yields at the time that BTeV could run.

For the mode $\bar{B} \rightarrow D^{*+}\rho^-$, CLEO uses three D^0 decay modes: $K^-\pi^+$, $K^-\pi^+\pi^0$ and $K^-\pi^+\pi^+\pi^-$. The reconstructed B mass plots are shown in Fig. 16.19.

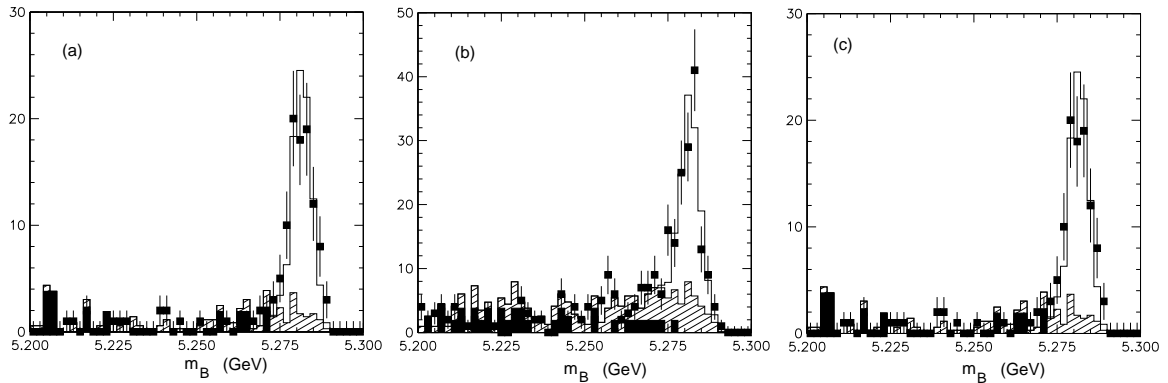


Figure 16.19: Reconstructed mass plots for $\bar{B} \rightarrow D^{*+} \rho^-$ from CLEO. The data measured on the $\Upsilon(4S)$ are shown as points with error bars, the scaled continuum data are shown as filled rectangles and the estimated $B\bar{B}$ background in cross-hatch. The solid histogram is the result of the fit to a signal Gaussian and the two background components. The three plots are for different D^0 decay modes: (a) $K^- \pi^+$, (b) $K^- \pi^+ \pi^0$ and (c) $K^- \pi^+ \pi^+ \pi^-$.

In Table 16.5 we give the measured CLEO yields. The signal to background (S:B) ratio for the $D^0 \rightarrow K^- \pi^+$ mode is approximately 4.5:1 and is worse for the other decay modes.

Table 16.5: CLEO yields for $\bar{B} \rightarrow D^{*+} \rho^-$.

D^0 mode	Yield	efficiency	\mathcal{B} (%)
$K^- \pi^+$	77	10.8 %	0.805 ± 0.107
$K^- \pi^+ \pi^0$	110	4.9 %	0.666 ± 0.086
$K^- \pi^+ \pi^+ \pi^-$	63	4.6 %	0.749 ± 0.136

16.3.6 Comparison and Summary

The signal to background expected in BTeV compares very favorably with that obtained by CLEO, and is expected to improve simply by optimizing the cuts after the backgrounds are studied in detail. The BTeV event yield per year is more than 230 times higher than is anticipated from CESR/CLEO III, BaBar, and BELLE.

This analysis, obtained with a full and realistic GEANT simulation, demonstrates BTeV's ability to study states with γ s and π^0 s. We have shown that even with a complicated underlying event and accompanying minimum bias events, we can successfully reconstruct the very low energy photons from these decays and can suppress the combinatoric background.

16.3.7 Implications for Measurement of α

Since the CP asymmetry in this class of decays is expected to be only of order 2%, a measurement requires many tens of thousands of tagged events. The final state $D^{*-}\pi^+$ does not have an additional π^0 and so will have a higher reconstruction efficiency than $D^{*-}\rho^+$. Because it is a vector-pseudoscalar decay rather than a vector-vector decay, there are fewer decay helicity amplitudes to deal with. The $D^{*-}\pi^+$ branching fraction is 0.00276 ± 0.00021 [5], which is only 40% of the $D^{*-}\rho^+$'s, but the reconstruction efficiency is 4-6 times more (depending on the cuts) so there will be more events. We expect 7-10,000 tagged $D^{*-}\rho^+$ and 15,000-25,000 $D^{*-}\pi^+$ per year, using just the $K\pi$ decay mode of the D^0 . We expect that the use of the $K3\pi$ decay mode of the D^0 will contribute an equal number for both decays. Finally, it should be possible to use the $K^+\pi^-\pi^0$ decay mode of the D^0 for the $D^{*-}\pi^+$ decay. It should be possible to reconstruct 50,000 tagged decays per year. A measurement of α by this technique may be feasible over a period of a few years.

16.4 Measurement of γ

Several suggestions on how to measure the CKM angle γ have been summarized in Chapter 1. While discrete ambiguities are inherent in each of these methods, using several methods will help remove some of these ambiguities as well help control systematic errors. We report here our simulations of three methods.

16.4.1 CP Violation in $B_s \rightarrow D_s K^-$

16.4.1.1 Introduction

When a final state f can come from both a pure B^0 and a pure \bar{B}^0 , the amplitudes for the direct decay $B^0 \rightarrow f$ and the mixing induced sequence $B \rightarrow \bar{B}^0 \rightarrow f$ can interfere. A time dependent CP-violating effect can thus appear. Consider the following decay widths [8]:

$$\Gamma(B \rightarrow f) = \frac{|M|^2}{2} e^{-t} \{ (1 + \rho^2) \cosh(yt) + (1 - \rho^2) \cos(xt) \\ + 2\rho \cos(\delta + \phi) \sinh(yt) - 2\rho \sin(\delta + \phi) \sin(xt) \}$$

$$\Gamma[\bar{B} \rightarrow \bar{f}] = \frac{|M|^2}{2} e^{-t} \{ (1 + \rho^2) \cosh(yt) + (1 - \rho^2) \cos(xt) \\ + 2\rho \cos(\delta - \phi) \sinh(yt) - 2\rho \sin(\delta - \phi) \sin(xt) \}$$

$$\Gamma[B \rightarrow \bar{f}] = \frac{|M|^2}{2} e^{-t} \{ (1 + \rho^2) \cosh(yt) - (1 - \rho^2) \cos(xt) \\ + 2\rho \cos(\delta - \phi) \sinh(yt) + 2\rho \sin(\delta - \phi) \sin(xt) \}$$

$$\Gamma[\bar{B} \rightarrow f] = \frac{|M|^2}{2} e^{-t} \{ (1 + \rho^2) \cosh(yt) - (1 - \rho^2) \cos(xt) \\ + 2\rho \cos(\delta + \phi) \sinh(yt) + 2\rho \sin(\delta + \phi) \sin(xt) \}$$

where:

$$M = \langle f | B \rangle$$

$$M' = \langle f | \bar{B} \rangle$$

$$\rho = |M'|/|M|$$

$$x = \Delta m / \Gamma$$

$$y = \Delta \Gamma / 2\Gamma$$

$\delta = \text{strong phase}$

$\phi = \text{CKM phase}$

An example of this type of decay is B_s which can decay into both $D_s^+ K^-$ and $D_s^- K^+$. The branching fractions are expected to both be $\sim 10^{-4}$ and in this case the weak angle $\phi = \gamma$. If $\Delta\Gamma = 0$ then the quantities ρ , $\sin(\gamma + \delta)$ and $\sin(\gamma - \delta)$ can be extracted from a time dependent study and $\sin\gamma$ can be extracted up to a 2-fold ambiguity. If $\Delta\Gamma$ is significantly different from zero then both $\sin(\gamma + \delta)$ and $\cos(\gamma + \delta)$ are determined from the fit and γ can be determined without ambiguities. It is assumed that the value of x_s will have been determined in a separate measurement, and $\Delta\Gamma$ can probably be determined more accurately from other measurements.

16.4.1.2 Reconstruction Efficiency

A study of the reconstruction efficiency has been done for the decay modes

$$B_s \rightarrow D_s K, D_s \rightarrow \phi\pi, \phi \rightarrow K^+ K^- \text{ and } B_s \rightarrow D_s K, D_s \rightarrow K^* K, K^* \rightarrow K^+ \pi^-$$

The events were generated by Pythia and the detector modeled using BTeVGeant. Each event consists of a $b\bar{b}$ interaction and a mean of 2 minimum bias interactions, to simulate a luminosity of $2 \times 10^{32} \text{ cm}^{-2}\text{s}^{-1}$. Loose cuts were applied initially and the tighter cuts were chosen after the background was studied.

For the $D_s \rightarrow \phi\pi$ decay mode the following cuts were used:

- At least one of the kaons from the ϕ decay and also the K from the B_s decay were required to be identified in the RICH.
- All tracks have at least 3 hits in the silicon pixel detector.
- The impact parameter with respect to the primary vertex was $> 3\sigma$ for all 4 charged tracks.
- To reduce the background due to “detached” tracks that really come from other interactions we require that the impact parameter with respect to the primary vertex be less than 0.2 cm for all tracks.
- The ϕ and D_s were required to be within $\pm 2.5\sigma$ of the nominal mass.
- The distance between the primary vertex and D_s decay vertex $L < 8.0 \text{ cm}$ and $L/\sigma_L(D_s) > 10.0$.
- $L/\sigma_L(B_s) > 4.0$.
- The transverse momentum of the B_s with respect to its line of flight from the primary vertex was required to be less than 1.0 GeV/c.

Table 16.6: Projected Number of Reconstructed $B_s^0 \rightarrow D_s K$ per year

Luminosity	$2 \times 10^{32} \text{ cm}^{-2} \text{ s}^{-1}$	
Running time	10^7 sec	
Integrated Luminosity	2 fb^{-1}	
$\sigma_{b\bar{b}}$	$100 \mu\text{b}$	
Number of $b\bar{b}$ events	2×10^{11}	
Number of $B_s^0 + \bar{B}_s^0$	5×10^{10}	
$\mathcal{B}(B_s^0 \rightarrow D_s^- K^+)$	2×10^{-4}	
$\mathcal{B}(B_s^0 \rightarrow D_s^+ K^-)$	1×10^{-4}	
$\mathcal{B}(D_s \rightarrow \phi \pi^+) \times \mathcal{B}(\phi \rightarrow K^+ K^-)$	1.8×10^{-2}	
$\mathcal{B}(D_s \rightarrow \bar{K}^{*0} K) \times \mathcal{B}(\bar{K}^{*0} \rightarrow K^- \pi^+)$	2.2×10^{-2}	
Reconstruction efficiency	0.045	0.023
Trigger efficiency L1	0.74	0.74
Trigger efficiency L2	0.90	0.90
Number of reconstructed $B_s^0(\bar{B}_s^0) \rightarrow D_s K$	8000	5100
Tagging efficiency ϵ	0.70	
Number of tagged events	5600	3570

- The impact parameter with respect to the primary vertex was required to be less than 3σ for the reconstructed B .

The distributions of L/σ_L and the mass peaks for the D_s and B_s are shown in Fig 16.20.

The combined geometric acceptance and reconstruction efficiency was found to be 4.5%. If we require both kaons from the ϕ decay to be identified in the RICH, the efficiency drops to 2.5%. Of the events that passed these analysis cuts, 74% passed the secondary vertex trigger. For the $D_s \rightarrow K^* K$ mode we used the same cuts except that both kaons from the D_s decay were required to be identified in the RICH. The combined reconstruction efficiency and geometric acceptance for the $D_s \rightarrow K^* K$ mode was found to be 2.3%, and the trigger efficiency for the events passing the analysis cuts was 74%.

The results of the tagging study described in Chapter 15 indicate that we can expect a tagging efficiency $\epsilon = 0.70$ and a dilution $D = 0.37$ giving an effective tagging efficiency $\epsilon D^2 = 0.01$.

The expected number of events in 10^7 seconds is shown in Table 16.6.

As the CP asymmetry is diluted by a factor of $e^{-\sigma_t^2 x_s^2/2}$ it is important to have good time resolution. Fig 16.21 is a plot of the generated proper time minus the reconstructed proper time for events passing the cuts described above. A Gaussian fit to the $t_{gen} - t_{rec}$ distribution gives $\sigma_t = 0.043 \text{ psec}$. Given that $\tau_{B_s} = 1.54 \text{ psec}$, then $\sigma_t/t = 0.03$.

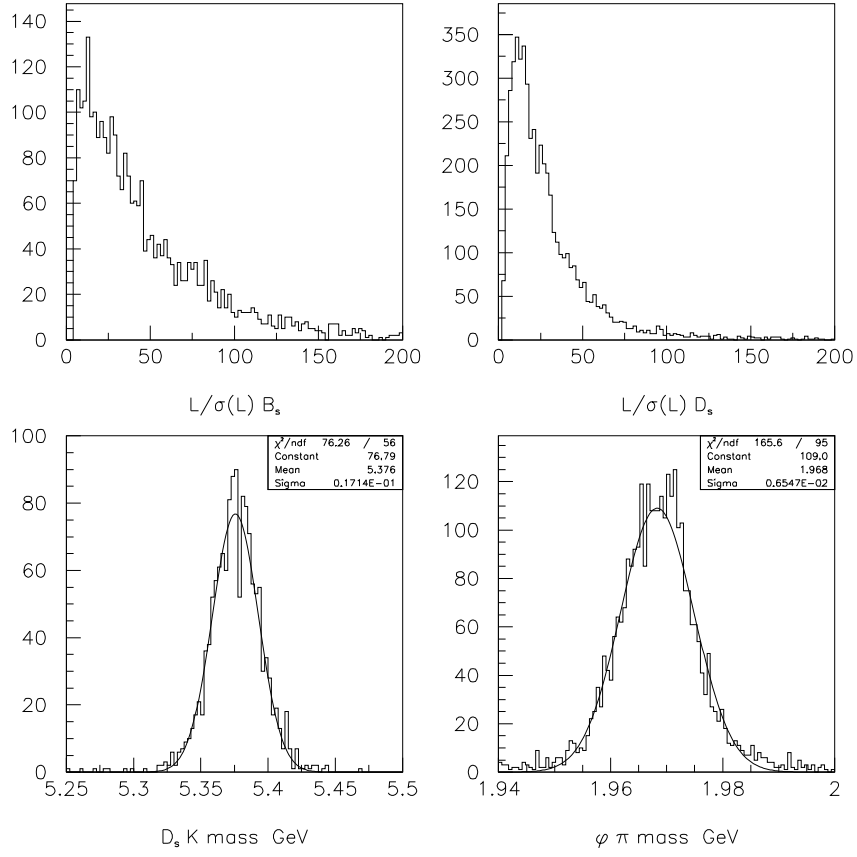


Figure 16.20: L/σ_L and mass peaks for B_s and D_s .

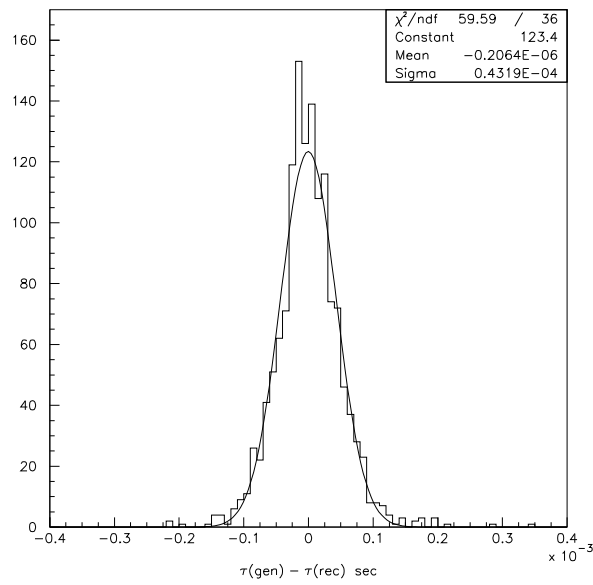


Figure 16.21: Proper time resolution for B_s : $t_{gen} - t_{rec}$ (nsec).

16.4.1.3 Background Studies

Background can arise from real physics channels such as $B_s \rightarrow D_s \pi$ and $B_s \rightarrow D_s^* \pi$ where the π is misidentified as a kaon or from random combinations of a real D_s with a K from the other B or a primary interaction.

Combinatoric Background The combinatoric background was studied in two steps. First, generic $b\bar{b}$ events were generated in order to study the signal to background of $D_s \rightarrow \phi \pi$. Preliminary results indicate we can achieve $S/B \sim 1$ and we estimate that most of the combinatoric background will come from real D_s .

Second, “ B ” $\rightarrow D_s X$, $D_s \rightarrow \phi \pi$ events were generated to determine the background from real D_s ’s combining with other tracks in the event. The D_s can be from directly produced charm or from B decays. Although the charm production cross-section is expected to be about a factor of 10 higher than the $b\bar{b}$ production cross-section, the trigger efficiency for charm events is much lower.

The background events were reconstructed as described above for the signal except that all pion tracks were used as kaon candidates to simulate misidentification in the RICH, then a pion misidentification rate was imposed later.

For 900K “ B ” $\rightarrow D_s X$, $D_s \rightarrow \phi \pi$ events, 10 events remained in the mass window $5.0 - 6.0 \text{ GeV}/c^2$ after all the cuts above were applied. In all these events the kaon candidate was really a pion. We then use a pion misidentification rate of 2% and estimate that the combinatoric background is about 1% of the signal.

Background from $B_s \rightarrow D_s \pi$ Background can also come from decays such as $B_s \rightarrow D_s \pi$, $B_s \rightarrow D_s^* \pi$ where the pion is misidentified as a kaon. Most of the background comes from $B_s \rightarrow D_s \pi$. For decays where there is a missing particle there is very little overlap of the reconstructed mass with the signal region. The signal and scaled background are shown in Fig. 16.22. We expect that this will be the largest source of background and estimate $S/B \sim 7$. These results assume that pions are misidentified as kaons at a rate of 2%. We have used the stand-alone simulation of the RICH detector described in Chapter 6 to study the efficiency of the signal vs. efficiency of the background from misidentified pions. The results are shown in Table 16.7.

16.4.1.4 Extracting ρ and $\sin \phi$ using Maximum Likelihood fits

A mini Monte Carlo study was performed to determine the expected error on γ .

For the first study, the input values of the parameters were chosen to be $x_s = 30.0$, $\rho = 0.7$, $\sin(\gamma) = 0.75$, $\delta = 10 \text{ deg}$ and $\Delta\Gamma = 0.16$.

A set of “events” (*i.e.* proper times) was generated, split into the 4 decay modes with correct time distributions. The proper times were then smeared with a Gaussian of width $\sigma_t = 0.03\tau$, and a cutoff at low t which simulated an L/σ_L cut: $t_{min} = 0.25\tau$. A fraction of the events were assigned to come from the “wrong flavor” parent. A mistag fraction of

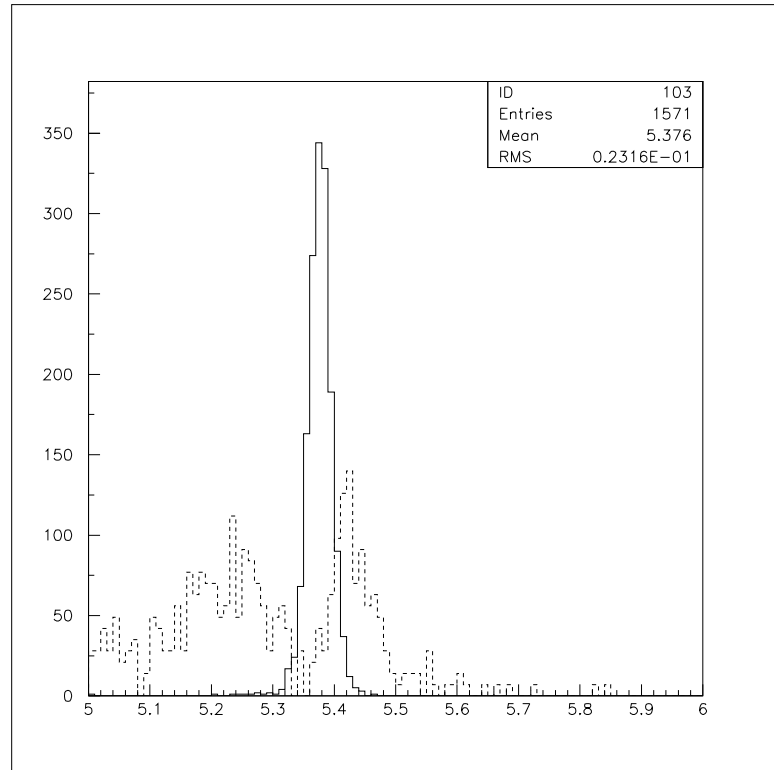


Figure 16.22: Comparison of $B_s \rightarrow D_s K$ signal and background from $B_s \rightarrow D_s X$, where X contains at least one pion misidentified as a K .

Table 16.7: RICH efficiency.

$B_s \rightarrow D_s K$	$B_s \rightarrow D_s \pi$
0.62	0.00000
0.66	0.00184
0.73	0.00551
0.75	0.00735
0.76	0.00919
0.78	0.01287
0.79	0.01471
0.80	0.01654
0.81	0.01838
0.82	0.04596
0.84	0.07700
0.85	0.12132
0.86	0.17647

32% is used. Background events with a pure exponential time distribution are added to the “signal” events. The background is assumed to have the same lifetime as the signal.

A maximum likelihood fit was used to find the values of ρ , γ , δ and $\Delta\Gamma$. One thousand trials were done, each of 6,800 events. The fitted values of the parameters are shown in Fig 16.23 .

The values of the input parameters were varied to study the impact on the error. The results of the fits are shown in Table 16.8.

16.4.1.5 Conclusions

The ability of BTeV to measure the angle γ of the unitarity triangle depends on several factors which are not well known at the moment, in particular the branching fractions for $B_s \rightarrow D_s K$ and the B_s mixing parameter x_s .

Using the estimates of branching fractions given by Aleksan *et al.* [9], we expect to have about 9200 reconstructed, tagged events per year at a luminosity of $2 \times 10^{32} \text{ cm}^{-2}\text{s}^{-1}$. The study of the sensitivity to γ presented above was done assuming 6800 tagged events and gave error on γ of about 7° . We expect that this will improve with the increased number of events.

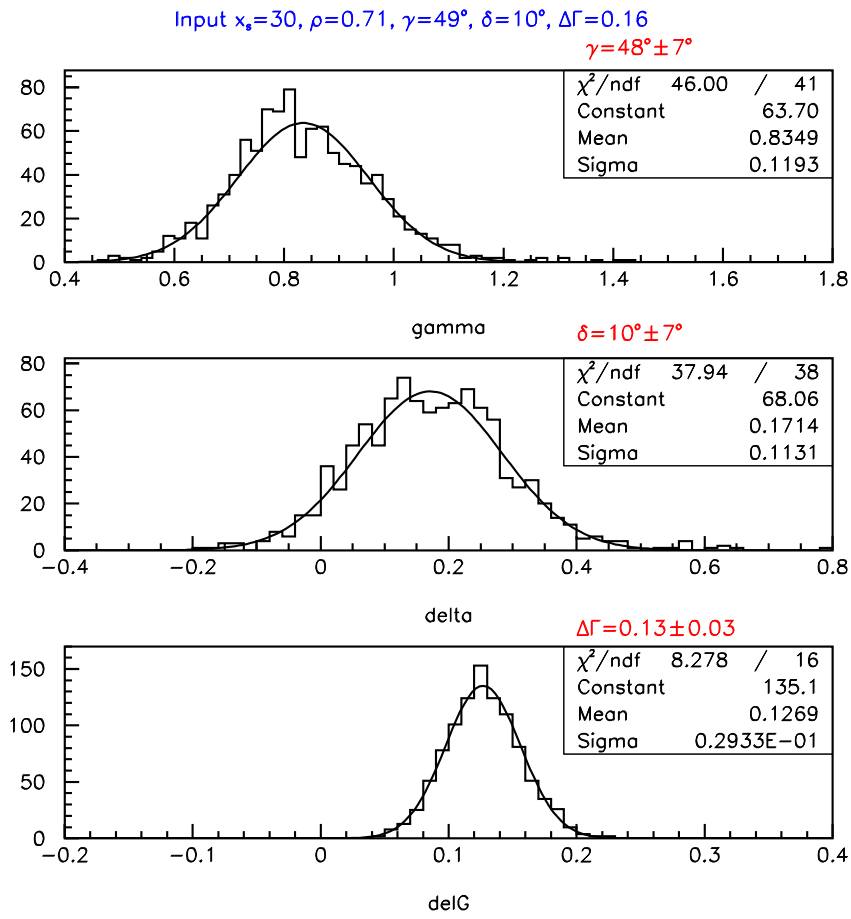


Figure 16.23: Fitted values of γ , δ , and $\Delta\Gamma$

Table 16.8: Results of fits with variation of input parameters.

x_s	ρ	δ	γ	$\Delta\Gamma$	$\sigma(\gamma)$	$\sigma(\Delta\Gamma)$
20	0.71	10°	49°	0.16	6°	0.03
30	0.71	10°	49°	0.16	7°	0.03
40	0.71	10°	49°	0.16	8°	0.03
30	0.50	10°	49°	0.16	8°	0.03
30	0.71	10°	30°	0.16	6°	0.03
30	0.71	10°	90°	0.16	15°	0.04
30	0.71	0°	49°	0.16	6°	0.03
30	0.71	20°	49°	0.16	6°	0.03
30	0.71	10°	49°	0.06	8°	0.04
30	0.71	10°	49°	0.26	6°	0.03

16.4.2 CP Violation in $B^\pm \rightarrow D^0 K^\pm$

16.4.2.1 Introduction

In the Standard Model, $b \rightarrow c\bar{u}s$ and $b \rightarrow \bar{c}us$ transitions have a relative CKM phase γ . In order to measure CP violation we must find a way for seemingly distinct final states to interfere. The Gronau-London-Wyler (GLW) method [10] extracts γ by measuring the B^\pm decay rates to D^0/\bar{D}^0 mesons. If the D^0 and \bar{D}^0 decay to a CP eigenstate then the two decays $B^- \rightarrow K^- D^0$ and $B^- \rightarrow K^- \bar{D}^0$ lead to a common final state and can give rise to CP violating effects. However, the two interfering amplitudes are very different in magnitude and thus the interference effects are limited to $O(10\%)$. Another problem is that it is necessary to measure separately the branching ratios $\mathcal{B}(B^- \rightarrow K^- D^0)$ and $\mathcal{B}(B^- \rightarrow K^- \bar{D}^0)$. While the former can be measured in a straightforward way, the latter is very difficult to measure.

Recently Atwood, Dunietz and Soni [11] have pointed out that CP violation can be greatly enhanced for decays to final states that are common to both D^0 and \bar{D}^0 that are not CP eigenstates. In particular, large asymmetries are possible for final states f such that $D^0 \rightarrow f$ is doubly Cabibbo suppressed and $\bar{D}^0 \rightarrow f$ is Cabibbo allowed.

16.4.2.2 Description of method

The Atwood, Dunietz and Soni method requires the determination of branching ratios for at least two distinct final states $f1$ and $f2$.

Define the following quantities:

$$a = \mathcal{B}(B^- \rightarrow K^- D^0) \quad (16.6)$$

$$b = \mathcal{B}(B^- \rightarrow K^- \bar{D}^0) \quad (16.7)$$

$$c(f1) = \mathcal{B}(D^0 \rightarrow f1), \quad c(f2) = \mathcal{B}(D^0 \rightarrow f2) \quad (16.8)$$

$$c(\bar{f}1) = \mathcal{B}(D^0 \rightarrow \bar{f}1), \quad c(\bar{f}2) = \mathcal{B}(D^0 \rightarrow \bar{f}2) \quad (16.9)$$

$$d(f1) = \mathcal{B}(B^- \rightarrow K^- f1), \quad d(f2) = \mathcal{B}(B^- \rightarrow K^- f2) \quad (16.10)$$

$$\bar{d}(f1) = \mathcal{B}(B^+ \rightarrow K^+ f1), \quad \bar{d}(f2) = \mathcal{B}(B^+ \rightarrow K^+ f2) \quad (16.11)$$

Assume that we can measure the quantities a , $c(f1)$, $c(f2)$, $c(\bar{f}1)$, $c(\bar{f}2)$, $d(f1)$, $d(f2)$, $\bar{d}(f1)$ and $\bar{d}(f2)$ but not b .

We can express $d(f1)$ in terms of a , b , $c(f1)$, $c(\bar{f}1)$, the strong phase ξ_1 and the weak phase γ .

$$d(f1) = a * c(f1) + b * c(\overline{f1}) + 2\sqrt{a * b * c(f1) * c(\overline{f1})} \cos(\xi_1 + \gamma) \quad (16.12)$$

$$\overline{d}(f1) = a * c(f1) + b * c(\overline{f1}) + 2\sqrt{a * b * c(f1) * c(\overline{f1})} \cos(\xi_1 - \gamma) \quad (16.13)$$

$$d(f2) = a * c(f2) + b * c(\overline{f2}) + 2\sqrt{a * b * c(f2) * c(\overline{f2})} \cos(\xi_2 + \gamma) \quad (16.14)$$

$$\overline{d}(f2) = a * c(f2) + b * c(\overline{f2}) + 2\sqrt{a * b * c(f2) * c(\overline{f2})} \cos(\xi_2 - \gamma) \quad (16.15)$$

These four equations contain the 4 unknowns ξ_1, ξ_2, b, γ which can be determined up to discrete ambiguities. Adding additional decay modes will reduce the ambiguities. The strong phases ξ_i are related to the D decay phase shifts δ_i by the relation:

$$\xi_1 - \xi_2 = \delta_1 - \delta_2 \quad (16.16)$$

If the D decay phase shifts can be determined elsewhere then we have an extra constraint on equations. This method measures direct CP violation and does not require tagging or time-dependent measurements.

If we add a third decay mode we have 6 equations in 5 unknowns which will help to resolve ambiguities.

16.4.2.3 Acceptance and Reconstruction Efficiency

The reconstruction efficiency of the proposed BTeV detector for $B^- \rightarrow K^- D^0$ has been studied for two decay modes of the D^0 : $D^0 \rightarrow K^+ \pi^-$ and $D^0 \rightarrow K^- K^+$. Note that the second decay mode is a CP eigenstate. In this case even though the branching fraction for $B^- \rightarrow K^- \overline{D^0}, \overline{D^0} \rightarrow K^+ K^-$ is expected to be only 1% of $B^- \rightarrow K^- D^0, D^0 \rightarrow K^+ K^-$ we could still get up to 20% CP asymmetry. The events are generated with Pythia and the detector is modeled with MCFast.

The final analysis cuts are selected to give a clean D^0 signal and reduce background from random combinations with kaons. The cuts are shown in Table 16.9. All tracks are required to be within the geometric acceptance of the RICH and have a momentum between 3 and 70 GeV/c. The reconstructed signal is shown in Fig 16.24. The fitted Gaussian has a width of 17 MeV.

The combined geometric acceptance and reconstruction efficiency of the B is 2.6% for the $D^0 \rightarrow K\pi$ mode and 2.4% for the $D^0 \rightarrow KK$ mode.

The requirement that all tracks be identified in the RICH was studied separately and found to be 70% efficient. The trigger efficiency for events that pass the final analysis cuts is 70% for both modes.

The expected number of events is shown in Table 16.10.

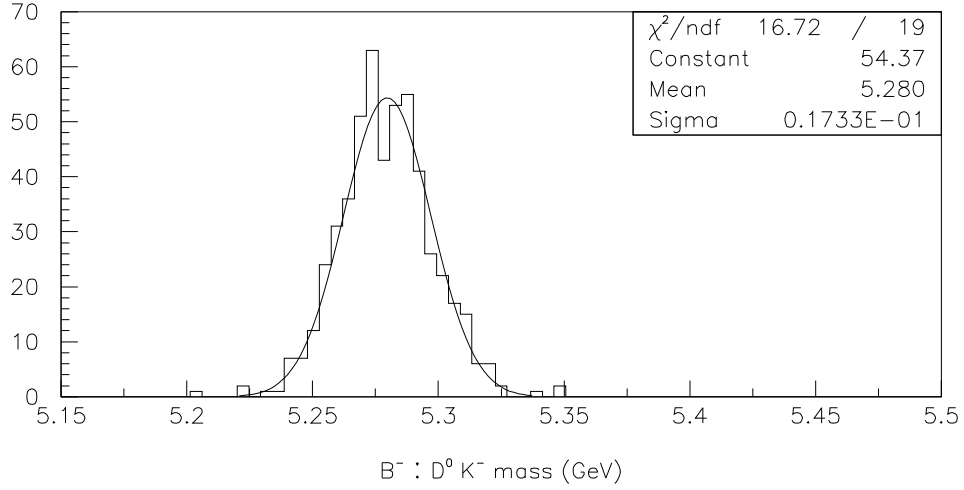


Figure 16.24: Invariant mass of $B^- \rightarrow \overline{D}^0 K^-$.

16.4.2.4 Background Studies

Generic $b\bar{b}$ and $c\bar{c}$ events were studied and it was found that for both types of events the $D^0 \rightarrow K^- \pi^+$ and $D^0 \rightarrow K^- K^+$ signals had $S/B > 5$ using the same cuts as for the D^0 in the $B^- \rightarrow K^- D^0$ decays. Therefore only background arising from real D^0 s need be considered.

Charm events with a $D^0 \rightarrow K^- \pi^+$ have a probability of 3.3% of passing the D^0 analysis cuts. The events which pass the cuts have a trigger efficiency of 10% and 0.6% of these events have another detached K . Generic $b\bar{b}$ events with a D^0 have a 7.0% probability of passing the D^0 analysis cuts. These events have a trigger efficiency of 35% and 4.0% of these have another detached K . Therefore we estimate that a generic $b\bar{b}$ event is 50 times more likely to contribute to background than a $c\bar{c}$ event. Thus even though the charm production cross-section is much larger than the $b\bar{b}$ cross-section, most of the background will come from $b\bar{b}$ events.

Table 16.9: Cuts for $D^0 \rightarrow K\pi$ and $D^0 \rightarrow K^+ K^-$

$L/\sigma_L(B^-)$	> 10
$L/\sigma_L(D^0)$	> 4
DCA to primary vertex (all tracks)	$> 3\sigma$
χ^2 (B vertex)	< 5
χ^2 (D vertex)	< 10
B point back to primary vertex	
p_t balance	$< 2 \text{ GeV}/c$
DCA	$< 2\sigma$
D^0 mass window	$1.85 - 1.88 \text{ GeV}/c^2$

Table 16.10: Projected number of reconstructed $B^- \rightarrow K^- D$ per year.

Decay Mode	$K^-(K^+\pi^-)$	$K^-(K^+K^-)$
Luminosity	$2 \times 10^{32} \text{ cm}^{-2}\text{s}^{-1}$	
Running time	10^7 sec	
Integrated Luminosity	2 fb^{-1}	
$\sigma_{b\bar{b}}$	$100 \mu\text{b}$	
Number of B^\pm	1.5×10^{11}	
Branching ratio	1.7×10^{-7}	1.1×10^{-6}
Reconstruction efficiency	0.026	0.024
RICH efficiency	0.70	0.70
Trigger efficiency L1	0.70	0.70
Trigger efficiency L1	0.90	0.90
Number of reconstructed B^\pm	300	1800

Background in both modes, $B^- \rightarrow K^-[K^+\pi^-]$ and $B^- \rightarrow K^-[K^+K^-]$, could arise from:

- $B^- \rightarrow \pi^- D^0$ where the π^- is misidentified as a K^- , and similar decays such as $B^- \rightarrow \pi^- D^{*0}$ and $B^- \rightarrow \rho^- D^0$ where there is a missing π^0 and the π^- is misidentified. These decays all have significantly higher branching fractions than the signal. If we assume that the probability of misidentifying a π^- as a K^- is 2%, the relative signal and background from these modes is shown in Fig 16.25. This is the most significant source of background for the $D^0 \rightarrow K^+K^-$ mode.
- “ B ” $\rightarrow \bar{D}^0 X$ events where the \bar{D}^0 makes a good vertex with a K^- from the other B or from the underlying event. This was studied by generating “ B ” $\rightarrow \bar{D}^0 X, \bar{D}^0 \rightarrow K^+\pi^-$ events and using the same reconstruction as for the signal. 1.6 million “ B ” $\rightarrow \bar{D}^0 X, \bar{D}^0 \rightarrow K^+\pi^-$ events were generated and after cuts as described for the signal, no events remained in the mass window $5.0 - 5.5 \text{ GeV}/c^2$, and 1 event in the $5.5 - 6.0 \text{ GeV}/c^2$ window.

We assume this type of background has the same trigger efficiency as the signal. We estimate we can achieve $S/B \sim 1$ in the $D^0 \rightarrow K^+\pi^-$ mode, and we expect this to be the dominant source of background for this mode. This type of background will be much less significant in the $D^0 \rightarrow K^+K^-$ mode because both the signal and background come from singly Cabibbo suppressed decays.

16.4.2.5 Extracting γ from decay rates

In order to estimate our ability to measure γ , several sets of input parameters (b, γ, ξ_1, ξ_2) were chosen and for each set the expected number of events in each channel was calculated. Then, 1000 trials were done for each set, smearing the number of events by $\sqrt{N+B}$. For

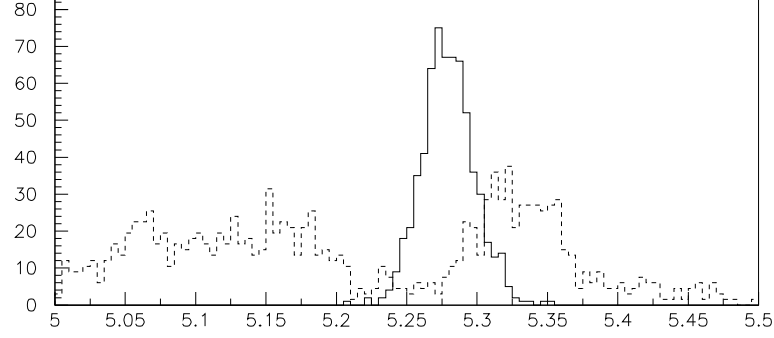


Figure 16.25: Signal (solid line) and background (dashed line) from $B^- \rightarrow \pi^- D^0$ and $B^- \rightarrow \pi^- D^0 X$ where the π^- is misidentified as a K^- .

each trial, values for b and γ are calculated. The fitted values of b and γ are shown in Table 16.11 and Fig. 16.26.

	Test 1	Test 2	Test 3	Test 4
$\mathcal{B}(\times 10^{-6})$	2.2	2.2	2.2	2.2
ξ_1	45°	0°	90°	70°
ξ_2	30°	45°	10°	30°
γ	65°	75°	85°	50°
γ fit	$(67 \pm 10)^\circ$	$(75 \pm 7)^\circ$	$(85.0 \pm 2.4)^\circ$	$(50.0 \pm 3.2)^\circ$

Table 16.11: Input values of parameters and results of fit for γ .

16.4.2.6 Conclusions

We expect to reconstruct about 300 $B^\pm \rightarrow (K\pi)K^\pm$ and 2,000 $B^\pm \rightarrow (KK)K^\pm$ per year at the design luminosity of $2 \times 10^{32} \text{ cm}^{-2}\text{s}^{-1}$. With this number of events, γ can be measured to $\pm 10^\circ$ for most values of γ , ξ_1 and ξ_2 . The error on γ depends on the value of γ and the strong phases, in particular the error decreases with increasing difference in the strong phases. If we assume that the ratio of Cabibbo favored to doubly Cabibbo suppressed branching fractions is the same for the two decay modes then the equations have no solution when $|\xi_1| = |\xi_2|$.

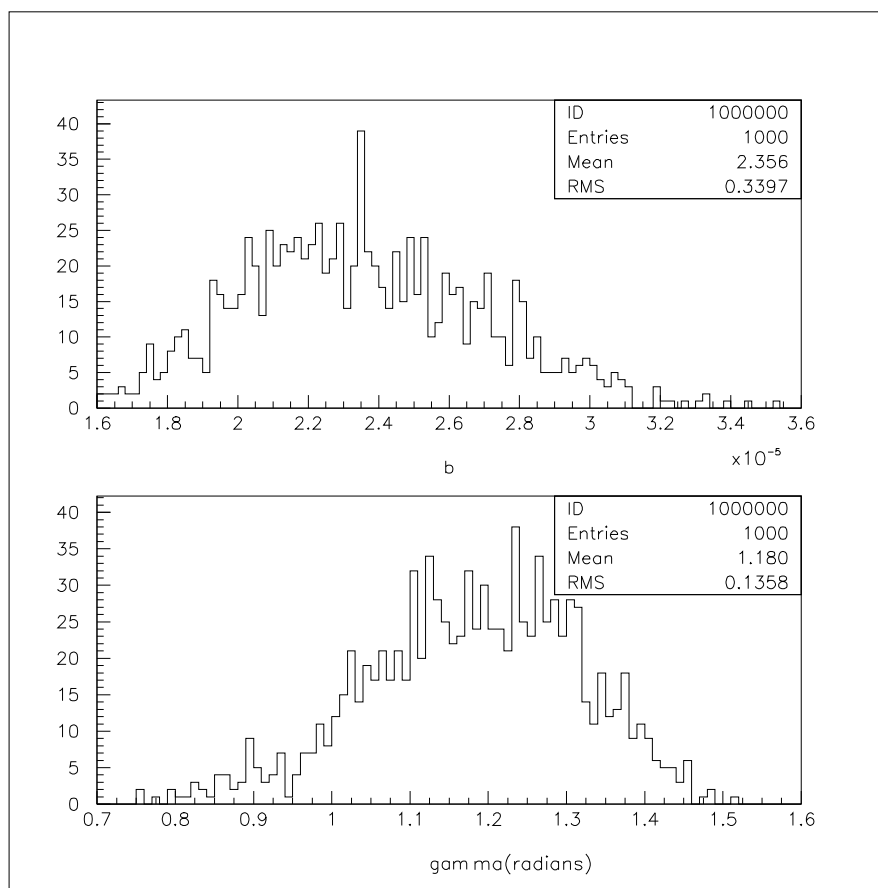


Figure 16.26: Calculated values of γ and b for input values $\gamma = 65^\circ (1.13 \text{ rad})$, $b = 2.2 \times 10^{-6}$.

16.4.3 CP Violation in $B \rightarrow K\pi$

This method uses the branching ratios of the decays $B^+ \rightarrow \pi^+ K^0$ and $B^0 \rightarrow \pi^- K^+$ and their complex conjugates as explained in a paper by Gronau and Rosner [12]. The decay $B^+ \rightarrow \pi^+ K^0$ proceeds only through a penguin amplitude and the decay $B^0 \rightarrow \pi^- K^+$ proceeds through both penguin and tree amplitudes. Ignoring electroweak penguin contributions, the penguin amplitudes in the charged and neutral B decays to $K\pi$ are equal.

It is useful to define

$$R \equiv \frac{\Gamma(B^0 \rightarrow K^+ \pi^-) + \Gamma(\bar{B}^0 \rightarrow K^- \pi^+)}{\Gamma(B^+ \rightarrow K^0 \pi^+) + \Gamma(B^- \rightarrow \bar{K}^0 \pi^-)}$$

$$A' \equiv \frac{\Gamma(B^0 \rightarrow K^+ \pi^-) - \Gamma(\bar{B}^0 \rightarrow K^- \pi^+)}{\Gamma(B^+ \rightarrow K^0 \pi^+) + \Gamma(B^- \rightarrow \bar{K}^0 \pi^-)}.$$

An expression for γ can be given in terms of R , A' and the ratio of tree to penguin amplitudes $r \equiv |T|/|P|$.

If we define δ to be the phase difference between the penguin and tree amplitudes, the ratios R and A' can be rewritten :

$$R = 1 - 2r \cos \gamma \cos \delta + R^2$$

$$A' = 2r \sin \delta \sin \gamma$$

Combining these equations to eliminate δ we get

$$R = 1 + r^2 \pm \sqrt{4r^2 \cos^2 \gamma - A'^2 \cot^2 \gamma}$$

Fleischer and Mannel[13] have claimed that if $R < 1$ a useful bound can be obtained regardless of the value of r or δ :

$$\sin^2 \gamma \leq R$$

If we have information on r we can get a more precise estimate of γ .

CLEO has determined $R = 0.65 \pm 0.40$, which suggests that the ratio could be less than 1.0 [14]. If this result holds with improved statistics then this method compliments other methods in that it will begin to exclude some of the region around $\gamma = \pi/2$. A recent updated result from CLEO gives $R = 0.95 \pm 0.31$ [15].

There has been much discussion about the effect of final state interactions on the measured branching ratios. Falk *et al.* [16] have shown that contributions to $B^+ \rightarrow \pi^+ K^0$ from rescattering of channels such as $B^+ \rightarrow \pi^0 K^+$ lead to a modification of the Fleischer-Mannel bound:

$$\sin^2 \gamma \leq R(1 + 2\epsilon\sqrt{1 - R})$$

where ϵ is the ratio of the rescattered amplitude to the penguin amplitude. They estimate $\epsilon = O(0.1)$. This rescattering contribution can be determined by measuring the K^+K^- final state branching ratio, which BTeV is well equipped to do.

To study the reconstruction efficiency of $B^+ \rightarrow \pi^+ K_s$ Monte Carlo events were generated using Pythia and the detector modeled with MCFast. First, the primary vertex was found, then K_s candidates were selected by combining all pairs of oppositely charged tracks not identified as kaons. These tracks were required to have an impact parameter greater than 5σ with respect to the primary vertex, to form a vertex with $\chi^2 < 5$ and to be within 6 MeV/c² of the nominal K_s mass. The K_s vertex was required to have $\ell/\sigma_\ell > 6$ with respect to the primary vertex. B candidates were selected by combining the K_s candidates with all other charged tracks not identified as kaons and having an impact parameter greater than 3.5σ with respect to the primary vertex. The reconstructed B candidate was required to have $\ell/\sigma_\ell > 4$, and point back to the primary with an impact parameter less than 2.5σ . The combined geometric acceptance and reconstruction efficiency of the $B^+ \rightarrow \pi^+ K_s$ mode is 3.3% and the trigger efficiency (Level 1 plus Level 2) is 24%. The reconstructed signal is shown in Fig. 16.27.

The background has been studied using 500K generic $b\bar{b}$ events with minimum bias events added to give an average of two interactions per beam crossing. Only one event with a mass above 5 GeV/c² survived the cuts as described above. From these limited statistics we estimate we can achieve a signal-to-background ratio of about 1:1.

The decay mode $B^0 \rightarrow \pi^- K^+$ has also been simulated. The two prong vertex can be distinguished from background with an ℓ/σ_ℓ cut and the requirement that the reconstructed B point back to the primary vertex. The reconstruction efficiency is found to be 8.4% and the trigger efficiency (Level 1 plus Level 2) for events which pass the analysis cuts is 57%. The background has been studied using 12×10^6 $b\bar{b}$ events and the signal-to-background ratio was found to be 20:1.

We expect to reconstruct 8,000 $B^\pm \rightarrow \pi^\pm K_s$ and 108,000 $B^0/\bar{B}^0 \rightarrow \pi^{-/+} K^{+/-}$ decays in 10^7 s of running at $\mathcal{L} = 2 \times 10^{32} \text{cm}^{-2} \text{s}^{-1}$. Gronau and Rosner [12] have estimated that a 5° precision in γ can be achieved with 2,400 events in each channel. This of course, doesn't take into account the aforementioned theoretical criticisms of the technique.

2000/05/05 13.45

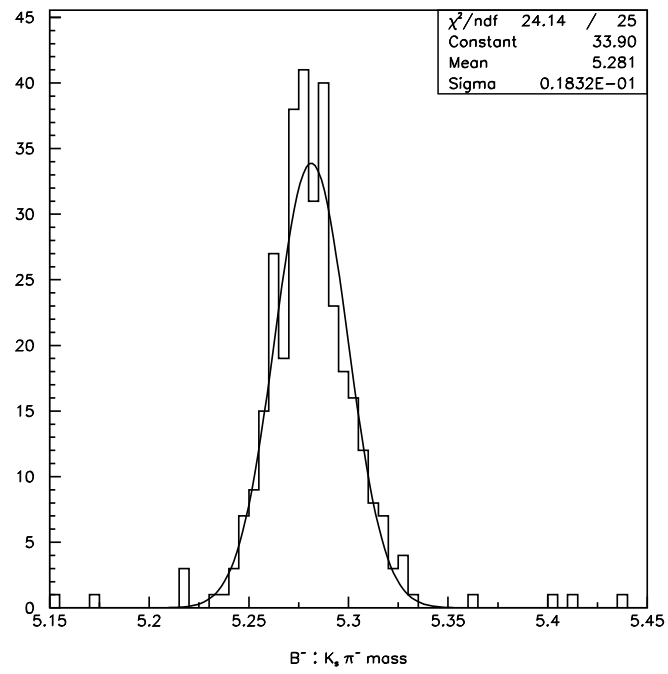


Figure 16.27: $K_s \pi$ mass

16.5 Analysis of $B \rightarrow \rho\pi$

The CKM angle α cannot be extracted from the $B^0 \rightarrow \pi^+\pi^-$ asymmetry in a model independent way because of the large “penguin pollution” problem. However, asymmetries in the decays $B^0 \rightarrow \rho\pi$ can be used to measure this angle (see Chapter 1) [17]. There are three final states in this decay: $B^0 \rightarrow \rho^0\pi^0$, $B^0 \rightarrow \rho^+\pi^-$ and $B^0 \rightarrow \rho^-\pi^+$. CLEO has measured the average branching ratio of the latter two modes to be $2.8_{-0.7}^{+0.8} \pm 0.4 \times 10^{-5}$ and limits the $\rho^0\pi^0$ to $< 5.1 \times 10^{-6}$ at 90% confidence level [18]. BTeV, with its crystal calorimeter, should be able to collect and reconstruct a substantial sample of $B \rightarrow \rho\pi$ events.

The reconstruction efficiencies for $B \rightarrow \rho\pi$ and backgrounds were studied using a full GEANT simulation, for $\rho^\pm\pi^\mp$ and $\rho^0\pi^0$, separately. All signal and background samples were generated with a mean of two interactions per crossing. While signal events are relatively easy to generate, backgrounds are more difficult. For channels with branching ratios on the order of 10^{-5} and efficiencies on the order of 1%, it is necessary to generate at least 10^7 $b\bar{b}$ background events. This is a difficult task that requires large amounts of CPU time and data storage. Since almost 90% of the time spent in generating the events is in the electromagnetic calorimeter, we pass all the generated events through the tracking system and perform a preliminary analysis on the charged tracks *before* generating the calorimeter information. The output of this procedure is as realistic as running all the events through the entire GEANT process but saves a factor of three in computing time.

We look for events containing a secondary vertex formed by two oppositely charged tracks. One of the most important selection requirements for discriminating the signal from the background is that the events have well measured primary and secondary vertices. We demand that both the primary and the secondary have vertex fits with $\chi^2/dof < 2$. We also make a cut on the the distance between the primary and the secondary vertices, divided by the error, $L/\sigma_L > 4$. The two vertices must also be separated from each other in the plane transverse to the beam. We define $r_{transverse}$ in terms of the primary interaction vertex position (x_P, y_P, z_P) and the secondary decay vertex position (x_S, y_S, z_S) as $r_{transverse} = \sqrt{(x_P - x_S)^2 + (y_P - y_S)^2}$ and cut out events where the secondary vertex is close to the reconstructed primary. Furthermore, to insure that the charged tracks do not originate from the primary, we require that both the π^+ and the π^- candidate have an impact parameter with respect to the primary vertex (DCA) $> 100 \mu\text{m}$.

Events passing these selection criteria are passed through the electromagnetic calorimeter simulation which uses GEANT. Our aim is to find good π^0 candidates. We select candidate “bumps” in the calorimeter using the cluster finder code described in Chapter 12.4. Photon candidates are required to have a minimum bump energy of 1 GeV and pass the shower shape cut which requires $E_9/E_{25} > 0.85$. The shower shape cut is used to select electromagnetic showers. We reduce the background rate by insuring that the photon candidates are not too close to the projection of any charged tracks on the calorimeter. For $\rho^\pm\pi^\mp$, the minimum distance requirement is > 2 cm, while for $\rho^0\pi^0$, we require the minimum distance > 5.4 cm. Candidate π^0 's are two-photon combinations with invariant mass between 125 and 145 MeV/ c^2 . More details of π^0 selection are given in the description of the analysis of the

Table 16.12: Selection Criteria

Criteria	$\rho^\pm \pi^\mp$	$\rho^0 \pi^0$
Primary vertex criteria	$\chi^2 < 2$	$\chi^2 < 2$
Secondary vertex criteria	$\chi^2 < 2$	$\chi^2 < 2$
$r_{transverse}$ (cm)	0.0146	0.0132
Normalized distance L/σ	> 4	> 4
Distance L , cm	< 5	< 5
DCA of track, μm	> 100	> 100
t_{proper}/t_0	< 5.5	< 5.5
E_{π^+} , GeV	> 4	> 4
E_{π^-} , GeV	> 4	> 4
$p_t(\pi^+)$, GeV/ c	> 0.4	> 0.4
$p_t(\pi^-)$, GeV/ c	> 0.4	> 0.4
Isolation for γ , cm	> 2.0	> 5.4
E_{π^0} , GeV	> 5	> 9
$p_t(\pi^0)$, GeV/ c	> 0.75	> 0.9
$\Delta p_t/\Sigma p_t$	< 0.06	< 0.066
m_{π^0} , MeV/ c^2	125 – 145	125 – 145
m_ρ , GeV/ c^2	0.55 – 1.1	0.55 – 1.1

channel $B^0 \rightarrow D^{*-} \rho^+$ in Section 16.3.

Kinematic cuts can greatly reduce the background to $B \rightarrow \rho\pi$ while maintaining the signal efficiency. Minimum energy and transverse momentum (p_t) requirements are placed on each of the three pions. Here p_t is defined with respect to the B direction which is defined by the position of the primary and secondary vertices. We demand that the momentum vector of the reconstructed B candidate point back to the primary vertex. The cut is implemented by requiring p_t balance among the π^+ , π^- , and π^0 candidates relative to the B -direction and then divided by the sum of the p_t values for all three particles ($\Delta p_t/\Sigma p_t$). We also make a cut on the B decay time requiring that the B candidate live no more than 5.5 proper lifetimes ($t_{proper}/t_0 < 5.5$). The selection criteria for the two modes are summarized in Table 16.12.

For this study, we generated and analyzed three large samples of events using BTeVGeant: 125,000 $B \rightarrow \rho^0 \pi^0$ events, 125,000 $B \rightarrow \rho^+ \pi^-$ events, and 4,450,000 generic $b\bar{b}$ background events. The results of the analysis after applying the cuts in Table 16.12 are presented in Fig. 16.28 (for $\rho^0 \pi^0$) and Fig 16.29 (for $\rho^+ \pi^-$). The background mass spectra are on the left side of the figures, and the signal events are on the right side.

The mass resolution for the B is $\approx 28 \text{ MeV}/c^2$. The mean π^0 mass value in the $B \rightarrow \rho\pi$ events is $135 \text{ MeV}/c^2$ with a resolution of about $3 \text{ MeV}/c^2$. The relevant yields for $\rho\pi$ are shown in Table 16.13. The reconstruction efficiency is $(0.36 \pm 0.02)\%$ for $\rho^0 \pi^0$ and $(0.44 \pm 0.02)\%$ for $\rho^+ \pi^-$. The background was obtained by considering the mass interval

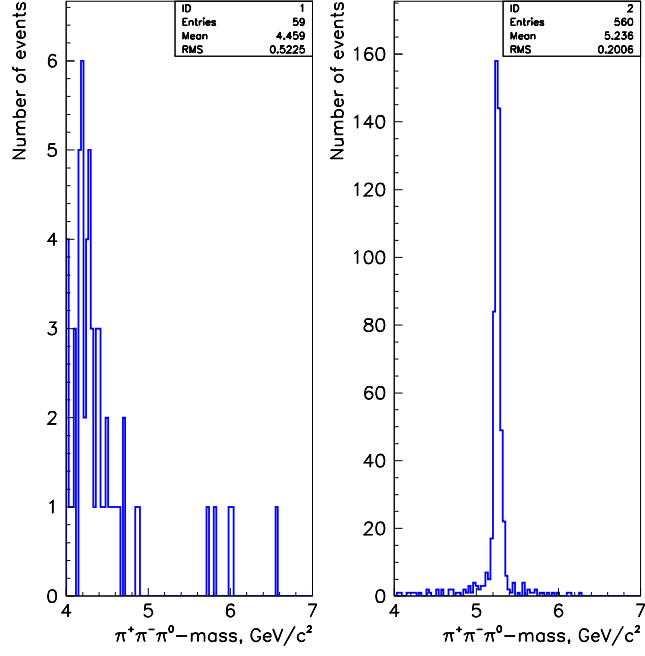


Figure 16.28: Invariant $\pi^+\pi^-\pi^0$ mass distributions for background (left) and signal (right) events for $B \rightarrow \rho^0\pi^0$.

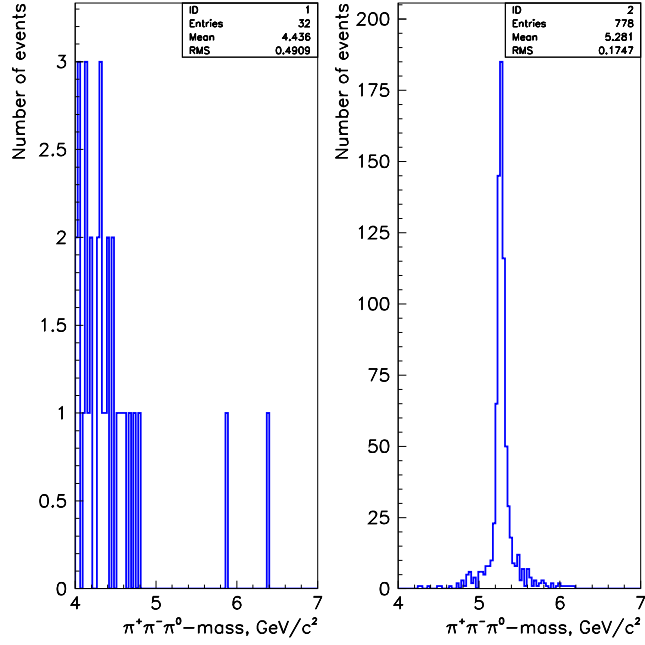


Figure 16.29: Invariant $\pi^+\pi^-\pi^0$ mass distributions for background (left) and signal (right) events for $B \rightarrow \rho^+\pi^-$.

Table 16.13: $B \rightarrow \rho\pi$ Yields

Quantity	$\rho^\pm\pi^\mp$	$\rho^0\pi^0$
Branching ratio	2.8×10^{-5}	0.5×10^{-5}
Efficiency	0.0044	0.0036
Trigger efficiency (Level 1)	0.6	0.6
Trigger efficiency (Level 2)	0.9	0.9
S/B	4.1	0.3
Signal/ 10^7 s	9,400	1,350
ϵD^2	0.10	0.10
Flavor tagged yield	940	135

between 5 and 7 GeV/ c^2 . The signal interval is taken as $\pm 2\sigma$ around the B mass or 112 MeV/ c^2 .

The final numbers of both signal and background events are reduced by including the Level 1 and Level 2 trigger efficiency, but the S/B ratio is not significantly changed. From this study we find that we can expect to reconstruct about 9,400 $\rho^\pm\pi^\mp$ events and 1,350 $\rho^0\pi^0$ events per year.

We can, therefore, expect to collect a sample of ~ 1000 flavor tagged $\rho^\pm\pi^\mp$ events and ~ 150 $\rho^0\pi^0$ per year with signal-to-background levels of approximately 4:1 and 1:3, respectively. A comparison with other experiments is given in Part IV. We have not yet done a full simulation to the sensitivity to α . Final results will depend on several unknown quantities including the branching ratio for $\rho^0\pi^0$ and the ratio of tree to penguin amplitudes. Analysis by Snyder and Quinn [17] showed that with 2,000 background free events they could always find a solution for α and the accuracy was in the range of 5-6°. We can collect these 2,000 events in 2×10^7 seconds, but we will have some background. Quinn and Silva have also proposed using non-flavor tagged rates as input which should improve the accuracy of the α determination [19].

16.6 Measuring χ with $B_s \rightarrow J/\psi \eta (\eta')$

16.6.1 Introduction

The CP violating angle, χ , defined in Chapter 1, can be measured by using B_s decay modes. The all-charged mode $B_s \rightarrow J/\psi \phi$ is one way to measure this, but due to the fact that this is a vector-vector final state of mixed-CP, a complicated angular analysis is required and therefore a very large data sample must be obtained. The channels $B_s \rightarrow J/\psi \eta'$ and $B_s \rightarrow J/\psi \eta$, can be used to determine the angle χ from a simple asymmetry measurement.

We estimate the branching ratios using the quark model [20]. The η and η' wave functions are given in terms of the quark wave functions as:

$$\psi(\eta) = (u\bar{u} + d\bar{d} - s\bar{s})/\sqrt{3} \ , \quad (16.17)$$

$$\psi(\eta') = (u\bar{u} + d\bar{d} + 2s\bar{s})/\sqrt{6} \ . \quad (16.18)$$

Thus the branching ratios are related to the measured decay $B^0 \rightarrow J/\psi K^0$, taking equal lifetimes as

$$\mathcal{B}(B_s \rightarrow J/\psi \eta) = \frac{1}{3} \mathcal{B}(B_s \rightarrow J/\psi K^0) \ , \quad (16.19)$$

$$\mathcal{B}(B_s \rightarrow J/\psi \eta') = \frac{2}{3} \mathcal{B}(B_s \rightarrow J/\psi K^0) \ . \quad (16.20)$$

It should be noted that a large enhancement in one of these rates is possible, as implied by the large branching fraction for $B \rightarrow \eta' K$.

We consider only the decays $\eta \rightarrow \gamma\gamma$, $\eta' \rightarrow \rho^0\gamma$ and $\eta' \rightarrow \pi^+\pi^-\eta$. The J/ψ was found in the $\mu^+\mu^-$ decay mode. All relevant branching ratios are listed in Table 16.14

Decay	Branching Fraction
$\mathcal{B}(B_s \rightarrow J/\psi \eta)$	3.3×10^{-4}
$\mathcal{B}(B_s \rightarrow J/\psi \eta')$	6.7×10^{-4}
$J/\psi \rightarrow \mu^+\mu^-$	0.059
$\eta \rightarrow \gamma\gamma$	0.392
$\eta' \rightarrow \rho\gamma$	0.308
$\eta' \rightarrow \pi^+\pi^-\eta$	0.438

Table 16.14: Relevant branching fractions.

16.6.2 Signal Selection

We now discuss selection requirements for signal events. First of all, the signal channels contain photons. They are selected as isolated neutral bumps in the PbWO₄ calorimeter that are at least 7 cm away from any track intersection and satisfy the following criteria:

E_γ	$>$	0.5 GeV
E9/E25	$>$	0.95
# of cell hit	$>$	4
Second moment mass	$<$	100 MeV/c ²

We now list the criteria for the individual particles.

$$J/\psi \rightarrow \mu^+ \mu^-$$

- Both muons should have hits in the rear end of the RICH and at least one must be identified in the muon system.
- P_T of each muon > 0.2 GeV/c and at least one with $P_T > 1.0$ GeV/c.
- χ^2 of common vertex of both muons < 4 .
- Invariant mass within 100 MeV of the J/ψ mass.

$$\eta \rightarrow \gamma\gamma$$

- Each photon has $E_\gamma > 4$ GeV and $P_T > 0.4$ GeV/c.
- Invariant mass of two-photon combinations must be within 15 MeV/c² of the η mass.

$$\eta' \rightarrow \rho^0 \gamma$$

- Two oppositely charged tracks, each with momenta greater than 1 GeV/c are taken as $\pi^+ \pi^-$ candidates.
- The $\pi^+ \pi^-$ invariant mass must be within 0.55 GeV/c² of the ρ mass.
- The $\pi^+ \pi^-$ must form a common secondary vertex with the $\mu^+ \mu^-$ from the J/ψ with a fit $\chi^2 < 10$.
- Addition of a single photon ($P_T > 0.3$ GeV/c) to these tracks produces an invariant mass within 15 MeV/c² of the η' mass.

$$\eta' \rightarrow \pi^+ \pi^- \eta$$

- The same selection criteria for the η defined above, except that $P_T > 0.2$ GeV/c for each photon is required.
- Two oppositely charged tracks, each with momenta greater than 1 GeV/c are taken as $\pi^+ \pi^-$ candidates.
- The $\pi^+ \pi^-$ must form a common secondary vertex with the $\mu^+ \mu^-$ from the J/ψ with a fit $\chi^2 < 10$.
- The η and the $\pi^+ \pi^-$ have an invariant mass within 15 MeV of the η' mass.

Signal events are also required to satisfy the following general criteria:

- A good primary vertex $\chi^2/N_p < 4$, where N_p is the number of charged tracks in the primary vertex.
- Distance between the primary and secondary vertices (L) $> 50 \mu\text{m}$ for η' and $> 100 \mu\text{m}$ for η .
- $L/\sigma_L > 3$.
- Normalized distance of closest approach with respect to the primary vertex ($\text{DCA}/\sigma_{\text{DCA}}$) of each charged track > 3 .
- No additional track is consistent the B_s vertex with $\chi^2 < 10$ for the η final state, or $\chi^2 < 20$ for the η' final states.
- Opening angle between ' B '-direction and the particle direction $< 10 \text{ mrad}$ and 15 mrad for $J/\psi\eta'$ and $J/\psi\eta$ respectively. Here the ' B '-direction is defined by the vector joining the primary and secondary vertices and the particle direction is defined as the vector sum of the 3-momenta of all measured particles.
- Invariant mass of $J/\psi\eta$ or $J/\psi\eta'$ within $40 \text{ MeV}/c^2$ of the B_s mass ($\sigma_{M_B} = 19 \text{ MeV}/c^2$).

We show in Fig. 16.30 the invariant mass distributions of signal candidates for $\gamma\gamma$, $\rho^0\gamma$ and $\pi^+\pi^-\eta$.

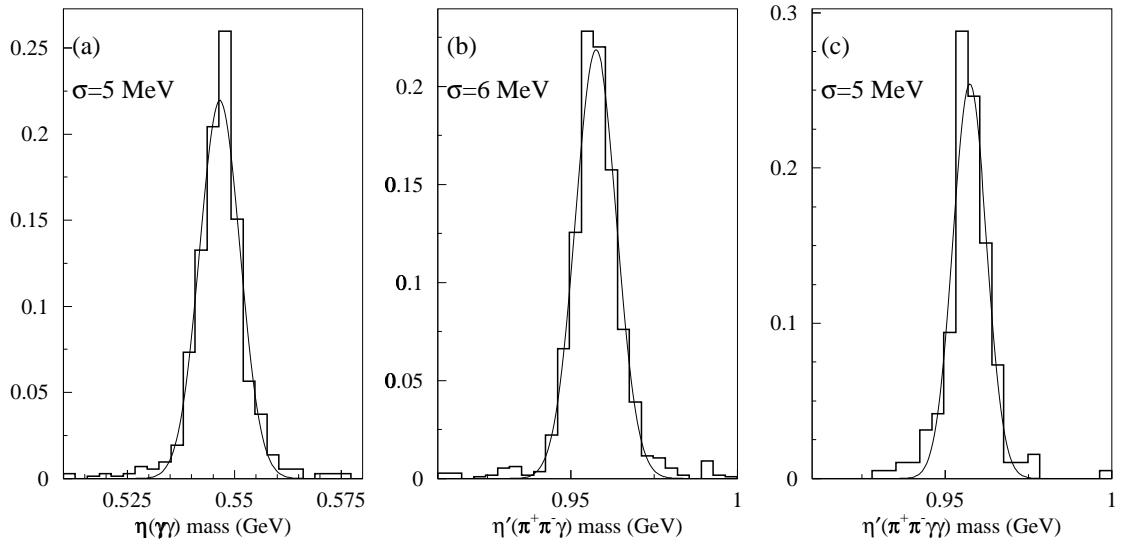


Figure 16.30: The invariant mass distributions for (a) $\eta \rightarrow \gamma\gamma$, (b) $\eta' \rightarrow \pi^+\pi^-\gamma$, and $\eta' \rightarrow \pi^+\pi^-\eta$, $\eta \rightarrow \gamma\gamma$. The Gaussian mass resolutions are indicated.

The $\mu^+\mu^-$ mass distribution from J/ψ decays is shown in Fig. 16.31(a). We can improve the B mass distributions by constraining the dimuons to be at the nominal J/ψ mass. This greatly improves the four-vector of the reconstructed J/ψ . After applying this constrained fit we find the B_s mass distributions shown in Fig. 16.31(b). Note, that we could also constrain the η and η' masses to their nominal values using the same fitting technique. This will be done for future analyses.

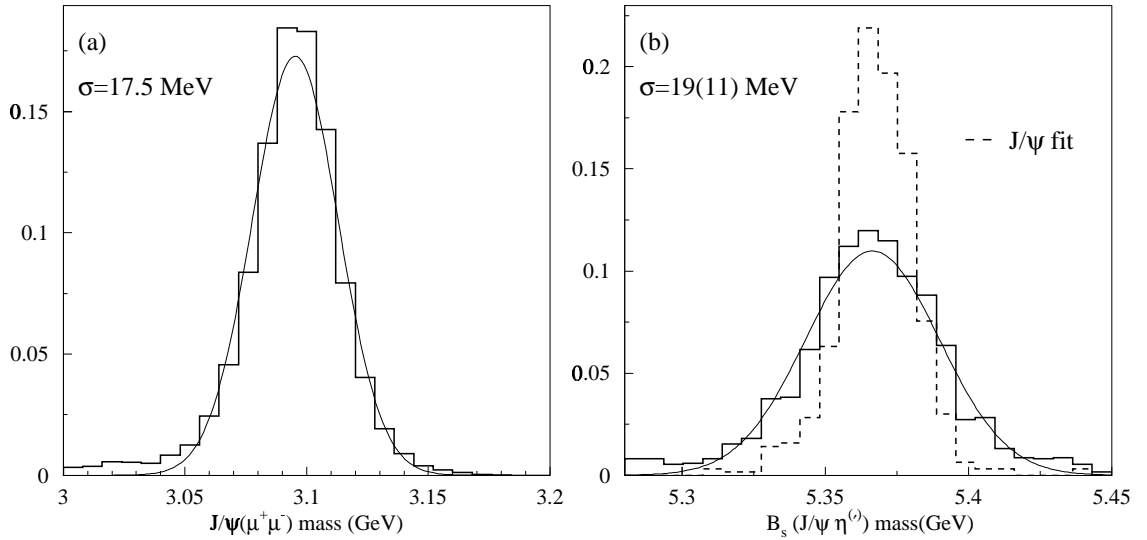


Figure 16.31: (a) The dimuon invariant mass. (b) The reconstructed B_s mass for all three final states of η and η' summed together. The solid curve is the done with without constraining the the $\mu^+\mu^-$ to the J/ψ mass, while the dashed curve is done using the constraint. The B_s mass resolution improves from 19 to 11 MeV/ c^2 .

16.6.3 Background Estimation

The dominant background to these decay modes is from $b(\bar{b}) \rightarrow J/\psi X$. (This is discussed in section 2.2 of this chapter.) To calculate reconstruction efficiencies of signals and estimation of background, Monte Carlo events were generated using Pythia and QQ to decay the heavy particles. Only events with real $J/\psi \rightarrow \mu^+\mu^-$ decays were kept for further analysis. The BTeV detector simulation was done using the GEANT simulation package. We add to the $b\bar{b}$ background events another set of light quark background distributed with a mean Poisson multiplicity of two.

Distributions of several variables for both signal and background are compared in Fig. 16.32.

These results are based on $\sim 4,500$ detector simulated signal events (each channel), which were preselected in generator level using the criteria that all particles of these signals are within geometrical acceptance region of detector. Similarly, 40,000 background events are

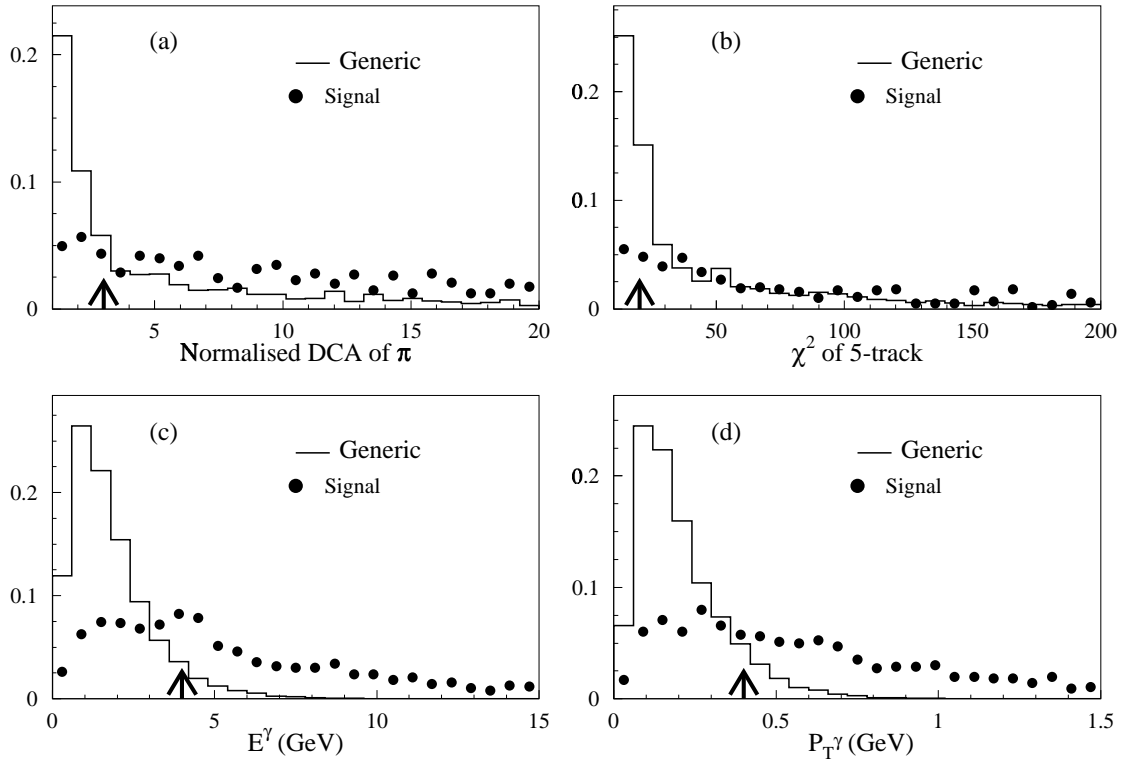


Figure 16.32: Distributions of backgrounds in several variables compared with signal. For $\eta' \rightarrow \rho\gamma$ (a) DCA/σ_{DCA} , (b) χ^2 of adding an additional track to the $J/\psi\pi^+\pi^-$ vertex; for $\eta \rightarrow \gamma\gamma$ (c) energy of the photons and (d) the transverse momentum of the photons with respect to the beam direction. The arrows show the position of the cuts.

also preselected from 5.8 million generic $b\bar{b}$ events. To determine backgrounds we only looked at the dimuon channels, and the $\gamma\gamma$ decay of the η and the $\rho^0\gamma$ decay of the η' .

After all selection criteria, 1 event survived in each of the $J/\psi\eta$ and $J/\psi\eta'$ channels within a wide B_s mass window of 400 MeV/c² (signal mass window is 44 MeV/c²). This leads to a signal-to-background expectation for $J/\psi\eta$ and $J/\psi\eta'$, of 15:1 and 30:1. That the backgrounds are so low is not surprising. We therefore feel confident that we can add the $\eta' \rightarrow \pi^+\pi^-\eta$ modes in without significant background.

16.6.4 Sensitivity to $\sin(2\chi)$

The expected yield of signal events and the resulting asymmetry measurement are given in Table 16.15. The trigger efficiency consists of Level 1 efficiencies from the detached vertex trigger and the dimuon trigger and the Level 2 trigger.

Luminosity	$2 \times 10^{32} \text{ cm}^{-2} \text{ s}^{-1}$		
Running time	10^7 sec		
Integrated Luminosity	2000 pb^{-1}		
$\sigma_{b\bar{b}}$	$100 \text{ } \mu\text{b}$		
Number of $b\bar{b}$ events	2×10^{11}		
Number of B_s events	0.5×10^{11}		
	$B_s \rightarrow J/\psi\eta'$		$B_s \rightarrow J/\psi\eta$
	$\eta' \rightarrow \rho^0\gamma$	$\eta' \rightarrow \pi^+\pi^-\eta$	$\eta \rightarrow \gamma\gamma$
Reconstruction efficiency (%)	1.2	0.60	0.71
S/B	30:1	-	15:1
Level 1 Trigger efficiency (%)	85	85	75
Level 2 Trigger efficiency (%)	90	90	90
Number of reconstructed signal events	5670	1610	1920
Tagging efficiency, ϵD^2	0.1		
Total Number tagged	994		
$\delta(\sin 2\chi)$	0.033		

Table 16.15: Projected yield of $B_s \rightarrow J/\psi\eta'$ ($B_s \rightarrow J/\psi\eta$) and the uncertainty on χ .

The accuracy on $\sin(2\chi)$ is not precise enough to measure the standard model predicted value, which is comparable to the error, in 10^7 seconds of running. Nevertheless, we are optimistic. The low background level makes it possible to loosen the cuts and gain acceptance. We could also add in the $J/\psi \rightarrow e^+e^-$ decay mode. This will not be as efficient as $\mu^+\mu^-$ due to radiation of the electrons, but will be useful. We also believe that ways can be found to improve flavor tagging efficiency, especially for B_s . Furthermore, we will have many years of running, and we can expect some improvement from the use of $B_s \rightarrow J/\psi\phi$.

16.7 Measurement of B_s Mixing Using $B_s \rightarrow D_s^- \pi^+$ and $B_s \rightarrow J/\psi \bar{K}^{*0}$

As discussed in Section 1.2.2, the measurement of B_s mixing allows a determination of $|V_{ts}/V_{td}|$, which corresponds to one side of the B unitarity triangle. While the theoretical discussion was given in terms of the mass splitting between the light and heavy B_s mass eigenstates, Δm_s , the discussion here will be in terms of x_s , where $x_s = \Delta m_s/\Gamma$.

In this section, the x_s reach of BTeV will be demonstrated. This study was carried out in several steps, the first step being a simulation of the BTeV detector response to signal events. The output of this step was treated as real data and passed through a physics analysis program to determine the yield, the time resolution and the signal-to-background ratio in each mode. This information was then passed to a separate program which computed the x_s reach; this program is discussed in Section 16.7.2. A separate background study was performed.

16.7.1 Yields, Resolutions and Signal-to-Background Ratios

The mode for which BTeV has the most sensitivity to x_s is $B_s \rightarrow D_s^- \pi^+$, where the D_s^- decays either by $D_s^- \rightarrow \phi \pi^-$, $\phi \rightarrow K^+ K^-$, or by $D_s^- \rightarrow K^{*0} K^-$, $K^{*0} \rightarrow K^+ \pi^-$. Both of these D_s^- modes have narrow intermediate states and characteristic angular distributions, both of which can be used to improve the signal-to-background ratio.

For this study, Monte Carlo events were generated using Pythia and QQ, as described in Section 12.3, and the detector response was simulated using BTeVGeant. The output of BTeVGeant was analyzed in a fashion similar to that described for $B_s \rightarrow D_s^\pm K^\mp$ in Section 16.4.1. The main difference is that the particle ID cuts were loosened significantly; the bachelor pion was not required to be identified by the RICH and it was required that only one of the two kaons be strongly identified. These changes were made because a state with a larger branching ratio requires less stringent background rejection in order to obtain a reasonable signal-to-background ratio. From this study the efficiency for a B_s candidate to survive all of the analysis cuts was found to be 2.7 % for the $\phi \pi$ mode and 2.3 % for the $K^{*0} K$ mode. For both modes the resolution on the mass of the B was found to be 18 MeV/ c^2 and the mean resolution on the proper decay time was found to be 43 fs.

The BTeV Level 1 trigger simulation, described in chapters 9 and 14, was run on the $B_s \rightarrow D_s^- \pi^+$ events which passed the analysis cuts; the trigger was found to have an efficiency of 74% for both the $\phi \pi^-$ and $K^{*0} K^-$ final states. Section 14.3.3 discusses the performance of the Level 2 trigger and reports an estimated efficiency of 90%.

The flavor tagging power of BTeV was discussed in Chapter 15, in which it was argued that the nominal tagging power is $\epsilon D^2 = 0.1$ which arises from $\epsilon = 0.70$ and $D = 0.37$.

It is believed that the dominant source of backgrounds will be events of the form $X_b \rightarrow D_s^- X$, where X_b may be any b flavored hadron. The background combinations arise when a true D_s^- combination is combined with some other track in the event. An MCFAST based study of 1 million $B \rightarrow D_s^- X$ events was performed using an older version of the de-

tector geometry, the one used for the BTeV Preliminary Technical Design Report (PTDR). Comparisons between BTeVGeant and MCFast, and comparisons between the old and new detector geometries, show that these background studies remain valid. When the 1 million $B \rightarrow D_s^- X$ events were passed through MCFast and analyzed as real data, 8 entries remained in a mass window 6 times larger than the mass window used to select signal B_s candidates. From this it is estimated that the signal-to-background ratio in this channel is 8.4:1. This study was performed without the proper treatment of multiple interactions in one beam crossing. To account for this, the signal-to-background ratio used in the estimate of the x_s reach is 3:1.

The background from direct charm production has not yet been investigated. While direct charm production has a cross-section about 10 times higher than that for production of charm via B decay, it is triggered much less efficiently. Moreover the requirement of two, distinct detached vertices greatly reduces the background from direct charm. In the end it is expected that the background from $B \rightarrow D_s^- X$ will dominate.

Table 16.16 gives a summary of the preceding results and discusses a list of all assumptions which went into the computation of the yield. In one year it is expected that 72,000 events will trigger, survive all analysis cuts and have their birth flavor tagged. This number is substantially higher than that reported in the BTeV Preliminary Technical Design Report (PTDR). The main reason is that the earlier result used only lepton tagging and kaon tagging, the tagging methods with the best dilutions but the smallest efficiencies.

Another mode with good x_s sensitivity is $B_s \rightarrow J/\psi \bar{K}^{*0}$, $J/\psi \rightarrow \mu^+ \mu^-$, $\bar{K}^{*0} \rightarrow K^- \pi^+$. Although this mode is Cabibbo suppressed, other factors are in its favor: the final state consists of a single detached vertex and the state is triggerable with several independent strategies, including impact parameter triggers, secondary vertex triggers and dimuon triggers [21]. While this mode does not have the x_s reach of $D_s^- \pi^+$ it does cover much of the expected range and it provides a powerful check with partly independent systematics.

For reasons of time limitations, the simulation of the $J/\psi \bar{K}^{*0}$ mode used MCFast, not BTeVGeant. The analysis of this mode proceeded as follows. To be considered as part of a signal candidate, a track was required to have at least 20 total hits and at least 4 pixel hits. The only further requirement placed on π^\pm candidates was that they have a momentum greater than 0.5 GeV/c. In order to be considered a muon candidate, a track was required to have a momentum $p > 5$ GeV/c, to penetrate the hadron filter and to leave hits in the most downstream muon chambers. Kaon candidates were required to satisfy a simplified model of the RICH system: the track was required to have a momentum in the range $3 < p < 70$ GeV/c and was required to have hits in the tracking station downstream of the RICH mirror. True kaons which satisfied this criteria were identified as kaons with an efficiency of 90%; other hadrons which satisfied this criteria were identified as kaons 3% of the time.

A $\mu^+ \mu^- K^- \pi^+$ combination was accepted as a B_s candidate if the confidence level of fitting all four tracks to a single vertex was greater than 0.005. It was also required that the resonant substructure requirements be satisfied. Combinations were considered for further analysis provided the decay length of the B_s candidate, L , satisfied $L/\sigma_L > 10$ and the impact

Quantity	Value	Yield (Events/year)
Luminosity:	$2 \times 10^{32} \text{ cm}^{-2} \text{ s}^{-1}$	
One Year:	10^7 s	
$\sigma_{b\bar{b}}$:	$100 \text{ } \mu\text{b}$	
$\mathcal{B}(B_s \rightarrow D_s^- \pi^+)$:	3.0×10^{-3}	
$\mathcal{B}(D_s^- \rightarrow \phi \pi^-)$:	0.030	
$\mathcal{B}(D_s^- \rightarrow K^{*0} K^-)$:	0.036	
$\mathcal{B}(\phi \rightarrow K^+ K^-)$:	0.49	
$\mathcal{B}(K^{*0} \rightarrow K^+ \pi^-)$:	0.67	
$\mathcal{B}(\bar{b} \rightarrow B_s)$	0.13	6,210,000
$\epsilon(\text{Geometry} + \text{cuts} : \phi \pi^-)$	0.027	
$\epsilon(\text{Geometry} + \text{cuts} : K^{*0} K^-)$	0.023	
$\epsilon(\text{Trigger}) \text{ Level 1}$	0.74	
$\epsilon(\text{Trigger}) \text{ Level 2}$	0.90	
$\epsilon(\text{Tag})$	0.70	72,000
Tagging Dilution	0.37	
S/B	3:1	
$\sigma(\text{Proper Decay time})$	43 fs	

Table 16.16: Projected yield for $B_s \rightarrow D_s^- \pi^+$ in one year of BTeV running. The numbers in the third column give the expected yield when all of the factors down to and including that line have been considered. The branching fraction $\mathcal{B}(B_s \rightarrow D_s^- \pi^+)$ was estimated to be the same as $\mathcal{B}(B_d \rightarrow D^- \pi^+)$. The value for $\mathcal{B}(\bar{b} \rightarrow B_s)$ was obtained from [3].

parameter of the B_s candidate with the primary vertex, d , satisfied $d < 3\sigma_d$. Each of the four B_s granddaughters were required to have an impact parameter with the primary vertex, d , of $d > 2\sigma_d$. Candidates with poor time resolution were rejected by demanding $\sigma_t \leq 0.09 \text{ ps}$. Also the mass of the J/ψ was constrained to its PDG value. The above procedure found that the efficiency for the 4 tracks to be within the fiducial volume of the tracking system was $14.2 \pm 0.3\%$ and the efficiency for the remaining candidates to pass the analysis cuts was 0.29 ± 0.01 . The resolution on the mass of the B_s was found to be $8.6 \pm 0.3 \text{ MeV}/c^2$ and the mean resolution on the proper decay time was found to be 36 fs.

The BTeV Level 1 trigger simulation was run on the $J/\psi \bar{K}^{*0}$ sample and, of the candidates which passed all analysis cuts, $68 \pm 2\%$ also passed the trigger; the error is statistical only. However, this mode can also be triggered by the dimuon trigger. Section 8.3, which describes the algorithms and performance of the muon trigger, estimates a trigger efficiency of 50% for this decay mode. There is, as yet, no calculation of the total Level 1 trigger efficiency which takes into account the correlations between the two triggers. For this proposal it will be estimated that the combined Level 1 trigger efficiency is 85%. Section 14.3.3 discusses the performance of the Level 2 tracking trigger and reports an estimated efficiency

Quantity	Value	Yield (Events/year)
Luminosity:	$2 \times 10^{32} \text{ cm}^{-2}\text{s}^{-1}$	
One Year:	10^7 s	
$\sigma_{b\bar{b}}$:	$100 \text{ } \mu\text{b}$	
$\mathcal{B}(B_s \rightarrow J/\psi \bar{K}^{*0})$:	8.5×10^{-5}	
$\mathcal{B}(J/\psi \rightarrow \mu^+ \mu^-)$:	0.061	
$\mathcal{B}(\bar{K}^{*0} \rightarrow K^- \pi^+)$:	0.667	
$\mathcal{B}(\bar{b} \rightarrow B_s)$	0.13	180000
$\epsilon(\text{Geometric})$	0.142	
$\epsilon(\text{Analysis cuts})$	0.26	6600
$\epsilon(\text{Trigger})$ Level 1 Tracking only	0.60	
$\epsilon(\text{Trigger})$ Level 1 Total	0.85	
$\epsilon(\text{Trigger})$ Level 2	0.90	5100
$\epsilon(\text{Tag})$	0.70	3600
Include $J/\psi \rightarrow e^+ e^-$	1.5	5300
Tagging Dilution	0.37	
S/B	2:1	
$\sigma(\text{Proper Decay time})$	36 fs	

Table 16.17: Projected yield for $B_s \rightarrow J/\psi \bar{K}^{*0}$ in one year of BTeV running. The numbers in the third column give the expected yield when all of the factors down to and including that line have been considered. The estimate for $\mathcal{B}(B_s \rightarrow J/\psi \bar{K}^{*0})$ was obtained from [21] and that for $\mathcal{B}(\bar{b} \rightarrow B_s)$ was obtained from [3]. The trigger efficiency is quoted as a fraction of those events which pass the analysis cuts.

of 90%.

By far the dominant background is expected to come from decays of the form $X_b \rightarrow J/\psi X$, $J/\psi \rightarrow \mu^+ \mu^-$, where X_b is any b flavored hadron. An MCFAST based simulation of 500,000 such decays was performed and the signal-to-background level was estimated to be about 2:1. Some sources of background that one might, at first, think to be important turn out not to be a problem. First, the more copious $B_s \rightarrow J/\psi \phi$ final state is not a significant source of background because of the excellent particle ID provided by the RICH system. Second, the mass resolution is sufficient to separate the decay $B_d \rightarrow J/\psi \bar{K}^{*0}$.

Finally, the expected yield can be increased by at least 50% by using the decay mode $J/\psi \rightarrow e^+ e^-$. This mode will have an efficiency for secondary vertex triggers which is comparable to that for $J/\psi \rightarrow \mu^+ \mu^-$; an electron trigger, which is not yet specified, is part of the BTeV baseline design.

The information reported here is summarized in Table 16.17 and is used in the mini Monte Carlo described in the next section.

16.7.2 Computation of the x_s Reach

The final step in the study was to use a mini-Monte Carlo to study the x_s reach of BTeV. This mini-Monte Carlo generates two lifetime distributions, one for mixed events and one for unmixed events, smears the distributions and then extracts a measured value of x_s from a simultaneous fit of the two distributions. The time smearing is a Gaussian of fixed width, using the mean time resolutions determined above. The model includes the effects of mistagging, background under the signal, and the minimum time cut which is implied by the L/σ_L cut. It is assumed that the lifetime distribution of the background is an exponential with the same mean lifetime as that of the B_s .

Figures 16.33 a) and b) show the proper time distributions which result from one run of the mini-Monte Carlo for a generated value of $x_s = 40$. The simulation is for the decay mode $B_s \rightarrow D_s^- \pi^+$ for one month of BTeV running. Part a) shows the proper time distribution for unmixed decays while part b) shows the distribution for mixed decays. Part c) of the figure shows, as a function of x_s , the value of the unbinned negative log likelihood function computed from the simulated events. A clear minimum near the generated value of x_s is observed and the likelihood function determines the fitted value to be $x_s = 39.96 \pm 0.08$. A step of 0.5 in the negative log likelihood function determines the 1σ error bounds and a line is drawn across the figure at the level of the 5σ error bound.

This figure nicely illustrates the distinction between two quantities which are often confused, the significance of the result and the error on x_s . The significance of the signal is determined by how far the depth of the global minimum falls below that of the next most significant minimum. The error on x_s is determined by the curvature of the likelihood function at the global minimum. While these quantities are clearly related, they are distinct; in particular, the significance of the signal is not the relative error on x_s .

The error returned by the fit was checked in two ways. First, an ensemble of mini-Monte Carlo experiments was performed and the errors were found to correctly describe the dispersion of the measured values about the generated ones. Second, the errors returned by the fit were found to be approximately equal to the Cramer-Rao minimum variance bound.

The mini-Monte Carlo was also used to study the level of statistics below which the experiment is unable to measure x_s . As the number of events in a trial is reduced, the negative log likelihood function becomes more and more ragged and the secondary minima become more pronounced. Eventually there are secondary minima which reach depths within 12.5 units of negative log likelihood (5σ) of the global minimum. When this happens in a sufficiently large fraction of the trials, one must conclude that only a lower limit on x_s can be established. In the region of the parameter space which was explored, the absolute error on x_s was approximately 0.1 when this limit was reached. This was independent of the generated value of x_s ; that is, the discovery measurement of x_s will have errors of something like ± 0.1 , even if x_s is large, say 40.

It is awkward to map out the x_s reach of the apparatus by running a large ensemble of mini-Monte Carlo jobs; instead the following automated procedure was used. Following ideas from McDonald [22], the sum over events in the likelihood function was replaced with an integral over the parent distribution. Because the parent distribution does not have any

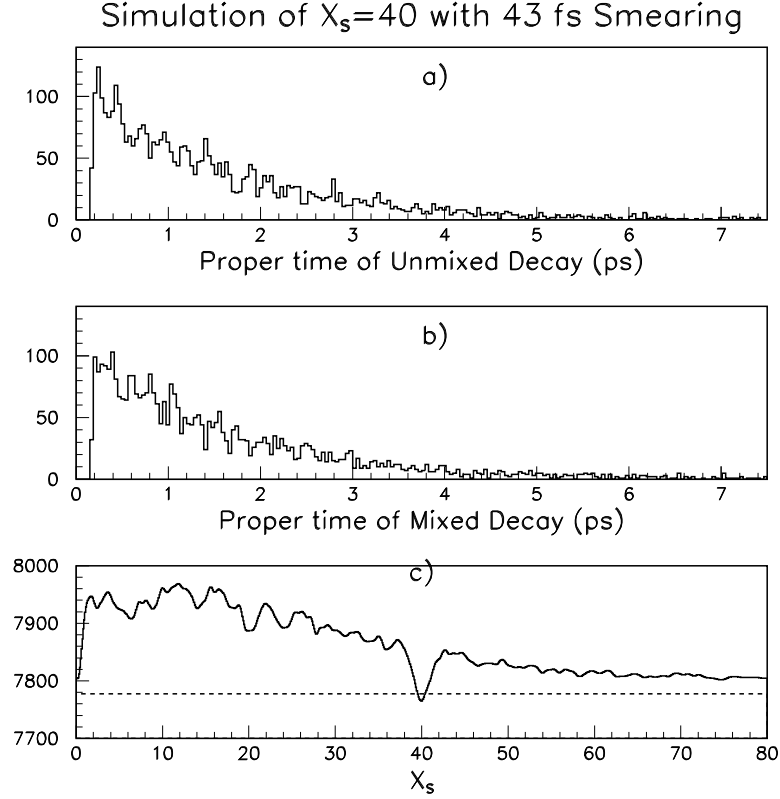


Figure 16.33: Mini-Monte Carlo proper lifetime plots of a) unmixed and b) mixed decays for a generated value of $x_s = 40$. The plots simulate the results of the $B_s \rightarrow D_s^- \pi^+$ channel after one month of running. The oscillations are prominent. Part c) shows the negative log likelihood function which was obtained from the entries in parts a) and b). A prominent minimum is seen at the generated value of x_s . The dashed line marks the level above the minimum which corresponds to 5σ significance.

statistical fluctuations, the fluctuations in the likelihood function are removed, leaving only the core information. An example of such a likelihood function is shown in Fig. 16.34.

A likelihood function computed in this way has the property that it scales linearly with the number of events being simulated. This can be stated formally as follows. Let x_0 denote the generated value of x_s and let $\mathcal{L}(x; x_0, N)$ denote the value of the likelihood function, evaluated at x , for a sample which has a true value of x_0 and which contains N events. Then,

$$\mathcal{L}(x; x_0, N) = N\mathcal{L}(x; x_0, 1) \quad (16.21)$$

Now, one can define the significance of the minimum, n , as,

$$n^2 = 2.0 N [\mathcal{L}(\infty; x_0, 1) - \mathcal{L}(x_0; x_0, 1)]. \quad (16.22)$$

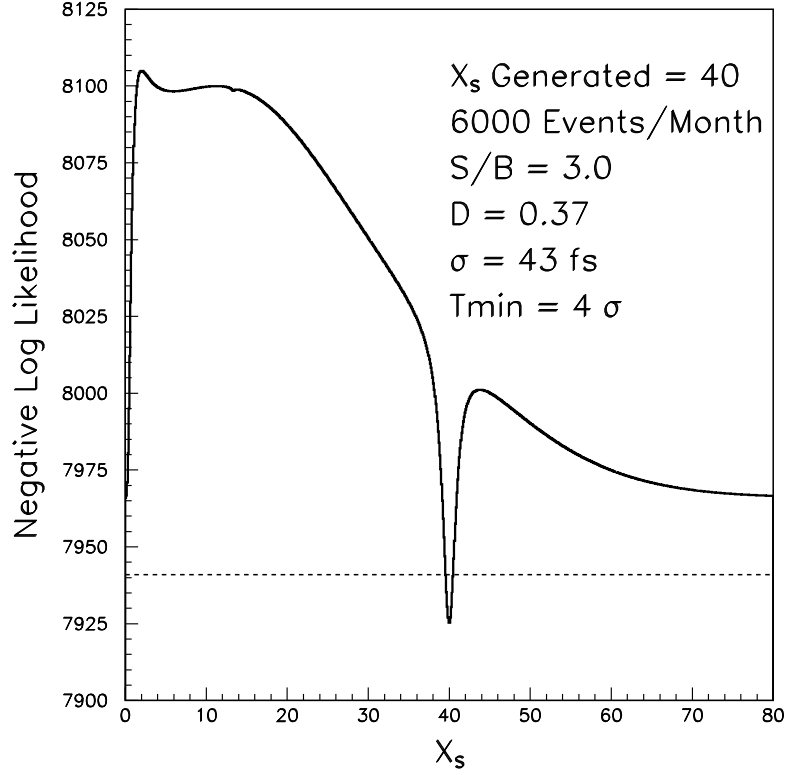


Figure 16.34: The same likelihood function as in part c) of the previous figure but obtained using the integral method described in the text. The overall shape is the same but the statistical fluctuations have been removed. There is also an overall level shift which is related to the goodness of fit in the previous figure.

For practical purposes ∞ was chosen to be 160. If one did not have to worry about the missing statistical fluctuations it would be normal to define a significant signal as 5σ , or $n^2 = 25$. Instead, sufficient significance was defined as $n^2 = 31.25$, by adding a somewhat arbitrary safety margin; this allows for the usual 5σ plus a downwards fluctuation of up to 2.5σ anywhere else in the plot. Equation 16.22 was solved for N , which was then converted into the running time required to collect N events. This procedure was repeated for many different values of x_0 to obtain Fig. 16.35. The solid line shows, for the $D_s^- \pi^+$ mode, the number of years needed to obtain a measurement with a significance of 5σ plus the safety margin. The safety margin reduces the x_s reach at 3 years by only 3 or 4 units of x_s . For small values of x_s , the effect of the safety margin is not visible. The dashed line shows the same information but for the $J/\psi \bar{K}^{*0}$ mode; for this mode the effect of the safety margin is similarly small.

Inspection of Fig. 16.35 shows that, using the $D_s^- \pi^+$ mode, BTeV is capable of observing

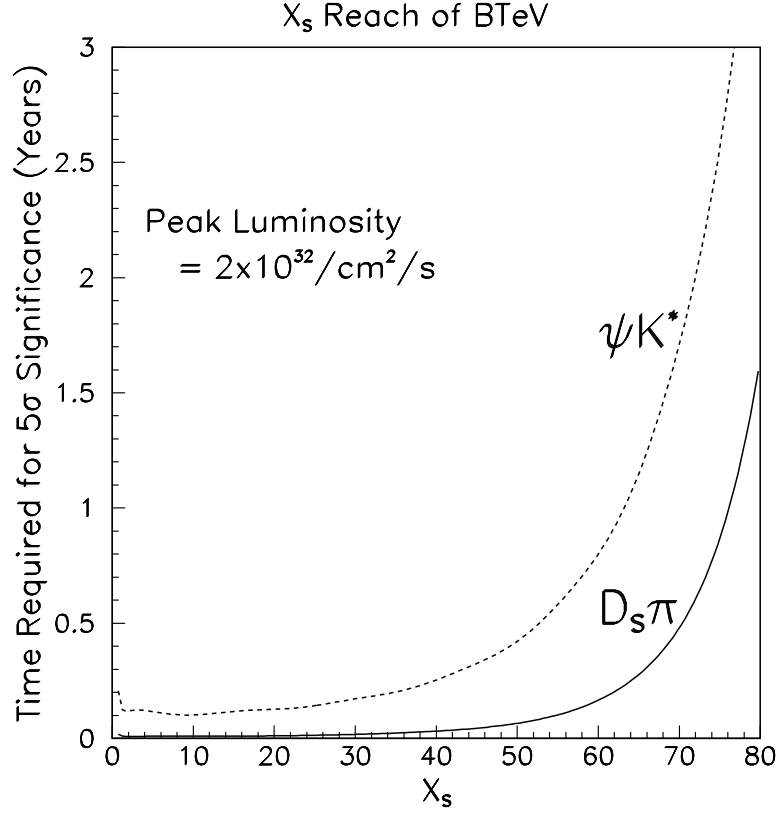


Figure 16.35: The x_s reach of the BTeV detector. The curves indicate the number of years of running which are required to make a measurement of x_s with a statistical significance of 5σ ; a safety margin, discussed in the text, has been included in the definition of 5σ . The curves are for the two different decay modes indicated on the figure.

all x_s less than 75 in one year of running. The improvement since the PTDR comes from two sources: there is an overall improvement which comes from using the full tagging power of BTeV; there is an additional improvement at large values of x_s which comes from the improved resolution on the proper decay time, which, in turn, was achieved by reducing the amount of material in the pixel detectors.

16.8 Flavor-changing Rare B Meson Decays

16.8.1 The Physics Significance of Rare B Meson Decays

Within the Standard Model, flavor-changing neutral current decays of b quarks may occur through loop diagrams, such as penguin diagrams or box diagrams. Such decays are suppressed in the Standard Model. If some of these decays occur at a much higher level than predicted by the Standard Model, this would be evidence for new particles which contribute to the loop or box diagrams. This would provide a path to observe new physics at a higher mass scale than can be probed directly at existing or planned accelerators. Table 16.18 gives a list of some interesting rare decays, their estimated Standard Model branching fractions, and current upper limits [23].

Decay Mode	Est. BR(SM)	Measurements and 90% CL upper limits
$(B_d, B_u) \rightarrow X_s \mu^+ \mu^-$	$(5.7 \pm 1.2) \times 10^{-6}$	$< 3.6 \times 10^{-5}$
$(B_d, B_u) \rightarrow X_d \mu^+ \mu^-$	$(3.3 \pm 1.9) \times 10^{-7}$	—
$(B_d, B_u) \rightarrow K \mu^+ \mu^-$	$(4.0 \pm 1.5) \times 10^{-7}$	$< 0.9 \times 10^{-5}$
$(B_d, B_u) \rightarrow K^* \mu^+ \mu^-$	$(1.5 \pm 0.6) \times 10^{-6}$	$< 2.5 \times 10^{-5}$
$B_s \rightarrow \mu^+ \mu^-$	$(3.5 \pm 1.0) \times 10^{-9}$	$< 8.4 \times 10^{-6}$
$B_d \rightarrow \mu^+ \mu^-$	$(1.5 \pm 0.9) \times 10^{-10}$	$< 1.6 \times 10^{-6}$
$(B_d, B_u) \rightarrow X_s e^+ e^-$	$(8.4 \pm 2.2) \times 10^{-6}$	—
$(B_d, B_u) \rightarrow X_d e^+ e^-$	$(4.9 \pm 2.9) \times 10^{-7}$	—
$(B_d, B_u) \rightarrow K e^+ e^-$	$(5.9 \pm 2.3) \times 10^{-7}$	$< 1.2 \times 10^{-5}$
$(B_d, B_u) \rightarrow K^* e^+ e^-$	$(2.3 \pm 0.9) \times 10^{-6}$	$< 1.6 \times 10^{-5}$
$B_s \rightarrow e^+ e^-$	$(8.0 \pm 3.5) \times 10^{-14}$	—
$B_d \rightarrow e^+ e^-$	$(3.4 \pm 2.3) \times 10^{-15}$	—

Table 16.18: Estimated branching fractions and current measurements of flavor-changing neutral current decays with muons and electrons.

Given the enormous production rate of B -mesons at the Tevatron, we should be able to observe some of these decays and set stringent limits on others. The precise vertexing of the silicon pixel detector will easily allow us to differentiate b decays from non- b backgrounds. We present expected sensitivities from studies of some of these decay channels.

16.8.2 Exclusive Channel $B^0 \rightarrow K^{*0} \mu^+ \mu^-$

There is great interest in studying $B^0 \rightarrow K^{*0} \ell^+ \ell^-$ as a window to new physics [24]. Observation of a total rate for $B^0 \rightarrow K^{*0} \mu^+ \mu^-$ different than the Standard Model prediction would be evidence for non-Standard Model particles. In fact, new physics may lead to *qualitative* differences in the distributions of the differential decay rate and the forward-backward asymmetry, A_{fb} , of the $\ell^+ \ell^-$ system as a function of Q^2 . It has been pointed out by several

theorists [25] that the Standard Model predicts $A_{fb} = 0$ for a certain value of Q^2 , as shown in Fig. 16.36. Furthermore, the position of this zero appears to be model-independent within the Standard Model. Many extensions to the Standard Model predict this asymmetry to be non-zero for all values of Q^2 . Figure 16.36 shows the predictions of one of these models for different values of the Wilson coefficients [26].

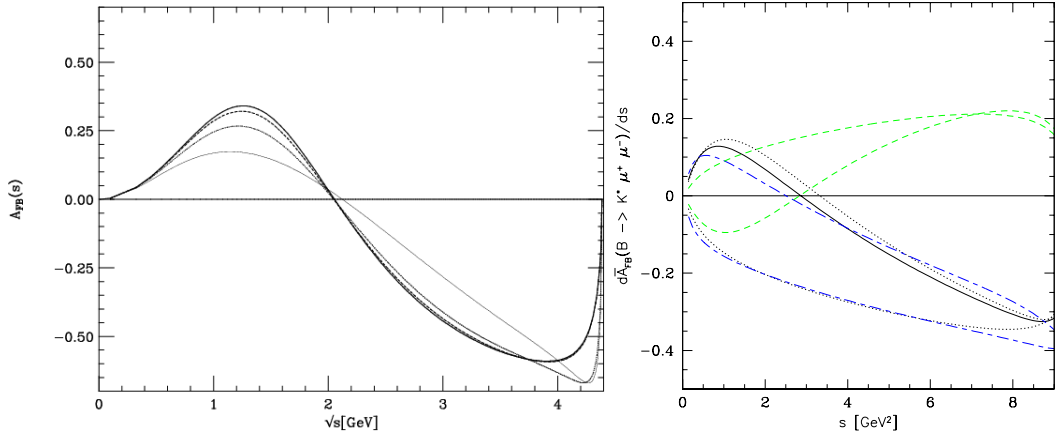


Figure 16.36: Forward-backward asymmetry in the Standard Model (left) [25]. Predictions of the SUGRA (MIA-SUSY) model [26], with various values of the Wilson coefficients (right).

It is unlikely that D0 or CDF will have sufficient sensitivity in Run II to confirm or deny the existence of a zero crossing in the A_{fb} versus Q^2 distribution. In addition, the rates at $e^+e^- B$ factories are of order 10 events/year at design luminosity. Therefore, the main competition to BTeV on these modes will come from LHC-b.

Since we expect large backgrounds under the signal, an understanding of these backgrounds is critical to understanding our sensitivity. The various sources of background are:

- b -events where portions of the two b hadrons in the event appear to form a vertex downstream of the production point. In approximately 1% of all $b\bar{b}$ events both B hadrons decay semileptonically producing two real muons. In addition, there is a charged kaon from at least one of the b 's over 90% of the time.
- Minimum bias events where three particles conspire to fake a secondary vertex and two of the particles either decay downstream of the magnet or make hadronic showers which leave a signal in the muon detector (hadron punch-through).
- Charm events with one or more real muons and kaons.
- More generally, any combination of the above.
- Decays from single B mesons where two charged pions fake muons.

The basic weapons to combat these backgrounds are:

- Excellent discrimination between the primary and secondary vertices, which eliminates backgrounds from minimum bias events and from the underlying event within a true b

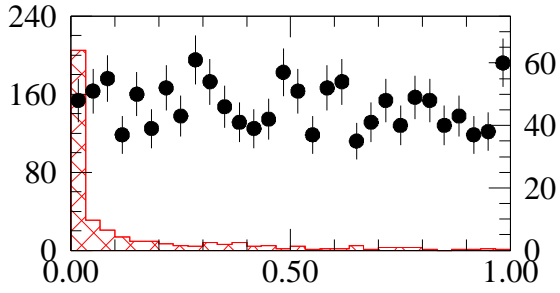
event. Tracks which are not part of the b vertex are easily rejected by requiring a non-zero vertex fit probability, as shown in Fig. 16.37(a). Also, the normalized decay length (L/σ_L), shown in Fig. 16.37(c), provides additional discrimination against background.

- Excellent mass resolution ($\sigma \approx 17 \text{ MeV}/c^2$) on the final state, shown in Fig. 16.38.
- Excellent “point-back” resolution of the reconstructed b candidate with respect to the primary vertex. This will help to reject vertices that have been artificially pieced together from particles from the two separate b ’s in the event. The normalized B impact parameter (b_B/σ_{b_B}) with respect to the primary vertex is quite different for signal and background events, as shown in Fig. 16.37(b).
- The ability to reject combinations which include tracks that are from the primary vertex or other vertices in the event, by cutting on the impact parameter of the track with respect to that vertex. Figures 16.37(e) and (f) show the normalized impact parameter of the kaon and pion with respect to the primary vertex (b_K/σ_{b_K} and b_π/σ_{b_π}).
- Excellent particle ID for the hadron (RICH) and the leptons (electromagnetic calorimeter and muon detector).

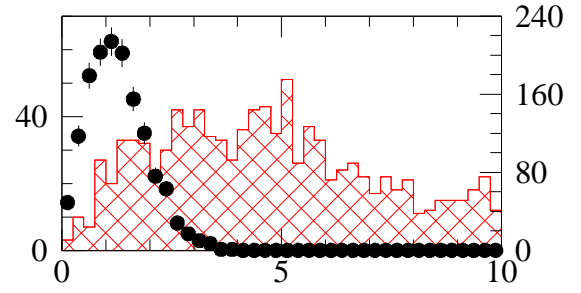
The $B^0 \rightarrow K^{*0} \mu^+ \mu^-$ events were selected using the following criteria:

- Two muons of opposite charge, each with momentum greater than 5 GeV/ c . Both muon tracks were required to have at least one hit in the muon chambers.
- Kaon track momentum greater than 3 GeV/ c . The kaon track was also required to have at least one hit in the forward drift chamber between the RICH and calorimeter. Perfect π/K separation and 100% efficiency for reconstructing the Cherenkov photons of tracks which traverse the RICH is assumed.
- Good primary vertex with confidence level greater than 1%.
- Good b vertex with confidence level greater than 1%.
- Decay length greater than 7σ .
- B impact parameter with respect to the primary vertex less than 2.5σ .
- K impact parameter with respect to the primary vertex greater than 2.5σ .
- π impact parameter with respect to the primary vertex greater than 2.5σ .
- B momentum greater than 20 GeV/ c .
- $|m(K\pi) - m_{K^{*0}}| < 50 \text{ MeV}/c^2$.
- Cut 100 MeV/ c^2 about the J/ψ and ψ' nominal masses to remove regions dominated by $B \rightarrow \psi K^*$ and $B \rightarrow \psi' K^*$, which interfere with the signal.

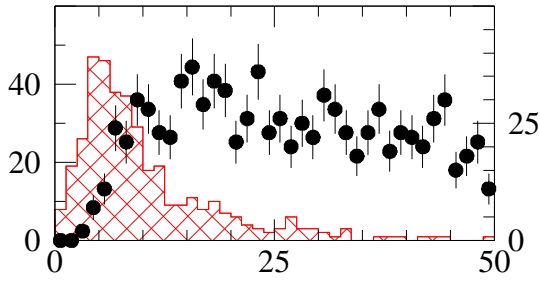
Of 4.4 pb^{-1} of MCFast $b\bar{b}$ background events generated (about one million events), nine pass the selection criteria. These events were not required to pass the trigger. For 2 fb^{-1} of data (one year of running at a luminosity of $2 \times 10^{32} \text{ cm}^{-2} \text{ s}^{-1}$), this would correspond



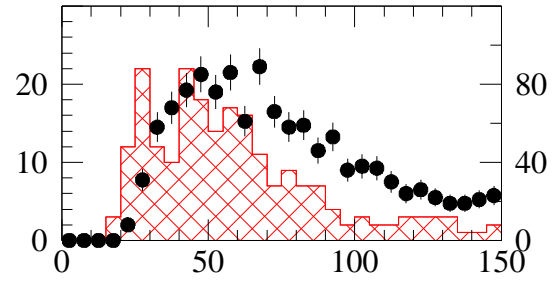
a) B Vertex Probability



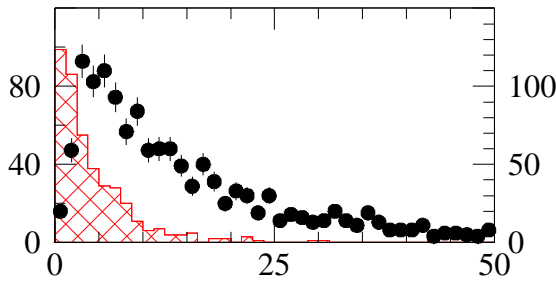
b) Norm. B Impact Param.



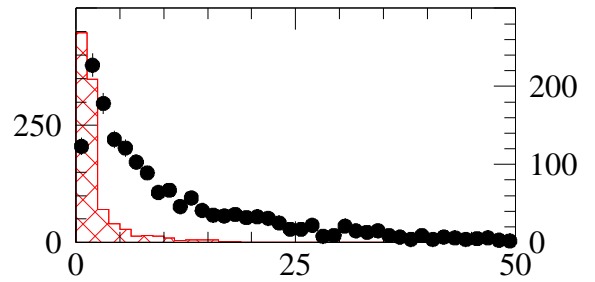
c) Norm. Decay Length



d) $p(K\pi\mu\mu)$ (GeV/c)



e) Norm. K Impact Param.



f) Norm. π Impact Param.

Figure 16.37: Distributions of cut variables for signal (points) and $b\bar{b}$ background (hatched) MCFast events.

to 4090 events in the range $4.7 \text{ GeV}/c^2 < m(K\pi\mu\mu) < 5.7 \text{ GeV}/c^2$, shown in Fig. 16.38. The width of the B^0 mass peak obtained from the MCFast signal Monte Carlo sample is $17 \text{ MeV}/c^2$. Thus, after the trigger efficiency is applied, we can expect about 200 background events from semileptonic $b\bar{b}$ decays under the B^0 mass peak, as shown in Table 16.19. With an expected yield of ~ 2200 signal events, this corresponds to a signal-to-background ratio of about 11.

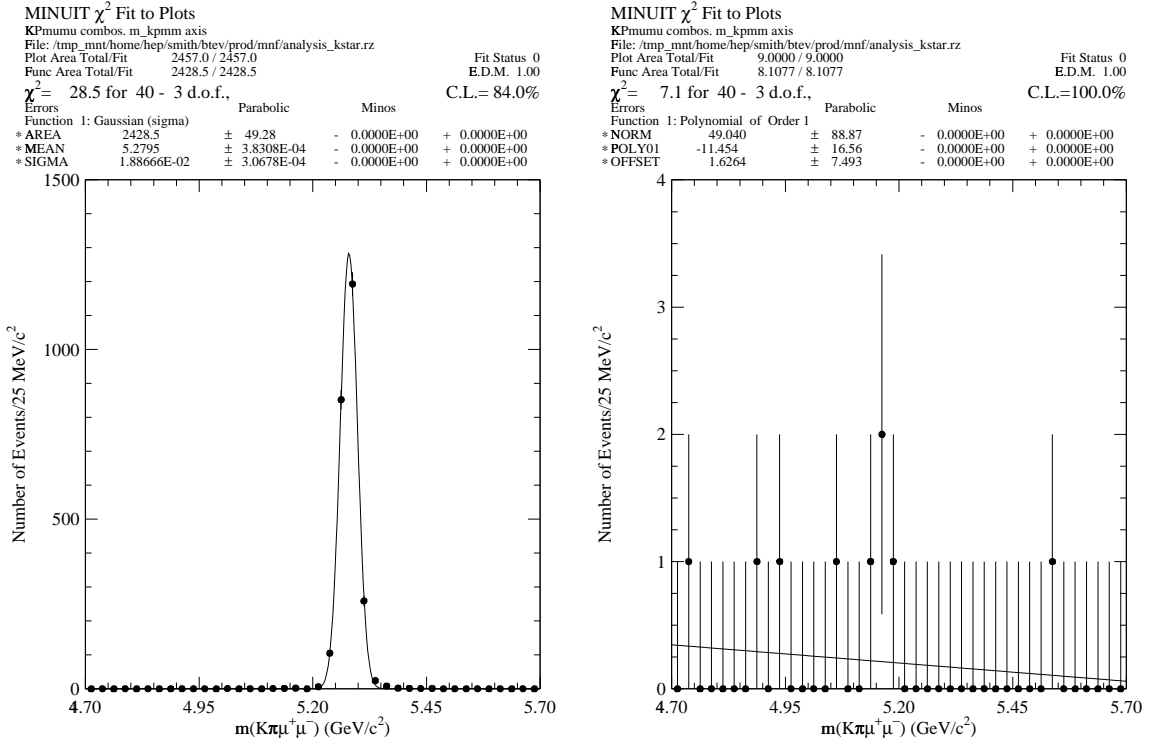


Figure 16.38: Distributions of tagged $B^0 \rightarrow K^{*0} \mu^+ \mu^-$ signal (left) and 4.4 fb^{-1} of $b\bar{b}$ background (right) MCFast events.

We did not include the $B^0 \rightarrow \psi K^{*0}$ as a background. That decay is large compared to the rare decay considered here and will interfere with the rare decay and distort the dimuon mass distribution in the vicinity of $3 \text{ GeV}/c^2$. In this study, a cut was applied to remove the regions around the J/ψ and ψ' . In fact, this state can be used to calibrate the efficiency of the analysis and as a normalization for a measurement of the relative branching fraction.

A sample of 2 fb^{-1} of signal MCFast Monte Carlo events were generated according to the Standard Model prediction for A_{fb} and Q^2 [24]. Figure 16.39 shows the distributions of reconstructed A_{fb} and number of events as a function of $m(\mu^+ \mu^-)$ for this sample, after all cuts and the trigger efficiency have been applied. We have included our anticipated $b\bar{b}$ semileptonic background, generated with $A_{fb} = 0$, in the asymmetry plot. We should be able to easily observe and measure the position of a zero in the asymmetry if it exists, or make a strong case for non-Standard Model physics, if it does not.

Luminosity	$2 \times 10^{32} \text{ cm}^{-2}\text{s}^{-1}$
Running Time/Year	10^7 s
$b\bar{b}$ Cross Section	$100\mu\text{b}$
Number of $b\bar{b}$ Pairs Produced	2×10^{11}
N_{B^0} Produced	1.5×10^{11}
Est. $\mathcal{B}(B^0 \rightarrow K^{*0}\mu^+\mu^-)$	$(1.5 \pm 0.6) \times 10^{-6}$
$\mathcal{B}(K^{*0} \rightarrow K^+\pi^-)$	0.67
Number of Signal Events Produced	1.5×10^5
Level 1 Trigger Efficiency (vertex + dimuon)	80%
Level 2 Trigger Efficiency	90%
Reconstruction Efficiency	2.0%
Number of Signal Events	2200
Number of Background in Signal Box	200
Signal/Background	11

Table 16.19: Estimate of sensitivity to $B^0 \rightarrow K^{*0}\mu^+\mu^-$ based on one year of running. Only backgrounds from $b\bar{b}$ semileptonic decays were included in this study.

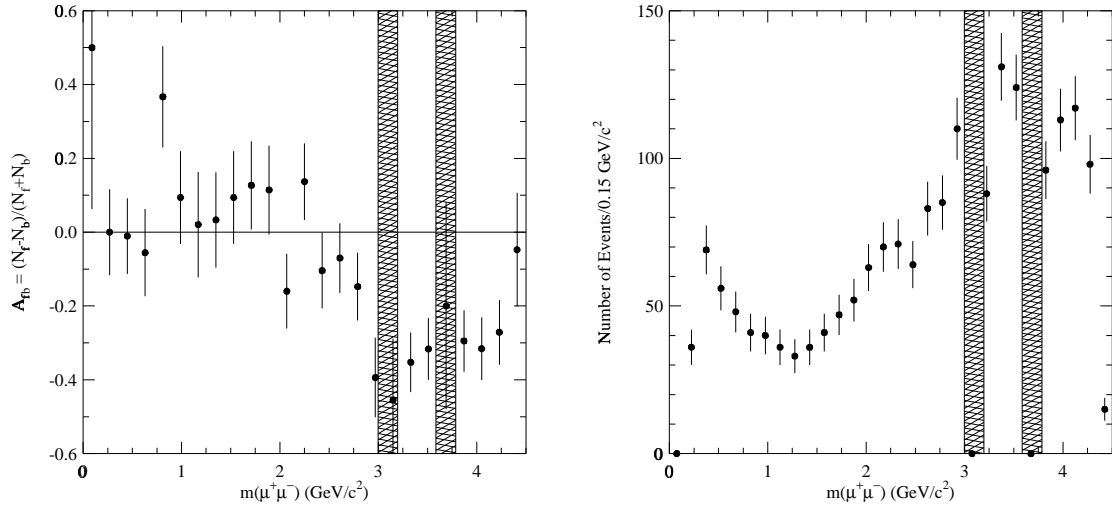


Figure 16.39: Expected forward-backward asymmetry distribution, including background, (left) and number of events (not including background) (right) as a function of $m(\mu^+\mu^-)$ after one year of running.

16.8.3 Exclusive Channel $B^+ \rightarrow K^+ \mu^+ \mu^-$

While the channel $B^+ \rightarrow K^+ \mu^+ \mu^-$ is not as rich as $B^0 \rightarrow K^{*0} \mu^+ \mu^-$, in that the asymmetry A_{fb} is expected to be small within the Standard Model and beyond the Standard Model, a measurement of the decay rate is still a sensitive probe of new physics. In particular, measurement of the differential decay rate will provide input to determine the magnitude and sign of the Wilson coefficients C_7 , C_9 , and C_{10} .

Most of the backgrounds to this channel are the same as those listed for the $B^0 \rightarrow K^{*0} \mu^+ \mu^-$ analysis in Section 16.8.2. Events for this study were selected using nearly the same criteria as the $B^0 \rightarrow K^{*0} \mu^+ \mu^-$ analysis:

- Kaon track momentum greater than 4 GeV/ c . The kaon track was also required to have at least one hit in the forward drift chamber between the RICH and calorimeter. Perfect π/K separation and 100% efficiency for reconstructing the Cherenkov photons is assumed.
- Two muons with momentum greater than 5 GeV/ c . Both muon tracks were required to have at least one hit in the muon chambers.
- Good primary vertex with confidence level greater than 1%.
- Good b vertex with confidence level greater than 1%.
- Decay length greater than 7σ .
- B impact parameter with respect to the primary vertex less than 2.5σ .
- K impact parameter with respect to the primary vertex greater than 2.5σ .
- B momentum greater than 20 GeV/ c .
- Cut 100 MeV/ c^2 about the J/ψ and ψ' nominal masses to remove regions dominated by $B \rightarrow \psi K$ and $B \rightarrow \psi' K$, which interfere with the signal.

We have not simulated all sources of background. Our estimates indicate that the most serious background is from events with pairs of b 's, each of which undergoes semileptonic decay. The background contribution was estimated by applying the selection criteria to a sample of 2.5 million MCFast semileptonic $b\bar{b}$ events, corresponding to a luminosity of 10 pb $^{-1}$. Of these events, 41 passed the selection cuts and fell within a 1 GeV/ c^2 window centered on the B^+ mass. Extrapolating to a year of running at a luminosity of 2×10^{32} cm $^{-2}$ s $^{-1}$ (2 fb $^{-1}$), we expect about 8200 events in this window. Assuming a uniform distribution across the B mass window (this is conservative, since it is falling, as shown in Fig. 16.40), we can expect about 400 events within 2σ of the B^+ mass after applying the trigger efficiency.

The overall efficiency for this state, with cuts designed to achieve good background rejection, is about 3.0%. Table 16.20 gives a calculation of the yield obtained in a one year run at a luminosity of 2.0×10^{32} cm $^{-2}$ s $^{-1}$. The number of signal events passing the trigger and all selection criteria is approximately 1280. Given the impressive signal-to-background ratio of 3.2, we will certainly observe this decay, even if the branching fraction is lower than theory predicts.

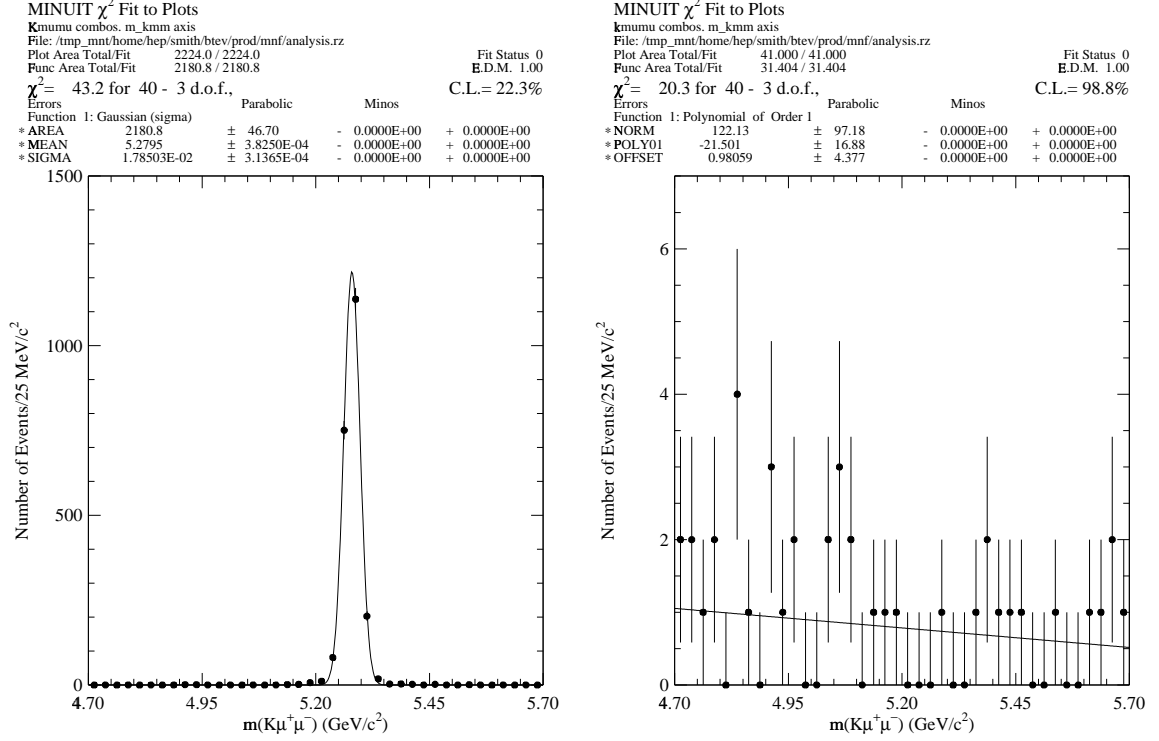


Figure 16.40: Distributions of $B^+ \rightarrow K^+ \mu^+ \mu^-$ signal (left) and 10 fb^{-1} of $b\bar{b}$ background (right) events.

Luminosity	$2 \times 10^{32} \text{ cm}^{-2} \text{ s}^{-1}$
Running Time/Year	10^7 s
$b\bar{b}$ Cross Section	$100 \mu\text{b}$
Number of $b\bar{b}$ Pairs Produced	2×10^{11}
Number of B^+ Produced	1.5×10^{11}
Est. $\mathcal{B}(B^+ \rightarrow K^+ \mu^+ \mu^-)$	$(4.0 \pm 1.5) \times 10^{-7}$
Number of Signal Events Produced	6.0×10^4
Level 1 Trigger Efficiency (vertex + dimuon)	80%
Level 2 Trigger Efficiency	90%
Reconstruction Efficiency	3.0%
Number of Background Events in Signal Box	400
Number of Signal Events	1280
Signal/Background	3.2

Table 16.20: Estimate of sensitivity to $B^+ \rightarrow K^+ \mu^+ \mu^-$ based on one year of running.

The CDF II TDR [27] predicts a signal of 100-300 $B^+ \rightarrow K^+ \mu^+ \mu^-$ events in Run II. CDF's lack of particle ID for tracks above 1 GeV/c leaves it exposed to background from all pions in an event conspiring with muons to create background. It is unlikely that CDF's signal-to-background in Run II (0.1 in Run I) will approach that expected at BTeV. In BTeV, only kaons contribute to the background, due to the RICH, and there are fewer of them. BTeV will have intrinsically less background than detectors without powerful particle ID.

16.8.4 Inclusive $(B_d, B_u) \rightarrow X_s \mu^+ \mu^-$

We have studied the ability of the BTeV detector to measure inclusive $(B_d, B_u) \rightarrow X_s \mu^+ \mu^-$. The method used is similar to that used by CLEO [28][29], in which a kaon and 0-4 pions are combined with the dilepton pair. For this study, no neutral pion or kaon candidates were included. Thus, the efficiency for modes containing a π^0 or K^0 was assumed to be zero.

Monte Carlo samples of signal and 0.24 pb^{-1} of $b\bar{b}$ semileptonic background events were generated with MCFast. The signal sample only includes decays to *charged* kaons and pions. In calculating the efficiency, we naïvely assume all final states contribute equally. This results in an efficiency of approximately 0.3% for a truly inclusive sample. We expect approximately 4000 reconstructed events in all-charged modes after one year of running.

The selection criteria are nearly identical to those used in the exclusive modes, generalized to 0-4 pions. We find that 68 of the $b\bar{b}$ semileptonic background events pass all selection criteria and fall within a $1 \text{ GeV}/c^2$ window about the B mass, as shown in Fig. 16.41. This extrapolates to 20,500 events in a 2σ signal region under the B mass after applying the trigger efficiency. The combinatoric background was assessed by analyzing anti-tagged combinations in an MCFast signal Monte Carlo sample corresponding to about 100 pb^{-1} , shown in Fig. 16.41. We find 399 events in a $1 \text{ GeV}/c^2$ window about the B mass, for a sample of 205 signal events. From this, we estimate a combinatoric contribution in the signal region of 400 events in one year of running. Furthermore, this contribution is insensitive to the number of multiple interactions. We find signal/background ~ 0.13 , as summarized in Table 16.21.

In this analysis, we have demonstrated that the precise vertex reconstruction in BTeV is very effective at removing combinations involving non- b daughters. As a result, we will have adequate sensitivity to measure the inclusive $(B_d, B_u) \rightarrow X_s \mu^+ \mu^-$ branching fraction. Of course, significant improvements can be made to this simple analysis, which has not been optimized. More inclusive measurements which include combinations with a K_s^0 or π^0 may also be feasible, although the backgrounds associated with the π^0 are expected to be large.

Other planned searches for inclusive $(B_d, B_u) \rightarrow X_s \mu^+ \mu^-$ at D0 and CDF only use the dilepton mass and are likely limited to the endpoint phase space region above the ψ' . Below this, backgrounds from semileptonic b decays overwhelm the signal. Since we include the entire phase space except where the J/ψ and ψ' dominate the cross section, we avoid the model dependence introduced by measuring only the endpoint region [30]. Therefore, this measurement will provide a long-awaited *model-independent* determination of the Wilson coefficients C_7^{eff} and C_{10} .

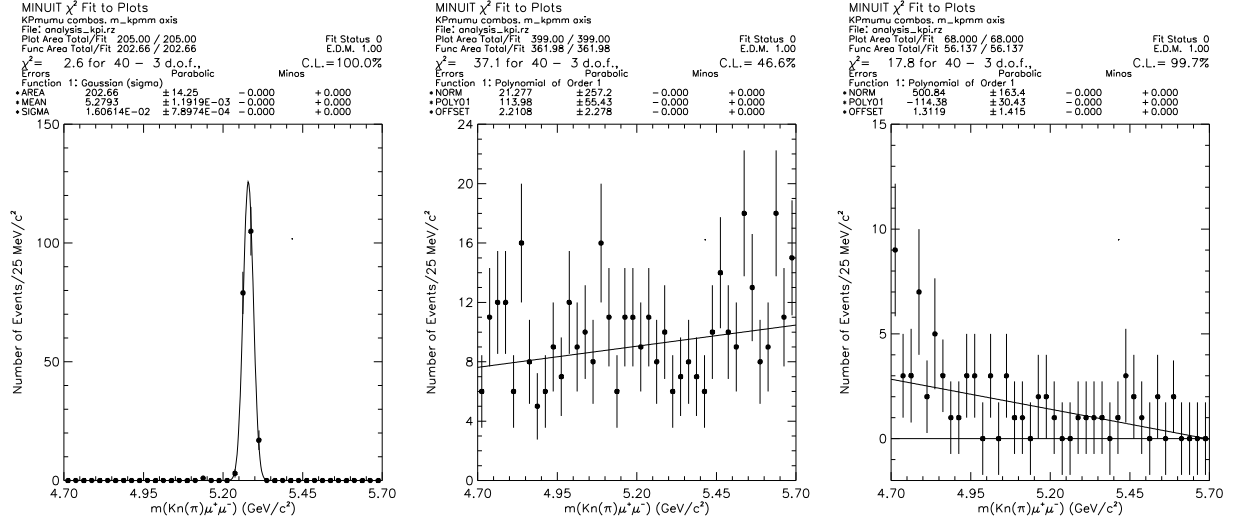


Figure 16.41: B mass distributions of $B^{+0} \rightarrow K^+ n(\pi^{+/-})\mu^+\mu^-$ ($n = 0 - 4$) from 100 pb^{-1} of tagged signal (left) and anti-tagged combinatoric background (center) events. B mass distribution of 0.24 pb^{-1} of $b\bar{b}$ background Monte Carlo events (right), where both b 's decay semileptonically.

Luminosity	$2 \times 10^{32} \text{ cm}^{-2}\text{s}^{-1}$
Running Time/Year	10^7 s
$b\bar{b}$ Cross Section	$100 \mu\text{b}$
Number of $b\bar{b}$ Pairs Produced	2×10^{11}
Number of B_d, B_u Produced	3.0×10^{11}
Est. $(B_d, B_u) \rightarrow X_s \mu^+ \mu^-$	$(5.7 \pm 1.2) \times 10^{-6}$
Number of Signal Events Produced	1.7×10^6
Level 1 Trigger Efficiency (vertex + dimuon)	80%
Level 2 Trigger Efficiency	90%
Selection Cut Efficiency	0.3%
Number of Background Events in Signal Box	27,800
Number of Signal Events	3600
Signal/Background	0.13
Significance of Signal	20σ

Table 16.21: Estimate of sensitivity to $(B_d, B_u) \rightarrow X_s \mu^+ \mu^-$ based on one year of running.

16.9 Consequences of Degraded Detector Performance

16.9.1 Introduction

A specific PAC request from the Aspen meeting of June 1999 is:

Simulations should also be used to analyze how much the physics reach of the experiment is degraded if various components of the detector do not meet design specifications.

Every effort will be made by BTeV collaborators to meet or exceed design specifications. Indeed, we believe the design of BTeV to be conservative with room for improvement in many areas within the budget envelope. Here, we summarize the studies that specifically address the PAC question.

16.9.2 Trigger Performance

Degradation in the trigger could, in principle, arise from either a loss in efficiency or a worsening of pixel resolution. In fact, the full pixel resolution is not used at the trigger stage since the algorithm does not take the time to do all the corrections, so modest changes in the resolution should not be important. We worsened the pixel resolution by assuming that we had no help from the analog information, and thus used pure digital resolution. The rejection for minimum bias events, worsened by less than 10%, while efficiencies on b decays were unaffected.

On the other hand, significant losses in efficiency would worsen the trigger efficiency and could only be fixed by adding more layers in the algorithm. That would increase the time required by the trigger and would be costly in terms of requiring more processors.

We have evaluated the trigger efficiency as a function of the pixel efficiency for the final state $B_s \rightarrow D_s^+ K^-$ and minimum bias events. To make things really interesting, we added a substantial (and unreasonable) number of noise hits randomly to each pixel plane. While we believe the final pixel efficiency will be well in excess of 99%, we allowed the efficiency to be as low as 98%. Fig. 16.42 shows the effect of these changes on signal efficiency and background rejection. While some loss is observable on signal events, it does not seriously degrade the physics performance.

16.9.3 Decay Time Resolution

The decay time resolution, σ_t , is a critical element of BTeV and will be negatively affected by having a degraded position resolution in the pixel detector. σ_t is improved both by having less material and by having better position resolution. Let us consider, for example, the time resolution in $B_s \rightarrow J/\psi \bar{K}^*$, $\bar{K}^* \rightarrow K^- \pi^+$. The resolution we obtain for the current baseline detector is $\sigma_t = 36$ fs.

If the position resolution were degraded by a factor of two, σ_t would increase by about 25%. We do not expect any degradation to approach this level. If additional material were added to the pixel detector, there would be deterioration due to multiple scattering. If the spatial resolution of the detector were zero, this deterioration would increase as $\sqrt{\text{thickness}}$.

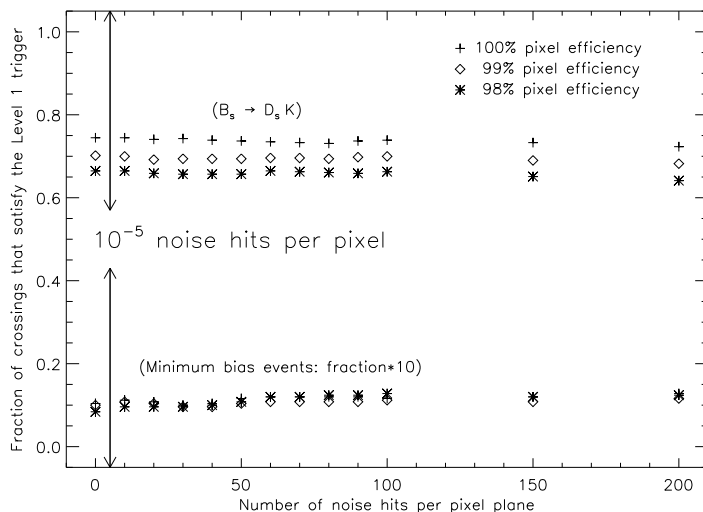


Figure 16.42: The Level 1 trigger efficiency for $B_s \rightarrow D_s^+ K^-$ and minimum bias events (multiplied by 10 for better viewing) for three values of assumed pixel efficiencies as a function of the number of added noise hits per plane. We expect, nominally, 5 noise hits per plane, corresponding to a density of 10^{-5} noise hits.

Since we have a finite spatial resolution, the dependence is somewhat weaker; in any case, we do not expect to have to increase the detector thickness. These results were abstracted from a detailed evaluation of the change in σ_t as a function of spatial resolution and material thickness that was done for the original baseline pixel detector, with 3 planes per station. We expect the results to be similar for the 2-plane per station design.

We mention in passing that it is possible to substantially improve the decay time resolution by moving the pixel detector closer to the beam line. Our design calls for the pixel detector to be 6 mm away. This is limited by radiation damage. New advances in pixel technology suggest that we can move the pixel detector closer. The practical limit determined by the machine is 3 mm. This would improve the decay time resolution by about 30%.

16.9.4 Ring Imaging Particle Identification

The primary way of degrading performance here is to not get as many photons as we expect. This could be caused by bad mirrors, poorer than specified quantum efficiency or contamination of the gas. The latter is hard to imagine because the detector operates in the visible light regime. In any case, we have evaluated the RICH performance on the decay mode $B^0 \rightarrow \pi^+ \pi^-$ using a detector with 50% fewer photons than design specification. (We do not view this as a realistic loss.)

Fig. 16.43 shows the efficiency for detecting $B^0 \rightarrow \pi^+ \pi^-$ versus the efficiency for misidentifying the competing decay $B^0 \rightarrow K^+ \pi^-$, for our design and a detector degraded by a 50% loss of photons.

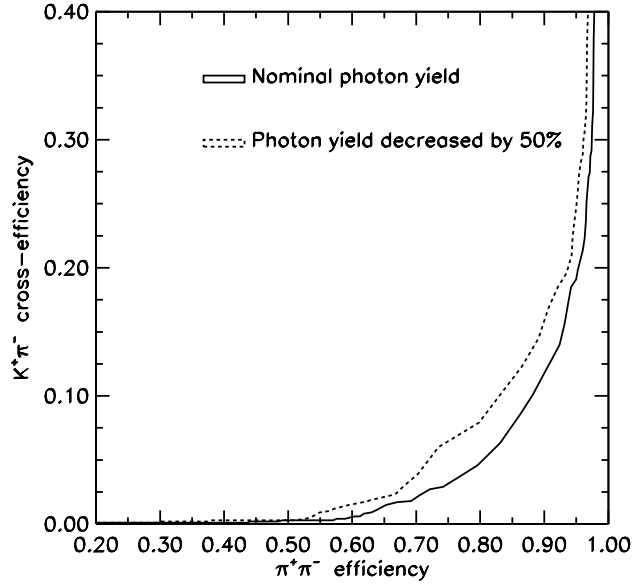


Figure 16.43: The efficiency for identifying both pions in the reaction $B^0 \rightarrow \pi^+\pi^-$ versus the efficiency for misidentifying $B^0 \rightarrow K^+\pi^-$ as $\pi^+\pi^-$. The solid-line is for the baseline design, while the dashed line is for a 50% loss of photons.

While there is a significant loss of efficiency for small fake rates, the interpolation to a more reasonable loss of $\sim 10\%$ would not be a disaster.

16.9.5 Electromagnetic Calorimeter

The performance of the EM calorimeter would be degraded if we failed to obtain the expected energy resolution

$$\frac{\sigma_E}{E} = \sqrt{\frac{a^2}{E} + b^2} = \frac{a}{\sqrt{E}} \oplus b, = \frac{1.6\%}{\sqrt{E}} \oplus 0.55\% \quad . \quad (16.23)$$

Our physics reach in final states with single photons will have increased backgrounds since the signal-to-background ratio depends directly on the energy resolution. Doubling the energy width would cut the single photon signal-to-background ratio in half.

The effects on π^0 mass resolution are more subtle because the position resolution is important here and that is also degraded by a worsening of the energy resolution. We evaluated the changes that would occur if the constant term, b , in the energy resolution changed from the nominal value of 0.55% for 10 GeV π^0 's, which is a typical value in many of our important processes. The mass resolution is 2.9 MeV, 3.0 MeV, 4.6 MeV and 7.5 MeV, for b values of 0.55%, 1.0%, 5.0% and 10.0%, respectively. For a reasonable range of constant terms, the mass resolution is unaffected.

We also evaluated the effect of changing the photon yield for 10 GeV π^0 's. Changing the photon yield from a nominal 7 photoelectrons/MeV to 4 photoelectrons/MeV, changes the π^0 mass resolution from 2.9 MeV to 3.2 MeV.

Bibliography

- [1] A. Gritsan “Charmless Hadronic B Meson Decays with CLEO,” presented at Lake Louise Winter Institute 2000, to appear in proceedings.
- [2] O.R. Long *et al.*, “Monte Carlo Simulation of $B^0 \rightarrow \pi^+ \pi^-$ from pp Interactions at $\sqrt{s}=40$ TeV”, UPR/216E, PRINCETONE/HEP/92-07,SSCL/PP/139(1992).
- [3] F. Abe *et al.*, The CDF Collaboation, *Phy. Rev.* **D54**, 6596 (1996).
FERMILAB-PUB-96/199-E.
- [4] “ J/ψ and $\psi(2S)$ Production in $p\bar{p}$ Collisions at $\sqrt{s} = 1.8$ TeV”, F. Abe *et al.*, The CDF Collaboration, *Phys. Rev. Lett.* **79**, 572 (1997).
- [5] Particle Data Group, C. Caso *et al.*, *The European Physical Journal* **C3**, 1 (1998).
- [6] I. Dunietz, *Phys.Lett.* **B427**, 179 (1998).
- [7] B. Barish *et al.*, CLEO CONF 97-01, EPS 97-339. This is available on the web at, <http://www.lns.cornell.edu/public/CONF/1997/Bhad-conf.ps>
- [8] Proceedings of the “ Workshop on B Physics at the Tevatron, Run II and Beyond”, in preparation. See also, <http://www-theory.fnal.gov/people/ligeti/Brun2/> .
- [9] “Determining the CP-violating phase γ ”,
R. Aleksan, I. Dunietz, B. Kayser, *Z. Phys.* **C54**, 653 (1992).
- [10] M. Gronau and D. London, *Phys. Lett.* **B253**, 483 (1991) and M. Gronau and D. Wyler, *Phys. Lett.* **B265**, 172 (1991).
- [11] D. Atwood, I. Dunietz and A. Soni, *Phys. Rev. Lett.* **78**, 3257 (1997).
- [12] M. Gronau and J. Rosner, CALT-68-2142, hep-ph/9711246 (November 1997).
- [13] R. Fleischer and T. Mannel, hep-ph/9704423.
- [14] R. Godang *et al.*, *Phys. Rev. Lett.* **80** 3456 (1998).
- [15] D. Cronin-Hennessy *et al.*, hep-ex/0001010.

- [16] A. Falk, A. Kagan, Y. Nir and A. Petrov, JHU-TIPAC-97018 (December 1997).
- [17] A. E. Snyder and H. R. Quinn, Phys. Rev. **D48**, 2139 (1993).
- [18] M. Bishai *et al.*, (CLEO) “Charmless Hadronic B Decays to Exclusive Final States with a K^* , ρ , ω or ϕ Meson,” CONF 99-13 (1999).
- [19] H. R. Quinn and J. P. Silva, “The Use of Early Data on $B \rightarrow \rho\pi$ Decays,” hep-ph/0001290 (2000).
- [20] Private communication from Jon Rosner.
- [21] P. McBride and S. Stone, Nucl. Instrum. Meth. **A368**, 38 (1995).
- [22] K.T. McDonald, “Maximum Likelihood Analysis of CP Violating Asymmetries”, PRINCETON-HEP-92-04, Sep 1992. 12pp, unpublished.
- [23] A. Ali, “Rare B Decays in the Standard Model”, *Beauty '96*, North Holland Press, 1996, the Netherlands, Table 1, page 13 and references therein.
- [24] C. Greub, A. Ioannissian, and D. Wyler, Phys. Lett. **B346**, 149 (1995).
- [25] G. Burdman, *Phys. Rev.* **D57**, 4254 (1998).
- [26] A. Ali, P. Ball, L. Handoko, and G. Hiller, *Phys. Rev.* **D61** (2000).
- [27] “The CDF II Detector Technical Design Report”, CDF collaboration, FERMILAB-Pub-96/390-E (1996).
- [28] CLEO Collaboration, M.S. Alam *et al.*, *Phys. Rev. Lett.* **74**, 2885 (1995).
- [29] CLEO Collaboration, S. Glenn *et al.*, *Phys. Rev. Lett.* **80**, 2289 (1998).
- [30] C. Bauer, C. Burrell, Phys. Lett. **B469**, 248 (1999).